ABSTRACT

Title of dissertation: AN EXPERIMENTAL STUDY OF STATIC AND OSCILLATING ROTOR BLADE SECTIONS IN REVERSE FLOW

Andrew Hume Lind, Doctor of Philosophy, 2015

Dissertation directed by: Professor Anya R. Jones
Department of Aerospace Engineering

The rotorcraft community has a growing interest in the development of high-speed helicopters to replace outdated fleets. One barrier to the design of such helicopters is the lack of understanding of the aerodynamic behavior of retreating rotor blades in the reverse flow region. This work considers two fundamental models of this complex unsteady flow regime: static and oscillating (i.e., pitching) airfoils in reverse flow. Wind tunnel tests have been performed at the University of Maryland (UMD) and the United States Naval Academy (USNA). Four rotor blade sections are considered: two featuring a sharp geometric trailing edge (NACA 0012 and NACA 0024) and two featuring a blunt geometric trailing edge (ellipse and cambered ellipse). Static airfoil experiments were performed at angles of attack through 180 deg and Reynolds numbers up to $Re = 1.0 \times 10^6$, representative of the conditions found in the reverse flow region of a full-scale high-speed helicopter. Time-resolved velocity field measurements were used to identify three unsteady flow regimes: slender body vortex shedding, turbulent wake, and deep stall vortex shedding. Unsteady airloads were measured

in these three regimes using unsteady pressure transducers. The magnitude of the unsteady airloads is high in the turbulent wake regime when the separated shear layer is close to the airfoil surface and in deep stall due to periodic vortex-induced flow. Oscillating airfoil experiments were performed on a NACA 0012 and cambered ellipse to investigate reverse flow dynamic stall characteristics by modeling cyclic pitching kinematics. The parameter space spanned three Reynolds numbers ($Re = 1.65 \times 10^5$, 3.3×10^5, and 5.0×10^5), five reduced frequencies between 0.100 and 0.511, three mean pitch angles ($-\alpha_{0,\mathrm{rev}} = 5, 10, 15\,\mathrm{deg}$), and two pitch amplitudes ($\alpha_1 = 5, 10\,\mathrm{deg}$). The sharp aerodynamic leading edge of the NACA 0012 airfoil forces flow separation resulting in deep dynamic stall. The number of associated vortex structures depends strongly on pitching kinematics. The cambered ellipse exhibits light reverse flow dynamic stall for a wide range of pitching kinematics. Deep dynamic stall over the cambered ellipse airfoil is observed for high mean pitch angles and pitch amplitudes. The detailed results and analysis in this work contributes to the development of a new generation of high-speed helicopters.

AN EXPERIMENTAL STUDY OF STATIC AND OSCILLATING ROTOR BLADE SECTIONS IN REVERSE FLOW

by

Andrew Hume Lind

Dissertation submitted to the Faculty of the Graduate School of the
University of Maryland, College Park in partial fulfillment
of the requirements for the degree of
Doctor of Philosophy
2015

Advisory Committee:

Professor Anya Jones, Chair/Advisor
Professor James Baeder
Professor Inderjit Chopra
Professor Allen Winkelmann
Professor James Duncan, Dean's Representative

To Mom, Dad, Teresa, and Grandma, for letting me play with Legos on the floor.

Acknowledgments

In March 2011, I visited the University of Maryland and first met with Anya. Before our meeting, she emailed me a handful of papers to read. I remember skimming them on the flight down from Boston and having no idea what they were about. When we met, I'm fairly certain she could tell that I was struggling to remember the new phrases I had just read about like "leading edge vortex" and "retreating blade stall," let alone say anything intelligible about these concepts. But in our conversation, it seemed like she trusted that I would be able to figure things out. I thank her for trusting me then, for giving me freedom in this project, for providing guidance on my experiments and rig designs, and for being critical of my results and writing along the way. I'm grateful to have had Anya as my advisor. She made my Ph.D. a productive and enjoyable learning experience.

Thank you to the U.S. Army/Navy/NASA Vertical Lift Research Center of Excellence for funding my research. I would especially like to thank Dr. Mahendra Bhagwat (Program Manager and Technical Agent), Dr. Peter Lorber (Sikorsky), Dr. John Vorwold (NSWC Carderock), and Dr. Matthew Floros (ARL VTD) for their contributions and feedback. This work was funded under grant number W911W6-11-2-0012.

I also want to thank my Mom, Dad, and sister, Teresa, for their continued love and support. Over the past four years, they willingly listened to my ramblings about finicky pressure sensors, malfunctioning lasers, exam preparations, and writing deadlines. They encouraged me during challenging times and helped me maintain balance by reminding me that there is a lot more to life than research. I would also like to thank my closest friends,

Patrick Duff, Heather Densmore, Hannah Kohut, and Bob Nowak, in part for the countless card games over the years.

I want to thank my teachers who helped me learn, learn how to learn, and develop my passion for engineering and teaching. From the Cape Cod Light House Charter School: Eric Horne, Paul Niles, and John Stewart. From Nauset Regional High School: Steven Swiniarski and Paul Chamberlain. From Brown University: Dr. Janet Blume, Dr. Allan Bower, and Dr. Rick Fleeter. From Cornell University: Dr. Ephrahim Garcia and Dr. Brian Kirby. I would like to thank my committee members for our conversations: Dr. James Baeder, Dr. Inderjit Chopra, Dr. Allen Winkelmann, Dr. Amir Riaz, and Dr. James Duncan.

Thanks to everyone from the lab. First, the original group: Sid Kolluru Venkata, Mark Glucksman-Glaser, Kristy Schlueter, Gino Perotta, and Nate Beals, all of whom remember the days when our lab didn't have walls (or outlets). Next, thanks to those in the golden age of the "new" students: Field Manar, Peter Mancini, and Vera Klimchenko, who helped shape the culture of the lab. I also want to thank Krista Cratty, Jonathan Lefebvre, Albert Medina, and Karen Mulleners. Finally, I especially want to thank Luke Smith and Ignacio Andreu. They contributed countless hours to fabricating models, running tests, and installing pressure sensors. Their patience and commitment to this project was greatly appreciated.

I also want to thank some of the friends I made while at Maryland: David Mayo, Teju Jarugumilli, Bharath Govindarajan, Arber Masati, Joe Milluzo, Anish Sydney, Frank Lagor, Daigo Shishika, Levi DeVries, Elena Shrestha, Stacy Sidle and Alex Barr, Joe Schmaus, Ben Berry, Graham Bowen-Davis, Chen Friedman, Tom Pillsbury, Andrew Becnel, Zohaib

Hasnain, Lina Castano, and Mac MacFarlane.

Finally, I want to thank my new best friend and girlfriend, Anna. The past nine months have been brighter because of her. I'm thankful for her love and support, especially in the weeks leading up to my defense. Anna, I love you. Let's get started on that list of adventures.

Table of Contents

List of Tables

List of Figures

Nomenclature

a	Chordwise distance between quarter-chord and measured pitching moment, in
AR	Aspect ratio
b	Model rotor blade span, in
c	Model rotor blade chord, in
c_a	Sectional chordwise (axial) force coefficient
c_d	Sectional drag force coefficient
c_l	Sectional lift force coefficient
c_m	Sectional pitching moment coefficient about geometric quarter chord
c_n	Sectional normal force coefficient
c_p	Coefficient of pressure, $c_p = (p - p_\infty)/q$
c_x	Interchangeable airload (c_l, c_d, c_m)
C	Chordwise force, lbf
d	Diameter or projected diameter, in
D	Drag, lbf or N
D'	Drag per unit length, lbf/ft or N/m
D_u	Component of drag force (measured from upper force balance), N
f	Airfoil oscillation frequency, Hz
f_s	Sampling frequency, Hz
f_{St}	Strouhal frequency, Hz
f_{vs}	Vortex shedding frequency (unforced), Hz

$\breve{f}$	Deviation from calculated vortex shedding frequency, %
Δf	Frequency resolution, Hz
i	Panel index
k	Scalar used in FFT analysis or reduced frequency, $k = \pi f c / U_\infty$
L	Lift, lbf or N
L'	Lift per unit length, lbf/ft or N/m
m	Panel midpoint
M	Sectional Mach number or pitching moment, in-lbf
n	Number of points used in FFT or number of samples used in time-averaging
$\hat{n}$	Unit normal vector
N	Signal length or normal force measurement, lbf or number of panels
p	Static pressure, psia or Pa
p_∞	Freestream pressure, psia or Pa
q	Dynamic pressure, $q = \frac{1}{2}\rho U_\infty^2$
Q	Peak ratio
r	Panel length or radial distance from the hub, ft or m
R	Rotor radius, ft or m
Re	Reynolds number based on rotor blade chord, c
r/R	Non-dimensional radial station
t/c	Airfoil thickness-to-chord ratio
t	Time, s

$t_{\max}$	Duration of a sample size, s
U_∞	Freestream velocity or forward flight speed, m/s
U_T	In-plane velocity component, m/s
U_P	Inflow velocity component, m/s
U_R	Radial velocity component, m/s

Greek Symbols

α	Angle of attack, deg
α_0	Mean pitch angle, deg (forward flow)
$\alpha_{0,\text{rev}}$	Mean pitch angle, deg (reverse flow)
α_1	Pitch amplitude
α_{cr}	Critical (stall) angle of attack, deg
α_{rev}	Reverse flow angle of attack ($\alpha_{\text{rev}} \equiv \alpha - 180\,\text{deg}$), deg
α_{rev}^{sb}	Maximum angle for which the slender body regime is present, deg
α_{rev}^{ds}	Minimum angle for which the deep stall regime is present, deg
Γ_1, Γ_2	Scalar vortex identification algorithm
ω	Vorticity, 1/s or airfoil oscillation frequency, rad/s
$\hat{\omega}_{x_o/c}$	Sum of vorticity at station x_o/c, 1/s
μ	Advance ratio, $U_\infty/\Omega R$
Ω	Rotor angular rate, rad/s

Ωr	Blade element speed, positioned at a distance r from the hub, m/s
ΩR	Rotor blade tip speed, m/s
Ψ	Rotor blade azimuth, deg
ρ	Density (of air), slugs/ft^3 or kg/m^3
σ	Standard deviation (i.e., variation)
θ	Angle between local unit normal vector and airfoil positive $x-$axis, deg

List of Abbreviations

ABC	Advancing blade concept
CA	Comprehensive analysis
CAD	Computer-aided design
CCWT	Closed-circuit wind tunnel
CFD	Computational fluid dynamics
DAQ	Data acquisition
MHK	Marine hydrokinetic
NACA	National Advisory Committee for Aeronautics
NFAC	National Full-Scale Aerodynamics Complex
NI	National Instruments
NR	Nominal RPM
PID	Proportional integral derivative

PIV	Particle image velocimetry
PDSV	Primary dynamic stall vortex
PTEV	Primary trailing edge vortex
RPM	Revolutions per minute
RVR	Reverse velocity rotor
SDSV	Secondary dynamic stall vorted
SMR	Single main rotor
SNR	Signal-to-noise ratio
SRT	Slowed rotor test
STEV	Secondary trailing edge vortex
TEV	Trailing edge vortex
UMD	University of Maryland
USNA	United States Naval Academy
VIV	Vortex-induced vibrations
X2TD	X2 Technology Demonstrator^{TM}

Chapter 1

Introduction

1.1 Motivation

The motivation to study rotor blade airfoils in reverse flow is largely driven by the demand for high-speed helicopters to serve in missions including emergency medical service, search-and-rescue, runway independent aircraft, and combat operations [1–4]. High-speed helicopters typically use a compound configuration (i.e., the inclusion of auxiliary propulsion, fixed wings, etc.) or a tilt-rotor configuration to attain maximum cruises speeds that are typically on the order of 250 kts or greater–much faster than the cruise speed of conventional helicopters (~ 150 kts). Production tilt-rotor aircraft (e.g., V-22 Osprey) can presently cruise at these high speeds, but their high disk loading, complexity, and operating costs can make them undesirable for routine missions. The U.S. Army Future Vertical Lift program aims to incorporate a new generation of faster (and cost-effective) vehicles in their fleet [5]. High-speed compound helicopters with edgewise rotors offer the potential for greater rotor efficiency and less complexity than tilt-rotors. Several concept vehicles have been designed, built, and tested, but there are currently no production aircraft due to the challenges associated with achieving high-speed cruise speeds while also offering a significant payload. This is, in part, due to the fact that the aerodynamics of reverse flow are not well understood.

1.2 Problem Statement

Reverse flow occurs on a rotor blade when the freestream velocity exceeds the angular velocity of the blade. Figure 1.1 shows the estimated in-plane velocity distribution for one of the rotors of an X2 Technology Demonstrator (X2TD), a modern high-speed coaxial helicopter, during cruise at 250 kts [6]. The velocity distribution at blade azimuth angles of $\psi = 90$ deg and 270 deg is shown with black arrows. On the advancing side of the rotor, flow travels over rotor blades from the geometric leading edge towards the geometric trailing edge (Figure 1.2(a)). This will be referred to as *forward flow*. At $\psi = 270$ deg, rotor blades operate in the *reverse flow region* where flow travels from the geometric trailing edge towards the geometric leading edge (Figure 1.2(b)). In reverse flow, the sharp geometric trailing edge serves as the aerodynamic leading edge and the blunt geometric leading edge serves as the aerodynamic trailing edge. Note that rotor blades typically operate at a negative angle of attack in reverse flow, resulting in the lower surface acting as the suction side.

Reverse flow is inherent to all helicopters in forward flight. However, the size of the reverse flow region increases with forward flight speed, or more precisely, with advance ratio, μ, the ratio of forward flight speed to rotor tip speed. An analytical solution for the circular boundary of the reverse flow region places the center at ($r/R = \mu/2$, $\psi = 270$ deg) with the boundary defined by $r/R = -\mu \sin\psi$. Figure 1.1 shows the X2TD rotor operating at $\mu = 0.77$ where up to 77 % of the retreating blade is subjected to reverse flow.

Prior work has shown that conventional rotor blade airfoils[1] in reverse flow have greater time-averaged drag (due to early flow separation at the sharp aerodynamic leading edge) and pitching moment (due the large moment arm imposed by the center of pressure near the geometric three-quarter-chord) [7–9]. The reverse flow region has also been shown to cause high unsteady blade torsion and pitch link loads on full-scale rotors, leading to vibrations

[1] Conventional rotor blade airfoils are defined here as being less than 15 % thick and featuring a sharp geometric trailing edge

and potentially component fatigue [10–12]. While these detrimental effects of reverse flow are known, the detailed aerodynamic characteristics of the aerodynamic mechanisms of these effects are largely unknown. The objective of the present work is to address this need for an improved understanding of reverse flow by providing an experimental characterization of the time-averaged and unsteady aerodynamics of two models of the reverse flow region: static and oscillating two-dimensional rotor blade airfoils (Figure 1.3).

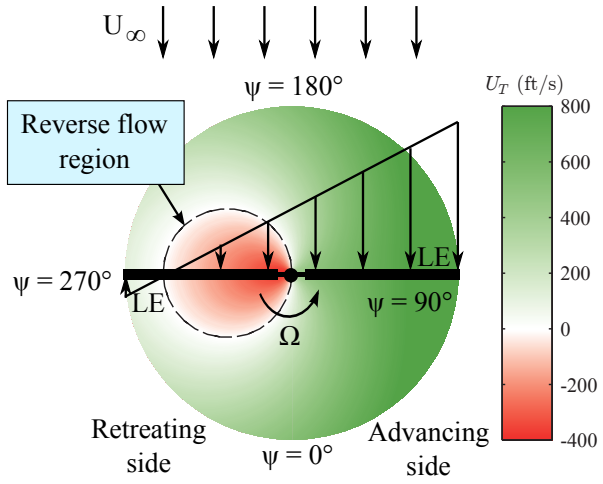

Figure 1.1: Estimated velocity and Reynolds number distributions for an X2TD^{TM} rotor at 250 kts ($\mu = 0.77$) [6].

The extent of prior work on static airfoils in reverse flow has been largely limited to measurement of time-averaged sectional airloads: lift, drag, and pitching moment (Section 1.3.2). While airloads are certainly important for rotor performance predictions, a deeper understanding of the effect of airfoil characteristics on reverse flow performance is needed. For example, the X2TD features an airfoil with a blunt geometric trailing edge on the inboard portion of the rotor blades in an effort to alleviate flow separation in the reverse flow region. However, little work is publicly available that evaluates the aerodynamic behavior of these types of airfoils. Studies have been conducted on the unsteady aerodynamics of stalled conventional airfoils in forward flow, including characterizations of vortex shedding

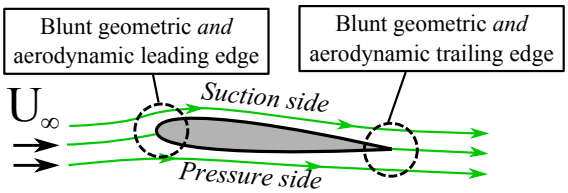

(a) Forward flow.

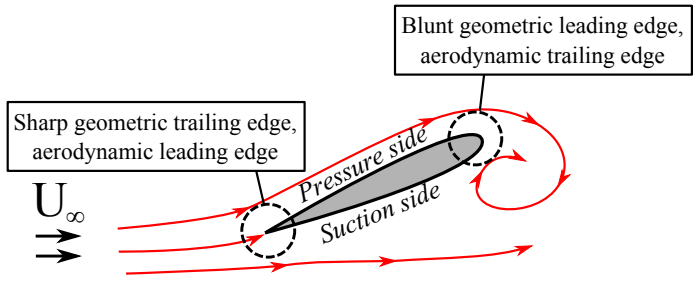

(b) Reverse flow.

Figure 1.2: Definitions for airfoils in forward and reverse flow.

(a) Static airfoil.

(b) Oscillating airfoil.

Figure 1.3: Two fundamental aerodynamic models considered in the present work representative of the behavior of rotor blades in the reverse flow region.

and unsteady airloads, but similar work on airfoils in reverse flow is limited (Section 1.3.3). The unsteady aerodynamics of oscillating airfoils in forward flow has been studied extensively to investigate the phenomenon of dynamic stall (Section 1.3.4), but no work has been performed to characterize dynamic stall in reverse flow. The present work aims to fill gaps in the literature by: 1.) identifying fundamental flow features on airfoils in reverse flow such as separation characteristics, laminar separation bubbles, and vortex shedding, 2.) relating these flow features to the resulting time-averaged and unsteady airloads and, 3.) providing insight into the importance of airfoil characteristics (e.g., trailing edge shape), Reynolds number, and pitching kinematics to airfoil performance in reverse flow.

It should be noted that the aerodynamic models of reverse flow considered in the present work assume two-dimensional flow and a constant freestream. The true reverse flow region of a high-speed helicopter is far more complex. Rotor blade elements near the root transition into and out of the reverse flow region with each revolution, leading to a rapid shift in the center of pressure and an impulsive pitching moment due to the *time-varying freestream* [13]. Like all other portions of the rotor disk, the reverse flow region is also subject to *three-dimensionality* due to radial flow and three-dimensional vortex shedding [11]. The present work, however, provides fundamental insight by analyzing two aerodynamic models representing fully-developed reverse flow, that is, the portion of the reverse flow region where the local freestream velocity is high.

1.3 Background

The effects of reverse flow on helicopters have been known for decades [10]. This section highlights important findings from prior work on the study of reverse flow as it relates to the design of high-speed helicopters. Section 1.3.1 provides an overview of high-speed helicopters, a description of Sikorsky's Advancing Blade Concept, and a comparison of conventional and modern rotor blade airfoils. Section 1.3.2 summarizes key results from work on static airfoils in reverse flow and at high angles of attack. Airfoils that operate at these angles of attack can be fully stalled, so Section 1.3.3 reviews prior work on the unsteady aerodynamics of stalled static airfoils. Finally, Sections 1.3.4 and 1.3.5 review classical dynamic stall of oscillating airfoils (in forward flow) and evidence of dynamic stall in the reverse flow region of high advance ratio rotors.

(a) Sikorsky XH-59A. First flight: 1973. Photo courtesy of Sikorsky.

(b) Sikorsky X2TD. First flight: 2008. Photo courtesy of Sikorsky.

(c) Eurocopter X^3. First flight: 2010. Photo by Agustus Didzgalvis.

(d) Sikorsky S-97 Raider. First flight: 2015. Photo courtesy of Sikorsky.

Figure 1.4: High-speed helicopters.

1.3.1 High-Speed Helicopter Designs

Figure 1.4 shows some of the high-speed helicopters that have been built and tested. All are compound helicopters using auxiliary propulsion and in some cases a fixed-wing lifting surface to unload the main rotor at high speeds (Figure 1.4(c)). The Sikorsky aircraft shown here have relied on a counter-rotating coaxial rotor configuration called the Advancing Blade Concept (ABC) in order to maintain lift at high speeds. All of the helicopters shown are capable of cruise speeds in excess of 200 kts.

The Advancing Blade Concept was first introduced in 1965, motivated by the need to overcome two aerodynamic barriers preventing conventional helicopters from achieving high-

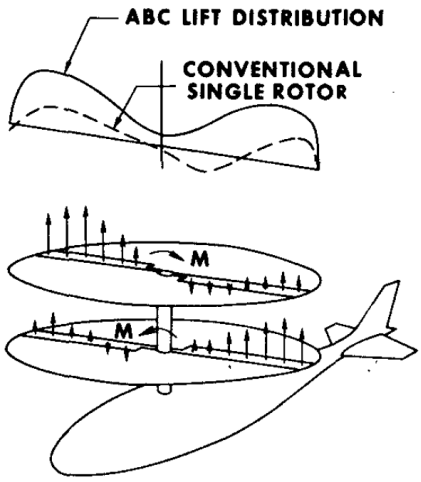

Figure 1.5: Lift distribution for conventional and ABC^{TM} rotors [14].

speed flight: compressibility effects on the advancing blade tips, and stall of the retreating blade due to excessively high angles of attack and reverse flow. For a conventional helicopter with a single main rotor (SMR), the maximum lift capability of the retreating blade is low and the advancing blade must compensate for this by operating at inefficient angles of attack leading to poor overall rotor performance at high speeds [14]. The ABC utilizes counter-rotating coaxial rotors to allow each advancing blade to achieve its lifting potential by optimizing the angle of attack distribution. The retreating blades are unloaded, but reverse flow still exists over much of the blade. Figure 1.5 shows that the overall lift distribution is symmetric along the longitudinal plane–much like a fixed-wing aircraft–but this is a result of asymmetric lift distributions for each rotor. To address this asymmetry, extremely stiff, hingeless rotor blades are required to cope with the high amplitude cyclic rolling moments experienced as they rotate through the rotor disk.

The XH-59A was the first ABC vehicle to undergo flight testing (Figure 1.4(a)) [15, 16]. In 2004, Sikorsky developed the X2TD to evaluate technologies that could enable cost-effective high-speed flight (Figure 1.4(b)). Modern rotor blades were designed to aid in achieving this goal [6, 17]. Unlike the XH-59A, the X2TD rotor features continuously

varying airfoil sections in the radial direction. Double-ended airfoils (i.e., airfoils with a blunt geometric trailing edge) are used for the inboard portion of the rotor blade where the highest dynamic pressures in reverse flow exist due to the low rotational speed. Figure 1.6 shows sketches of the airfoil sections used on the inboard portion of the XH-59A and X2TD rotor blades, as well as the lateral lift and drag distributions predicted using Sikorsky's "Generalized Rotor Performance" methods. Three key findings are shown in Figure 1.6. First, the blunt geometric trailing edge of the X2TD airfoil (red) delays flow separation leading to lower drag (D') than the conventional airfoil found on the XH-59A (purple). Second, the twist angle decreased with decreasing radial station (i.e., wash in) for $0.14 \leq r/R \leq 0.4$ in order to reduce the negative angle of attack and resulting negative lift (L') on the retreating side. Finally, the advancing side lift distributions are generally similar for the XH-59A and X2TD rotor blades, suggesting minimal influence of the blunt geometric trailing edge of the X2TD airfoil on advancing side performance. The decision to employ an airfoil with a blunt geometric trailing edge on the X2TD rotor blade was driven by the numerous detrimental aerodynamic of conventional airfoils in reverse flow given in the next section.

1.3.2 Conventional Airfoil Behavior in Reverse Flow

Prior work on airfoil behavior in reverse flow focused on conventional airfoils held at static angles of attack. These studies provide insight on the high time-averaged pitching moment and drag, stall characteristics, and Reynolds number effects, all of which affect rotor blade performance in the reverse flow region of a high-speed helicopter. Much of the prior work also considered airfoil behavior at high angles of attack.[2] This is relevant to the present work as well since local airfoil sections experience a large change in angle of attack as they transition into and out of the reverse flow region (Figure 1.1). The Reynolds numbers

[2] "High" angles of attack are defined in the present work as $30 \leq \alpha \leq 150\,\text{deg}$ and $210 \leq \alpha \leq 330\,\text{deg}$.

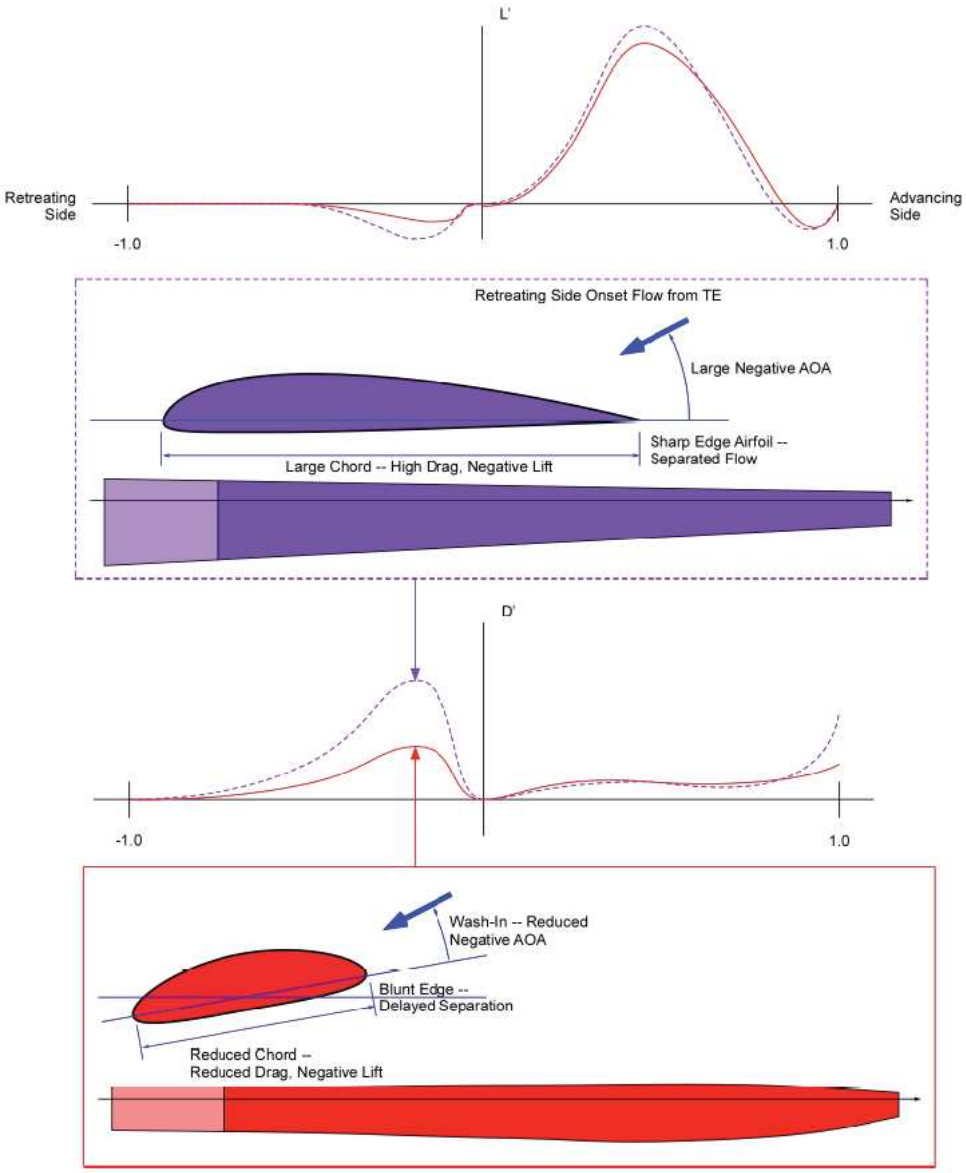

Figure 1.6: Lateral lift and drag distributions for the XH-59A and X2TD rotor blades [6].

of the prior work discussed in this section closely match values encountered by rotor blades in the reverse flow region of a modern high-speed helicopter ($0 \leq Re \leq 1.5 \times 10^6$).

Early studies were predominantly conducted by the National Advisory Committee for Aeronautics (NACA) in order to study reverse flow for fixed-wing inverted flight maneuvers of warplanes and gusty ground conditions in which flow can travel backwards over wings and control surfaces [18–20]. Naumann studied the pressure distribution of two finite wings, one with a NACA 2212 airfoil section and another with a M6 airfoil section. He concluded that the pressure distributions were essentially independent of the variations of the two airfoils that were tested, suggesting that flow separation at the sharp leading edge of a conventional airfoil in reverse flow dominates the pressure distribution rather than the shape of the airfoil itself. Pope measured pressure distributions of a NACA 0015 at angles of attack through 180 deg [7]. Figure 1.7 shows that the center of pressure on the pressure side of the airfoil shifts from the leading edge towards the trailing edge as the angle of attack passes through 90 deg. This is the source of the large pitching moment that arises in reverse flow as the shift in center of pressure increases the moment arm about the geometric quarter-chord.

Critzos et al. examined the time-averaged airloads acting on a NACA 0012 at two Reynolds numbers, $Re = 5 \times 10^5$ and 1.8×10^6 [8]. Figure 1.8 shows time-averaged airload measurements collected at angles of attack through 360 deg. All three curves show symmetry about $\alpha = 180$ deg with the pitching moment and lift curves reflected about $c_m = 0$ and $c_l = 0$. This is expected since the NACA 0012 airfoil section is symmetrical about $z/c = 0$. Focusing first on the lift curve (lower curve), the value of $c_{l,\max}$ in reverse flow is nearly two-thirds of the value in forward flow (0.8 and 1.25 respectively). It is also worth noting that in forward flow, the airfoil exhibits a leading edge stall with a sharp reduction in lift. In reverse flow, the airfoil appears to exhibit a thin-airfoil stall. Shifting attention to Figure 1.9, a comparison of forward (normal) and reverse flow is shown for a NACA 0012 at $Re = 1.0 \times 10^6$ [9]. Indeed, the lift and drag curves in reverse flow show a thin-airfoil stall: a moderate, steady increase

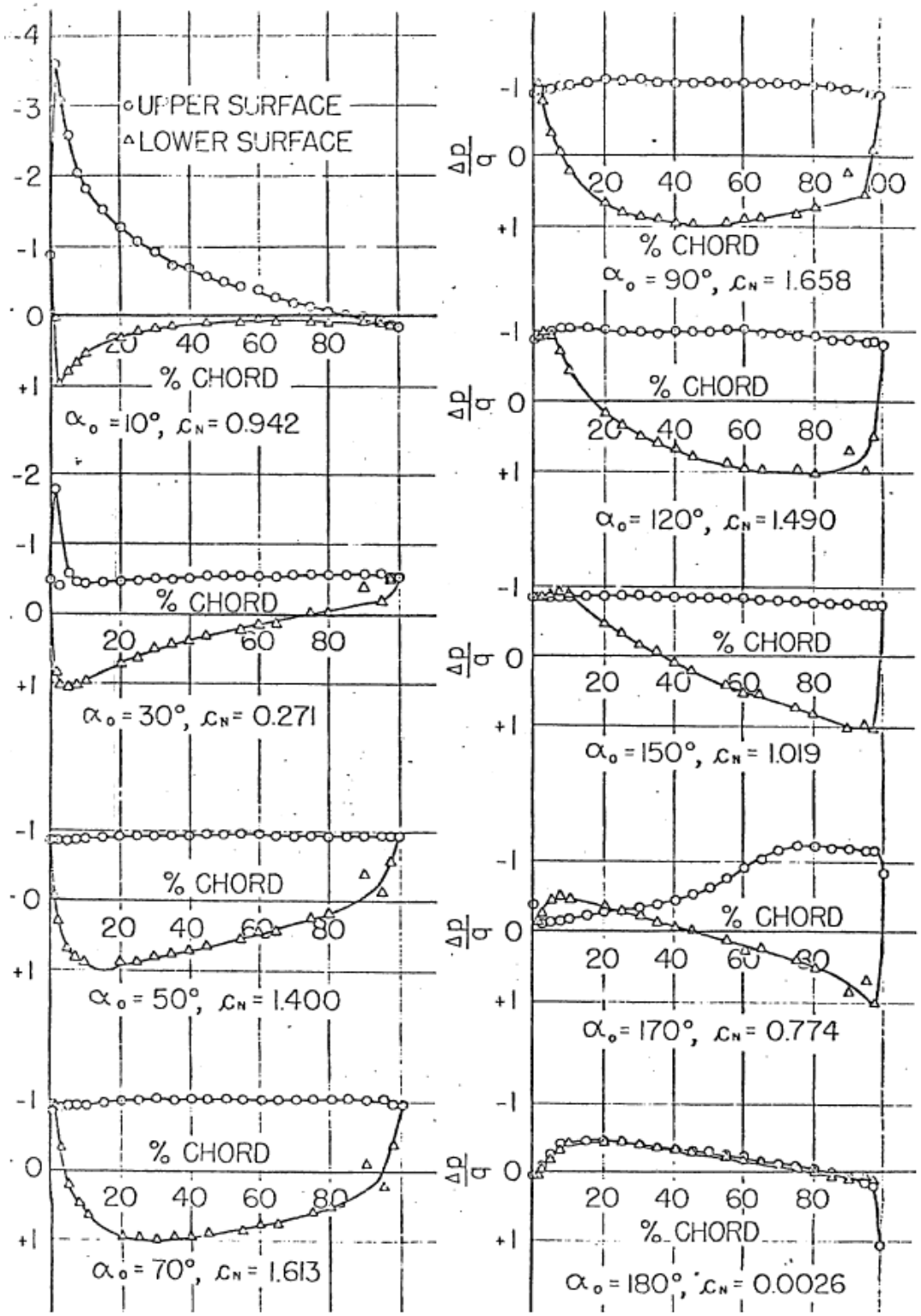

Figure 1.7: Pressure distributions for a NACA 0015 airfoil through high angles of attack and in reverse flow at $Re = 1.23 \times 10^6$ [7].

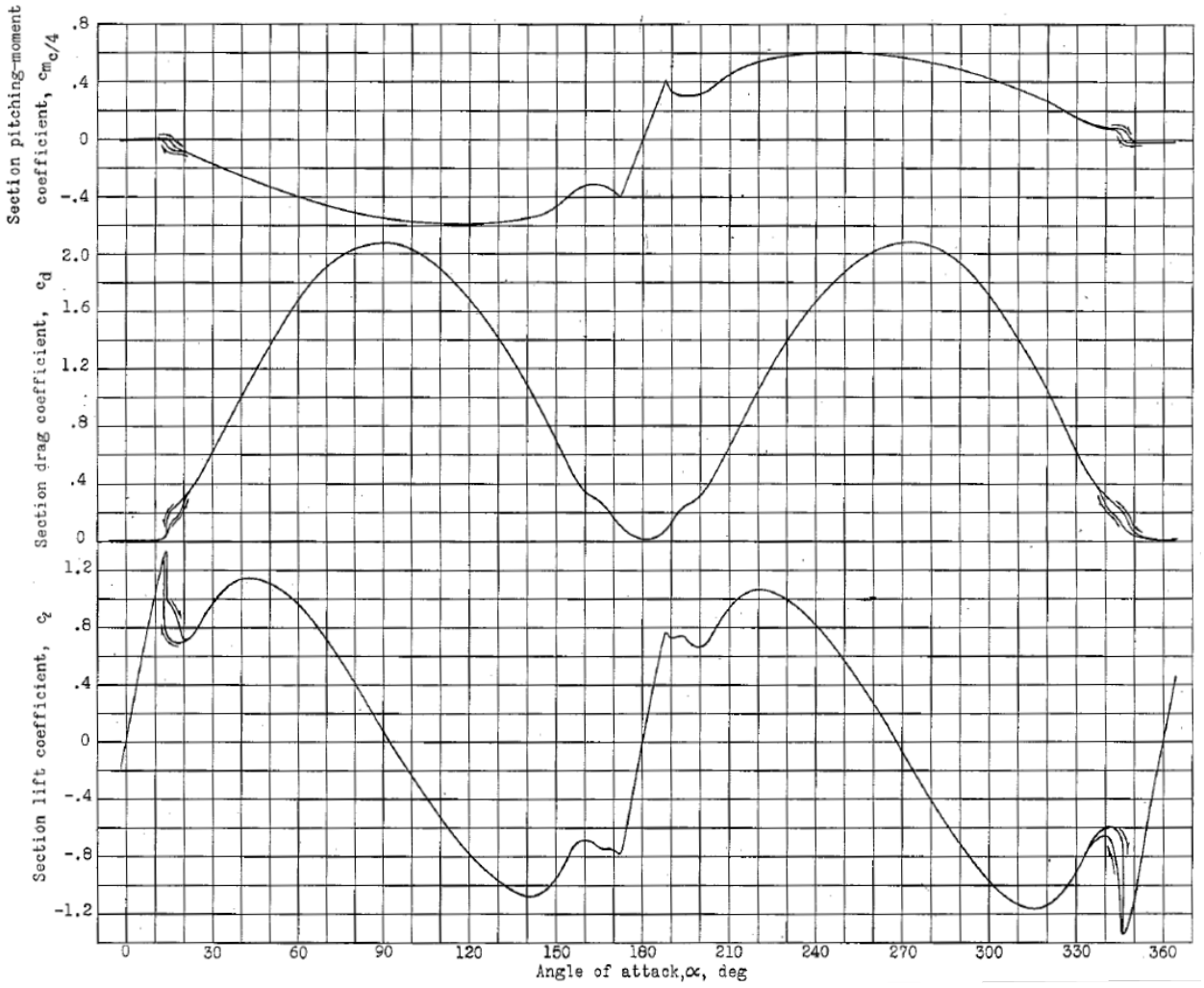

Figure 1.8: Sectional airload coefficients for a smooth NACA 0012 over an angle of attack from 0–360 deg at $Re = 1.8 \times 10^6$ [8]

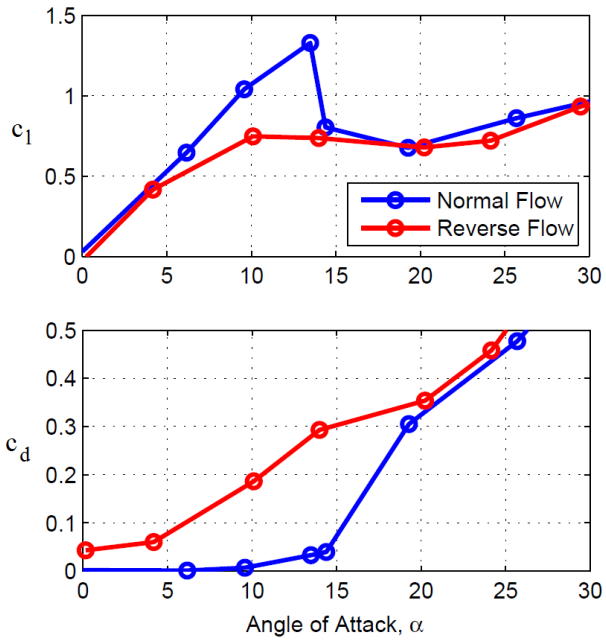

Figure 1.9: Drag and lift coefficients of a NACA 0012 near stall in both normal (i.e., forward) and reverse flow at $Re = 1.0 \times 10^6$. Data courtesy of J. G. Leishman.

in drag with angle of attack and flattening of the lift curve near $\alpha = 10\,\text{deg}$ [21, 22]. Note that for $\alpha = 0\,\text{deg}$, drag is significantly greater in reverse flow due to flow separation near the blunt aerodynamic trailing edge. Crtizos et al. found similar behavior, noting that the minimum drag coefficient was twice as large in reverse flow. Returning to Figure 1.8, the drag curve (center curve) has maximums when the airfoil is perpendicular to the freestream at $\alpha = 90\,\text{deg}$ and $\alpha = 270\,\text{deg}$. This corresponds closely with the theoretical value for a flat plate at an angle of attack of 90 deg. Finally, focusing on the sectional pitching moment curve about the geometric quarter-chord (upper curve), the pitching moment is essentially zero for attached flow in forward flow, consistent with thin airfoil theory [22, 23]. In reverse flow ($150 \leq \alpha \leq 210\,\text{deg}$), the pitching moment curve is highly sensitive to angle of attack due to the large moment arm between the center of pressure and the quarter-chord [7]. As a result, the pitching moment curve mimics the behavior of the lift curve in reverse flow.

Recall that the local freestream velocity in the reverse flow region of a high-speed helicopter varies radially and azimuthially. This leads to a wide range of Reynolds numbers encountered by retreating rotor blades. Figure 1.10 shows the effect of Reynolds number on a NACA 0012 in reverse flow [8]. At $Re = 0.5 \times 10^6$ (Figure 1.10(a)), the lift curve has a discontinuity at $\alpha = 180\,\text{deg}$. The authors believe that this discontinuity was a consequence of different chordwise locations of the separation points on the pressure and suction sides of the airfoil. They suggested that at small angles of attack in reverse flow (e.g., $\alpha = 181\,\text{deg}$), a small separation bubble forms on the suction side near the sharp leading edge, causing the boundary layer to transition to turbulent. On the pressure side of the airfoil, it is believed that a favorable pressure gradient exists and that the boundary layer remains laminar. However, this leads to earlier flow separation near the blunt trailing edge as compared to the suction side of the airfoil where the boundary layer is turbulent. This allows for a greater amount of suction. This behavior occurs on opposite sides of the airfoil for $\alpha = 179\,\text{deg}$, leading to the appearance of a discontinuity. At $Re = 1.8 \times 10^6$ (Figure 1.10(b)), the Reynolds number is sufficiently high that the boundary layer transitions to turbulent on both sides of the airfoil leading to similar separation points and no discontinuity.

Little work has considered Reynolds number effects on reverse flow over airfoils with a blunt geometric trailing edge [24]. However, insight can be gained by considering forward flow over conventional airfoils since the aerodynamic leading edge is blunt in both cases. Figure 1.11 shows the effect of Reynolds number on a NACA 0012 in forward flow [25]. An increase in Reynolds number results in an increase in $c_{l,\max}$, stall angle, and $c_{d,0}$. This is a result of the formation of a more energetic turbulent boundary layer closer to the leading edge. The boundary layer is able to overcome stronger adverse pressure gradients near the leading edge, delaying flow separation to a larger angle of attack.

Collectively, the results in Figures 1.10 and 1.11 illustrate the importance of Reynolds number on boundary layer behavior over an airfoil and the resulting impact on time-averaged

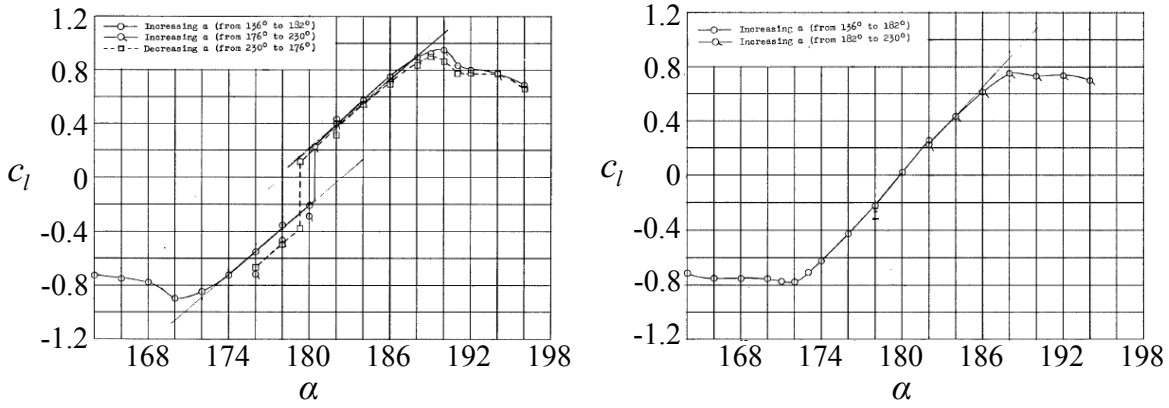

(a) $Re = 0.5 \times 10^6$ (b) $Re = 1.8 \times 10^6$

Figure 1.10: Reynolds number effects on the lift curve of a NACA 0012 in reverse flow [8].

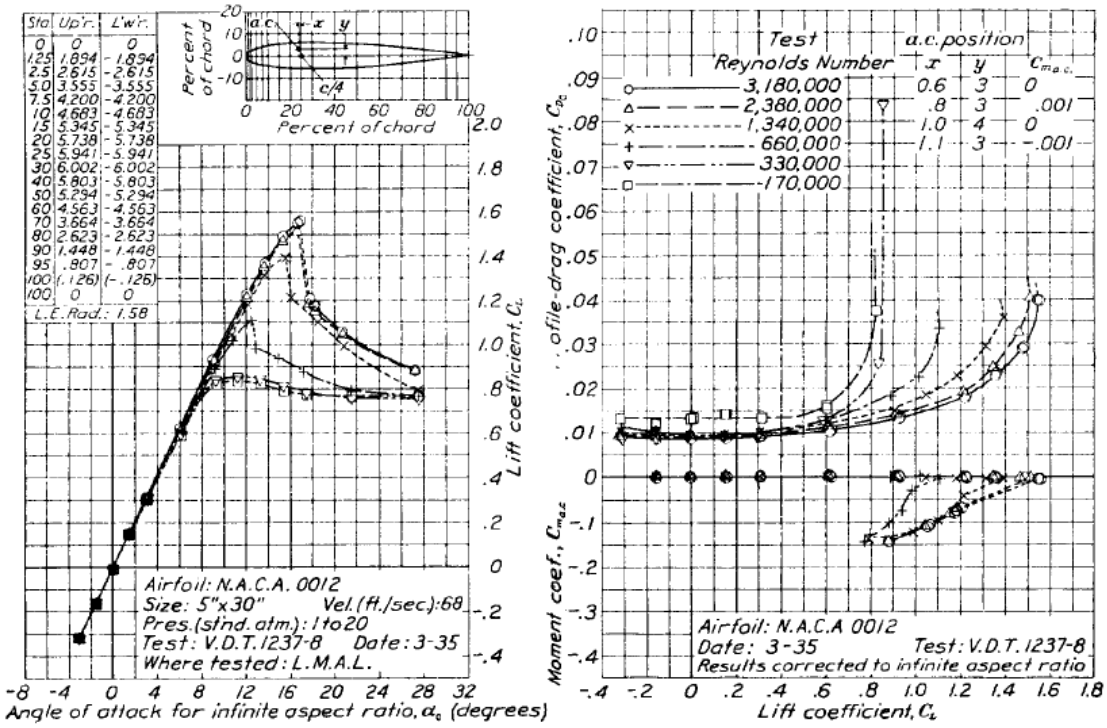

Figure 1.11: Reynolds number effects on the lift curve of a NACA 0012 in forward flow [25].

airloads. Reynolds number effects are particularly important for reverse flow because 1.) some level of flow separation will always occur at the blunt aerodynamic trailing edge and 2.) the shape of the aerodynamic leading edge can play a significant role in boundary layer transition and separation.

In reverse flow, drag and pitching moment are greater than in forward flow, conventional airfoils undergo a thin airfoil stall, and lift is sensitive to Reynolds number near $\alpha = 180\,\text{deg}$. These results give fundamental insight on the airloads that rotor blade airfoils in the reverse flow region may be subjected to, but flowfield measurements are needed to characterize these effects on conventional and blunt-trailing-edge airfoils in reverse flow. Flowfield measurements will also highlight the importance of airfoil parameters on flow separation characteristics and resulting airloads.

1.3.3 Unsteady Aerodynamics of Stalled Static Airfoils

The flowfield over an airfoil operating at a stalled angle of attack is characterized by massive flow separation over the suction side. This typically leads to a decrease in time-averaged lift and increase in both drag and pitching moment. Flow separation can also lead to unsteady forcing on airfoils, sometimes referred to as buffeting [26]. This forcing can exist over a wide frequency band (i.e., aperiodic) or a narrow band in the presence of vortex shedding (i.e., periodic). If the vortex shedding frequency matches a structural resonance frequency, the unsteady periodic forcing can induce vibrations [27]. Rotor blade airfoils can be stalled in the reverse flow region of a high-speed helicopter. An understanding of both the *frequency content* and *magnitude* of unsteady airloads is important for the prediction and mitigation of rotor blade vibrations due to the reverse flow region.

Vortex shedding in the wake of static airfoils has been studied, though most of the work considers forward flow angles of attack [28–33]. Huang and Lin studied a NACA 0012 in forward flow at Reynolds numbers $O(10^4 - 10^5)$ using smoke flow visualization (Figure 1.12)

and spectral analysis of hotwire measurements collected in the wake [29]. Figure 1.13 shows that vortex shedding was classified into one of four regimes depending on both Reynolds number and angle of attack: laminar, subcritical, transitional, or supercritical. These modes were closely related to the behavior of the boundary layer over the suction side of the airfoil. High frequency vortex shedding was found in the laminar and subcritical regimes. In the transitional flow regime, turbulence began to dominate and break up structures in the wake before periodic vortex shedding could be established. Low frequency turbulent vortex shedding superimposed with high frequency shear layer instability waves was observed in the supercritical regime. The vortex shedding frequency was found to increase with increasing freestream velocity (for a fixed angle of attack) and decrease with increasing angle of attack (for a constant freestream velocity).

Pellegrino and Meskell recently performed numerical simulations of the unsteady flow over a static two-dimensional wind turbine blade section (NREL S809) [34]. This airfoil profile has a sharp geometric trailing edge, is 21% thick at $x/c = 0.395$, and has a maximum of 1% camber at $x/c = 0.823$. Figure 1.14 shows the variation of Strouhal number with angle of attack with two different characteristic lengths. Using the airfoil chord as the characteristic length (red circles), it can be seen that the Strouhal number varies greatly with angle of attack, with minimum values near $\alpha = -90\,\text{deg}$ and $\alpha = 90\,\text{deg}$. For high angles of attack ($-110 \leq \alpha \leq -60\,\text{deg}$ and $60 \leq \alpha \leq 110\,\text{deg}$), the Strouhal number based on the projection of the airfoil chord ($d = c\sin\alpha$, blue triangles) is relatively constant, suggesting that this length scale may serve well as a universal length scale at these high angles of attack, though only a single airfoil was considered.

The magnitude of unsteady airloads is also important as this can determine the severity of resulting structural vibrations. Unsteady airloads can be measured using direct time-resolved force measurements, but this typically requires a dynamic calibration of the force balance system to separate the structural and aerodynamic responses to unsteady aero-

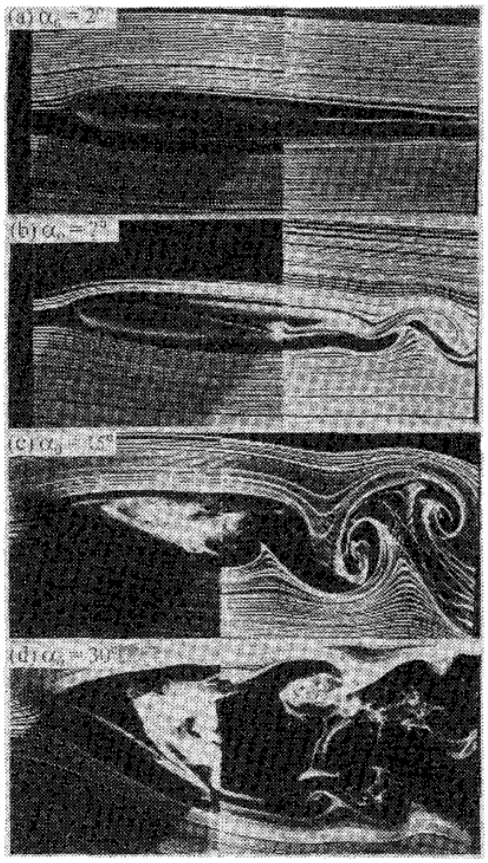

Figure 1.12: Instantaneous smoke flow visualization of a NACA 0012 at pre-stall and post-stall angles of attack ($Re = 3.195 \times 10^3$) [29]

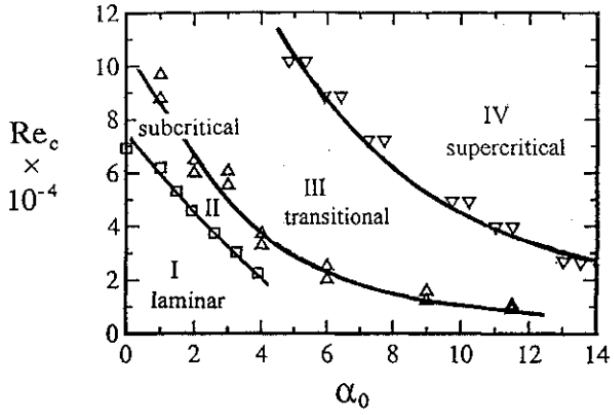

Figure 1.13: Variation of characteristic vortex shedding modes with Reynolds number and angle of attack [29].

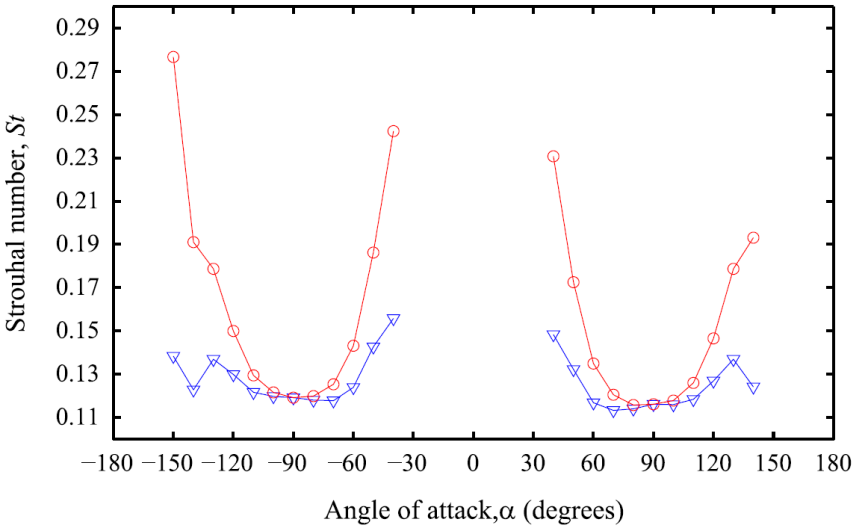

Figure 1.14: Variation of Strouhal number with angle of attack with different characteristic lengths: red circular markers use the airfoil chord, c, and blue triangular markers use a projection of the airfoil chord, $d = c\sin\alpha$. [34].

dynamic forcing. Direct force measurements do not allow for identification of sources of unsteady loading in the chordwise direction. Time-resolved (i.e., unsteady) surface pressure measurements provides a means to study the separated (and separating) flow characteristics and can be integrated to determine the impact on the unsteady airloads. For example, unsteady surface pressure measurements have been used to study airfoil buffeting and the development of static stall [35, 36]. Figure 1.15 shows that fluctuations in lift and pitching moment were found to be greatest post-stall ($\alpha = 15\,\text{deg}$) and decrease in magnitude as angle of attack is increased ($\alpha = 20\,\text{deg}$) [36]. While fundamental insight can be gained from this work, a need remains for work that quantifies the magnitude and frequency unsteady airloads on static airfoils in reverse flow to contribute to the prediction and mitigation of rotor blade vibrations.

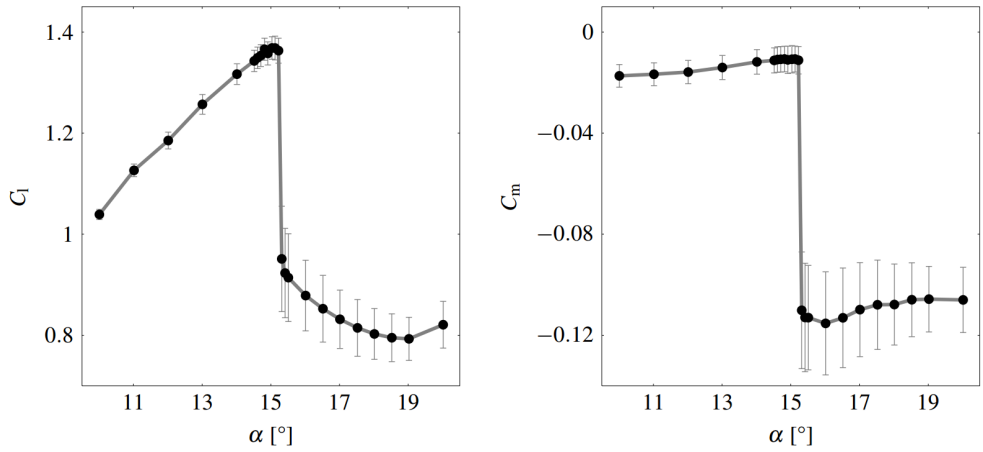

Figure 1.15: Variation of lift (left) and pitching moment (right) with static angle of attack for the OA209 airfoil and $Re = 1.8 \times 10^6$. The error bars represent the magnitude of unsteady variations of the airloads [36].

1.3.4 Dynamic Stall

Dynamic stall has long been known to be a source of unsteady airloads for helicopters [13]. Cyclic pitch inputs during forward flight lead to airfoil oscillations in pitch that, if the pitching kinematics are severe enough, can cause dynamic stall. This often occurs on the retreating side of a helicopter rotor (the portion that operates in forward flow), so dynamic stall is often referred to as *retreating blade stall* in the rotorcraft community. Dynamic stall results in highly non-linear and unsteady airloads, unsteady aerodynamic response, high pitch-link loads, and stall flutter [37–40]. This aerodynamic behavior also been observed in the reverse flow region of a full-scale helicopter (Section 1.3.5), motivating the need for an investigation of reverse flow dynamic stall. The rich history of experimental work on classical dynamic stall gives insight that can be applied to the present work, part of which concerns dynamic stall from oscillating airfoils in reverse flow.

Due to the complex nature of dynamic stall, most prior work has focused on experiments on 2-D conventional airfoils oscillating about the quarter-chord in a constant freestream (forward flow). This simplified model of rotor blade dynamic stall accurately

captures the behavior of dynamic stall on a full-scale rotor [40]. Even when using this simplified aerodynamic model, the problem remains complex due to the large number of parameters that affect the evolution of dynamic stall. Pitching kinematics (frequency, mean pitch angle, and pitch amplitude) play a strong role as they contribute to the amount of flow separation and time scale of the evolution of dynamic stall [41]. Reynolds number can affect the timing of dynamic stall events since it affects the ability of the boundary layer to overcome adverse pressure gradients associated with dynamic stall. [41] Mach number also plays a role, especially near sonic conditions when shock waves can affect the motion of the center of pressure as well as boundary layer separation and reattachment characteristics. [13]

Dynamic stall can be broadly categorized into one of three types: onset, light, or deep. Figure 1.16 illustrates the effect of these three types of dynamic stall on unsteady airloads [37]. In stall onset, the airfoil oscillations lead to little to no flow separation and the airload curves closely resemble a quasi-steady flow. Stall onset occurs when the maximum pitch angle is near (or below) the static stall angle. During light dynamic stall, the static stall angle is exceeded, but the flow generally remains attached until the maximum pitch angle is achieved. Some mild flow separation then leads to a loss of lift, increase in drag, and nose-down pitching moment (similar to static stall). The degree of flow separation is strongly linked to the shape of the leading edge; a leading edge of a thin airfoil generally forms a strong adverse pressure gradient over the first few percent of the chord. In this case, a dynamic leading edge stall may be observed. For thicker airfoils, the pressure gradient near the leading edge is less severe, so a dynamic trailing edge stall may occur [42]. In either case, this results in a small amount of hysteresis in the lift and pitching moment curves (Figure 1.16). Deep dynamic stall is typically achieved with pitch oscillations that drastically exceed the static stall angle of attack (typically by 10 degrees or more). This leads to a large hysteresis loop in the lift curve, nose-down pitching moment, and increase in drag (Figure 1.16).

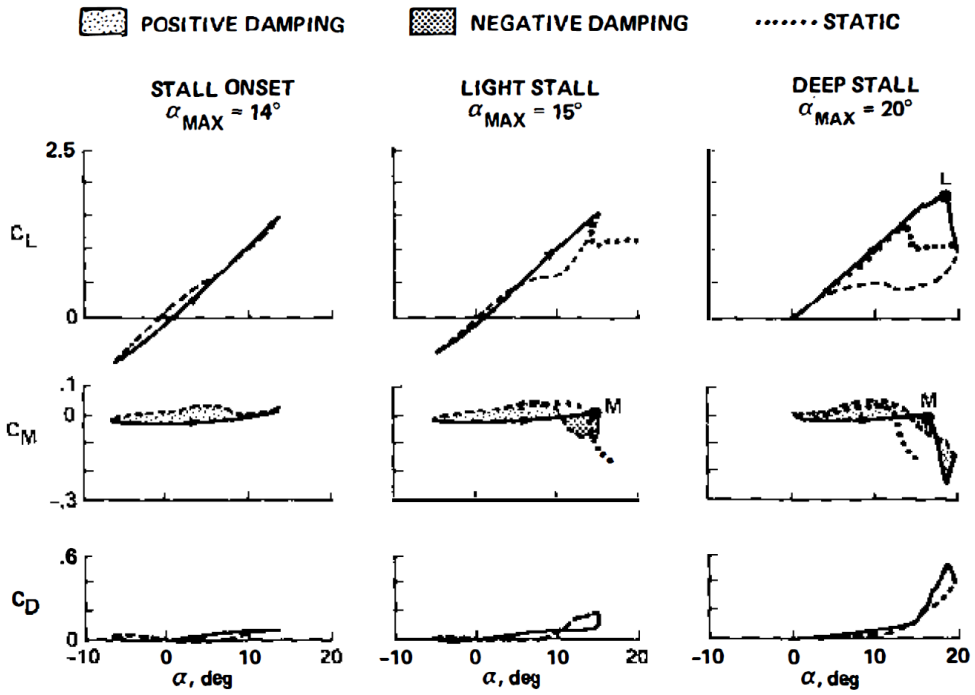

Figure 1.16: Types of dynamic stall [37].

The evolution of deep dynamic stall is of greatest interest due to the large variations in unsteady airloads. Detailed descriptions on the flow morphology and effects on the unsteady airloads are given by Carr [43], Beddoes [38], and Leishman [13]. Figure 1.17 shows a summary of the progression of deep dynamic stall events on the normal force and pitching moment [38]. Note that $c_n \approx c_l$. During the first portion of the pitching cycle, the angle of attack increases and the lift exceeds static $c_{l,\max}$. This is due to the reduction of the effective angle of attack (and associated introduction of induced camber) due to the pitching motion of the airfoil allowing the flow to remain attached [13, 43]. This is indicated in Figure 1.17 as event #1. Eventually, the adverse pressure gradient at the leading edge becomes strong enough that rapid turbulent flow separation occurs over the entire airfoil. The dynamic stall vortex then begins to form at event #2. As the vortex grows, it enhances lift (#2-#3) while its convection towards the trailing edge induces a large negative pitching moment. This is a direct result of a shifting "wave" of low pressure associated with the dynamic stall

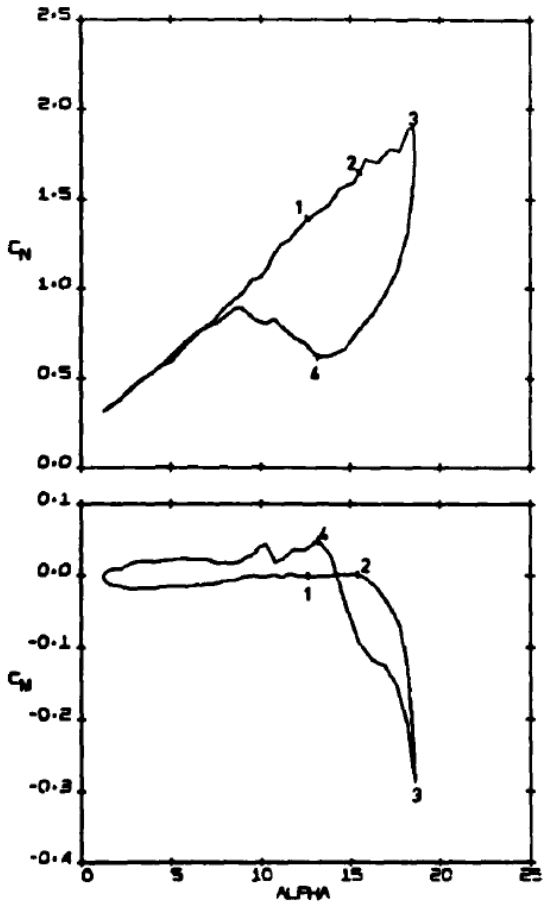

	FORCES AND MOMENTS
1	EXCEEDS STATIC MAXIMUM LIFT. EXTRAPOLATE LINEAR RANGE.
2	PITCHING MOMENT DIVERGENCE. VORTEX LIFT PRESENT.
3	MAXIMUM LIFT, RAPID DECAY. MAXIMUM PITCHING MOMENT.
4	READJUST TO LINEAR RANGE.

	FLOW STRUCTURE
1	FLOW REVERSALS WITHIN BOUNDARY LAYER. FORMATION OF VORTEX
2	VORTEX DETACHES AND MOVES OVER AIRFOIL SURFACE.
3	VORTEX PASSES TRAILING EDGE. FULL STALL DEVELOPS.
4	REATTACHMENT OF FLOW.

Figure 1.17: Typical progression of deep dynamic stall events [38].

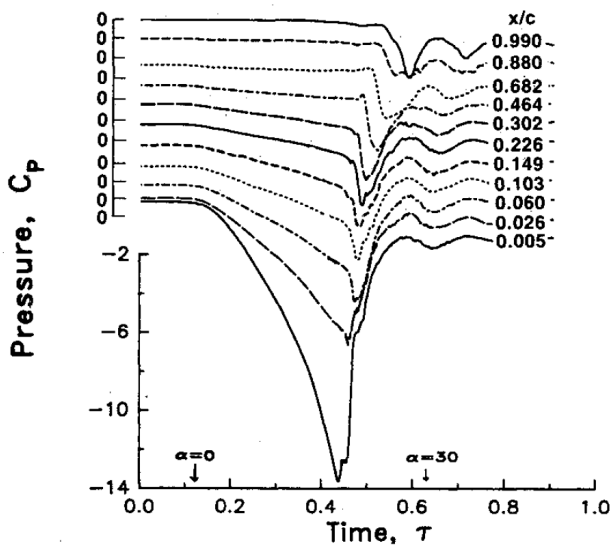

Figure 1.18: Effect of the convection of the dynamic stall vortex on the pressure distribution of the suction side of a SSC-A09 airfoil undergoing a constant-rate pitching motion [39].

vortex. Figure 1.18 shows a representative example of the convection of low pressure from the leading edge towards the trailing edge [39]. The precipitous increase in the magnitude of pitching moment is called *moment stall* [43]. Once the vortex convects off the trailing edge (event #3 in Figure 1.17), the pitching moment rapidly begins to return towards zero, but the lift also decreases rapidly since the flow is fully separated and the lift enhancement from the dynamic stall vortex is no longer present. This is *lift stall*, and it always occurs *after* moment stall during deep dynamic stall.[3] As the angle of attack is decreased through the second half of the cycle (event #4 in Figure 1.17), the flow begins to reattach and the lift curve becomes linear once more. In summary, deep dynamic stall delays massive flow separation to a greater angle of attack than static stall, but the influence of the dynamic stall vortex results in severe and rapid variations and hysteresis of unsteady airloads.

Deep dynamic stall is highly sensitive to pitching kinematics [41, 44]. The first pitching kinematic that will be considered is *reduced frequency*, $k = \pi f c/U_\infty$, where f is the

[3]Lift stall and moment stall occur at the same angle of attack during static stall [41].

dimensional oscillation frequency in Hz.[4] Figure 1.19 shows the effect of reduced frequency on unsteady airloads in deep dynamic stall for a fixed mean pitch angle and pitch amplitude [41]. At low reduced frequencies ($k \leq 0.05$), the airload curves somewhat resemble their quasi-steady counterparts, with only moderate airload enhancement due to the dynamic stall vortex. The dynamic stall vortex forms and convects before the maximum angle of attack is achieved [43]. However, at $k = 0.150$ in Figure 1.19, the maximum magnitude of the airloads is larger than for the lower reduced frequencies as the timing of the formation of the dynamic stall vortex is concurrent with the maximum angle of attack. For an even greater reduced frequency of $k = 0.250$, dynamic stall vortex formation occurs so late in the pitching cycle that lift is enhanced during the beginning of the downstroke. This appears in the unsteady lift curve as a small "figure-8" loop near the maximum angle of attack.

Reduced frequency also affects the magnitude of the suction peak induced by the dynamic stall vortex. Early work showed that the suction peak grows with greater values of reduced frequency, suggesting that this corresponds to a stronger dynamic stall vortex [41]. This was reasoned to be linked with the circulation of the airfoil at the time that the vortex is formed. It was later suggested that vortex strength is independent of reduced frequency for $k > 0.15$ [42]. However, these postulations were based on pressure measurements only, rather than direct flowfield measurements of the dynamic stall vortex strength. Further work is needed to characterize the influence of reduced frequency on the strength of the dynamic stall vortex and resulting impact on unsteady airloads since the value of reduced frequency varies greatly across the rotor disk of a high advance ratio vehicle.

Dynamic stall is also sensitive to the mean pitch angle, α_0, and pitch amplitude, α_1. Figure 1.20 shows the effect of varying mean pitch angle with a constant pitch amplitude at a constant reduced frequency. For $\alpha_0 = 6\,\text{deg}$, the airfoil operates in the stall onset regime with only mild effects on the pitching moment curve noted. For $\alpha = 11\,\text{deg}$, the airfoil operates

[4]Reduced frequency can also be defined $k = \omega c/2U_\infty$, where ω is the oscillation frequency in rad/s.

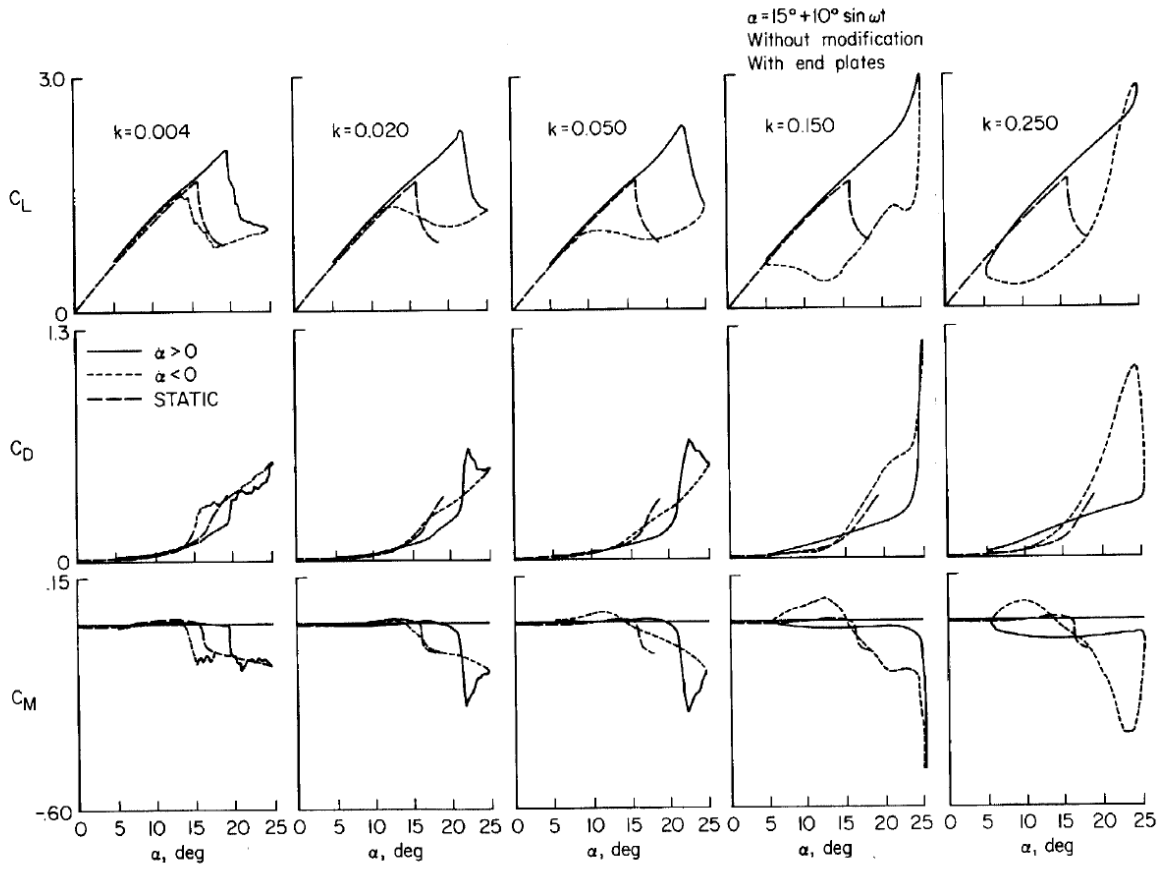

Figure 1.19: Effect of reduced frequency on unsteady airloads of a NACA 0012 in deep dynamic stall [41].

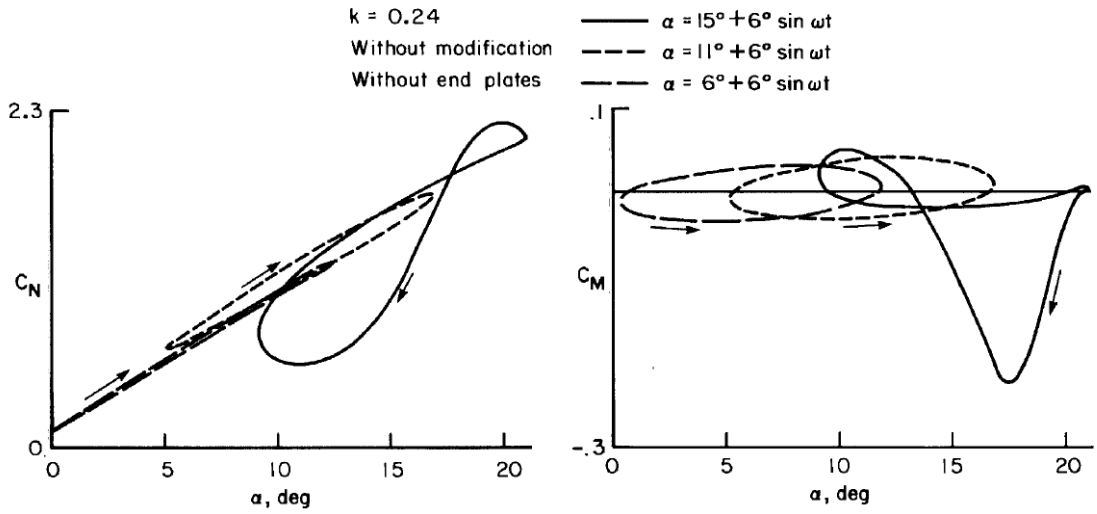

Figure 1.20: Effect mean pitch angle on dynamic stall of a NACA 0012 airfoil at $Re = 2.5 \times 10^6$ [41].

in light dynamic stall as evidenced by the mild hystereseis in the lift curve. Finally, at $\alpha = 15\,\text{deg}$, the airfoil operates in deep dynamic stall with more a more significant impact on the unsteady airloads. The combination of mean pitch angle and pitch amplitude determine the degree to which the static stall angle is exceeded (or not exceeded), and therefore play a key role in determining the type of dynamic stall observed, the timing of the stall events, and the degree to which the dynamic stall vortex affects the unsteady pressure distribution [43].

1.3.5 Dynamic Stall in the Reverse Flow Region

Evidence of *reverse flow dynamic stall* was observed in a recent study on the full-scale aerodynamics and rotor dynamics of a UH-60A operating at high advance ratios [11,12,45,46]. Figure 1.21(a) shows the experimental setup of this slowed rotor test (SRT) with a full-scale UH-60A rotor installed in the National Full-Scale Aerodynamics Complex (NFSAC) 40- by 80-ft wind tunnel [12]. Figure 1.21(b) shows the airfoil sections of a UH-60A rotor blade [47]. Experiments were performed at advance ratios up to $\mu = 1.0$ by slowing the rotor down to 40% of its nominal RPM (NR). Measurements were collected on rotor performance, blade

(a) Rotor installed in the NFAC 40- by 80-ft wind tunnel [12].

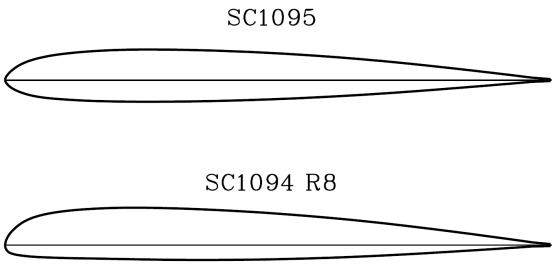

(b) Rotor blade sections [47].

Figure 1.21: Experimental rig for full-scale UH-60A slowed rotor test (SRT).

loads, hub loads, and surface pressure measurements. The test conditions were also simulated with coupled computational fluid dynamics and comprehensive analysis (CFD/CA) [11, 46].

Figure 1.22 shows offset plots of surface pressure measurements ($-M^2C_p$, where M is the sectional Mach number) at an inboard radial station of $r/R = 0.225$ for the slowed UH-60A rotor operating at $\mu = 0.8$. Figure 1.22(a) shows a low pressure wave in the reverse flow region ($190 \leq \psi \leq 350\,\text{deg}$). The authors suggest that this is the result of a reverse flow dynamic stall vortex.[5] Figure 1.23 shows the existence of the reverse flow dynamic stall vortex from a sub-scale experiment [48]. This vortex forms at the sharp aerodynamic trailing edge and convects along the lower surface as the rotor blade progresses through the

[5]The authors call this phenomenon *reverse chord dynamic stall* [12].

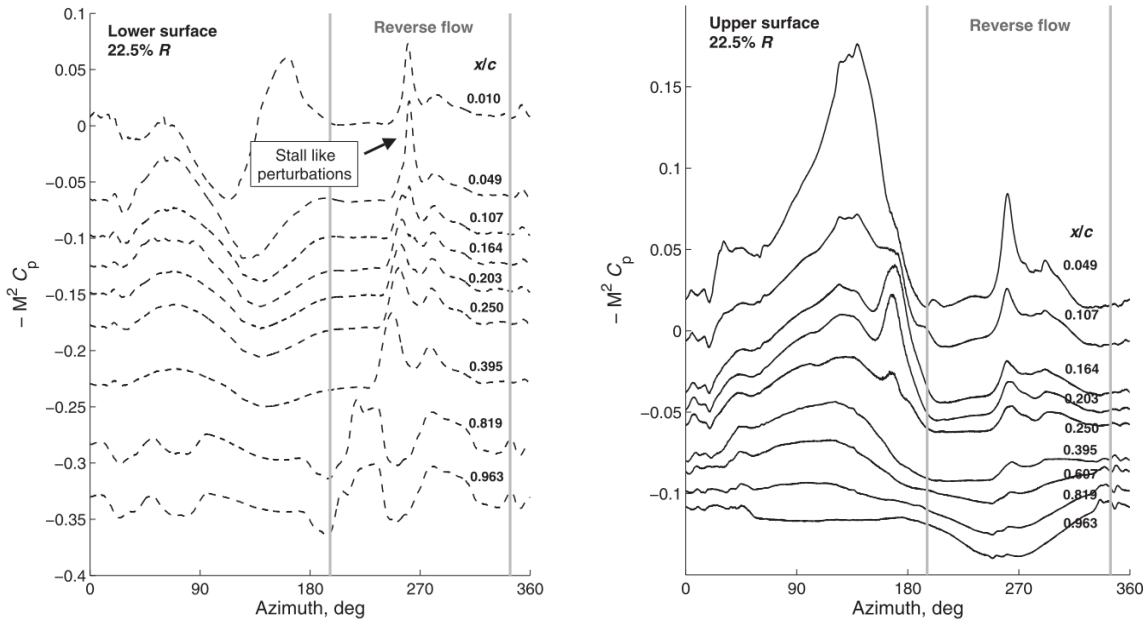

(a) Suction side (lower surface).

(b) Pressure side (upper surface).

Figure 1.22: Surface pressures measured at $r/R = 0.225$ for a slowed UH-60A rotor operating at $\mu = 0.8$, $C_T/\sigma = 0.045$, and $\theta_{75} = 8\,\text{deg}$ [12].

reverse flow region. This vortex creates a local low pressure that convects with it, similar to classical dynamic stall. This trend is labeled in Figure 1.22(a) as "stall like perturbations." The formation of this vortex is likely due to coupled effects from both the time-varying freestream and the pitching kinematics. However, the resulting imprint on the unsteady pressure distribution is similar in nature to classical dynamic stall (Figure 1.18). Note the presence of a second suction suction peak at later azimuthal angles. The authors suggest that this could be the result of a secondary vortex shedding phenomenon. Figure 1.22(b) shows the pressure distributions for the upper surface (pressure side) during the same test. Note that the reverse flow dynamic stall vortex influences the pressure near the blunt aerodynamic trailing edge ($0.049 \leq x/c \leq 0.250$) starting near $\psi = 250\,\text{deg}$.

The surface pressure measurements from the full-scale UH-60A SRT were integrated to provide unsteady sectional airloads around the rotor azimuth. Figure 1.24 shows the

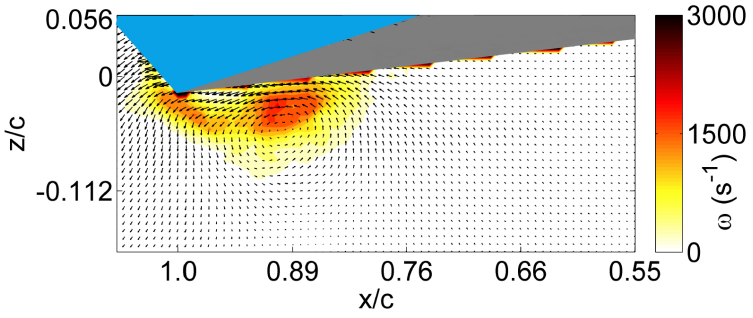

Figure 1.23: Instantaneous velocity field measurement showing a reverse flow dynamic stall vortex on a sub-scale model rotor with a NACA 0013 airfoil section at $r/R = 0.5$ and $\psi = 270$ deg operating at $\mu = 0.8$ [48]. The freestream has been subtracted from the vector field.

unsteady sectional normal force and pitching moment for two test conditions: $\mu = 1.0$ and $\mu = 0.8$. In both cases, an impulsive force and moment begin near $\psi = 220$ deg, consistent with the formation of the reverse flow dynamic stall vortex. Note that the normal force (which is approximately the same as lift for small angles of attack) is negative (downward-acting) in the reverse flow region. These impulsive unsteady airloads result in large rotor blade torsion and pitch link loads [12]. Figure 1.25(a) shows the variation of pitch link load with rotor azimuth at four advance ratios. Note that for the highest advance ratio tested ($\mu = 0.9$, solid line), a "reverse impulse" is observed, that is, an impulsive change in the pitch link loads associated with the reverse flow region. This impulse also affects dynamic pitch link loads, as shown in Figure 1.25(b). At $\mu = 0.9$, the 2/rev loads are nearly double that of those at $\mu = 0.7$. The 3/rev, 4/rev, and 5/rev dynamic pitch link loads are three times as large (or more) than at $\mu = 0.7$. These high dynamic pitch link loads are a direct consequence of the reverse flow region and could lead to pitch link fatigue and vehicle vibrations [12].

Computational studies were also performed which followed the test conditions of the full-scale UH-60A SRT to provide a fundamental understanding the flow features responsible for the pressure and airload behaviors seen in the experimental work [11]. The authors identified a progression of a suction peak over the suction side of the rotor blade, similar to Figure 1.22(a) [11]. To investigate this further, Figure 1.26 shows instantaneous sectional

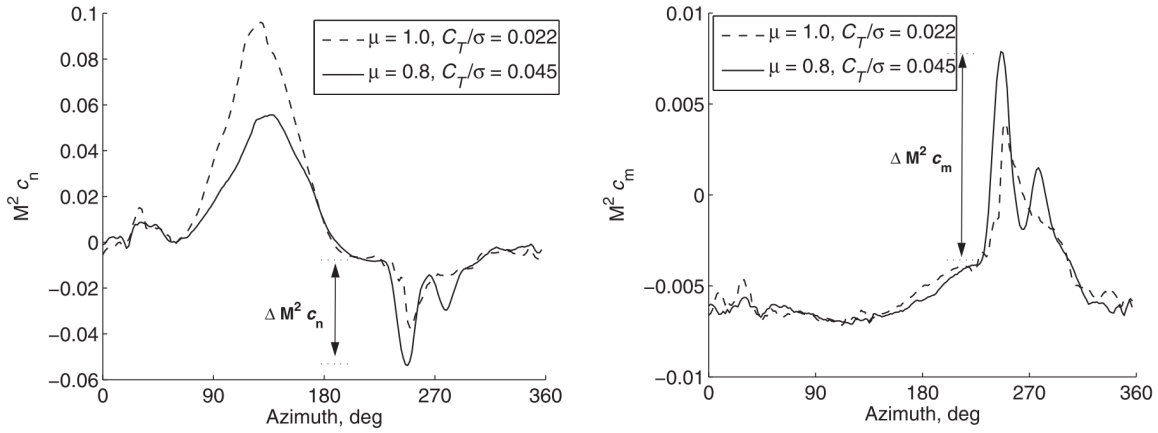

(a) Normal force. (b) Pitching moment.

Figure 1.24: Sectional airloads at $r/R = 0.225$ for a slowed UH-60A rotor operating at two high advance ratio points [12].

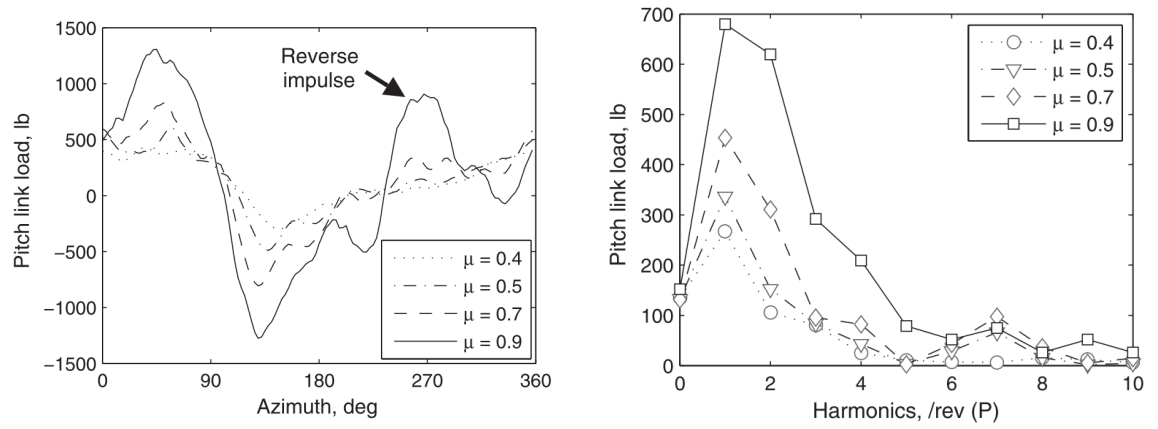

(a) Waveform. (b) Harmonic content.

Figure 1.25: Pitch link load variation with advance ratio for a slowed UH-60A rotor [12].

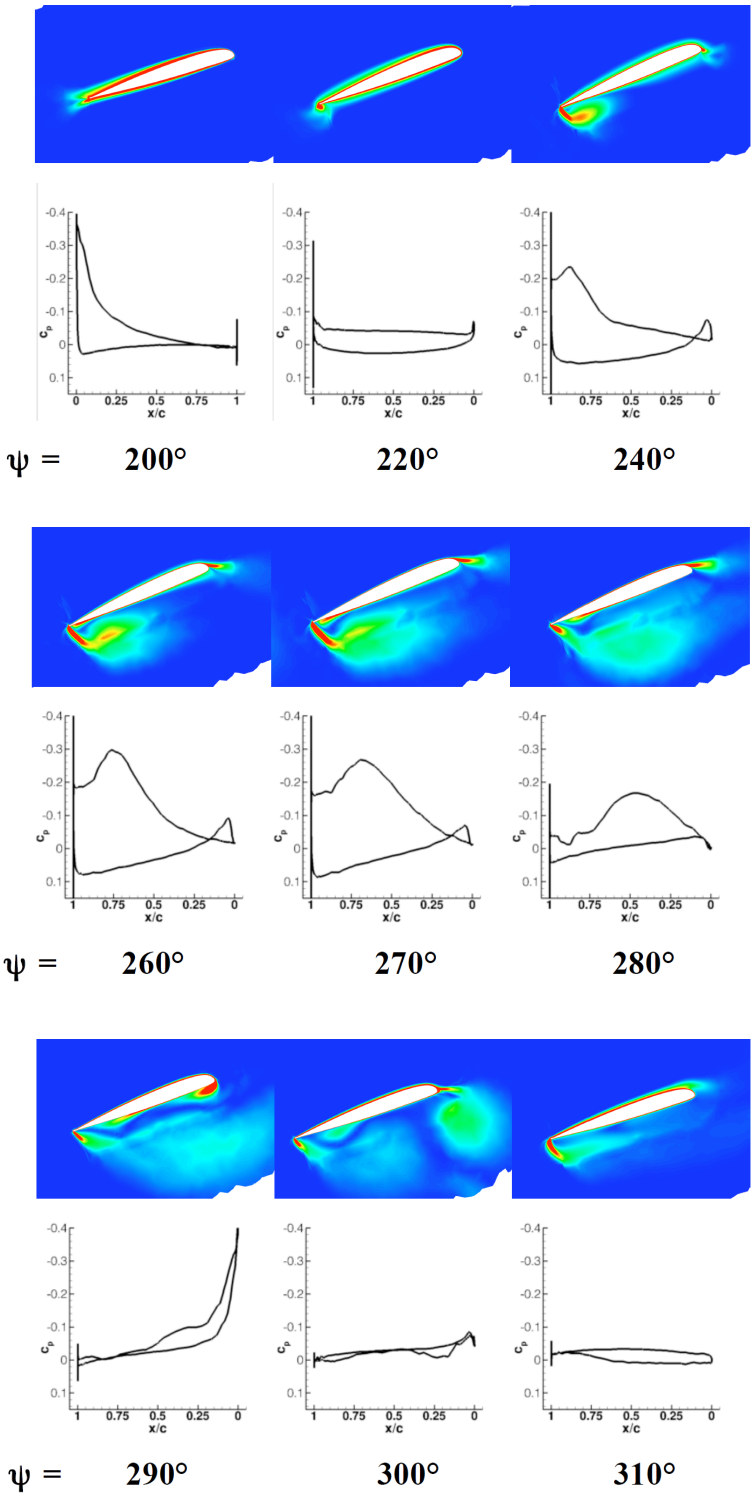

Figure 1.26: Illustration of reverse flow dynamic stall through an azimuthal progression of the sectional vorticity and surface pressure distribution at $r/R = 0.55$ predicted from coupled CFD/CA for a UH-60A operating at $\mu = 0.8$ [11].

vorticity fields of the blade at $r/R = 0.55$ from the simulation of the UH-60A rotor operating at $\mu = 0.8$. At $\psi = 200\,\text{deg}$, the airfoil is operating in forward flow (Figure 1.2(a)). As the blade element passes through $\psi = 220$ and $240\,\text{deg}$, the local reverse flow velocity increases and a vortex forms near the sharp aerodynamic leading edge on the suction side of the airfoil (Figure 1.2(b)). This vortex continues to grow at $\psi = 260\,\text{deg}$, resulting in the growth of a corresponding suction peak. The suction peak moves aft ($\psi = 280\,\text{deg}$), though the magnitude of the suction is lower and timing of the convection is slightly different from the experimental work. At $\psi = 290\,\text{deg}$, a large amount of suction is present near the blunt aerodynamic trailing edge. The authors suggest that this is due to movement of the Kutta condition around to the lower surface. This leads to the formation of a trailing edge vortex at $\psi = 300\,\text{deg}$, along with an associated suction peak at the aerodynamic trailing edge. At $\psi = 310\,\text{deg}$, the flow is fully separated. The airfoil section returns to forward flow near $\psi = 330\,\text{deg}$.

The experimental and computational work reviewed in this section confirms the existence of reverse flow dynamic stall on a rotor and its influence on unsteady airloads, blade torsion, and pitch link loads. However, a detailed understanding of the mechanisms of reverse flow dynamic stall and its sensitivity to Reynolds number and pitching kinematics is lacking. Furthermore, the work reviewed in this section was limited to conventional airfoils and did not consider airfoils with a blunt geometric trailing edge for modern high-speed helicopters.

1.4 Summary

Reverse flow is an aerodynamic phenomenon that is inherent to a region of the retreating side of all helicopter rotors in forward flight. The reverse flow region grows in size with increasing advance ratio, leading to high drag, downward-acting lift, pitching moment, and unsteady airloads. These detrimental effects make high-speed flight challenging, especially

since modern high-speed helicopters typically operate with a slowed rotor which increases the size of the reverse flow region. Despite these challenges, some prototypes have demonstrated flight speeds in excess of 250 kts including the Sikorsky X2TD and S-97 Raider. These aircraft rely on airfoil sections with a blunt geometric trailing edge near the blade root in order to mitigate flow separation over the retreating blade thereby reducing profile drag.

Numerous studies have considered the time-averaged aerodynamics of static airfoils in reverse flow, a fundamental model of rotor blade aerodynamics in the reverse flow region. The sectional drag is much higher in reverse flow due to early flow separation at the sharp aerodynamic leading edge as well as separation at the blunt aerodynamic trailing edge. The effect of Reynolds number plays an important role in boundary layer transition and separation characteristics for conventional airfoils in forward flow and in reverse flow at low angles of attack.

The unsteady aerodynamics of reverse flow are highly complex. Insight can be gained by considering prior work on the aerodynamics of stalled static airfoils and dynamic stall. The unsteady airloads of a static conventional airfoil in forward flow have been found to be greatest just past stall and decrease in magnitude at higher angles of attack. Vortex shedding can also occur, with a frequency that decreases with increasing angle of attack, reaching a minimum near $\alpha = 90\,\text{deg}$. For oscillating airfoils in forward flow, the primary source of unsteady airloads is the formation and convection of a dynamic stall vortex. This flow feature can result in large hysteresis of unsteady airloads with values of lift, drag, and pitching moment well beyond corresponding static airloads. The evolution of dynamic stall depends strongly on pitching kinematics. Reverse flow dynamic stall has been observed from work on a full-scale UH-60A and sub-scale experiments. Similar to classical dynamic stall, the reverse flow dynamic stall vortex forms at the leading edge and convects along the suction side (lower surface) leading to unsteady airloads. The reverse flow region was also shown to have a strong influence on pitch link loads and blade torsion.

1.5 Present Work

The review of prior work on reverse flow motivates the need for a better understanding of the aerodynamics of reverse flow, particularly the unsteady aerodynamics that arise during reverse flow dynamic stall. To this end, wind tunnel experiments have been carried out to identify fundamental features of airfoil behavior in reverse flow. The present work considers two fundamental, two-dimensional models of this complex flow regime: static and oscillating rotor blade airfoils subject to a constant freestream in reverse flow (Figure 1.3). The specific objectives of the present work are as follows:

1. Relate the time-averaged airloads on static airfoils in reverse flow to fundamental flow features, such as separation points and stall characteristics.

2. Identify the unsteady wake regimes for airfoils in reverse flow and relate these regimes to the magnitude and frequency content of resulting unsteady airloads.

3. For oscillating airfoils in reverse flow, determine the influence of Reynolds number, reduced frequency, mean pitch angle, and pitch amplitude on the evolution of reverse flow dynamic stall.

4. Throughout the analysis of both static and oscillating airfoils in reverse flow, characterize the influence of airfoil parameters (i.e., trailing edge shape, thickness, camber) on the resulting aerodynamic behavior.

The present work is entirely experimental in nature, but the results and analysis presented here provide a basis for evaluating numerical simulations of similar two-dimensional models. Experimental and numerical collaborative work has also been completed on an oscillating NACA 0012 with a selected set of pitching kinematics [49]. It should also be noted that the two-dimensional models of reverse flow considered in the present work neglect

three-dimensional effects due to the radial and azimuthal variations of the local freestream (Figure 1.1). Additionally, it will be discussed in Chapter 4 that while the oscillating airfoil model does mimic the cyclic pitching kinematics of a rotor blade, the model is a simplification of the true flow encounter by a blade element as it travels around the rotor azimuth. Section 5.4 suggests areas of future work that include more accurate models of the reverse flow region.

1.6 Dissertation Outline

Chapter 2 describes the experimental methods used in the present work. Force measurements, time-resolved pressure measurements, time-resolved flowfield measurements, and surface oil flow visualization were all used to characterize reverse flow aerodynamics. The time-averaged and unsteady aerodynamics of static airfoils at high angles of attack and in reverse flow are given in Chapter 3. This chapter describes the time-averaged airloads and relates them to time-averaged flowfields, three unsteady wake regimes and their influence on unsteady airloads (using integrated time-resolved surface pressure measurements), and the effect of Reynolds number. Chapter 4 provides a fundamental characterization of reverse flow dynamic stall for two airfoils: a conventional airfoil with a sharp trailing edge (NACA 0012) and an airfoil representative of those found on modern high-speed helicopters (cambered ellipse). The effects of Reynolds number and pitching kinematics on the evolution of reverse flow dynamic stall are explored in depth. Finally, Chapter 5 gives a summary of the present work, a list of contributions and key conclusions, and suggestions for future work.

Chapter 2

Methodology

2.1 Overview of Experimental Work

2.1.1 Wind Tunnel Facilities

Experiments were carried out in two wind tunnel facilities. Static and oscillating experiments were performed in a 20×28 in open-circuit, low-speed wind tunnel at the University of Maryland with a maximum test section speed of 100 mph (44.7 m/s) (Figure 2.1(a)). Static airfoil experiments at high angles of attack and in reverse flow were performed in a 42×60 in low-speed, closed-circuit wind tunnel (CCWT) at the United States Naval Academy (USNA) with a maximum test section speed of 200 mph (89.4 m/s) (Figure 2.1(b)).

2.1.2 Model Rotor Blades

Four airfoil profiles were selected for study, two featuring a sharp geometric trailing edge (NACA 0012 and NACA 0024, shown in Figure 2.2(a)) and two featuring a blunt geometric trailing edge (ellipse and cambered ellipse, shown in Figure 2.2(b)). A NACA 0012 was selected to be representative of a conventional, thin rotor blade airfoil. A NACA 0024 was selected since it could potentially be used on the inboard portion of a coaxial high-speed

(a) Open-circuit wind tunnel at the University of Maryland (20×28 in).

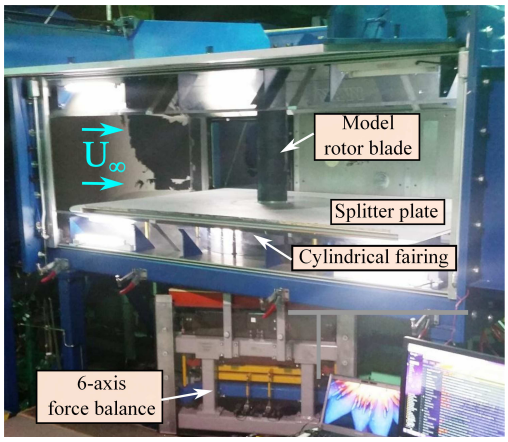

(b) Closed-circuit wind tunnel at the United States Naval Academy (42×60 in).

Figure 2.1: Wind tunnel facilities used in the present work.

helicopter rotor blade where high blade stiffness is required (Section 1.3.1). For comparison, an elliptical airfoil was selected that features the same thickness as the NACA 0024 (24 % thick) but has a blunt aerodynamic trailing edge. Finally, a cambered elliptical airfoil (26 % thick, 4 % camber at $x/c = 0.5$) was selected since it closely resembles the Sikorsky DBLN-526 airfoil.

Table 2.1 summarizes the primary material used to fabricate the model rotor blades. Except for the DBLN-526 ($AR = 7.10$) and NACA 0012 ($AR = 2.56$), the models were constructed by assembling airfoil sections onto metal spars. All $AR = 7.10$ and $AR = 2.56$ models were uninstrumented. The $AR = 3.86$ and $AR = 2.47$ models featured a 3-D printed section to accomodate unsteady pressure transducers. Figure 2.3 shows the techniques used for constructing the $AR = 3.86$ models used in the USNA wind tunnel, though the process was similar for the $AR = 7.10$ and $AR = 2.47$ models. Blocks of raw material (1) were first appropriately cut to size (2). Then, a CNC mill cut airfoil sections (3-5). These smaller sections were glued together (6) to form large rotor blade sections (7). Two metal spars ran through the models at $x/c = 0.25$ and $x/c = 0.6$. A 3-D printed airfoil section was placed at the mid-span of instrumented models. The models were painted and sanded with 600-grit

sandpaper (8). Finally, the unsteady pressure transducers were installed in the 3-D printed airfoil sections and wires passed through the wire channel to the DAQ system (9).

Table 2.2 summarizes the maximum solid blockage for each of the four aspect ratios of airfoils. A majority of the results were collected at lower angles of attack, leading to solid blockage within the typical range of 1-10 % [50]. As a result, none of the results presented here have been corrected for solid blockage (or wake blockage) effects. It should be noted that the term "airfoil" implies purely two-dimensional flow conditions. The present work does not account for any three-dimensional effects associated with corner vortices, stall cells, or dynamic stall vortex formation. However, since the flow conditions are predominantly two-dimensional, "airfoil" is used throughout this thesis to describe the results.

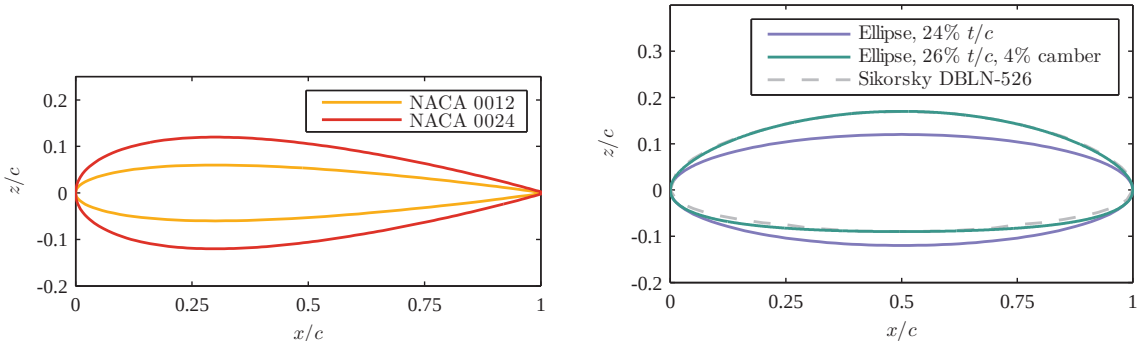

(a) Sharp geometric trailing edge.

(b) Blunt geometric trailing edge.

Figure 2.2: Profiles of airfoil sections tested in the present work.

Table 2.1: Primary material used during fabrication of model rotor blades.

	Static			*Oscillating*
	$AR = 7.10$ UMD	$AR = 3.86$ USNA	$AR = 2.56$ USNA	$AR = 2.47$ UMD
NACA 0012	Delrin plastic	Basswood	Aluminum	Basswood
NACA 0024	∼	Basswood	∼	∼
Ellipse	Aluminum	Basswood	∼	∼
Cambered ellipse	∼	Basswood	∼	Basswood
DBLN-526	ACCURA 60	∼	∼	∼

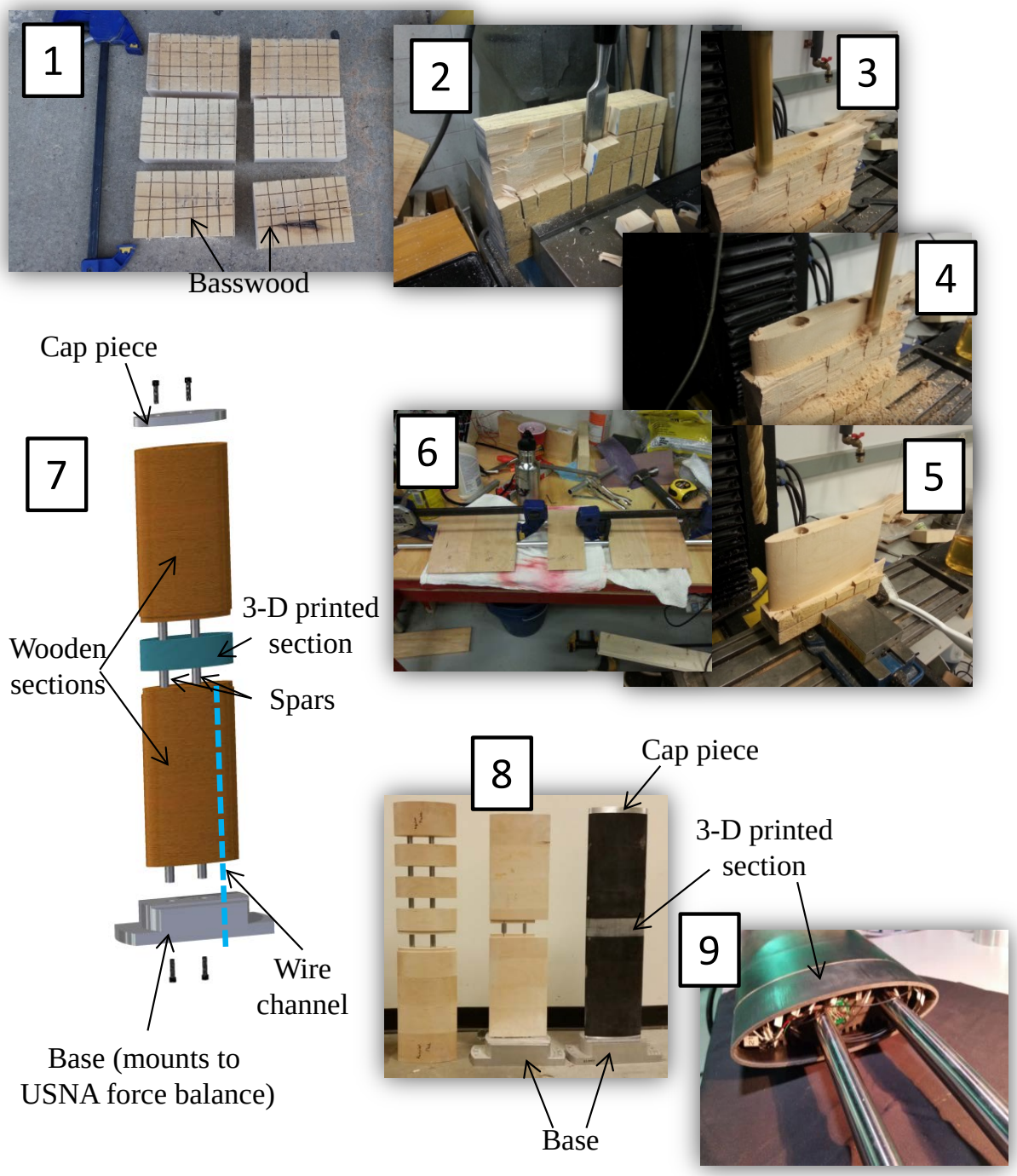

Figure 2.3: Fabrication of model rotor blades for experiments in the USNA wind tunnel.

Table 2.2: Summary of maximum solid blockage and the associated angle of attack.

	Static			*Oscillating*
	$AR = 7.10$	$AR = 3.86$	$AR = 2.56$	$AR = 2.47$
% solid blockage	10.0 %	13.3 %	10.0 %	12.1 %
Angle of attack	90 deg	90 deg	30 deg	25 deg

2.1.3 Force Balance Measurements

Figure 2.4(a) shows a schematic of the custom-built force balance system mounted on the UMD wind tunnel test section. Model rotor blades were suspended between two force balances to reduce reaction bending moments. The details of one balance can be seen in Figure 2.4(b). Each of balance is comprised of three sub-assemblies. The lift and drag sub-assemblies feature linear air bearings (New Way Air Bearings, 0.75 in bushings) to remove friction from the load measurements. Loads were measured using single-axis load cells with a maximum capacity of 10 lb or 25 lb (Interface SM-10 or SM-25). The third sub assembly measures pitching moment. Two mechanisms were fabricated to measure pitching moment, depending on the size of the airfoil being tested. The first mechanism (shown in Figure 2.4(b)) was used for the $AR = 2.46$ airfoils with $c = 8$ in. This sub-assembly includes an angle of attack control plate (described later). The upper portion of the pitching moment sub-assembly has been removed for clarity, revealing the pitching moment load cell and a needle-style thrust bearing to minimize friction about the geometric quarter-chord. The second mechanism (not shown) was used for the $AR = 7.10$ airfoils and measured pitching moment using a torque transducer (Transducer Techniques RTS-100).

The angle of attack of each model rotor blade was adjusted using a pitching mechanism consisting of an aluminum plate attached to the pitching moment mechanism. The angle of attack control plate used for the $AR = 2.46$ models can be seen in Figure 2.4(b) and features equally spaced holes to allow the angle of attack to be pinned in place with 0.5 deg

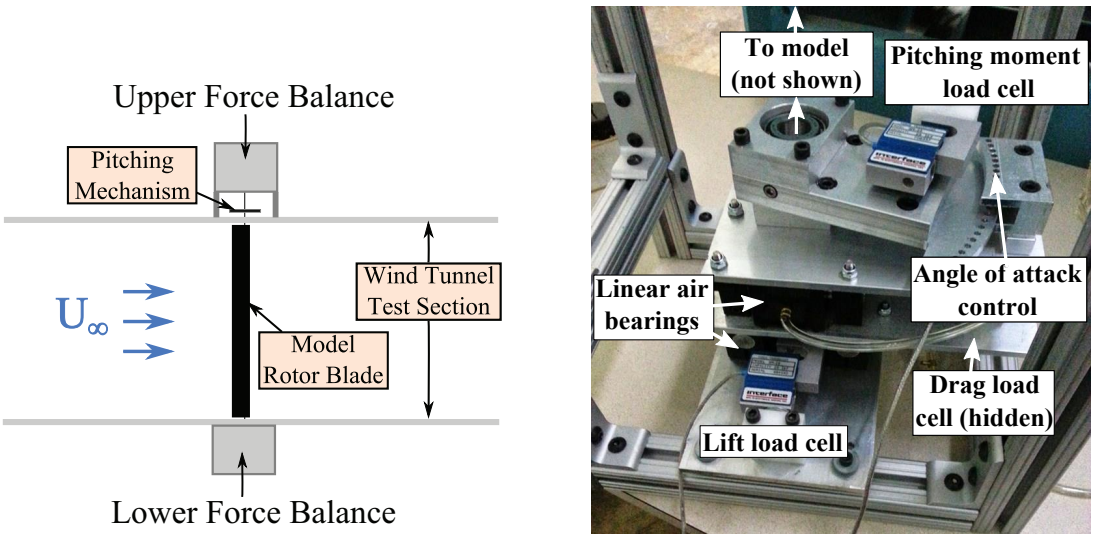

(a) Schematic of force balance system.

(b) Close-up of one force balance.

Figure 2.4: Force balance system used at UMD during static airfoil tests.

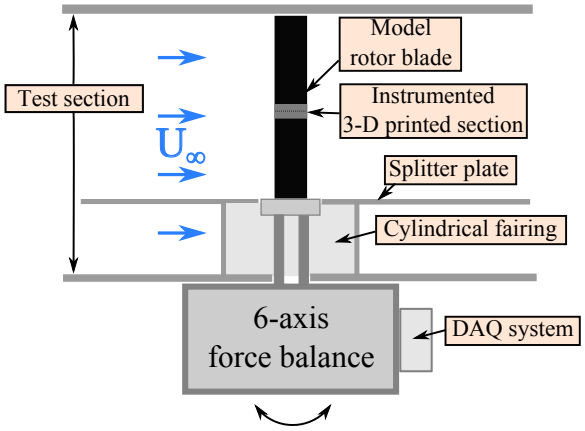

Figure 2.5: Schematic of a model rotor blade mounted on the USNA force balance during static airfoil tests.

resolution. Due to the large chord of the $AR = 2.46$ models, the angle of attack range was limited to ± 30 deg. The angle of attack control plate used with the $AR = 7.10$ model rotor blades allowed for full 360 deg angle of attack range with 1 deg resolution.

Figure 2.5 shows a schematic of the experimental setup at the USNA. Instrumented model rotor blades were cantilevered from a 6-axis force balance that rotated with the models as the angle of attack was changed. A splitter plate was installed above the floor of the test section to reduce the usable height of the test section to 31 in. This was done to reduce the magnitude of the airloads acting on the blades (and force balance) and to minimize bending of the cantilevered model blades. A cylindrical fairing prevented contamination of the force balance measurements from air flow beneath the splitter plate. Each model spanned the upper portion of the test section; the models were aligned flush with the splitter plate in the spanwise direction and 0.125 in ($0.0156\,c$) from the test section ceiling.

2.1.4 Dynamic Pitching Rig

A separate dynamic pitching rig was designed and fabricated to carry out investigations of oscillating airfoils using the 20×28 in wind tunnel at UMD. Figure 2.6 shows a CAD rendering of the dynamic pitching rig. The wind tunnel test section has been removed from this image for clarity, though the freestream direction is indicated. Note that the figure shows the rig set up with the cambered elliptical airfoil in forward flow, oscillating about the geometric/aerodynamic quarter-chord.

Figure 2.6 shows that the dynamic pitching rig is composed of upper and lower structures that mount to the wind tunnel and a drive sub-assembly that mounts to the lower structure. A series of thrust bearings, shaft couplers, and ball bearings along the primary spar allow the model rotor blade to pivot about the geometric quarter-chord. Oscillations are achieved using a four-bar linkage: an airfoil cam, a linkage, a rotary cam plate, and the lower structure itself. This rig was designed to allow for the pitching kinematics to be

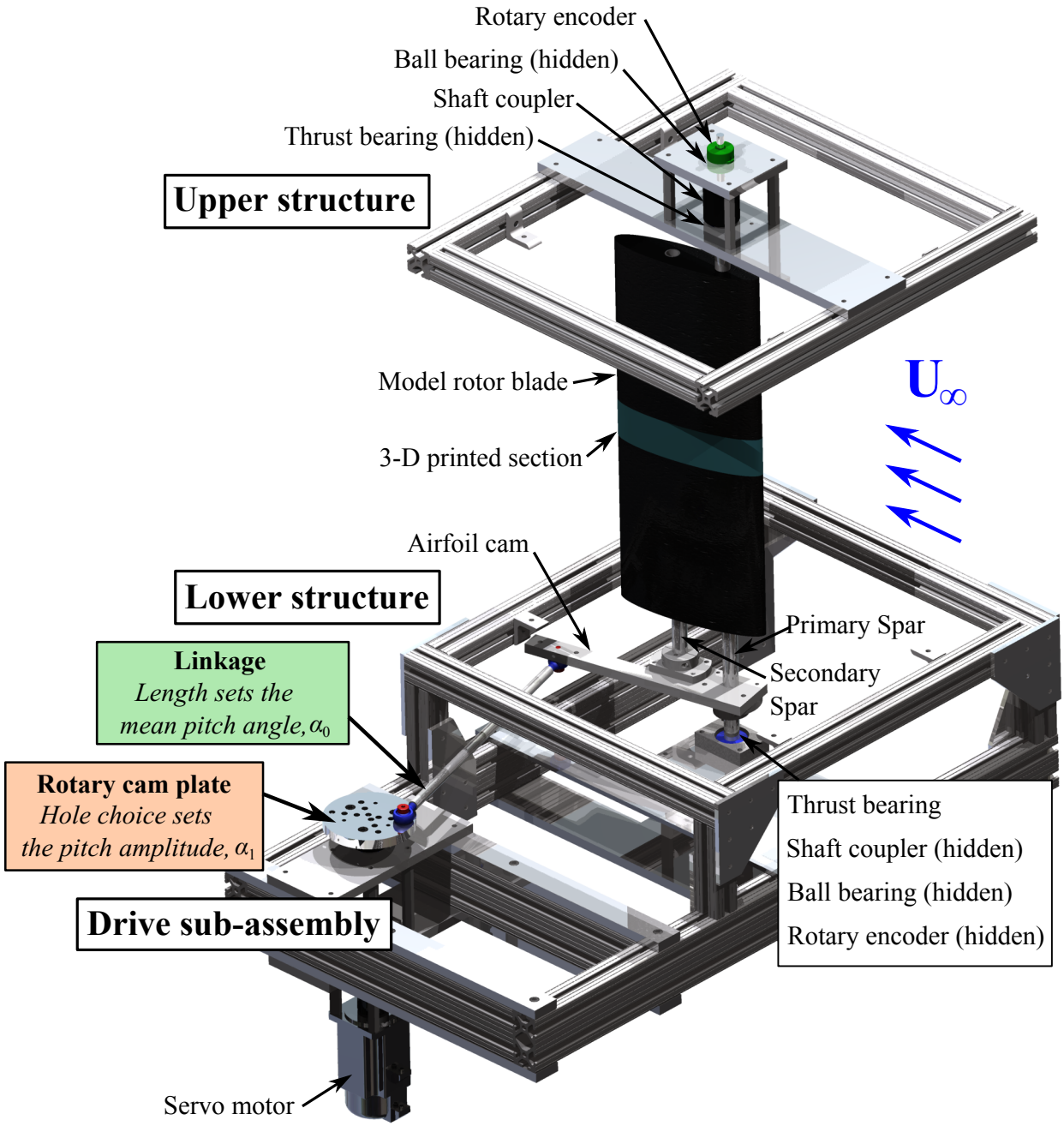

Figure 2.6: Dynamic pitching rig.

changed with relative ease. The linkage (highlighted in green) was used to set the mean pitch angle, α_0 (or $-\alpha_{0,\text{rev}}$ in reverse flow). Fine control of the linkage length was made possible by using threaded eye-bolts on either end of the linkage (shaded in blue). The typical resolution of mean pitch angle was 0.2 deg. The rotary cam plate (highlighted in orange) was used to set the pitch amplitude, α_1. The placement of the drive sub-assembly and hole pattern on the rotary cam plate was designed to provide 1 deg resolution of pitch amplitude. A programmable servo motor (Applied Motion Products M0750-102-5-000) was used to drive the airfoil oscillations at constant frequencies. A servo motor controller (Applied Motion Products BLuAC5-Q) was used to tune PID gains to achieve the smoothest motion possible.

The angle of attack of the model rotor blade was monitored using two rotary shaft encoders (Applied Motion Products YAA encoders), one on the upper structure (shaded in green) and another on the lower structure (hidden). The use of two shaft encoders provided allowed for blade twist to be detected (typically less than 2 deg). Section 2.5.2 describes the angle of attack measurements collected during the oscillating airfoil tests.

Figure 2.7(a) shows the dynamic pitching rig installed on the wind tunnel and identifies important data collection equipment used during oscillating airfoil experiments. Figure 2.7(b) shows a block diagram of the setup. Two computers were used for user control and data recording. The particle image velocimetry (PIV) acquisition computer first communicated a "wait for external trigger" command to a high-speed controller. Next, a multi-function computer was used to command the servo motor to initiate. After 10 pitching cycles, the servo motor control activated a 5 V trigger that was recorded by a multi-function DAQ (NI USB-6341) and the pressure DAQ (NI cDAQ-9178 and eight NI 9237 modules). The trigger was also sent to the high-speed controller to initiate collection of PIV data. The multi-function DAQ also recorded signals from the two angle of attack encoders, servo motor encoder, laser Q-switch, and camera trigger. Pressure data was collected for 500 oscillation

cycles while PIV data was collected for 10 oscillation cycles due to data storage constraints.

2.1.5 Parameter Space

Table 2.3 summarizes the parameter space for the static airfoil experiments based on airfoil, Reynolds number, and measurement type. Measurements at $0.55 \times 10^5 \leq Re \leq 1.65 \times 10^5$ were collected at UMD whereas measurements at $3.3 \times 10^5 \leq Re \leq 10 \times 10^5$ were collected at the USNA.[1] *Airloads* refers to time-averaged lift, drag, and pitching moment measured using a force balance. *Pressure* refers to time-resolved surface pressure measurements that were also integrated to calculate unsteady airloads. *PIV* refers to time-resolved particle image velocimetry (PIV) measurements (at UMD only). *Oil* refers to surface oil flow visualization.

For measurements at UMD, airload data was generally collected in 1 deg increments in reverse flow ($150 \leq \alpha \leq 210$ deg), 2 deg increments in forward flow ($330 \leq \alpha \leq 30$ deg), and 3 deg increments at high angles of attack ($30 \leq \alpha \leq 150$ deg and $210 \leq \alpha \leq 330$ deg). PIV data was typically collected at 3 deg increments. Surface oil flow visualization was typically performed at 1 deg increments. For measurements at the USNA, airload data was generally collected in 1 deg increments in both forward and reverse flow, except near stall where data was collected in 0.5 deg increments. Data was collected at high angles of attack ($30 \leq \alpha \leq 150$ deg) in 3 deg increments.

The parameter space of the oscillating airfoil experiments spans five parameters, so it cannot be easily represented as a table. Section 4.2 provides a detailed description (and visualization) of the selected parameter space.

[1] Note that the * indicator signifies that measurements were taken at UMD at slightly different Reynolds numbers. See table caption.

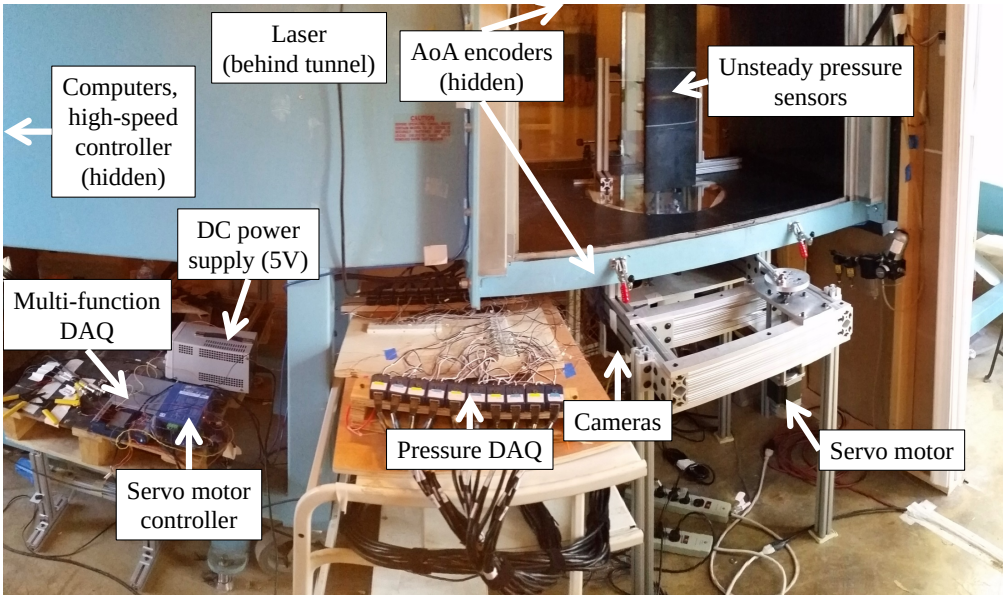

(a) Experimental set-up.

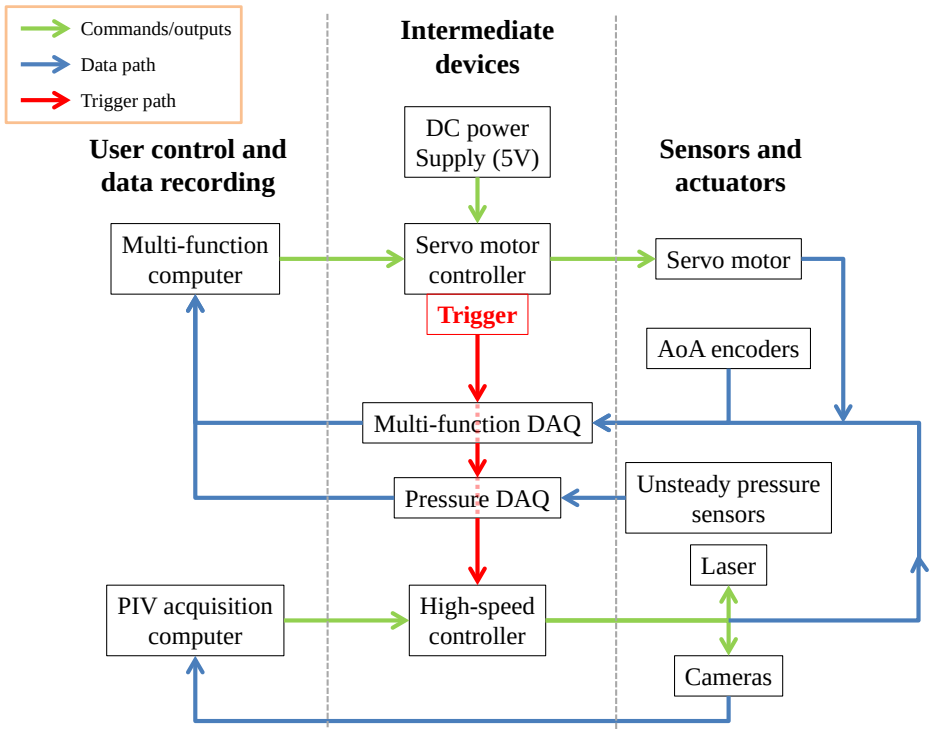

(b) Block diagram.

Figure 2.7: Oscillating airfoil experiments.

Table 2.3: Summary of the static airfoil parameter space. ●: Forward flow angles of attack ($0 \leq \alpha \leq 30$ deg). ●: Reverse flow angles of attack ($150 \leq \alpha \leq 180$ deg). ●: High angles of attack ($30 \leq \alpha \leq 150$ deg, also $150 \leq \alpha \leq 310$ deg for $Re = 1.1 \times 10^5$ and all cambered ellipse cases). *: PIV data collected at UMD for $Re = 3.14, 4, 5, 6 \times 10^5$.

		Reynolds number $\times 10^5$					
Airfoil	Meas. type	0.55	1.1	1.65	3.3	6.6	10
NACA 0012	Airloads	●●	●●●	●●	●●●	●●●	●●●
	Pressure				●●●	●●●	●●●
	PIV	●	●●	●	●●*	●●*	
	Oil		●	●		●	●●
NACA 0024	Airloads				●●●	●●●	●●●
	Pressure				●●●	●●●	●●●
	PIV						
	Oil				●●	●●	●●
Ellipse	Airloads	●●	●●●	●●	●●●	●●●	●●●
	Pressure				●●●	●●●	●●●
	PIV	●●	●●	●●	●●*	●●*	
	Oil		●●	●●	●●	●●	●●
Cambered ellipse	Airloads				●●●	●●●	●●●
	Pressure				●●●	●●●	●●●
	PIV				●●*	●●*	
	Oil				●●	●●	●●
DBLN-526	Airloads		●●●				
	Pressure						
	PIV		●●				
	Oil		●				
			UMD			*USNA*	

2.2 Airload (Force) Measurements

2.2.1 Calibration

Each of the single-axis load cells and torque transducer in the force balance system were independently calibrated on an isolated test stand using class M2 calibration weights. The maximum nonlinearity (defined as the percent error between the measured load and the load predicted by a regression line) was typically 0.05 %. Each balance was leveled in both the streamwise and normal directions within 0.1 deg while being installed on the wind tunnel. Prior to testing, each model rotor blade was loaded in the four directions to assess the linearity, hysteresis, and repeatability of the force balance system as a whole, using the individual load cell calibration constants. Figure 2.8 shows an assessment of the linearity of the force balance system. An increasing amount of weight was applied to load the balance in the chordwise direction (c_a, based on the $AR = 7.10$ models at $Re = 1.1 \times 10^5$). The resulting measured lift and drag components are shown in Figure 2.8(b) and the total measured force is shown in Figure 2.8(c). The nonlinearity of individual load cells varied up to 1.5 % when installed in the force balance, but the nonlinearity of the force balance system as a whole varied within 0.2 % of the applied load. A similar procedure was performed to characterize the nonlinearity of the pitching moment measurements. The hysteresis of the force balance system was measured by comparing the zero values after loading the balance for 15 min; variations were less than 0.1 %. Hysteresis was also measured by applying a dynamic load using a vibration shaker for 10 min, exciting the force balance system at its fundamental structural resonance frequency; variation in the zero-reading was less than 0.2 %. Finally, non-repeatability was measured by applying a static load for five cycles; variations were less than 0.2 %.

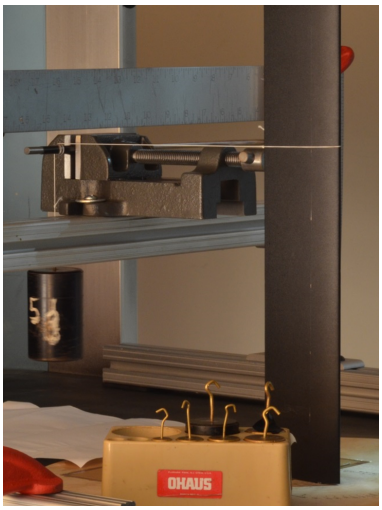

(a) Setup.

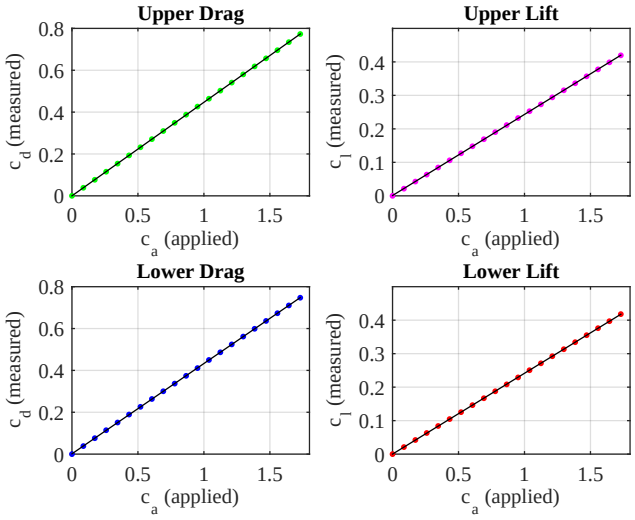

(b) Individual load cells.

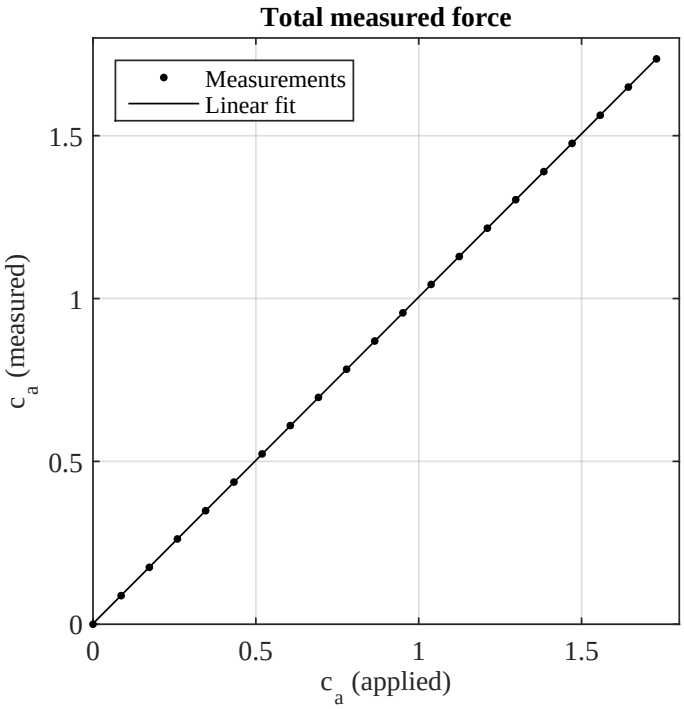

(c) Total measured force.

Figure 2.8: Assessment of the linearity the UMD force balance system.

2.2.2 Acquisition

UMD 3-component force measurements

Airload measurements were acquired using NI LabVIEW and a NI USB-6341 DAQ card. Data was collected at each angle of attack for 5 s at a sampling rate of 10 kHz (50,000 samples per angle of attack). An air-off tare run was performed prior to data collection and later subtracted from the airload measurements. The wind tunnel was set to a fixed fan speed for the duration of each test.

USNA 6-component force measurements

Airload measurements were acquired using a pre-installed data acquisition system. For each angle of attack, instantaneous samples were internally averaged over 1 s and then recorded for 5 s at 1 Hz. Prior to an angle of attack sweep run, an air-off tare run was performed and later subtracted from the force measurements. During wind tunnel testing, the wind tunnel fan speed was adjusted (via open-loop control) to maintain the dynamic pressure in the test section within 1 % of the desired value.

2.2.3 Time-averaging

Figure 2.16(a) shows a sample of the time-resolved force data (600 samples) taken from the drag load cell in the upper force balance for the NACA 0012 in a fully-stalled state. The high frequency content observed in the raw data is electrical noise; the low frequency oscillations are from aeroelastic vibrations of the model rotor blade coupled with the structural dynamics of the force balance system. Figure 2.9(b) shows the results of a convergence study of lift and drag at $\alpha = 135\,\text{deg}$ where lift and drag are both high. The $\widehat{(\cdot)}$ notation implies a percentage deviation from the average value calculated using the entire

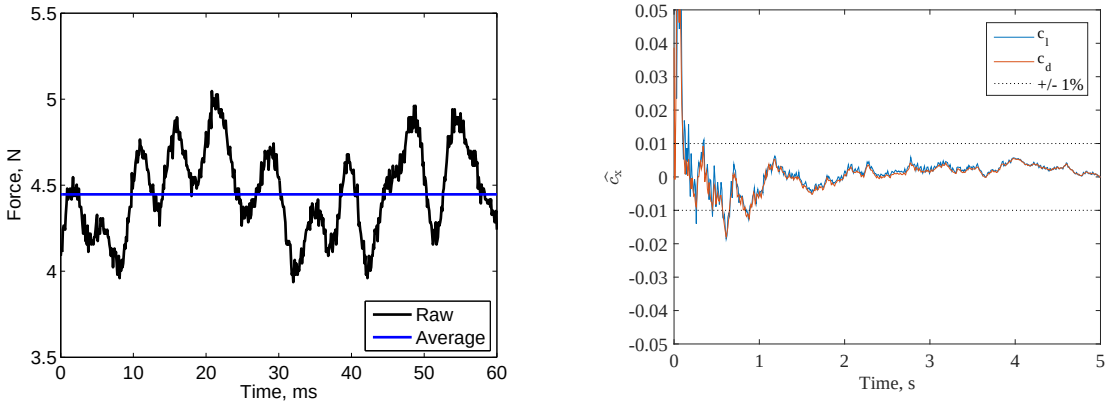

(a) Sample time trace from a single load cell in the upper force balance ($\alpha = 30$ deg).

(b) Convergence of time-averaged lift and drag ($\alpha = 135$ deg).

Figure 2.9: Time-averaging of airload measurements for the NACA 0012 in deep stall conditions at $Re = 1.1 \times 10^5$.

duration of the measurement:

$$\widehat{c_x} = c_x(t)/c_x(t_{max}) - 1 \tag{2.1}$$

Convergence to within 1 % is achieved after 1 s for this highly unsteady case, illustrating that the 5 s sampling duration is sufficient for determining reliable average force measurements.

2.2.4 Measurement Uncertainty

The noise of the UMD force balance lift, drag, and pitching moment measurements corresponding to $Re = 1.1 \times 10^5$ was $2\sigma(c_l) = 7.0 \times 10^{-3}$, $2\sigma(c_d) = 1.4 \times 10^{-2}$, $2\sigma(c_m) = 2.0 \times 10^{-5}$. In order to quantify the repeatability of airload measurements, multiple independent angle of attack sweeps were performed. The variation (twice the standard deviation) between independent runs in forward flow for coefficients of lift and drag was less than 0.01. In reverse flow, variation was typically below 0.03. Pitching moment measurements were taken independently of lift and drag measurements.

The signal-to-noise ratio of the force measurements collected at the USNA are sum-

marized in Table 2.4 using the elliptical airfoil at $\alpha = 3\,\text{deg}$ as a representative example. Figure 2.10 demonstrates the repeatability of the force measurements. The maximum difference in airload coefficients between the two runs was 0.02, 0.01, and 0.01 for lift, drag, and pitching moment, respectively. The greatest source of uncertainty in the force measurements originates from imperfections in the three model rotor blades fabricated from basswood. Figure 2.11(a) shows the lift curve for the ellipse in forward and reverse flow. It is expected that all airloads will be symmetric since the airfoil is symmetric about $x/c = 0.5$. The maximum difference in lift is 0.05, likely due to airfoil imperfections. Note that data is only shown for increasing α (forward flow) and decreasing $-\alpha_{\text{rev}}$ (reverse flow), revealing an aerodynamic hysteresis loop between $15 \leq \alpha \leq 25\,\text{deg}$ (Section 3.4). Figure 2.11(b) shows the lift curve for the cambered ellipse in forward and reverse flow. The maximum difference in the lift is nearly 0.2. While the magnitude of the time-averaged airloads are affected by airfoil imperfections, the general trends are preserved allowing for insight to be gained.

Table 2.4: Signal-to-noise ratio for elliptical airfoil at $\alpha = 3\,\text{deg}$.

Re	Normal force	Chordwise force	Pitching moment about $c/2$
3.3×10^5	466	14	80
6.6×10^5	970	20	80
1.0×10^6	1703	415	154

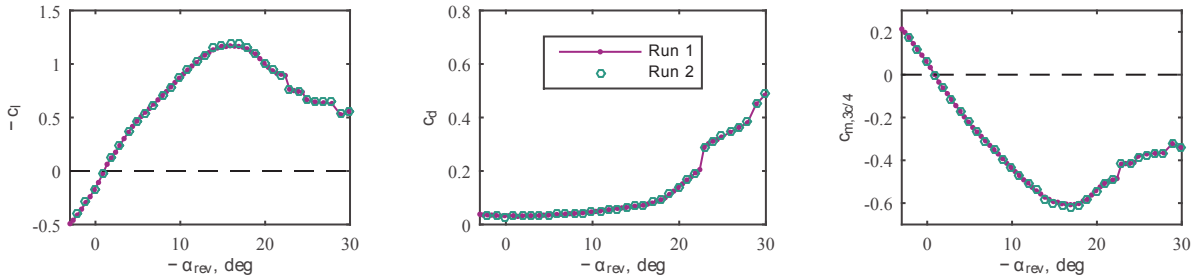

Figure 2.10: Repeatability test, 24% thick ellipse, $c = 8\,\text{in}$, $Re = 6.6 \times 10^5$.

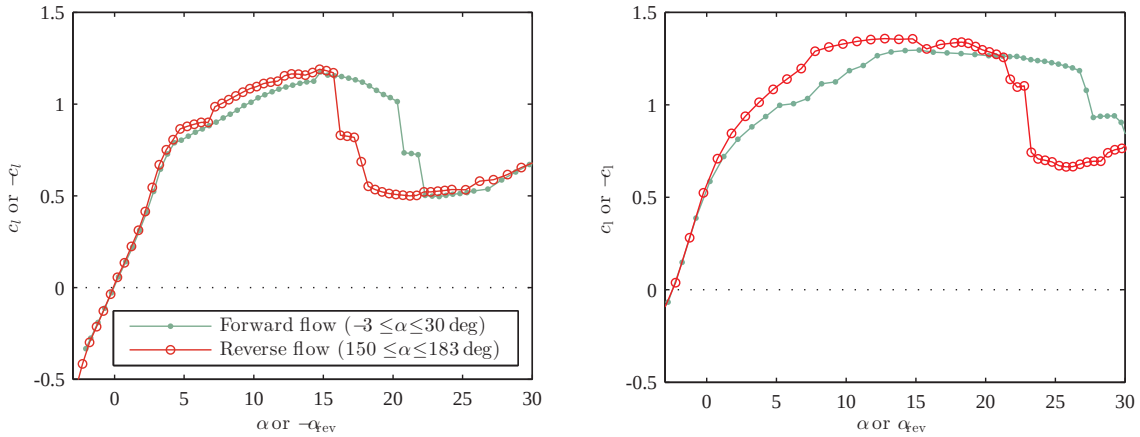

(a) Ellipse.

(b) Cambered ellipse, curved suction side.

Figure 2.11: Variations in symmetry of lift curves for airfoils symmetric about $x/c = 0.5$ at $Re = 3.3 \times 10^5$.

2.3 Pressure Measurements

2.3.1 Unsteady Pressure Transducers

Time-resolved surface pressure measurements were collected using unsteady absolute pressure transducers made by Kulite (Figure 2.12(a)) and Endevco (Figure 2.12(b)). Both feature a silicon diaphragm with integrated resistors forming a wheatstone bridge. The 3-D printed section of model rotor blades was instrumented with these unsteady pressure transducers. For the static airfoil tests at the USNA, Kulite pressure transducers (model: LL-3-072-25A, range: 0-25 psia) were potted into a 3-D printed case (Figure 2.12(a)). This design allowed the transducer/case units to be modular; they could be mounted and re-mounted in different model rotor blades. Figure 2.12(c) shows the pressure transducer units mounted along the inner surface of a NACA 0024 3-D printed airfoil section. Pressure taps with a diameter of 0.03 in were included in the design of these sections, positioned along a single spanwise location. Each transducer/case unit was sealed with silicon RTV. A similar installation process was used for the oscillating airfoil tests, though most of the pressure

sensors used in these experiments in were made by Endevco (Figure 2.12(b)). It should be noted, however, that some Kulite pressure transducers were also used in the oscillating airfoil experiments. There were no noticeable differences between the performance of each brand of sensor.

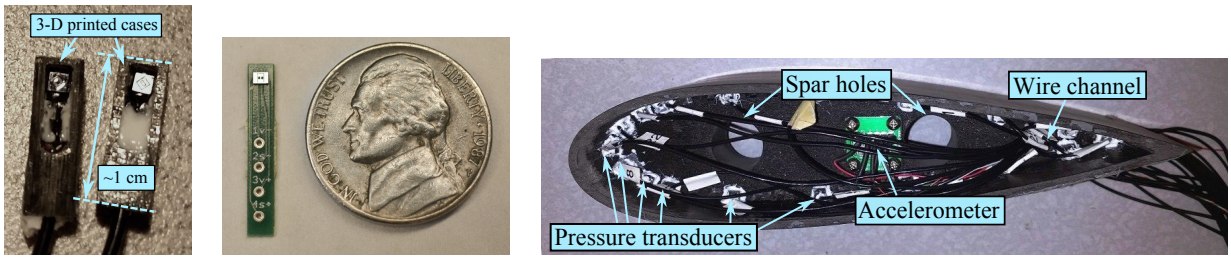

(a) Kulite. (b) Endevco [51]. (c) Instrumented 3-D printed airfoil section (NACA 0024).

Figure 2.12: Model rotor blade instrumentation.

Figure 2.13 shows the locations of the pressure transducers along the blade surfaces. Note that the oscillating airfoil experiments featured a greater number of pressure transducers due to the lower cost of the Endevco pressure sensors. Transducers that either had excessively high noise or an improper seal were deemed "inoperational." These transducers were omitted from all analyses. Geometry constraints prevented the installation of pressure transducers near the thinnest portions of the airfoils with a sharp trailing edge. For the static airfoil experiments on the airfoils with a sharp trailing edge, the pressure on the upper and lower surface at $x/c = 0.99$ as well as $x/c = 1$ was linearly extrapolated to allow for a more accurate integration of the pressure distribution when calculating airloads. For the oscillating NACA 0012 experiments, this extrapolation scheme gives non-physical results due to the severe pressure gradients near the sharp aerodynamic leading edge. The pressure at the trailing edge was still extrapolated from the pressure side of the airfoil, but the pressure on the suction side was then assumed to vary linearly between the pressure measurement closest to the sharp leading edge and this extrapolated pressure. The effect of this extrapolation scheme on calculated airloads is discussed in Section 2.3.9.

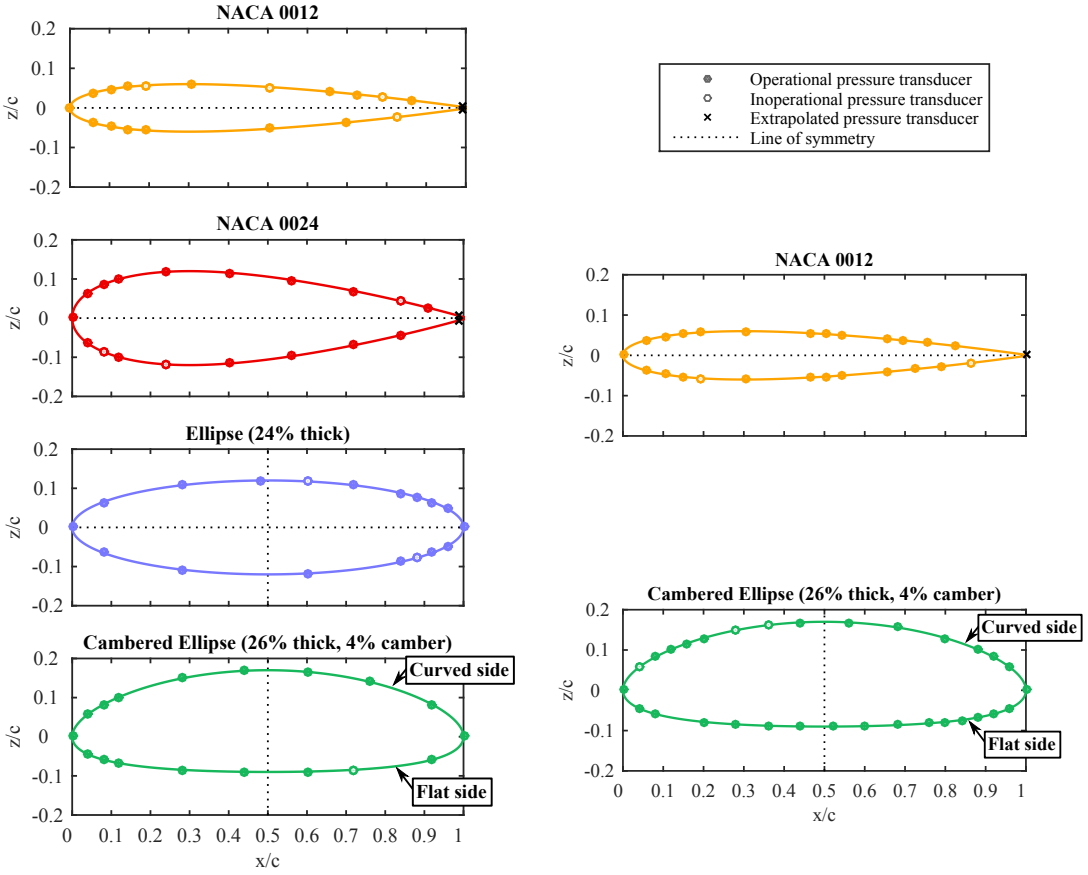

(a) Static airfoil tests (USNA).

(b) Oscillating airfoil tests (UMD).

Figure 2.13: Pressure sensor locations.

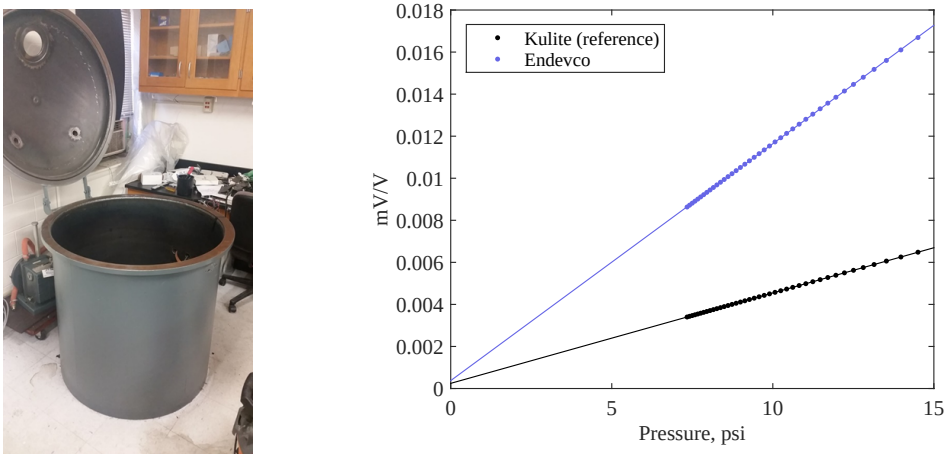

(a) Vacuum chamber.

(b) Sample calibration curve.

Figure 2.14: Calibration of Endevco pressure transducers.

2.3.2 Calibration

The Endevco pressure transducers needed to be calibrated since they included a resistor (nominally 2 kΩ) in series with the excitation voltage. The cambered elliptical airfoil, instrumented with both Kulite and Endevco pressure transducers, was placed in a vacuum chamber. Data from all pressure transducers was sampled continuously while the pressure inside the chamber was reduced to approximately 0.5 atm over 300 s. This slow reduction in pressure, coupled with a high sample rate (1 kHz) allowed for quasi-steady pressure measurements to be calculated by successively averaging 1 s. A tare was performed ahead of time to determine the zero-pressure voltage offsets of one of the Kulite pressure transducers based on the ambient pressure. This allowed the Kulite to serve as the reference pressure using the manufacturer-provided calibration constants. Calibration constants were then calculated for each of the Endevco pressure transducers. Figure 2.14 shows the vacuum chamber and a representative calibration curve.

2.3.3 Acquisition

All pressure measurements were collected with a NI cDAQ-9178 chassis and (8) NI 9237 strain gauge modules (32 channels). Each transducer was provided an excitation voltage of 5 V. Pressure data was sampled at 2 kHz for 5 s during the static airfoil tests. The sampling rate was typically 10 kHz during the oscillating airfoil experiments, and measurements were collected for 500 oscillations. The sampling duration and number of samples per cycle varied with the oscillation frequency. Typical sampling times were between 40–200 s giving 800-4000 samples per cycle. Note that all pressure sensors were sampled simultaneously. No progressive scanning equipment was used.

Prior to each test, a tare run was performed by collecting pressure data for 5 s. This allowed for the calculation of the zero-pressure voltage offset in conjunction with the local

ambient conditions and calibration constants. The inclusion of the temperature compensating resistor with the Endevco pressure transducers led to minimal drift over the duration of a run, typically in the range of $0.01 \leq \Delta c_p \leq 0.03$.

2.3.4 Pressure Integration

The magnitude of the time-averaged and unsteady airloads acting on each airfoil was computed from raw time-resolved surface pressure data. Figure 2.15 illustrates the panel technique used to integrate the surface pressure measurements. The NACA 0012 airfoil is shown for illustrative purposes. The integration approach used here determines discrete, local values of normal and tangential force components (Δc_n and Δc_a) using airfoil geometry and unsteady or time-averaged pressure measurements. These force components are then summed over the entire surface of the airfoil and transformed into airloads.

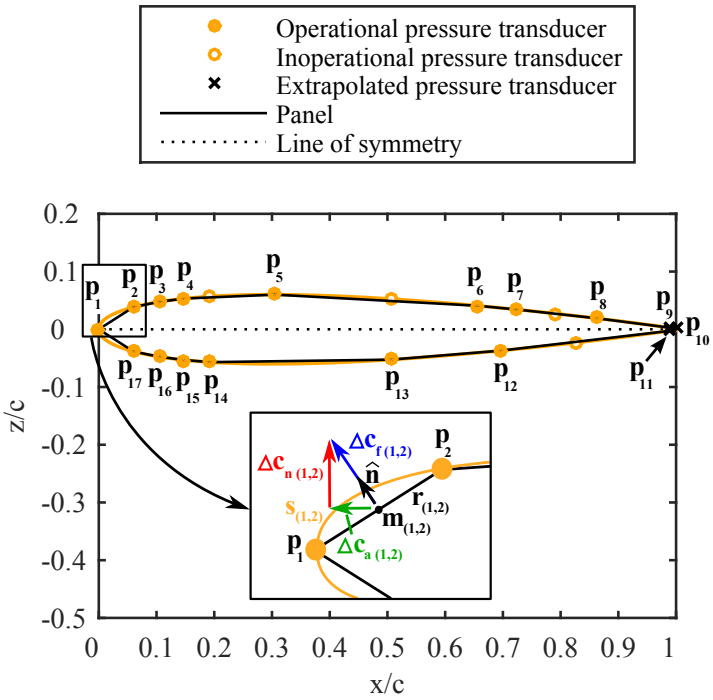

Figure 2.15: Panel technique used to calculate airloads (NACA 0012).

Panels were defined to sequentially connect the geometric coordinates of the operational and extrapolated pressure transducers in a closed path around each airfoil. The inset of Figure 2.15 shows details of the panel between stations 1 and 2 on the NACA 0012. It is assumed that pressure varies linearly between any two stations, hence the pressure acting on this panel is $c_{p(1,2)}$ (the average of p_1 and p_2). The force acting on this panel, $\Delta c_{f(1,2)}$, could be found by integrating over the length of the panel, $r_{(1,2)}$. It is more accurate, however, to assume that the local pressure acts over the actual distance along the airfoil curvature, $s_{(1,2)}$. It is assumed that the force components act at the midpoint of each panel (e.g., $m_{(1,2)}$ in the inset of Figure 2.15). The coordinates of the panel midpoints were used in conjunction with Δc_n and Δc_a to calculate the local pitching moment, Δc_m, about the geometric quarter-chord. Finally, the airloads were calculated by summing over all N panels. It is important to note that the calculated drag is the *pressure drag*.

2.3.5 Magnitude of Unsteady Airloads

Figure 2.16(a) shows sample time traces (one-tenth of the total measurement sampling time) of the calculated time-resolved lift at three static angles of attack for the NACA 0012 airfoil in forward flow. In all three cases, the black dashed line is positioned at the time-averaged lift value and the bounds of the shaded regions are two standard deviations ($\pm 2\sigma$). At $\alpha = 2\,\text{deg}$ (blue), the time-averaged lift value is near 0.2 and the 2σ-variation is approximately 0.03; this value is small relative to the other two shaded regions shown in Figure 2.16(a). At this low angle of attack, the flow is attached and steady leading to small lift fluctuations. At $\alpha = 14\,\text{deg}$ (red), the time-averaged lift is greater (nearly 0.6), but the 2σ-variation is also much greater than at $\alpha = 2\,\text{deg}$ (nearly 0.2). At this angle of attack, the airfoil is stalled, leading to larger fluctuations in lift.

Shifting attention to Figure 2.16(b), the time-averaged lift measured using the 6-axis force balance is compared with time-averaged lift calculated from integrating time-averaged

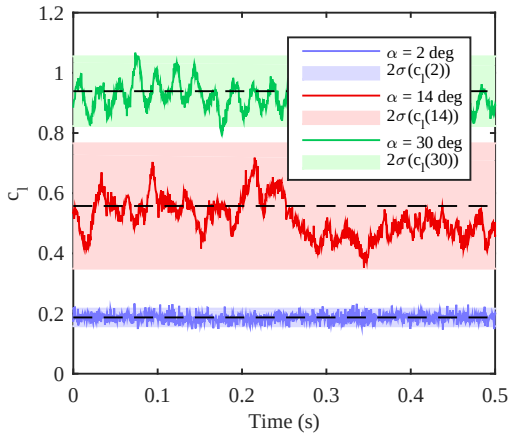

(a) Time trace.

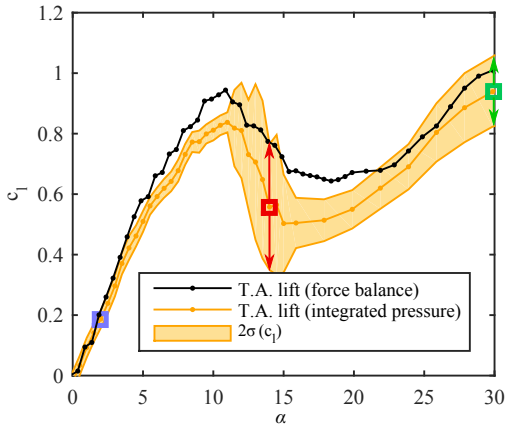

(b) Lift curve in forward flow.

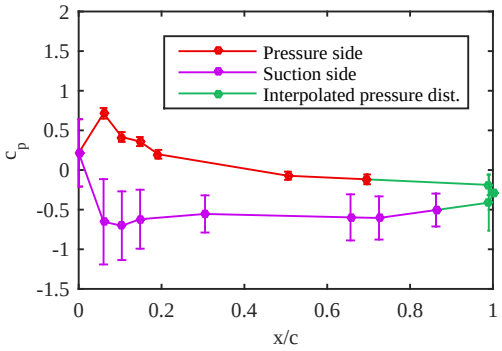

(c) Pressure distribution at $\alpha = 14\,\text{deg}$. The error bars represent $2\sigma(c_p)$.

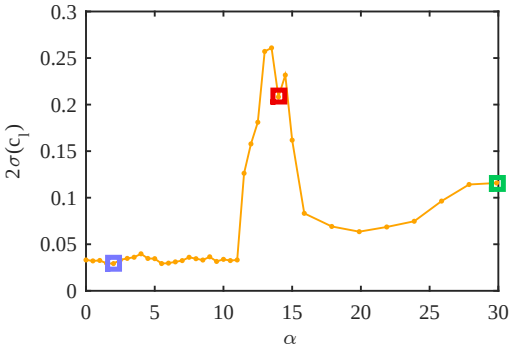

(d) Unsteady Lift.

Figure 2.16: Calculation of the magnitude of unsteady lift (NACA 0012 at $Re = 3.3 \times 10^5$).

pressure measurements. Similar to Figure 2.16(a), the shaded region surrounding the time-averaged lift curve (calculated from integrated pressure measurements) also represents the 2σ-variation of lift. Figure 2.16(c) shows the pressure distribution at $\alpha = 14\,\text{deg}$. The error bars in this figure represent the local 2σ-variation of pressure fluctuations, $2\sigma(c_p)$. It can be seen that the time-averaged pressure distribution along the suction side of the airfoil is nearly flat (typical for a stalled airfoil) while the pressure fluctuations are large due to the unsteadiness of the separated flow. This contrasts with the pressure side of the airfoil; the flow is attached here leading to a non-zero pressure gradient and small pressure fluctuations. The value of $2\sigma(c_l)$ (the height of the filled regions in Figures 2.16(a) and 2.16(b)) is plotted against angle of attack in Figure 2.16(d). Quantities such as $2\sigma(c_l)$ will be referred to as *unsteady lift* acting on a static airfoil as it represents the range of lift fluctuations for a given set of flow conditions.

2.3.6 Convergence Study

Figure 2.17(a) shows the convergence of time-averaged pressure measurements and calculated airloads of the static NACA 0012 at $\alpha = 90\,\text{deg}$. This angle of attack was selected as an example to show here since it represents a "worst case" in terms of unsteadiness in the flow. Focusing on the upper plot, the value of $\widehat{c_p}$ is plotted against time for each of the 17 pressure transducers (operational and extrapolated). It can be seen that after 3.15 s, the time-averaged pressure measurements converge to within 1 % of the average pressure calculated for the full 5 s measurement duration. The time-averaged airloads calculated from the pressure measurements converge within 1.65 s. Figure 2.17(b) shows the convergence of the unsteady pressures and airloads illustrating that the total sampling time of 5 s is sufficient.

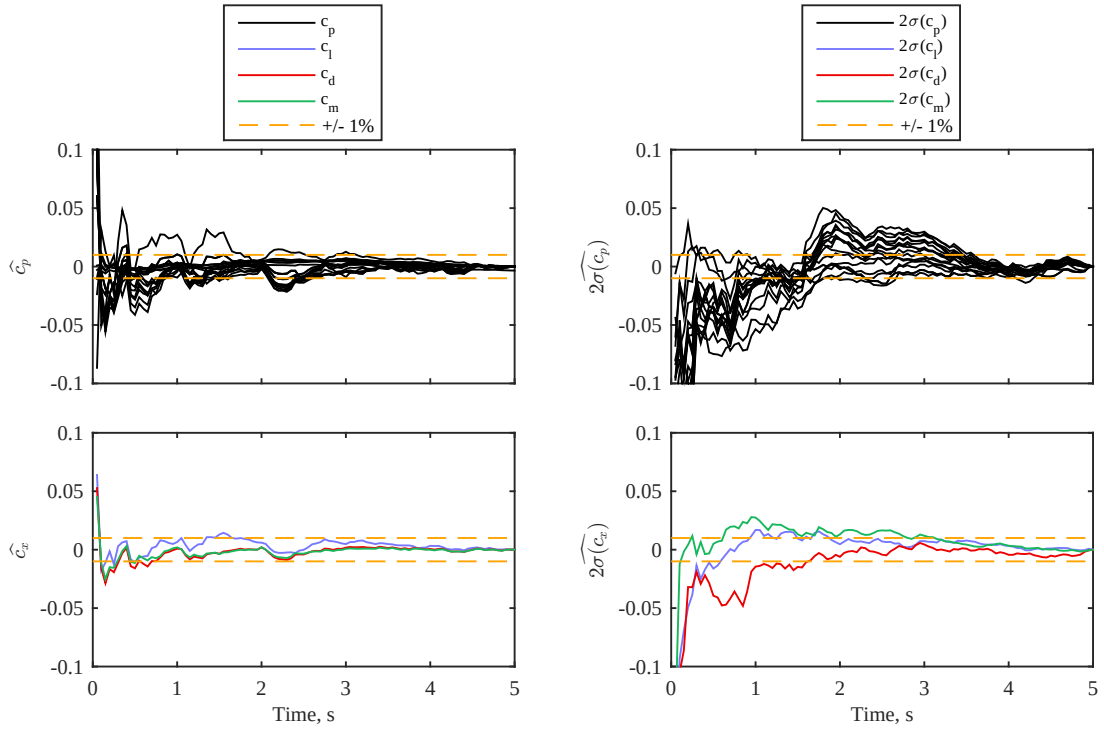

(a) Time-Averaged. (b) Unsteady.

Figure 2.17: Sample results from a convergence study on the time-averaged and unsteady pressure measurements (upper plots) and airloads (lower plots). The case shown is for the NACA 0012 airfoil at $\alpha = 90\,\text{deg}$ and $Re = 6.6 \times 10^5$.

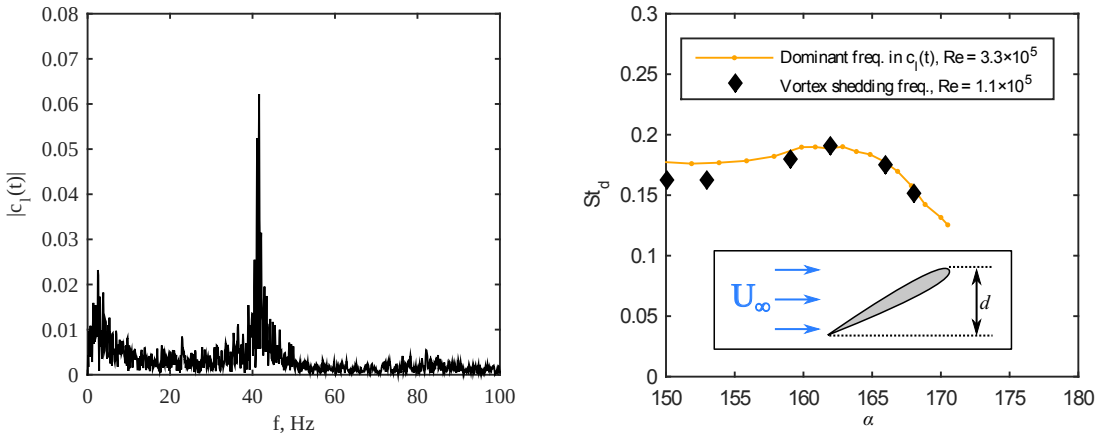

(a) Frequency content of $c_l(t)$ at $\alpha = 150\,\text{deg}$. (b) Comparison with flowfield measurements (Section 2.4.4).

Figure 2.18: Identification of vortex shedding frequencies (NACA 0012 at $Re = 6.6 \times 10^5$).

2.3.7 Frequency Content

In addition to quantifying the magnitude of unsteady airloads, the frequency content was also calculated. An $n-$point FFT was performed using the time-resolved lift signals (such as those presented in Figure 2.16(a)) to determine the frequency content with 0.1 Hz resolution. Figure 2.18(a) shows the frequency content of the lift signal for the NACA 0012 at $\alpha = 150$ deg, revealing a dominant peak at 41.6 Hz. This dominant frequency (if present) was determined for each angle of attack from $0 \leq \alpha \leq 180$ deg. Figure 2.18(b) shows a non-dimensionalized form of this dominant frequency in reverse flow ($150 \leq \alpha \leq 180$ deg) using $St_d = fd/U_\infty$, where d is the projected diameter of the airfoil for a given angle of attack (see inset). This dominant frequency is plotted with known vortex shedding frequencies from flowfield measurements (Section 2.4.4), confirming that the dominant frequency in the time-resolved lift measurements corresponds to vortex shedding in the flowfield.

2.3.8 Phase-averaging

During the oscillating airfoil experiments, time-resolved pressure measurements were collected for 500 pitching cycles. For each cycle, the non-dimensional cycle time is defined as t/T where $t/T = 0$ is the beginning of each pitching cycle (minimum angle of attack) and $t/T = 0.5$ is the middle of the pitching cycle (maximum angle of attack). At each value of t/T (i.e., phase) the measurements from each individual pressure transducer were averaged over the 500 cycles. Figure 2.19(a) shows the results of a convergence study for a single pressure transducer on an oscillating cambered elliptical airfoil undergoing deep dynamic stall. While similar trends are captured for the four cases shown (phase-averaging over 10, 50, 100, and 500 cycles), convergence is achieved after 100 cycles. Instantaneous airloads were calculated using the pressure integration technique outlined in Section 2.3.4. Figure 2.19(b) shows 5 cycles of instantaneous pitching moment (black), the phase-averaged

pitching moment over 500 cycles (blue), and the 2σ-variation of pitching moment (shaded blue). The results of the convergence study on the mean pitching moment and 2σ-variation are shown in Figures 2.19(c) and 2.19(d). Convergence is again achieved within 100 cycles, demonstrating that phase-averaging over 500 cycles certainly gives reliable phase-averaged and 2σ-variations of unsteady pressure measurements and calculated airloads.

2.3.9 Measurement Uncertainty

The primary source of uncertainty in airloads calculated from pressure measurements arises from integration error due to the fact that the pressure measurements are discrete and thus do not fully capture complete pressure distributions. As an example, Figure 2.20 shows time-averaged airloads for a NACA 0012 airfoil for $0 \leq \alpha \leq 180\,\text{deg}$ at $Re = 3.3 \times 10^5$. Force balance measurements are compared with time-averaged airloads calculated using the pressure integration technique. Similar to Figure 2.16(b), the plots in Figure 2.20 also show the unsteady airloads as a filled region surrounding the time-averaged airload curves. The time-averaged lift calculated through integration of the pressure distribution is in good agreement with force balance measurements for $20 \leq \alpha \leq 160\,\text{deg}$. In forward flow ($0^\circ \leq \alpha \leq 20^\circ$), the pressure gradients at the leading edge are high and the relatively sparse distribution of pressure sensors is unable to fully resolve the pre-stall suction and pressure peaks or the post-stall pressure side peak. Recall that geometric constraints imposed by the thin trailing edge prevented the installation of pressure sensors for $0.875 \leq x/c \leq 1$. In reverse flow ($160^\circ \leq \alpha \leq 180^\circ$), the lack of physical pressure measurements restricts the resolution of suction and pressure expected here in reverse flow. The consequences of these integration errors are observed in the lift and pitching moment curves. The discrepancies in the pitching moment curve are driven by the effect of integration error on the calculation of the moment arm between the quarter-chord and center of pressure.

A secondary source of uncertainty that ultimately appears in the integrated time-

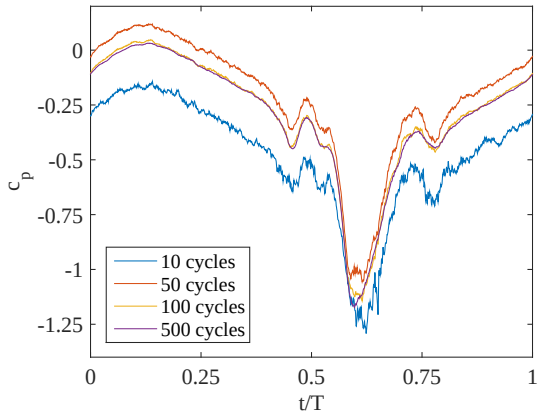

(a) Convergence of measurements from a single pressure transducer.

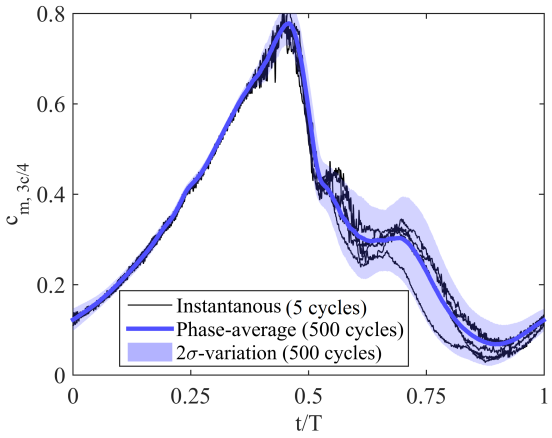

(b) Phase-averaged pitching moment.

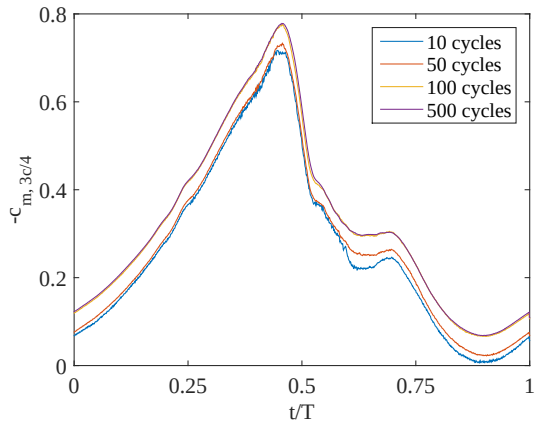

(c) Convergence of mean pitching moment.

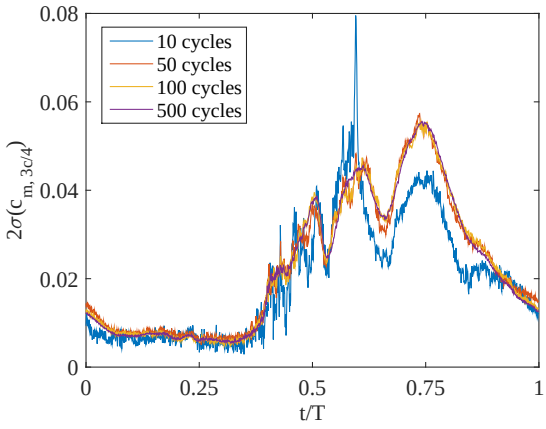

(d) Convergence of 2σ-variation of pitching moment.

Figure 2.19: Phase-averaging of pressure measurements and unsteady pitching moment for an oscillating cambered elliptical airfoil undergoing deep dynamic stall with $-\alpha_{0,\mathrm{rev}} = 15\,\mathrm{deg}$, $\alpha_1 = 10\,\mathrm{deg}$, $k = 0.160$, and $Re = 3.3 \times 10^5$.

resolved airloads arises from the noise of the data acquisition system. Tables 2.5 and 2.6 list the maximum noise of each airload at each Reynolds number tested for the static and oscillating airfoil experiments. The noise was calculated by integrating the unsteady airloads for 5 s while the wind tunnel was off. Since the unsteady airloads are non-dimensionalized by dynamic pressure, the noise decreases with increasing Reynolds number.

Table 2.5: Static airfoil noise.

Re	$2\sigma(c_l)$	$2\sigma(c_d)$	$2\sigma(c_m)$
3.3×10^5	0.029	0.0067	0.0160
6.6×10^5	0.0064	0.0016	0.0031
1.0×10^6	0.0029	0.0007	0.0014

Table 2.6: Oscillating airfoil noise.

Re	$2\sigma(c_l)$	$2\sigma(c_d)$	$2\sigma(c_m)$
1.65×10^5	0.0257	0.0089	0.0070
3.3×10^5	0.0064	0.0022	0.0017
5.0×10^6	0.0028	0.0010	0.0008

2.4 Flowfield Measurements

2.4.1 PIV Equipment, Acquisition, and Cross-Correlation

Time-resolved, planar (two-component) PIV was performed to quantify the flow environment around the model rotor blades in both forward and reverse flow. Figure 2.21 shows the PIV setup. A double-pulsed Nd:YLF laser (Litron LDY304, 30 mJ/pulse, 10 kHz max) illuminated the flow with a sheet thickness of approximately 2 mm. The air was seeded at the inlet of the wind tunnel using vaporized mineral oil via a custom-built seeding generator with three laskin nozzles and a smoke rake. High-speed cameras (Phantom V641, 4 Mpx, 1450 fps max) were synchronized with the laser using a high-speed controller (LaVision model no. 1108075). The flow was imaged at 700 Hz (double-frame) through an acrylic window positioned on the floor of the wind tunnel test section. For the static airfoil experiments, a single camera was used and tilted relative to the laser sheet by approximately 15 deg. A scheimpflug adapter was used in conjunction with a Nikon 85 mm f/1.8 D lens to achieve uniform focus. For each angle of attack, 200 velocity field measurements were collected. For the oscillating airfoil experiments, two cameras with Nikon 50 mm f/1.8 D lenses were used

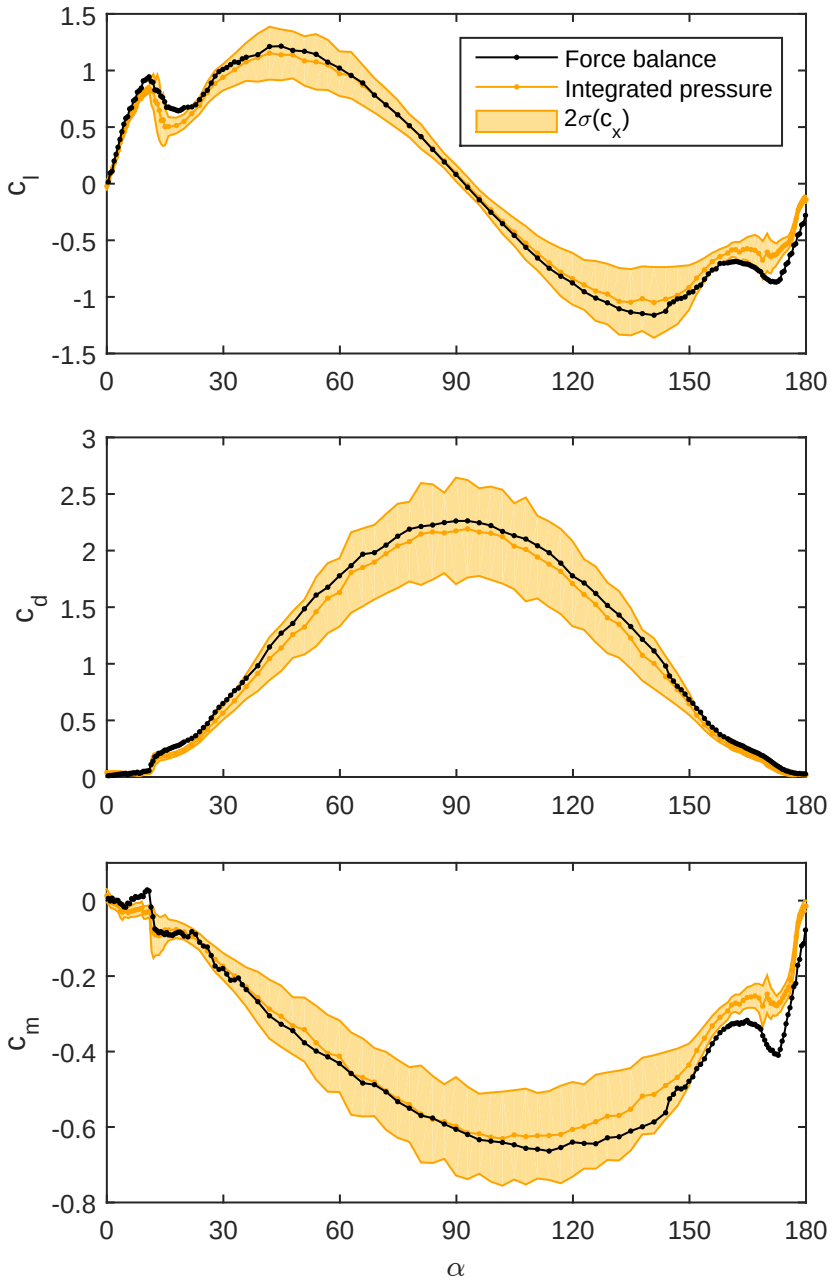

Figure 2.20: Time-averaged airloads of a NACA 0012 airfoil at $Re = 3.3 \times 10^5$.

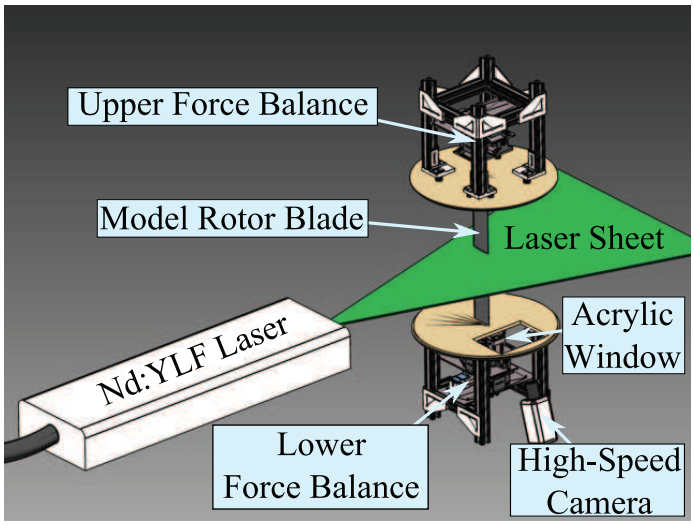

Figure 2.21: PIV setup. The wind tunnel test section is not shown for clarity.

and the resulting velocity fields from each camera were stitched together. For each run, velocity field measurements were collected for 10 pitching cycles with 50-100 measurements per cycle, depending on the oscillation frequency (500-1000 images per case). The sampling frequency was set to a multiple of the oscillation frequency to allow for phase-averaging of the velocity field measurements (Section 2.3.8).

Capturing and processing of velocity field measurements was performed using DaVis software (v.8.1.3–8.2.3) by LaVision, Inc. Prior to data collection, a well characterized calibration target was used to calibrate the PIV measurements. A background subtraction process was performed on the raw images to remove the reflection of the laser off the model rotor blade, increasing the signal-to-noise ratio in this area. Regions where the velocity field was undefined (such as the blade and laser shadow) were masked from processing. The maximum particle displacement between the two frames of each image pair was approximately 8 pixels. A multi-pass cross-correlation algorithm was performed with one pass of a 48×48 pixel window and two passes of a 24×24 pixel window; each pass implemented a 50% window overlap. Circular windows were used to eliminate the bias effects encountered along the diagonals of traditional square windows. The resulting vector field provided a spatial

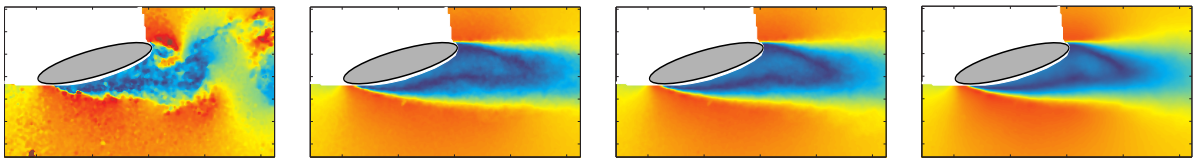

(a) $n = 1$, 0 % converged. (b) $n = 25$, 82.4 % converged. (c) $n = 50$, 92.0 % converged. (d) $n = 200$, 99.7 % converged.

Figure 2.22: Time-averaged total velocity field of an elliptical airfoil at $\alpha = -16$ deg (stalled) using an increasing number, n, of velocity measurements.

resolution of 80 vectors per chord for the static airfoil tests and 181 vectors per chord for the oscillating airfoil tests.

2.4.2 Time-averaged and Unsteady Velocity Fields

Ensemble-averaging of a time-series of velocity field measurements was performed to determine time-averaged flowfields. Figure 2.22 shows an example of the effects of this progressive averaging scheme on an increasing number of time-resolved velocity field measurements for the elliptical airfoil in a stalled condition. Unsteady velocity fields were calculated using the 2σ-variation of total velocity at each spatial location over the 200 measurements in order to highlight unsteady regions in the flow.

2.4.3 Phase-averaged Velocity Fields

The purpose of phase-averaging is to highlight periodic flow features (such as the dynamic stall vortex) and effectively filter out aperiodic flow features (such as the flow near the surface of the airfoil over $0.05 \leq x/c \leq 0.3$). Figure 2.23 shows the phase-averaging process. Figure 2.23(a) shows an instantaneous velocity field measurement with a dynamic stall vortex near the suction side of the airfoil. Figure 2.23(b) shows the phase-averaged velocity field over 10 cycles. It should be noted that phase-averaging can also smear the apparent size and strength of a vortex if there is substantial aperiodicity in the location of

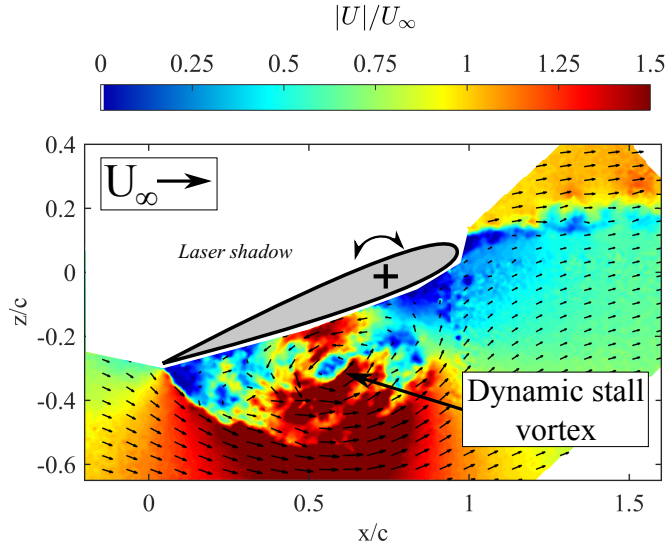

(a) Instantaneous velocity field measurement.

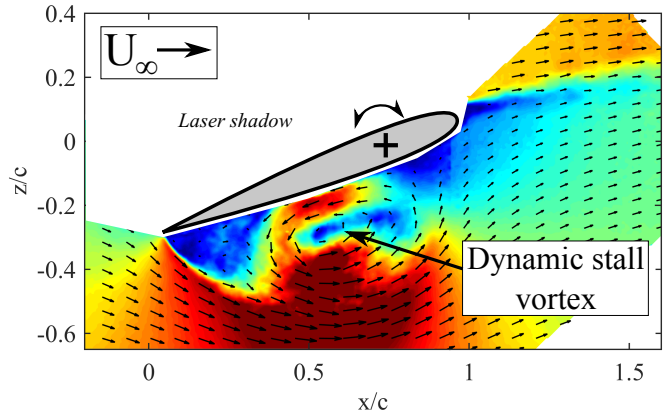

(b) Phase-averaged velocity field (over 10 cycles).

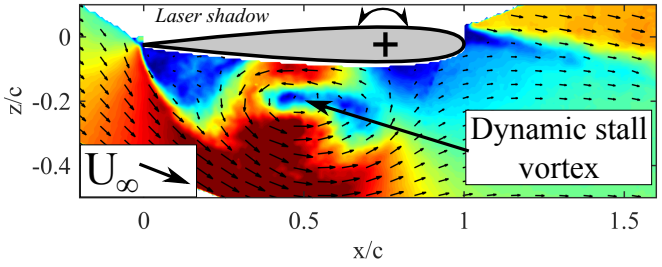

(c) Blade-fixed phase-averaged velocity field.

Figure 2.23: Phase-averaging process. An oscillating NACA 0012 is shown at $t/T = 0.64$ with $-\alpha_{0,\mathrm{rev}} = 15\,\mathrm{deg}$, $\alpha_1 = 10\,\mathrm{deg}$, $Re = 1.65 \times 10^5$, and $k = 0.511$.

its center. Finally, the phase-averaged velocity fields presented in the present work have been rotated to a blade-fixed frame of reference (Figure 2.23(c)) in order to more easily compare the flowfields at different phases.

2.4.4 Frequency Content

Vortex shedding frequencies in the flowfield measurements were identified by examining the frequency content of a signal, $\widehat{\omega}_{x_o/c}(t)$, constructed by taking the sum of vorticity along a vertical cut of the flowfield positioned at a station x_o/c downstream of airfoils. For a time-resolved PIV data set of finite duration, $\widehat{\omega}_{x_o/c}(t)$ is defined as:

$$\widehat{\omega}_{x_o/c}(t) = \sum_{i=(z/c)_{\min}}^{(z/c)_{\max}} \omega(x_o/c, i, t)c/U_\infty, t \in [0, t_{\max}] \tag{2.2}$$

The summation limits of $(z/c)_{max}$ and $(z/c)_{min}$ are selected far enough above and below the wake so that the vorticity is zero (i.e., in the freestream). This "vorticity slice" method is illustrated in Figure 2.24 with $x_o/c = 1.4$. The value of $\widehat{\omega}_{x_o/c}(t)$ varies based on the vorticity contained along the downstream slice. A convergence study was performed for the elliptical airfoil using increasing samples, N, for the three Reynolds numbers at $|\alpha_{\text{rev}}| = 0, 18, 30$ deg to determine that the error in the vortex shedding frequencies measured with this wake survey technique is less than 1 %.

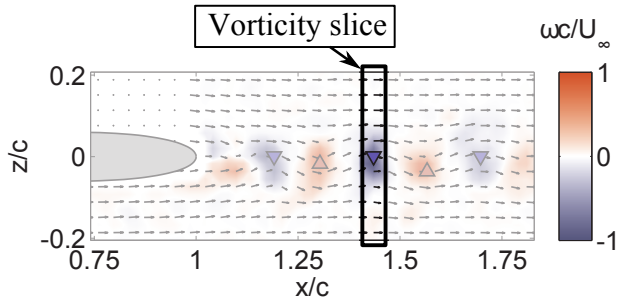

Figure 2.24: Illustration of the vorticity slice method.

2.5 Angle of Attack Measurements

2.5.1 Static Airfoil Tests

At UMD, static angle of attack was set using an aluminum plate with equally spaced holes milled using a CNC. Prior to calibration or testing, a custom-built jig was used to ensure that each blade was initially installed at 0 deg angle of attack with an estimated error of ± 0.5 deg. These airload measurements were left uncorrected for installation error.

At the USNA, angle of attack was set using a motor-controller to 0.01 deg accuracy. The measured airload curves were corrected such that the zero-lift angle of attack was 0 deg for airfoils symmetric about $z/c = 0$. This correction was typically ≈ 0.5 deg with a maximum of ≈ 1.5 deg. For the cambered ellipse airfoil (symmetric about $x/c = 0.5$ but not $z/c = 0$), data was taken through 180 deg. This allowed for shifting the lift curve so that the zero-lift angle of attack was equal in both forward and reverse flow, resulting in a correction of 0.4 deg.

2.5.2 Oscillating Airfoil Tests

Angle of attack was calculated by averaging the angle recorded by two rotary shaft encoders attached to the quarter-chord of the airfoil (Section 2.1.4). Each encoder was accurate to 0.045 deg (8000 counts/rev). A square was used to reference all angle of attack measurements to the wind tunnel test section. This allowed for the desired *nominal* mean pitch angle to be set with 0.2 deg accuracy. For each airfoil (and in both forward and reverse flow), time-averaged pressure measurements were collected to calculate static airload curves. The static zero-lift angle of attack for each airfoil was used to correct the oscillating airfoil data angle of attack after data collection. The corrections for the NACA 0012 were $+1.1$ deg in forward flow and -0.9 deg in reverse flow. The corrections for the cambered elliptical

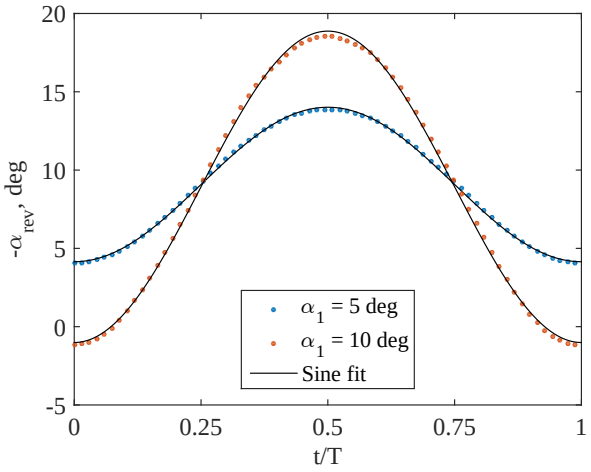

Figure 2.25: Phase-averaged dynamic pitching kinematics for the NACA 0012 with a nominal mean pitch angle of $-\alpha_{0,\text{rev}} = 10\,\text{deg}$. Markers are shown at 1/25 of the total number of recorded phases.

airfoil were $+0.9\,\text{deg}$ in forward flow and $+1.6\,\text{deg}$ in reverse flow. References in the text to mean pitch angles refer to the nominal (uncorrected) angle of attack, though all oscillating airfoil results have accounted for this angle of attack correction. Figure 2.25 shows sample phase-averaged pitching kinematics for the NACA 0012 airfoil. A sinusoidal curve fit is plotted for comparison.

2.6 Summary

Two dimensional static and oscillating airfoil experiments were performed at two wind tunnel facilities. Sub-scale experiments on static airfoils were performed for $5.5 \times 10^4 \leq Re \leq 1.65 \times 10^5$ at UMD using a custom-built force balance, time-resolved particle image velocimetry, and surface oil flow visualization to evaluate the time-averaged aerodynamics and unsteady wakes. Full-scale experiments on static airfoils were performed for $3.3 \times 10^5 \leq Re \leq 1.0 \times 10^6$ at the USNA, using a 6-axis force balance, time-resolved (i.e., unsteady) surface pressure measurements, and surface oil flow visualization to evaluate Reynolds number effects on the time-averaged aerodynamics and unsteady airloads. The

results and analysis from the experiments on static airfoils are presented in Chapter 3. Oscillating airfoil experiments were performed for $1.65 \times 10^5 \leq Re \leq 5.0 \times 10^5$ at UMD, using a custom-built dynamic pitching rig, time-resolved particle image velocimetry, and unsteady surface pressure measurements to characterize reverse flow dynamic stall. The results and analysis experiments on oscillating airfoils are presented in Chapter 4.

Chapter 3

Aerodynamics of Static Rotor Blade Sections in Reverse Flow

This chapter examines the time-averaged and unsteady aerodynamics of several rotor blade airfoils at fixed angles of attack through 360 deg with special attention to $0 \leq \alpha \leq 30$ deg in forward flow and $0 \leq -\alpha_{\text{rev}} \leq 30$ deg in reverse flow (where $\alpha_{\text{rev}} \equiv \alpha - 180$ deg). This is the most fundamental approach to studying airfoils in reverse flow and provides insight into time-averaged and unsteady airloads, performance, and flowfield characteristics. Airfoils that operate at high angles of attack and in reverse flow inherently feature some degree of flow separation and, in some cases, vortex shedding. This can lead to periodic (or in the absence of vortex shedding, aperiodic) unsteady flowfields and airloads. For full-scale high advance ratio rotors, these unsteady airloads can cause vibrations and component fatigue since a large portion of the retreating rotor blade operates in reverse flow.

3.1 Time-Averaged Aerodynamics

This section examines the time-averaged airloads, flowfields and pressure distributions of airfoils at high angles of attack and/or in reverse flow. The time-averaged airloads given in this chapter are particularly valuable since they have been carefully acquired with high precision so that they can serve as look-up tables for comprehensive rotorcraft codes. Sec-

tional lift characteristics are important for determining the total rotor thrust and trim (i.e. control settings), drag directly influences the profile power required in forward flight, and pitching moment affects the torsional loads on rotor blades as well as axial loads on pitch links. The airload database produced in this work will allow for the evaluation of the impact of various airfoil types on rotor performance, especially in the reverse flow region.

3.1.1 Airloads

Figure 3.1 shows time-averaged airloads of the NACA 0012, ellipse (24% thick), and the DBLN-526 for $0 \leq \alpha \leq 360\,\text{deg}$ and $Re = 1.1 \times 10^5$. Forward flow occurs for $0 \leq \alpha < 90\,\text{deg}$ and $270 < \alpha \leq 360\,\text{deg}$, whereas reverse flow occurs for $90 < \alpha < 270\,\text{deg}$. Over the entire range $0 \leq \alpha \leq 360\,\text{deg}$, each airfoil undergoes four stall events. The flow over the airfoils is fully separated between stalls 1 and 2 and between 3 and 4. The orientation of the airfoil during these four stalls is illustrated in Figure 3.2. The closed-circuit sections of the curves for the elliptical and DBLN-526 are aerodynamic hysteresis loops; these are illustrated more clearly in Figure 3.3 and Section 3.4. Note that the angle of attack in reverse flow is defined as $\alpha_{\text{rev}} = \alpha - 180$. Recall that the NACA 0012 and elliptical airfoils are symmetrical about $z/c = 0$. As a result, the lift curves for these airfoils are inverted and symmetric about $\alpha = 180\,\text{deg}$, therefore $c_l(\alpha_{\text{rev}}) = -c_l(-\alpha_{\text{rev}})$ (Figure 3.1). The drag curves for these two airfoils are symmetric about $\alpha = 180\,\text{deg}$, hence $c_d(\alpha_{\text{rev}}) = c_d(-\alpha_{\text{rev}})$. Recall that the DBLN-526 airfoil is not symmetric about $z/c = 0$ due to camber. Sketches of the orientation of the DBLN-526 airfoil at selected angles of attack are included on the lift curve plots to illustrate the changing role of the geometric lower surface (exaggerated as perfectly flat) and the geometric upper surface (exaggerated as highly curved). Some general similarities between the force curves for the three airfoils will now be discussed.

Starting at $\alpha = 0\,\text{deg}$, all airfoils increase in lift with increasing angle of attack to some maximum value before the onset of stall 1, characterized by a decrease in lift and

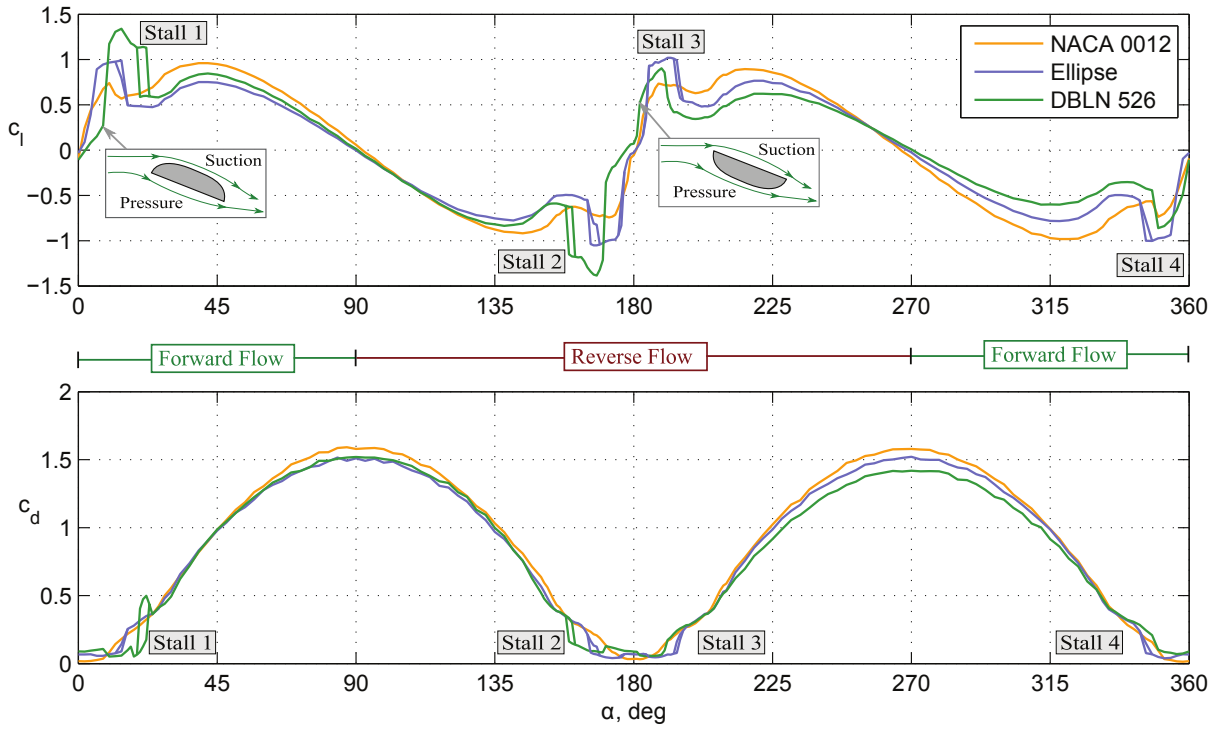

Figure 3.1: Time-averaged lift and drag force balance measurements for $0 \leq \alpha \leq 360\,\text{deg}$ at $Re = 1.1 \times 10^5$.

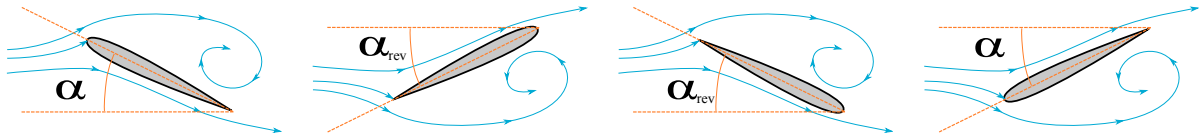

(a) *Stall 1*, $\alpha > 0$. (b) *Stall 2*, $\alpha_{\text{rev}} < 0$. (c) *Stall 3*, $\alpha_{\text{rev}} > 0$. (d) *Stall 4*, $\alpha < 0$.

Figure 3.2: Airfoil orientation during the four stalls experienced through 360 deg. Stalls 1 and 4 occur in forward flow. Stalls 2 and 3 occur in reverse flow.

corresponding increase in drag. Stall 1 occurs for the NACA 0012 near $\alpha = 10\,\text{deg}$ whereas the elliptical and DBLN-526 airfoil stall near $\alpha = 14\,\text{deg}$; both exhibit a trailing edge stall followed by an abrupt leading edge stall. As the angle of attack is increased further, drag increases smoothly and equally for each airfoil.

At $\alpha = 90\,\text{deg}$, the resultant lift component tends towards zero while drag approaches its maximum. At this angle of attack, the airfoils behave similar to a flat plate in a crossflow. It is worth noting that at $\alpha = 90\,\text{deg}$, both airfoils with a blunt trailing edge produce zero lift while the NACA 0012 aifoil produces a small amount of positive lift. One possible explanation for this is that the flow accelerates over the blunt geometric leading edge (facing upward) before separating. The airfoils with a blunt trailing edge are also slightly more aerodynamic at $\alpha = 90\,\text{deg}$, causing a lower maximum drag than the NACA 0012 whose upstream surface is more normal to the freestream flow.

As the angle of attack is increased further, the airfoils are at a negative angle of attack in reverse flow, leading to negative values of lift. For the NACA 0012 airfoil, the stall characteristics and magnitude of the drag are different between forward and reverse flow; this will be discussed in greater detail later in the current section and in Section 3.1.2. At $\alpha = 270\,\text{deg}$, the airfoils with a blunt trailing edge again produce zero lift while the NACA 0012 produces a slight negative lift; the blunt geometric leading edge is now facing downward. It is also worth noting that the drag of the cambered DBLN-526 airfoil is lower than for the symmetric elliptical airfoil. The geometric upper surface of the DBLN-526 airfoil faces upstream; this surface has greater curvature than the ellipse, making it slightly more streamlined. Finally, the airfoils again stall with a negative angle of attack in forward flow ($340 \leq \alpha \leq 350\,\text{deg}$); the magnitude of lift then decreases to zero. Table 3.1 summarizes the approximate critical angle of attack and $|c_{l,\max}|$ for each airfoil.

To gain further insight into the stall characteristics, Figure 3.3 compares the time-averaged airload measurements in forward and reverse flow. Note that $c_l(0) \neq 0$ for the

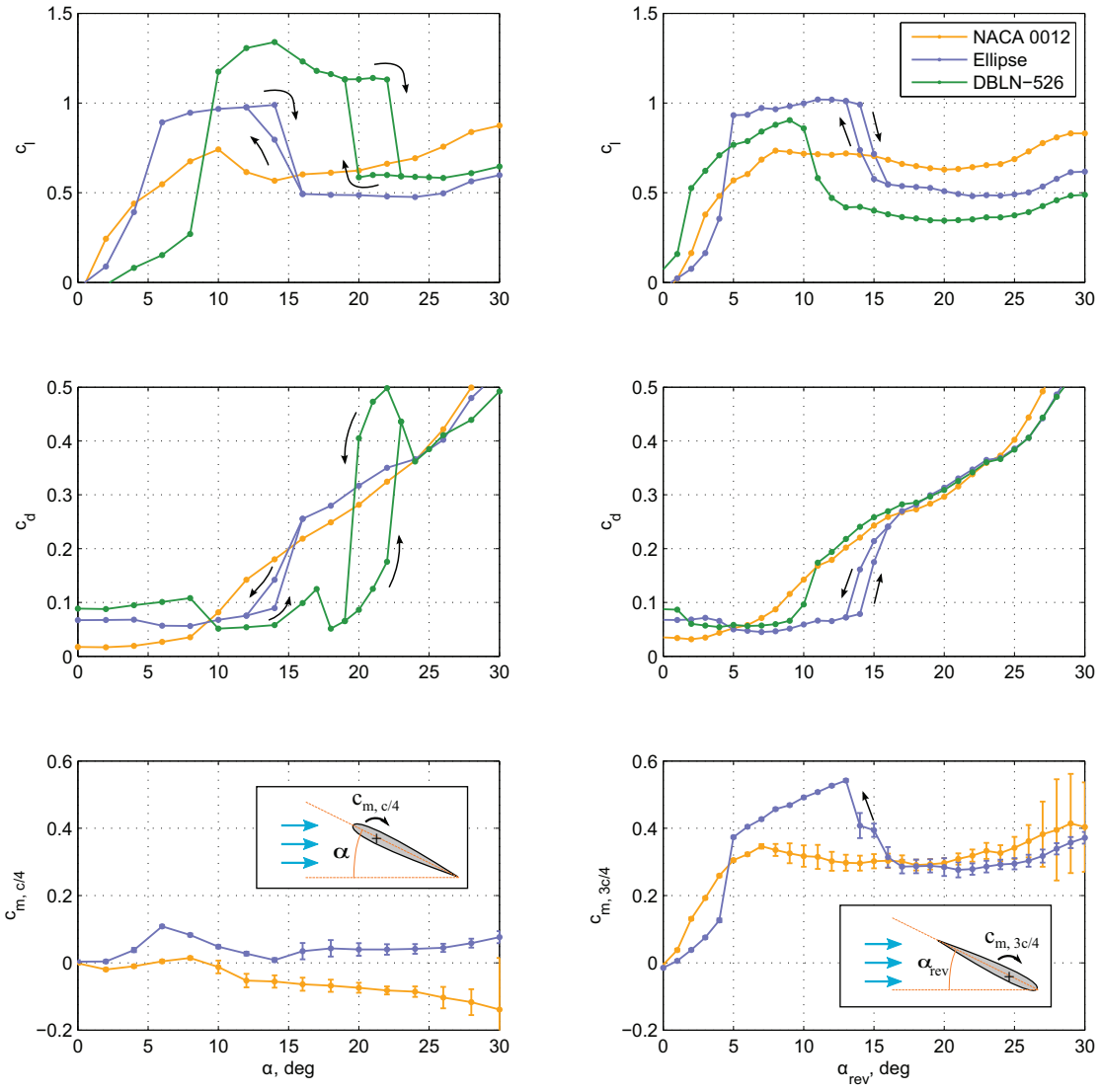

(a) Forward flow.

(b) Reverse flow.

Figure 3.3: Time-averaged lift, drag, and pitching moment measurements for $0 \leq \alpha \leq 30\,\text{deg}$ (forward flow) and $0 \leq \alpha_{\text{rev}} \leq 30\,\text{deg}$ (reverse flow).

Table 3.1: Summary of approximate static stall characteristics for the four stalls experienced by the three airfoils in the range of $0 \leq \alpha \leq 360\,\text{deg}$ and $Re = 1.1 \times 10^5$. To allow for a more intuitive comparison of critical angles of attack, α_{cr} is calculated for Stalls 2 and 3 using $\alpha_{\text{cr}} = |\alpha - 180|$ and for Stall 4 using $\alpha_{\text{cr}} = |\alpha - 360|$.

	α_{cr}, deg				$\lvert c_{l,\max} \rvert$			
Airfoil	*Stall 1*	*Stall 2*	*Stall 3*	*Stall 4*	*Stall 1*	*Stall 2*	*Stall 3*	*Stall 4*
NACA 0012	10	8	8	10	0.74	0.74	0.73	0.74
Ellipse	14	14	14	14	0.99	1.05	1.02	1.00
DBLN-526	14, 22	12, 21	9	10	1.34	1.39	0.90	0.86

symmetric airfoils due to installation error. The measurements were left uncorrected in this set of results since a similar installation process was used for the cambered DBLN-526 airfoil. The error bars on the lift and drag curves represent 2σ-variation across multiple independent angle of attack sweeps. Recall that for each sweep, data was collected at each angle of attack for 5 s with a sampling rate of 10 kHz (Section 2.2.2). The error bars on the pitching moment curve represent 2σ-variation of the measurements from a single angle of attack sweep. In forward flow, the NACA 0012 exhibits a nonlinear increase in lift that is typical for airfoils operating at low Reynolds numbers due to the influence of laminar separation bubbles [52, 53]. In reverse flow, lift levels out near $\alpha_{\text{rev}} = 8\,\text{deg}$, indicating a thin airfoil stall. To confirm this, Figure 3.4 compares lift measurements for the NACA 0012 in reverse flow with a flat plate at the same Reynolds number [54]. The behavior of the NACA 0012 in reverse flow is similar to a flat plate due to its sharp aerodynamic leading edge which forces boundary layer separation at a low angle of attack. Recall that similar behavior was also observed at $Re = 1.0 \times 10^6$ (Figure 1.9).

Returning to Figure 3.3, the maximum lift coefficient and critical stall angle for the NACA 0012 in reverse flow for the current work (0.73, 8 deg) are comparable to the values found by Critzos et al. (0.8, 8 deg) despite the order of magnitude difference in test Reynolds number [8]. This suggests the possibility that time-averaged airloads near $\alpha_{\text{cr,rev}}$ are less dependent on Reynolds number in reverse flow due to early separation resulting from the

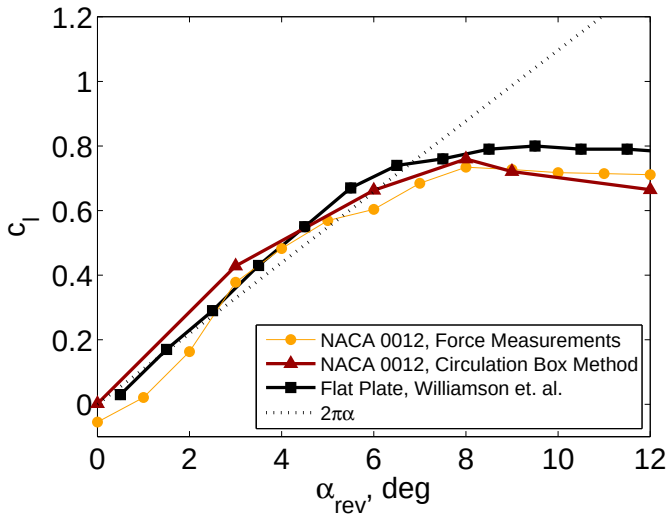

Figure 3.4: Comparison of lift measurements flat plate [54] on the NACA 0012 in reverse flow made using the force balance and circulation box technique.

sharp aerodynamic leading edge (Section 3.5.1). Turning attention to the drag curves, there is a 25% increase in drag at $\alpha_{\text{rev}} = 4\,\text{deg}$, suggesting that flow separation begins to occur at this low angle of attack. At $\alpha = 0\,\text{deg}$ the measured drag is $c_d = 0.017$ in forward flow and $c_d = 0.035$ in reverse flow; the drag in reverse flow is nearly double the drag in forward flow for $0 \leq \alpha \leq 10\,\text{deg}$. This behavior was also described in Section 1.3.2. In forward flow, the pitching moment about the aerodynamic quarter-chord of the NACA 0012 remains near zero prior to stall and decreases with angle of attack post-stall as the center of pressure moves aft. The trend is dramatically different for reverse flow; there is a rapid increase to $c_{m,3c/4} \approx 0.35$ at $\alpha_{\text{rev}} = 7\,\text{deg}$, followed by a gradual decrease, then increase. Recall that the pitching moment about the aerodynamic three-quarter chord is considered in reverse flow due to the influence of this airload on rotor blade torsion and pitch link loads. This highly-positive, destabilizing pitching moment (directed towards increasing $|\alpha_{\text{rev}}|$) is sketched in the inset of Figure 3.3(b). Note the small error bars in pitching moment for $0 \leq \alpha_{\text{rev}} \leq 7\,\text{deg}$, indicating attached flow or separated flow with nearly steady airloads. For $\alpha_{\text{rev}} \geq 8\,\text{deg}$, the error bars change in magnitude with angle of attack due to contributions of unsteady airloads

(i.e. periodic vortex shedding) and the aeroelastic response of the model rotor blade.

The elliptical blade shows similar lift and drag curves in both forward and reverse flow due to symmetry. A rapid increase in lift occurs from $0 \leq \alpha \leq 6\,\text{deg}$, followed by a gradual increase in lift until stall. The pitching moment of the elliptical airfoil in forward flow starts at zero and increases to $c_{m,c/4} \approx 0.11$ at $\alpha = 6\,\text{deg}$, followed by a linear decrease to $c_{m,c/4} \approx 0.01$ at $\alpha = 14\,\text{deg}$. Note that for all angles of attack, the pitching moment is positive (unstable). Like the NACA 0012 in reverse flow, the pitching moment curve for the elliptical airfoil in reverse flow qualitatively mirrors the lift curve; lift acts near the aerodynamic quarter-chord giving a large moment about the three-quarter chord. The differences between the shape of the lift and moment curves result from variation of the center of pressure with angle of attack (Figure 1.7 and Section 3.1.3). There is a rapid increase in pitching moment to $c_{m,3c/4} \approx 0.37$ at $\alpha_{\text{rev}} = 5\,\text{deg}$, followed by a linear increase to $c_{m,3c/4} \approx 0.54$ at $\alpha_{\text{rev}} = 13\,\text{deg}$, and a rapid decrease associated with stall. During the slope transition of the lift and pitching moment curves near $\alpha \approx 5 - 6\,\text{deg}$, there is a corresponding slight decrease in drag; this feature will be discussed in more detail in Section 3.1.2.

It is worth pausing here to directly compare the NACA 0012 airfoil in reverse flow with the elliptical airfoil as this will provide a representative comparison between sharp and blunt trailing edge airfoils. The force curves cross over, allowing for the identification of three angle of attack ranges. For "low" angles of attack ($0 \leq \alpha_{\text{rev}} \leq 4\,\text{deg}$), the downward-acting lift and unstable pitching moment of the elliptical airfoil are less than that of the NACA 0012, but the drag is greater. In the "medium" angle of attack range ($5 \leq \alpha_{\text{rev}} \leq 15\,\text{deg}$), the drag of the ellipse is lower, whereas the lift and pitching moment are greater. Finally, for "high" angles of attack ($\alpha_{\text{rev}} \geq 16\,\text{deg}$), the lift and pitching moment are less than for the NACA 0012 and the drag is approximately equal. The preceding discussion highlights the strong dependence of angle of attack on the evaluation of a sharp or blunt trailing edge airfoils in reverse flow.

The lift and drag curves of the DBLN-526 airfoil exhibit similar trends to the symmetric

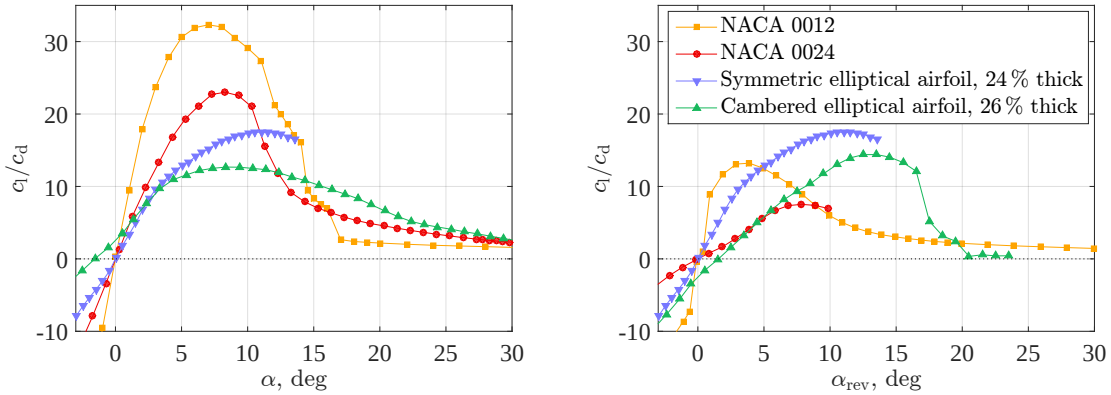

(a) Forward flow.

(b) Reverse flow.

Figure 3.5: Lift-to-drag ratio of four rotor blade airfoils in forward and reverse flow at $Re = 1.0 \times 10^6$.

elliptical airfoil, but are shifted to a greater angle of attack due to the effects of camber. The trailing edge stall also occurs over a larger range of angles of attack in forward flow ($18 \leq \alpha \leq 23$ deg, increasing angle of attack branch), with an increase in drag and slight decrease in lift.

Finally, Figure 3.5 compares the lift-to-drag ratio of four airfoils in forward and reverse flow at a much higher Reynolds number of 1.0×10^6. Note the inclusion of the NACA 0024 and cambered elliptical airfoil, an analog to the DBLN-526. Not surprisingly, Figure 3.5(a) shows that the lift-to-drag ratio in forward flow is generally higher for the two NACA series airfoils. However, it is worth noting the lift-to-drag ratio of the cambered elliptical airfoil is noticeably lower than the symmetric elliptical airfoil for $4 \leq \alpha \leq 18$ deg. This is due to the fact that cambered elliptical airfoil is subjected to a large amount of flow separation in this angle of attack range (Section 3.5.1). This suggests that the symmetrical elliptical airfoil may operate more efficiently than the cambered elliptical airfoil in forward flow on the advancing side of the rotor, where $Re > 1.0 \times 10^6$. In reverse flow (Figure 3.5(b)), the lift-to-drag ratio is lowest for the cambered elliptical airfoil and NACA 0024 for $0 \leq \alpha_{rev} \leq 7$ deg. This serves as an indicator of low lift, a desirable quality for rotor blade airfoils in in the reverse flow

region since lift acts downward. Note that the lift-to-drag ratio is much higher than the NACA 0012 for $7 \leq \alpha_{\text{rev}} \leq 16\,\text{deg}$. The next section will show that this is a result of delayed flow separation from the elliptical airfoils.

3.1.2 Flowfields

This section presents flowfield measurements to investigate some features of the air-load curves discussed in the previous section. For all results presented in this section, the freestream flow is from left to right. The airfoils are shown at *negative* angles of attack to represent the pitch settings of a retreating rotor blade operating in reverse flow. Recall that in this orientation, the lower surface of the airfoil acts as the suction side while the upper surface serves as the pressure side leading to downward-acting lift (Figure 1.2(b)).

Figure 3.6 shows contours of time-averaged total velocity, normalized by the freestream. Blue areas indicate low velocity regions while red areas indicate high velocity regions. Spatial coordinates have been normalized by the airfoil chord length and the origin is placed at the aerodynamic leading edge (for $\alpha = 0\,\text{deg}$). For clarity, only 1/16 of the calculated vectors are shown in the x-direction and 1/3 of the calculated vectors are shown in the z-direction. The figure compares the NACA 0012 in forward flow (left column), reverse flow (center column), and the elliptical airfoil in reverse flow (right column) at five negative angles of attack. Flowfield results for the DBLN-526 airfoil (not shown) are qualitatively similar to the results for the elliptical airfoil. Beginning with a comparison of forward and reverse flow (left and center columns), it can be seen that the wake of the NACA 0012 in reverse flow is generally larger than in forward flow. Separation occurs near the blunt aerodynamic trailing edge for $\alpha_{\text{rev}} = 0$ and $-3\,\text{deg}$ and at the leading edge for $\alpha_{\text{rev}} \leq -6\,\text{deg}$ resulting in a larger wake for $0 \geq \alpha \geq -9\,\text{deg}$. Figure 3.7 examines the size of the wakes more closely by comparing vertical cuts of the velocity field downstream of the NACA 0012 in forward and reverse flow for $\alpha = 0\,\text{deg}$ and $-6\,\text{deg}$. The key conclusion from Figure 3.7 is that for both

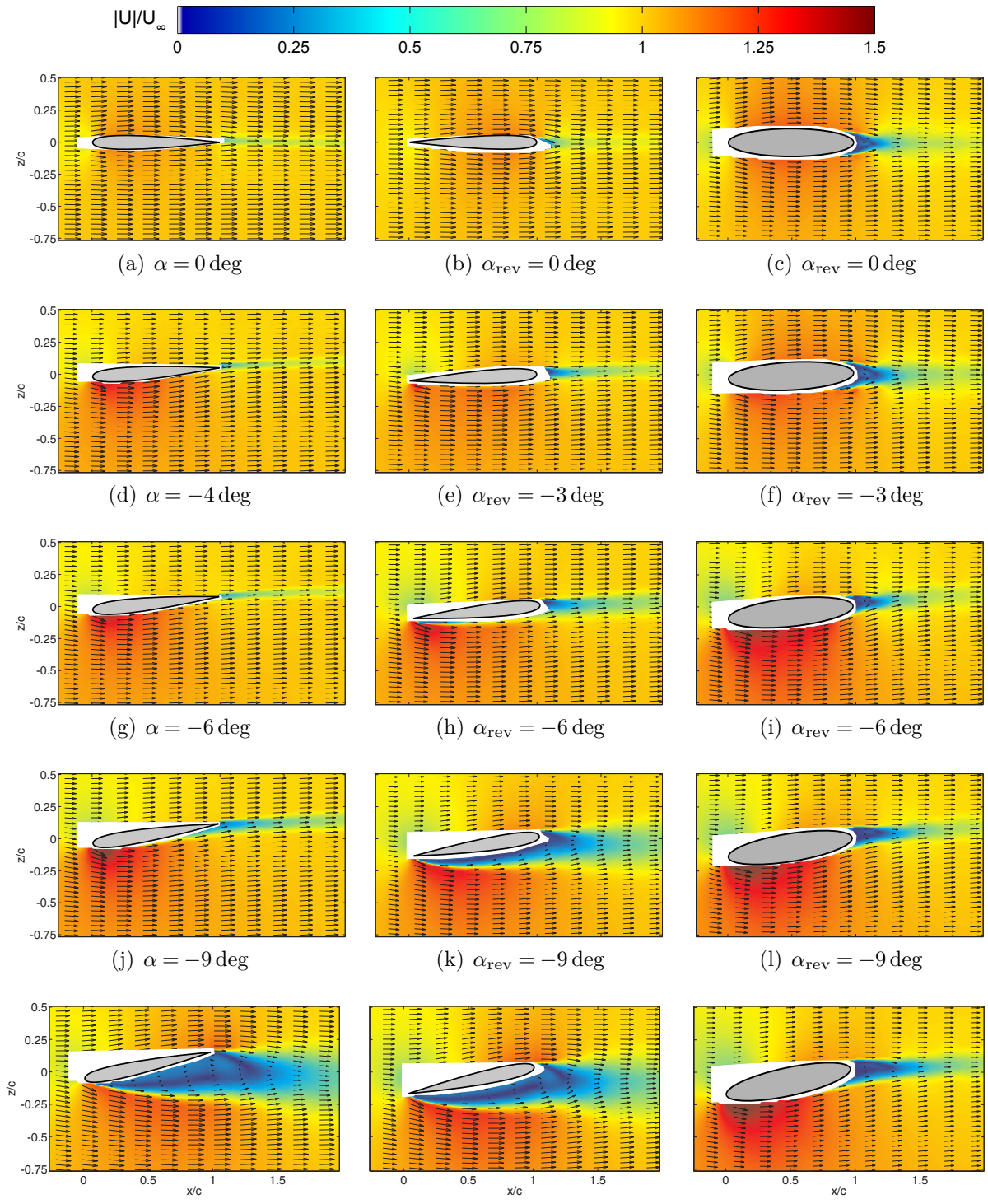

(a) $\alpha = 0\,\text{deg}$ (b) $\alpha_{\text{rev}} = 0\,\text{deg}$ (c) $\alpha_{\text{rev}} = 0\,\text{deg}$

(d) $\alpha = -4\,\text{deg}$ (e) $\alpha_{\text{rev}} = -3\,\text{deg}$ (f) $\alpha_{\text{rev}} = -3\,\text{deg}$

(g) $\alpha = -6\,\text{deg}$ (h) $\alpha_{\text{rev}} = -6\,\text{deg}$ (i) $\alpha_{\text{rev}} = -6\,\text{deg}$

(j) $\alpha = -9\,\text{deg}$ (k) $\alpha_{\text{rev}} = -9\,\text{deg}$ (l) $\alpha_{\text{rev}} = -9\,\text{deg}$

(m) $\alpha = -12\,\text{deg}$ (n) $\alpha_{\text{rev}} = -12\,\text{deg}$ (o) $\alpha_{\text{rev}} = -12\,\text{deg}$

Figure 3.6: Time-averaged PIV velocity field measurements for the NACA 0012 in forward flow (left), reverse flow (center), and the elliptical airfoil in reverse flow (right).

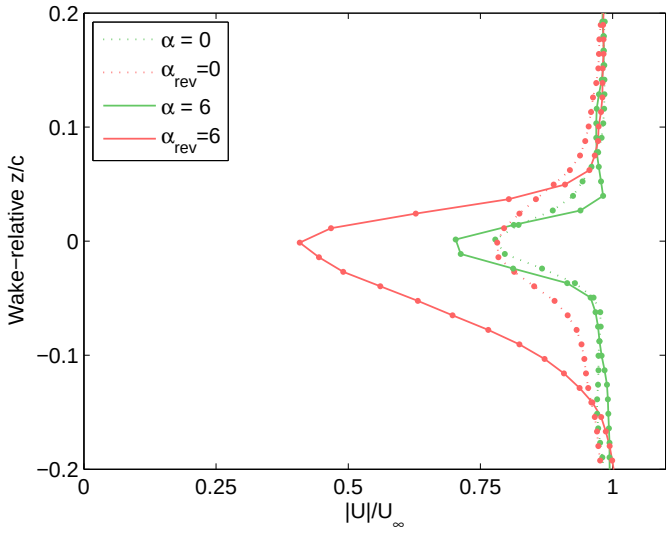

Figure 3.7: Profiles of total velocity taken at $x/c = 1.4$, downstream of a NACA 0012 in forward and reverse flow at $\alpha = 0$ and -6 deg.

angles of attack, the velocity (i.e. momentum) deficit due to the drag of the airfoil is larger in reverse flow. Integrating the momentum deficit for $\alpha = -6$ deg in forward and reverse flow gives $c_d = 0.032$ and 0.061, respectively; these values are comparable with the corresponding force balance measurements (0.027 and 0.058).

Turning attention back to the NACA 0012 in forward flow (Figure 3.6), the intensity of the high velocity region near the aerodynamic leading edge grows with angles of attack that are larger in magnitude (more negative), corresponding to decreasing pressure on the suction side (bottom) of the airfoil and increasing downward-acting lift. In reverse flow, recall that the center of pressure acts near the geometric three-quarter-chord as it serves as the aerodynamic quarter-chord. This correlates with the increase in pitching moment about the aerodynamic three-quarter-chord shown in Figure 3.3(b). Figure 3.6(h) shows separated flow over the NACA 0012 in reverse flow at $\alpha_{\text{rev}} = -6$ deg. The airfoil is fully stalled at -12 deg in both forward and reverse flow.

The flowfield of the NACA 0012 in reverse flow (center column) is also compared

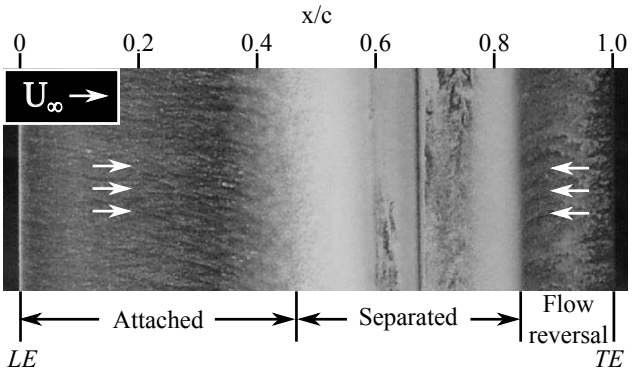

(a) $\alpha_{\mathrm{rev}} = -3\,\mathrm{deg}.$

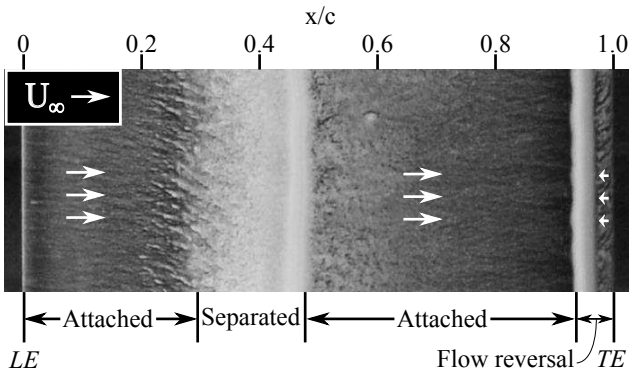

(b) $\alpha_{\mathrm{rev}} = -6\,\mathrm{deg}.$

Figure 3.8: Surface oil flow visualization of the suction side of an elliptical airfoil.

with the elliptical airfoil in reverse flow (right column). For $\alpha_{\text{rev}} = 0\,\text{deg}$ (Figures 3.6(b) and 3.6(c)), the flow separates near the blunt aerodynamic trailing edge of both airfoils providing further support for the higher drag measurements observed at low angles of attack (Figure 3.3(b)). As the angle of attack of the elliptical airfoil is decreased to $\alpha_{\text{rev}} = -6\,\text{deg}$, the wake contracts slightly (Figure 3.6(i)). Figure 3.8 shows surface oil flow visualization of the suction side of the elliptical airfoil at two angles of attack to illustrate flow attachment and separation in the angle of attack range over which wake contraction occurs. Figure 3.8(a) shows the airfoil at $\alpha_{\text{rev}} = -3\,\text{deg}$ where the flow separates near $x/c \approx 0.45$. Flow reversal is observed near $0.85 \leq x/c \leq 1.0$, indicating the presence of recirculation in this region of the separated wake. Figure 3.8(b) shows the airfoil at $\alpha_{\text{rev}} = -6\,\text{deg}$, where the separation point has moved upstream to $x/c \approx 0.3$. However, the flow reattaches near $x/c \approx 0.5$ and remains attached until $x/c \approx 0.92$. These results correlate with the PIV results to collectively show that the contracted wake justifies the reduced drag measurements seen at $\alpha_{\text{rev}} = -6$ in Figure 3.3(b). Returning to Figure 3.6 At $\alpha_{\text{rev}} = -9\,\text{deg}$, the NACA 0012 is fully stalled while the flow over the elliptical airfoil remains mostly attached (Figures 3.6(k) and 3.6(l)). The wake of the elliptical airfoil is much smaller, and the intensity of the high velocity region is greater. This trend continues, supporting the key finding that a blunt trailing edge airfoil delays deep stall to a higher angle of attack.

3.1.3 Pressure Distributions

Time-averaged pressure distributions of four rotor blade airfoils for $0 \leq \alpha \leq 180\,\text{deg}$ and $Re = 6.6 \times 10^5$ are shown in Figure 3.9 using contour plots. The uppermost contour plots show the pressure distributions for the NACA 0012; the suction side is shown on the left (Figure 3.9(a)) while the pressure side is shown on the right (Figure 3.9(b)). In these contour plots, angle of attack is plotted along the abscissa with a minimum of $\alpha = 0\,\text{deg}$ (pure forward flow) and a maximum of $\alpha = 180\,\text{deg}$ (pure reverse flow). The chord position

is plotted along the ordinate where $x/c = 0$ is the *geometric* leading edge (blunt for the NACA 0012) and $x/c = 1$ is the *geometric* trailing edge (sharp for the NACA 0012). The dotted lines on each plot mark the locations of pressure transducers. The sketches above the NACA 0012 contour plots illustrate the orientation of the airfoil at selected angles of attack, highlight the side of the airfoil shown in the contour plots, and show the definition of leading and trailing edge in the present work (fixed to the geometry of the airfoil). Note that for $90 < \alpha < 180\,\text{deg}$, the geometric trailing edge serves as the aerodynamic leading edge since the airfoil is operating in reverse flow. Refer to the sketch of the airfoil at $\alpha = 150\,\text{deg}$.

Focusing on the suction side of the NACA 0012 airfoil (Figure 3.9(a), uppermost contour plot), for low angles of attack ($0 \leq \alpha \leq 10\,\text{deg}$) the pressure near the leading edge decreases with increasing angle of attack (shown in purple), consistent with a suction peak. In this angle of attack range, the stagnation point shifts along the pressure side of the airfoil away from the leading edge (Figure 3.9(b), upper plot). Discontinuities in the contours can be seen at $\alpha = 12$ and $15\,\text{deg}$ that indicate a two-stage stall. Turning attention back to the contour plot of the suction side of the NACA 0012, the pressure distribution is nearly uniform for $15 \leq \alpha \leq 175\,\text{deg}$ since the flow is fully separated from the suction side of the airfoil here. However, on the pressure side of the airfoil, the pressure distribution is non-uniform and the center of pressure (dark red) shifts from near the leading edge towards the trailing edge with increasing angle of attack. These two trends are consistent with prior work (Figure 1.7) [7]. The suction side maintains a relatively uniform distribution and the center of pressure on the pressure side shifts towards the trailing edge with increasing angle of attack. Figure 1.7 shows that at $\alpha = 170\,\text{deg}$, the pressure decreases on the suction side of the NACA 0015 airfoil in reverse flow; this is also observed in the contour plot for the NACA 0012 in Figure 3.9(a). In reverse flow, the NACA 0012 undergoes a thin-airfoil stall due to flow separation at the sharp aerodynamic leading edge (Section 3.1.1). As a result of this partially separated flow, the suction near the trailing edge in reverse flow ($170 \leq \alpha \leq 180\,\text{deg}$) is less than the suction

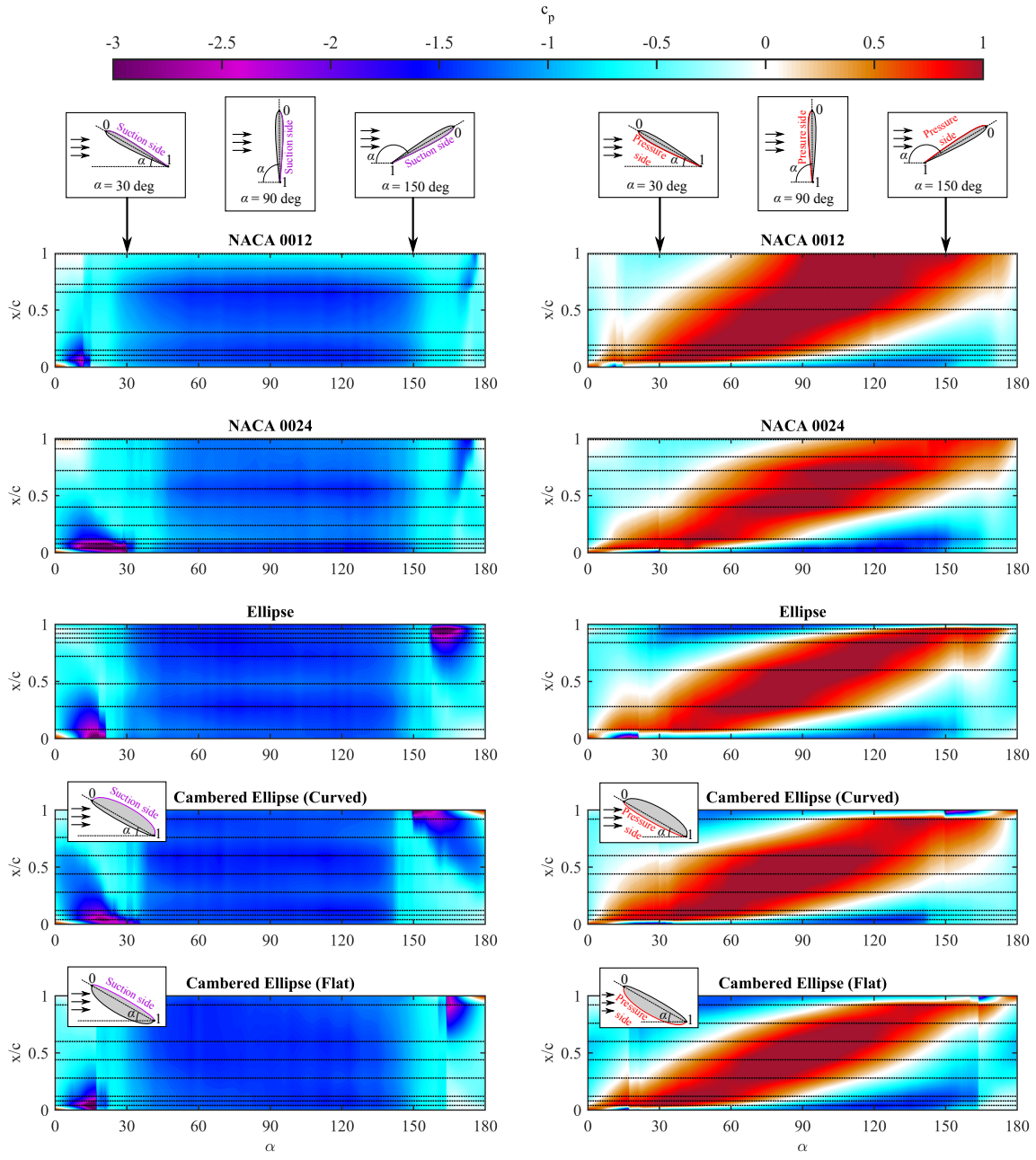

(a) Suction side.

(b) Pressure side.

Figure 3.9: Time-averaged pressure distributions over four airfoils through 180 deg angle of attack at $Re = 6.6 \times 10^5$. Dashed lines indicate chordwise stations of pressure measurements.

near the leading edge in forward flow ($0 \leq \alpha \leq 10\,\text{deg}$).

The contour plots for the other airfoils share some similar features: a suction peak develops with increasing angle of attack in forward flow, the stagnation point moves aft of the leading edge, then stall occurs and the pressure distribution is nearly uniform on the suction side of the airfoil while the center of pressure on the pressure side moves towards the trailing edge. There are also several features of these contours that are unique to each airfoil. For example, the NACA 0024 airfoil has a much greater stall angle ($\alpha = 29.5\,\text{deg}$), and the NACA 0024 exhibits a trailing edge stall in forward flow. Examining the contour of the suction side (beginning at $\alpha = 10\,\text{deg}$), it can be seen that the region of low pressure (blue) that originally extends from $x/c \approx 0.15$ to $x/c \approx 0.45$ affects a decreasing portion of the chord with increasing angle of attack. This indicates movement of the separation point towards the leading edge, consistent with a trailing edge stall [55].

Moving on to the elliptical airfoil, the pressure contours from $0 \leq \alpha \leq 90\,\text{deg}$ are nearly mirror images of the contours from $90 \leq \alpha \leq 180\,\text{deg}$ (mirrored about $x/c = 0.5$). This symmetry stems from the fact that the airfoil is symmetric about both $x/c = 0.5$ and $z/c = 0$. The cambered elliptical airfoil contour plots are given twice: one set in which the curved surface acts as the suction side (i.e., the geometric upper surface as indicated in the sketch above the contour, and also in Figure 2.13(a)), and another set in which the flatter surface acts as the suction side. Since the cambered elliptical airfoil is symmetric about $x/c = 0.5$, each set of contour plots for the cambered elliptical airfoil are symmetric in the same way as the contour plots for the elliptical airfoil. When the curved surface acts as the suction side, the airfoil undergoes a trailing edge stall, similar to the NACA 0024 airfoil. Because the cambered elliptical airfoil is symmetric about the mid-chord, the same trailing edge stall that is observed in forward flow ($5 \leq \alpha \leq 30\,\text{deg}$) is seen also seen in reverse flow ($150 \leq \alpha \leq 175\,\text{deg}$). However, when the flatter surface of the cambered elliptical airfoil serves as the suction side, the airfoil undergoes a leading edge stall at $\alpha = 17\,\text{deg}$ (represented by the discontinuity in

the contour plot). This is likely due to a high adverse pressure gradient due to the curvature near the leading edge.

3.2 Unsteady Wake Regimes

The discussion thus far has focused on the time-averaged aerodynamics of static rotor blade airfoils at high angles of attack and in reverse flow. Much of the remainder of this chapter is focused on the corresponding *unsteady* aerodynamic behavior. A characterization of the unsteady wakes (i.e., flowfields) is presented in this section to provide a basis for interpreting the resulting unsteady airloads (Section 3.3). Collectively, these results are fundamental for predicting the onset of vortex-induced vibrations on rotor blade airfoils.

The wake of an airfoil held at a static angle of attack in reverse flow can be broadly categorized into one of three flow regimes: slender body vortex shedding, turbulent wake, or deep stall vortex shedding. Note that the three unsteady wake regimes regimes are observed for both airfoils with a sharp geometric trailing edge (e.g., NACA 0012) and airfoils with a blunt trailing edge (e.g., elliptical airfoil). Figure 3.10 illustrates examples of the three flow regimes for the NACA 0012. Note that the airfoil is in reverse flow, so the freestream is from left to right. Also note that the airfoil is shown at a negative angle of attack, representative of the pitch settings of a retreating helicopter rotor blade in reverse flow. To allow for a more intuitive interpretation, the absolute value of the angle of attack in reverse flow, $|\alpha_{\text{rev}}|$ will be used. The origin is at the location of the leading edge of the airfoil when $|\alpha_{\text{rev}}| = 0\,\text{deg}$; angle of attack was set about the aerodynamic three-quarter-chord. Total velocity vectors (normalized by U_∞) are overlayed onto contours of vorticity (normalized by U_∞/c). One-half of the calculated velocity vectors are shown in both the x- and z-directions for clarity. Vortex centers are indicated with triangles; upward-facing red triangles indicate positive vorticity (counter-clockwise) and downward-facing blue triangles indicate negative vorticity

(clockwise). Vortex centers were identified using the Γ-method [56]. For the flow regimes illustrated in Figures 3.10(a)–3.10(b), Γ_2 was used due to the convective influence of the freestream. For the deep stall regime shown in Figure 3.10(c), the vortices are much larger in size and have a slower convection speed. Vortex centers here are identified here using Γ_1.

The slender body vortex shedding regime occurs for low angles of attack; the maximum angle of attack for which the slender body vortex shedding regime is present is defined as $|\alpha_{\text{rev}}^{sb}|$. For the NACA 0012, $|\alpha_{\text{rev}}^{sb}| \approx 2\,\text{deg}$ at $Re = 5.50 \times 10^4$. The flow visualization image in Figure 3.10(a) shows that the flow remains attached over a majority of the airfoil before separating near the blunt aerodynamic trailing edge and forming a von Kármán vortex street in the wake. The alternating vorticity of these vortex pairs can be seen in the PIV measurement. In the slender body vortex shedding regime, the wake is relatively thin and the size of the shed vortices is on the order of the airfoil thickness, $0.12\,c$. This behavior is similar to the laminar vortex shedding regime identified by Huang et al. for airfoils in forward flow (Section 1.3.3) [29].

The turbulent wake regime (Figure 3.10(b)) occurs for angles of attack in the range $|\alpha_{\text{rev}}^{sb}| < |\alpha_{\text{rev}}| < |\alpha_{\text{rev}}^{ds}|$. Note that $|\alpha_{\text{rev}}^{ds}|$ is defined as the minimum angle of attack for which the deep stall vortex shedding regime is present. In the turbulent wake regime, flow separation occurs shortly downstream of the sharp aerodynamic leading edge. Small-scale turbulent eddies are present due to shear layer breakdown. These eddies occasionally roll up into a coherent vortex (note the identification of a single vortex in Figure 3.10(b)), but the wake structure is generally aperiodic, turbulent, and lacking coherent vortices. This behavior is similar to the transitional regime identified by Huang et al. for airfoils in forward flow [29]. In this regime, the size of the wake depends on the geometric trailing edge shape. For an airfoil with a sharp trailing edge, the time-averaged wake is *greater* in size for the turbulent wake regime than for the slender body regime; for an airfoil with a blunt trailing edge, the wake is *smaller* in size (Figure 3.6).

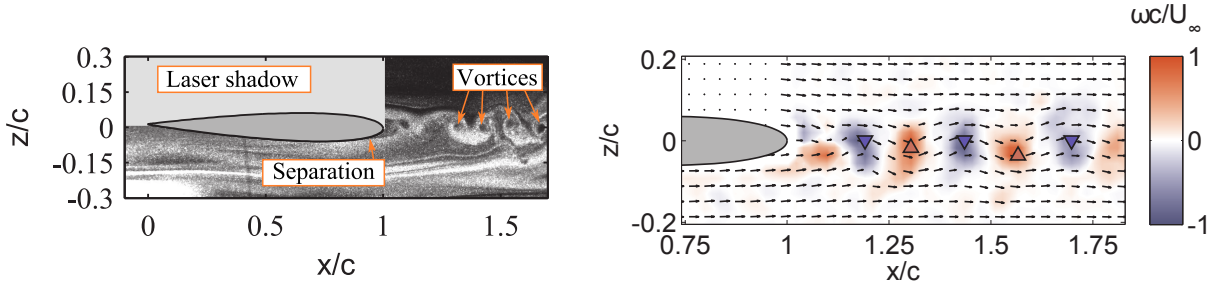

(a) Slender body vortex shedding regime, $|\alpha_{\text{rev}}| = 0\,\text{deg}$.

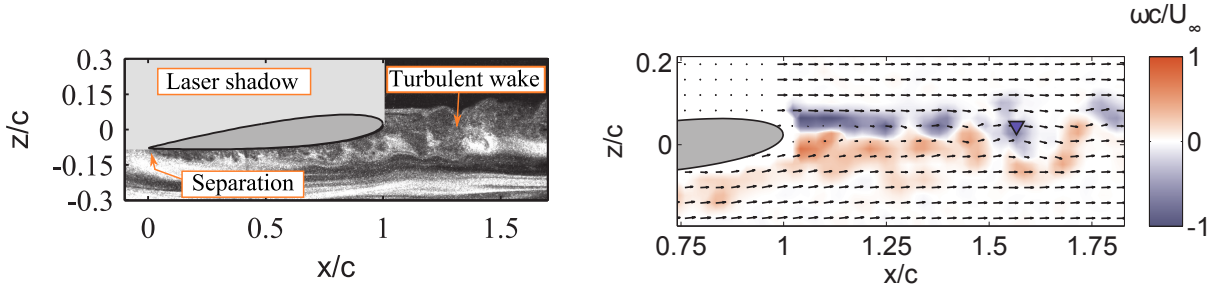

(b) Turbulent wake regime, $|\alpha_{\text{rev}}| = 6\,\text{deg}$.

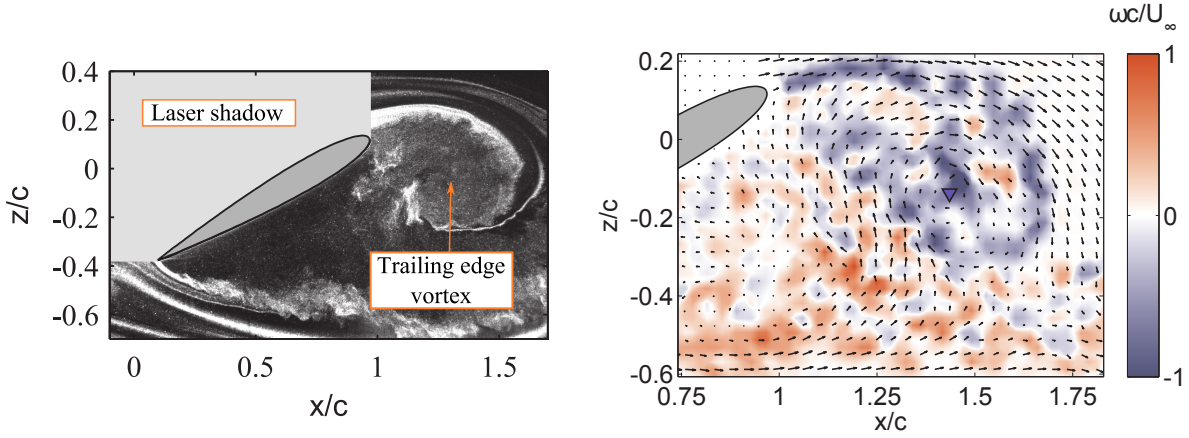

(c) Deep stall vortex shedding regime, $|\alpha_{\text{rev}}| = 30\,\text{deg}$.

Figure 3.10: Three flow regimes observed for a NACA 0012 in reverse flow. Left column shows instantaneous smoke flow visualization images at $Re = 1.10 \times 10^5$. Right column shows instantaneous PIV measurements (taken separately from the flow visualization images) at $Re = 5.50 \times 10^4$.

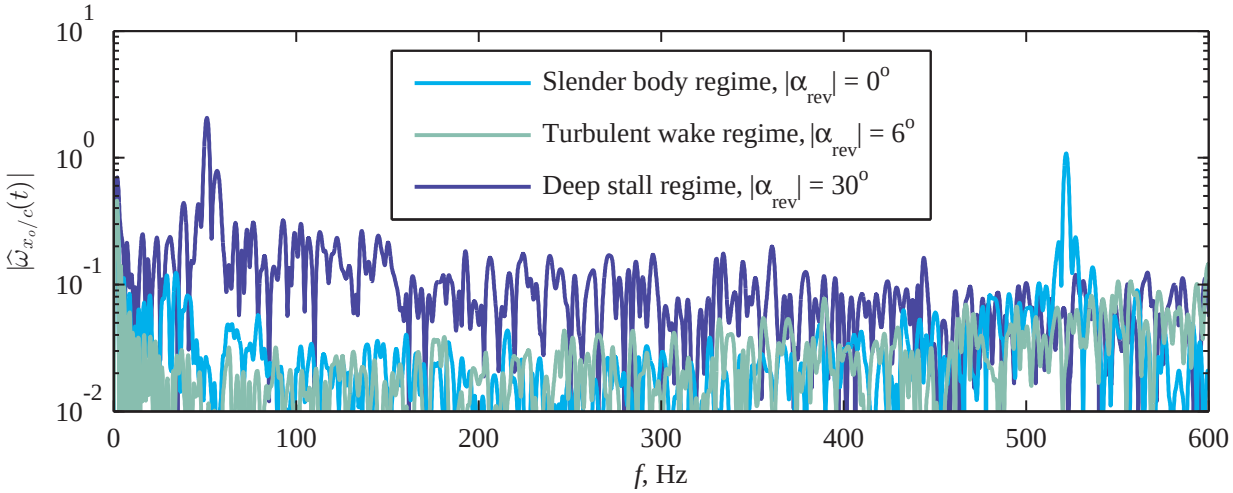

Figure 3.11: FFT of $\widehat{\omega}_{x_o/c}(t)$ at $x_o/c = 1.5$ for a NACA 0012 with $Re = 5.50 \times 10^4$.

The deep stall regime (Figure 3.10(c)) occurs for $|\alpha_{\text{rev}}| \geq |\alpha_{\text{rev}}^{ds}|$ where typically $|\alpha_{\text{rev}}^{ds}| \approx 12\,\text{deg}$ for the NACA 0012 at the Reynolds numbers studied here. The locations of flow separation are similar to the turbulent wake regime. However, this regime is characterized by the periodic roll up of large-scale vortices that are subsequently shed into the wake. This is consistent with the "supercritical" deep stall behavior of a NACA 0012 in forward flow [29,33]. Figure 3.10(c) presents measurements of a trailing edge vortex; the PIV measurement reveals that vorticity from the trailing edge shear layer is responsible for the growth of the vortex. The size of the shed vortices in this regime is on the order of the airfoil chord, c; they are significantly larger than the vortices observed in the slender body flow regime. Leading edge vortices also form in the deep stall regime, but are less periodic than trailing edge vortices. Note that turbulence within the trailing edge vortex is manifested as small-scale variations in vorticity.

Figure 3.11 shows the frequency content of $\widehat{\omega}_{x_o/c}(t)$ for the NACA 0012 at $Re = 5.50 \times 10^4$ with $x_o/c = 1.5$, $z/c \in [-0.75, 0.51]$, $f_s = 1.6\,\text{kHz}$, and $t_{\max} = 0.625\,\text{s}$ (Section 2.4.4). For the wake of the slender body flow regime ($|\alpha_{\text{rev}}| = 0\,\text{deg}$), a peak is observed at 521.9 Hz. Here,

one period of $\widehat{\omega}_{x_o/c}(t)$ corresponds to the passage of a pair of vortices with alternating vorticity. Thus, the peak at 521.9 Hz represents the vortex shedding frequency as it is classically defined for flow over a cylinder [57]. There is no distinct peak for the turbulent wake regime ($|\alpha_{\text{rev}}| = 6\,\text{deg}$), confirming the absence of periodic vortex shedding observed in the instantaneous PIV measurement (Figure 3.10(b)). Huang et al. also noted the absence of a frequency peak in the frequency content of hotwire measurements collected in the wake of a NACA 0012 operating in the "transitional regime" in forward flow [29]. Figure 3.10(b) shows that the magnitude of turbulent fluctuations (energy content that is not associated with distinct frequency peaks) does appear to increase with frequency in this range, suggesting a broadband contribution of high-frequency turbulent eddies in the wake. The deep stall flow regime ($|\alpha_{\text{rev}}| = 30\,\text{deg}$) features a peak at 51.2 Hz, an order of magnitude lower than the vortex shedding frequency identified for the slender body flow regime. This strong dependence of vortex shedding frequency on angle of attack is consistent with observations from prior work [29, 34]. It was also seen in Figure 3.10(c) that the wake is much larger for the deep stall flow regime. This is manifested in Figure 3.11 as a higher magnitude of turbulent fluctuations observed for $0 \leq f \leq 450\,\text{Hz}$.

3.3 Unsteady Airloads

The effects of the unsteady wake regimes on unsteady airloads and pressure distributions for four rotor blade airfoils are now considered. Recall that the filled region surrounding the time-averaged airload curves in Figures 2.16(b) and 2.20 represent the 2σ-variation of airloads acting on static airfoils and that the magnitude of the 2σ-variations is here referred to as the *unsteady airloads*. Figure 3.12 shows the unsteady lift (left column), drag (center column), and pitching moment (right column) for the four airfoils considered here (including the two orientations of the cambered elliptical airfoil). For the NACA 0012 and NACA 0024

airfoils, results are shown for both forward and reverse flow. Only forward flow results are shown for the elliptical and cambered elliptical airfoil since these two airfoils are symmetric about $x/c = 0.5$, giving similar behavior in forward and reverse flow.

Throughout the following discussion on unsteady airloads, reference will also be made to Figure 3.13. The layout of these contours is identical to Figure 3.9, but Figure 3.13 shows unsteady pressure distributions ($2\sigma(c_p)$) rather than time-averaged. Reference will also be made to Figure 3.14 which shows unsteady total velocity fields along the suction side of the NACA 0012 airfoil at selected angles of attack in forward and reverse flow. Note that the velocity fields have been rotated to be fixed to the airfoil reference frame.

3.3.1 Forward and Reverse Flow

Begin by examining the unsteady airloads acting on the NACA 0012 in forward flow (top row in Figure 3.12). The unsteady airloads are low in forward flow until the airfoil stalls at $\alpha = 12\,\text{deg}$, leading to a rapid increase. The unsteady airloads generally remain at this elevated level for $12 \leq \alpha \leq 15\,\text{deg}$ due to unsteady pressure fluctuations along the suction side of the airfoil. This is apparent in Figure 3.13(a) as a "band" of unsteady pressure (in blue, $12 \leq \alpha \leq 15\,\text{deg}$). To understand this increase in unsteadiness more fully, the unsteady velocity fields are given in Figure 3.14(a). They show very low unsteadiness at $\alpha = 2$ and $6\,\text{deg}$ because the flow is attached. However, once the airfoil is stalled ($\alpha = 10\,\text{deg}$ in Figure 3.14(a)), an unstable shear layer undulates near the suction side of the airfoil, leading to high unsteadiness along the entire chord. This is consistent with the band of unsteady pressure observed immediately after stall (Figure 3.13(a)).

Returning to the top row of Figure 3.12, the unsteady airloads in forward flow decrease in magnitude as the angle of attack is increased from $\alpha = 15$ to $21\,\text{deg}$. Recall that this behavior was also observed for a different conventional airfoil in forward flow (Figure 1.15) [36]. The unsteady pressure distribution (Figure 3.13(a)) also decreases in this angle of

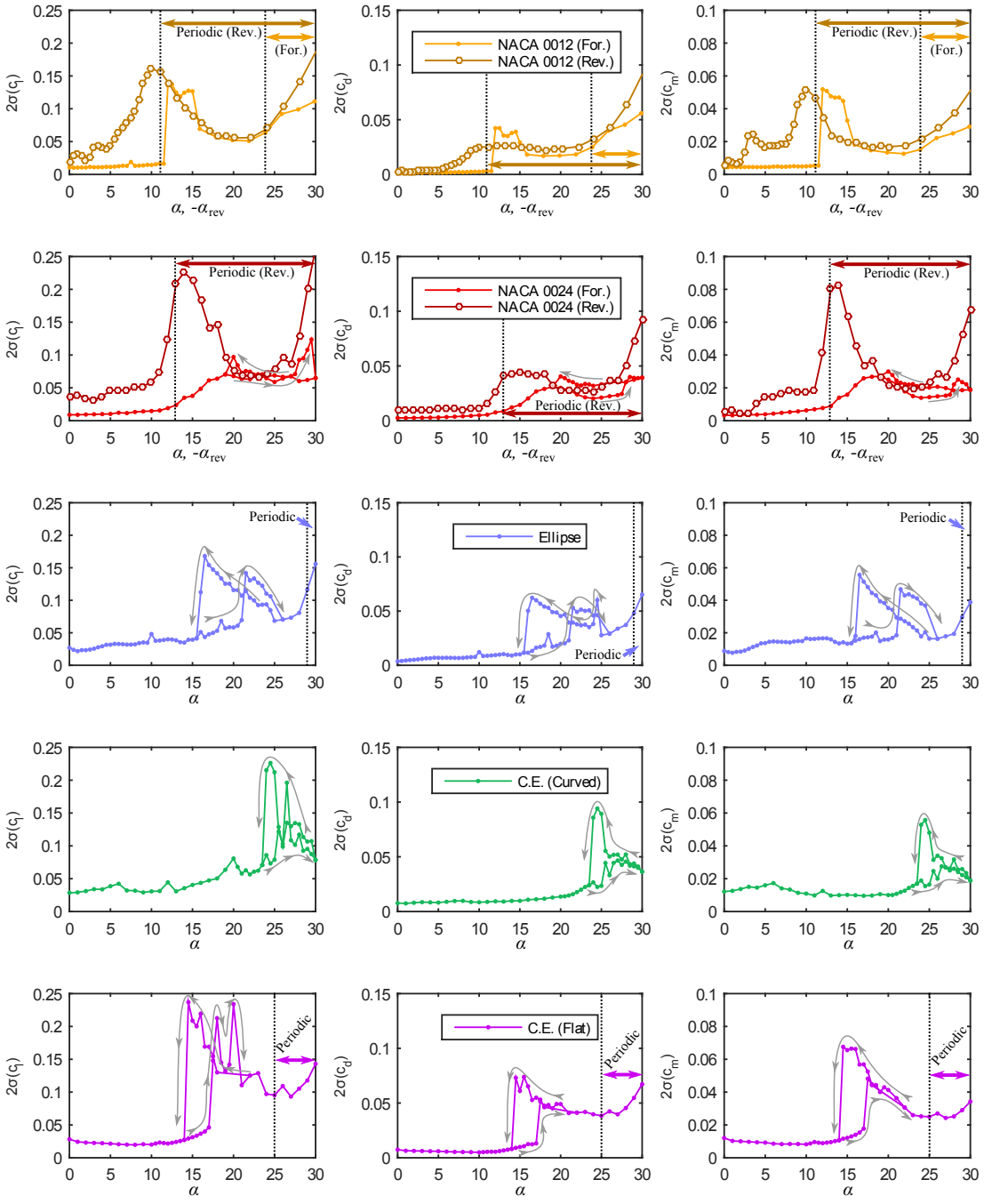

Figure 3.12: Unsteady airloads acting on four airfoils in forward and reverse flow at $Re = 6.6 \times 10^5$.

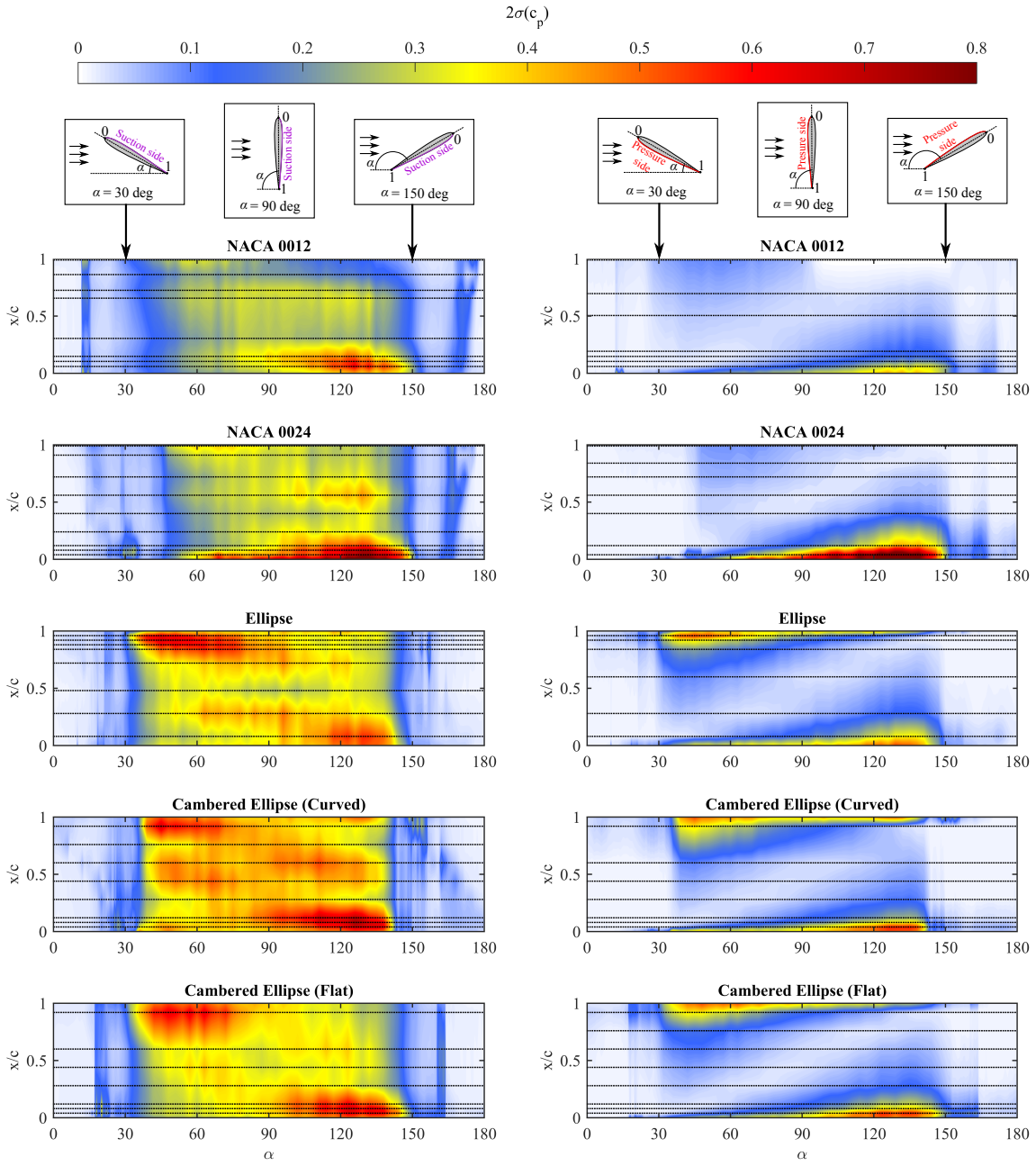

(a) Suction side. (b) Pressure side.

Figure 3.13: Distribution of unsteady pressure fluctuations for four airfoils through 180 deg angle of attack at $Re = 6.6 \times 10^5$. Dashed lines indicate chordwise stations of unsteady pressure measurements.

attack range and is linked to the unsteady velocity field (Figure 3.14(a), $\alpha = 21\,\text{deg}$). Here, the shear layer is stable (that is, confined to a narrow region extending from the leading edge) and serves as a boundary between the external flow and a separated flow region near the airfoil. There is significantly less unsteadiness in the flow at the surface than at $\alpha = 10\,\text{deg}$. The unsteadiness near the surface increases as the angle of attack is increased to $\alpha = 30\,\text{deg}$, consistent with the increase in unsteady airloads observed in Figure 3.12. It should be noted that the airloads become periodic for $\alpha \geq 24\,\text{deg}$; a distinct vortex shedding frequency was detected using the approach described in Section 2.3.7.

Next, consider the unsteady airloads on the NACA 0012 in reverse flow. As the reverse flow angle of attack is increased, the unsteady airloads increase more quickly than in forward flow. Flow separation occurs at the sharp aerodynamic leading edge leads to moderate unsteadiness in the flowfield at angles of attack as low as $-\alpha_{\text{rev}} = 3\,\text{deg}$ (Figure 3.14(b)). As the angle of attack is increased to $-\alpha_{\text{rev}} = 6\,\text{deg}$, flow separation at the sharp geometric trailing edge forms an unstable shear layer with the greatest unsteadiness over $1 \geq x/c \geq 0.4$. At $-\alpha_{\text{rev}} = 9\,\text{deg}$, the high unsteadiness extends over the entire chord. This expansion of the region of unsteadiness in the chordwise direction is also reflected in the unsteady pressure distribution (blue band in the upper plot of Figure 3.13(a), $180 \geq \alpha \geq 170\,\text{deg}$, interpreted from right to left). This angle of attack range corresponds to the turbulent reverse flow wake regime described in the previous section, and to the transitional flow regime identified by Huang et al. [29] Returning to Figure 3.13, note that the reverse flow airloads become periodic at $-\alpha_{\text{rev}} = 11\,\text{deg}$; this marks the beginning of the deep stall vortex shedding regime. Like in forward flow, the unsteady airloads then begin to decrease (up to $-\alpha_{\text{rev}} = 22\,\text{deg}$) as a stable shear layer forms a boundary with the separated flow region (see $-\alpha_{\text{rev}} = 21\,\text{deg}$ in Figure 3.14(b)). For $-\alpha_{\text{rev}} > 22\,\text{deg}$, the unsteady airloads in reverse flow increase, exceeding the corresponding unsteady airloads in forward flow. Indeed, the flow unsteadiness at the surface of the airfoil at $|\alpha| = 30\,\text{deg}$ is higher in reverse flow than in forward flow (Figure 3.14).

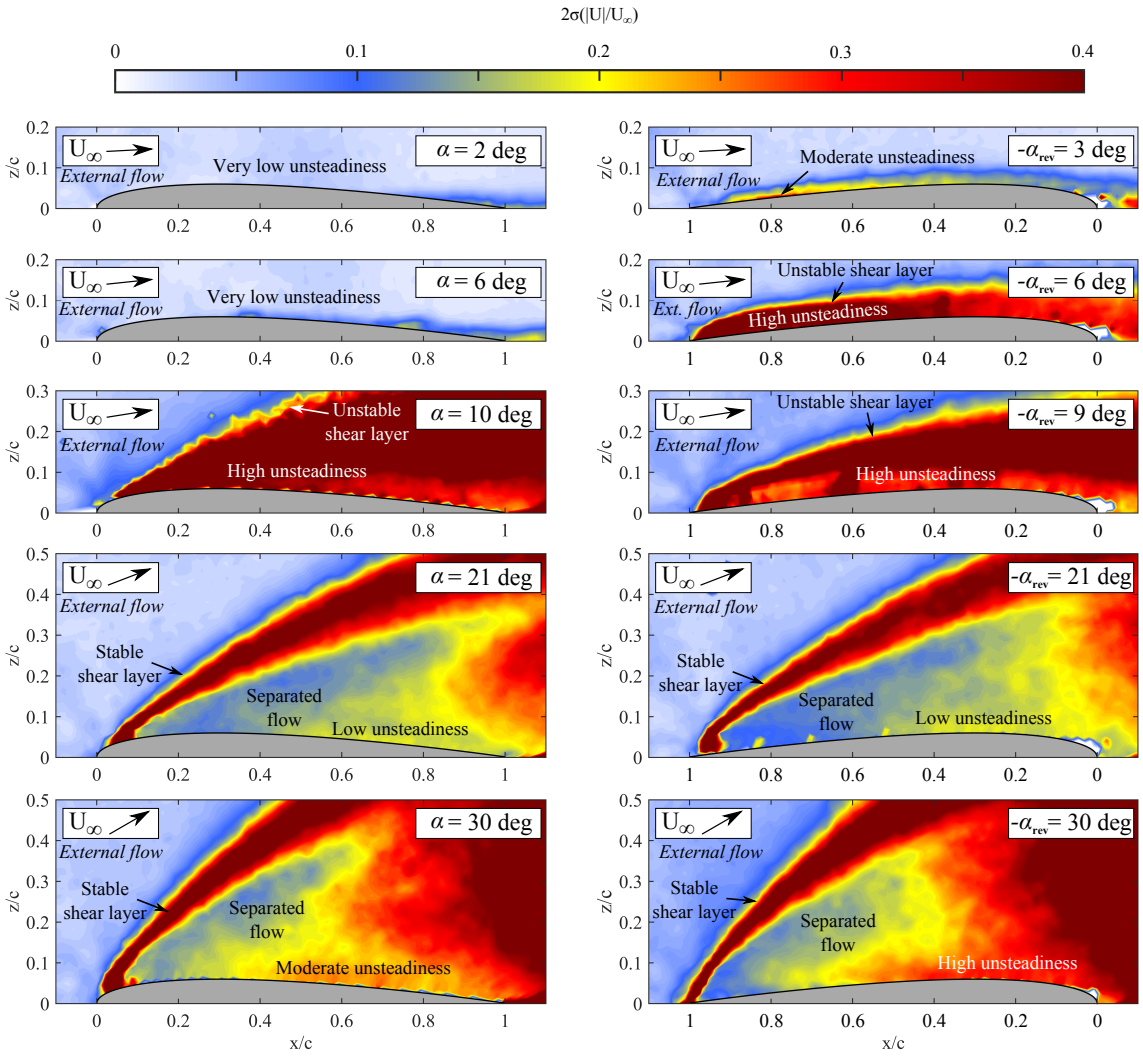

(a) Forward Flow. (b) Reverse Flow.

Figure 3.14: Unsteady velocity fields near the suction side of a NACA 0012 at $Re = 1.1 \times 10^5$.

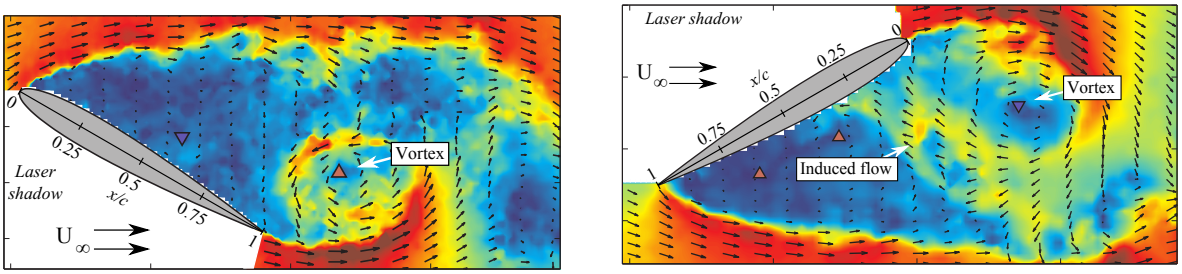

(a) Forward flow, $\alpha = 30\,\text{deg}$.

(b) Reverse flow, $-\alpha_{\text{rev}} = 30\,\text{deg}$.

Figure 3.15: Instantaneous flowfield measurement of the suction side of a NACA 0012 airfoil at $Re = 1.1 \times 10^5$.

This is because the deep stall vortex shedding characteristics differ in forward and reverse flow. Figure 3.15 shows instantaneous velocity field measurements in forward and reverse flow at similar stages of vortex development. In both cases, a vortex periodically forms and sheds from the aerodynamic trailing edge. The vortex generally forms closer to the airfoil in reverse flow (Figure 3.15(b)), inducing flow near the geometric leading edge (aerodynamic trailing edge). Note that the forward flow instantaneous measurement (Figure 3.15(a)) shows that there is no induced flow near the surface of the airfoil. The time-series of the instantaneous measurements (not shown) confirms that little flow is induced by vortex shedding near the surface of the airfoil in forward flow at this angle of attack. This contrasts with reverse flow, where the unsteadiness in the induced flow is responsible for the high unsteady pressure near the blunt geometric leading edge. Vortices also form in the shear layer extending from the sharp geometric trailing edge (aerodynamic leading edge), but they are positioned further downstream of the airfoil and do not affect the flow at the surface as much as the vortices shedding from the blunt leading edge.

The behavior of the NACA 0024 in reverse flow (second row of Figure 3.12) is qualitatively similar to the NACA 0012 in reverse flow. The unsteady airloads on the NACA 0024 increase with reverse flow angle of attack, although the rate of increase is less than the NACA 0012, likely due to the greater airfoil thickness. The unsteady airloads then be-

come periodic and begin to decrease as the shear layer becomes stable and moves away from the suction side. The unsteady airloads increase again as the vortex shedding becomes stronger. The behavior of the NACA 0024 in *forward* flow is dramatically different from the NACA 0012. In Section 3.1.3, the trailing edge stall characteristics of the NACA 0024 were described. This manifests as a more gradual increase in the unsteady airloads with increasing angle of attack (rather than the rapid increase in unsteady airloads observed for the NACA 0012 during its leading edge stall in forward flow). Note that for the NACA 0024 in forward flow, deep stall occurs at $\alpha = 30\,\text{deg}$ and the airloads become periodic (i.e., vortex shedding begins) at $\alpha = 42\,\text{deg}$; these features are not on the scale of Figure 3.12.

Attention is now turned to the airfoils featuring a blunt geometric trailing edge. The unsteady airloads on the elliptical airfoil are shown in the third row of Figure 3.12. As was mentioned previously, the thick airfoils undergo aerodynamic hysteresis. The grey arrows indicate the direction in which angle of attack is changed. For now, consider increasing angle of attack only. Beginning at low angles of attack ($0 \leq \alpha \leq 10\,\text{deg}$), it can be seen that the unsteady airloads of the elliptical airfoil are greater than either of the two NACA-series airfoils in forward flow (due to flow separation at the blunt trailing edge), but are generally less than the unsteady airloads of the NACA-series airfoils in reverse flow. Note, however, that for $0 \leq \alpha \leq 10\,\text{deg}$ the unsteady airloads on the elliptical airfoil and the NACA 0024 in reverse flow are nearly the same since both have a thick blunt aerodynamic trailing edge here. Unlike the NACA 0024, the unsteady airloads on the elliptical airfoil remain low with increasing angle of attack since the flow remains mostly attached until full flow separation (and a corresponding rapid increase in unsteady airloads) occurs at $\alpha = 21\,\text{deg}$. Similar to the NACA-series airfoils, the unsteady airloads decrease as the angle of attack is increased post-stall ($21 \leq \alpha \leq 26\,\text{deg}$) and the leading edge shear layer moves away from the airfoil. As the angle of attack is increased further ($\alpha \geq 26\,\text{deg}$), the unsteady airloads increase (similar to the NACA-series airfoils) and eventually become periodic.

The unsteady airloads on the cambered elliptical airfoil depend on which surface of the airfoil serves as the suction side. Recall that this airfoil is similar to the one used on the X2TD. Figure 1.6 shows the airfoil orientation in reverse flow. Here, the flatter geometric lower surface acts as the suction side. On the advancing side of the rotor, the airfoil operates in forward flow and the curved geometric upper surface acts as the suction side. The fourth row of Figure 3.12 shows the unsteady airloads for in this orientation (curved surface acting as the suction side). Here, unsteady airloads generally gradually increase with angle of attack. Since the airfoil exhibits a trailing edge stall in this orientation, there is not as large of a rapid increase of unsteady airloads as the airfoil increases in angle of attack through stall. The fifth row of Figure 3.12 shows the unsteady airloads for when the flatter surface acts as the suction side. Here, the airfoil undergoes a leading edge stall, so the unsteady airloads increase rapidly (similar to the NACA 0012 and elliptical airfoil). Figure 3.13 shows a corresponding rapid increase in the unsteady pressure along the suction side at $\alpha = 17.5\,\text{deg}$. Like the NACA series airfoils and elliptical airfoil, the unsteady airloads (and unsteady pressure distribution) generally decrease in magnitude post-stall and then begin to increase at the onset of vortex shedding. There is an important difference, however, between the NACA series airfoils and the airfoils with a blunt geometric trailing edge. In reverse flow, the unsteady airloads of the NACA series airfoils become periodic at a relatively low angle of attack ($-\alpha_{\text{rev}} \approx 12\,\text{deg}$), whereas airloads become periodic at much greater angles of attack ($\alpha \geq 25\,\text{deg}$) for airfoils with a blunt trailing edge. This is worth noting because the periodicity of the airloads could induce rotor blade vibrations if the vortex shedding frequency is close a natural structural frequency.

3.3.2 High Angles of Attack

Figure 3.16 expands on Figure 3.12 by showing the unsteady airloads and dimensionless vortex shedding frequency, St_d, for the four airfoils for $0 \leq \alpha \leq 180\,\text{deg}$. This figure segments

the results into four angle of attack ranges: low-α forward flow ($0 \leq \alpha \leq 30$ deg, attached flow and through stall), high-α forward flow ($30 \leq \alpha \leq 90$ deg, deep stall), high-α reverse flow ($90 \leq \alpha \leq 150$ deg, deep stall), and low-α reverse flow ($150 \leq \alpha \leq 180$ deg, deep stall to nearly fully attached flow). For all airfoils, there is a local maximum in the unsteady lift in the high-α forward flow range. The unsteady lift has a local minimum near $\alpha = 90$ deg where the unsteady drag reaches its maximum since the airfoil is perpendicular to the freestream. The unsteady pitching moment generally increases rapidly at the beginning of the high-α forward flow range, then slowly increases through most of the high-α reverse flow range before decreasing rapidly (as the unsteady lift and drag decrease).

There is another important difference in the behavior of the unsteady airloads acting on the two NACA series airfoils as compared to the elliptical airfoils. The unsteady lift and drag of the elliptical and cambered elliptical airfoils are generally symmetric about $\alpha = 90$ deg; recall that symmetry was seen previously for these airfoils in the time-averaged pressure distributions (Figure 3.9). The unsteady lift and drag of the NACA series airfoils is generally greater in the high-α reverse flow range than in the high-α forward flow range. This can be linked to the unsteady pressure distributions in Figure 3.13. For the NACA series airfoils, the unsteady pressures are greatest near the blunt aerodynamic trailing edge ($x/c = 0$) in the high-α reverse flow range (suction side and pressure side). Recall that vortex shedding in reverse flow leads to the unsteady induced flow near the blunt aerodynamic trailing edge. In the high-α forward flow range, it is believed that vortex formation occurs further downstream in the wake, causing the unsteady airloads to be less than those found in the high-α reverse flow range.

To summarize, the dominant source of unsteady airloads in the high-α range (forward and reverse) is induced flow from bluff body vortices that form as the flow turns around a blunt aerodynamic trailing edge. For the elliptical and cambered elliptical airfoils, this occurs in both forward and reverse flow, leading to symmetry of the unsteady pressure contours of

Figure 3.13. For the NACA series airfoils, this phenomenon only occurs in the high-α reverse flow range since this is where the blunt geometric leading edge serves as the aerodynamic trailing edge.

3.3.3 Vortex Shedding Frequency

The vortex shedding frequency from the four airfoils is shown in the lower plot of Figure 3.16. Recall that the dimensionless vortex shedding frequency used in the present work is $St_d = fd/U_\infty$, where d is the projected diameter of the airfoil at a given angle of attack (see inset of Figure 2.18(b)). Also recall that the vortex shedding frequency was identified by examining the frequency content of $c_l(t)$ (Section 2.4.4). At the beginning of the high-α forward flow range, the vortex shedding frequency of nearly all airfoils decreases slightly, but then remain generally constant until the end of the high-α reverse flow range when the shedding frequency increases slightly. This behavior is generally similar to observations from prior work (Figure 1.14) [34]. Vortex shedding for the NACA series airfoils continues into the low-α reverse flow range with the appearance of "hooks" in the plot. At low angles of attack, the leading edge shear layer is in close proximity to the trailing edge shear layer, causing shear layer interactions that affect the vortex shedding frequency here.

The vortex shedding frequency at high angles of attack also depends on the shape of the surface of the airfoil oriented upstream as this affects the angle at which the shear layers depart from the airfoil (i.e., separation angles) [58–60]. More streamlined bodies have lower separation angles, and thus greater vortex shedding frequencies. Focusing on $\alpha = 90\,\text{deg}$, the cambered elliptical airfoil with the flat surface acting as the suction side has the greatest vortex shedding frequency ($St_d = 0.189$). This is because the curved surface faces upstream in this orientation. When oriented perpendicular to the flow, this curved surface is the most streamlined of the airfoils tested, giving the greatest vortex shedding frequency. The next most streamlined surface is the elliptical airfoil, and hence it has a slightly lower vortex

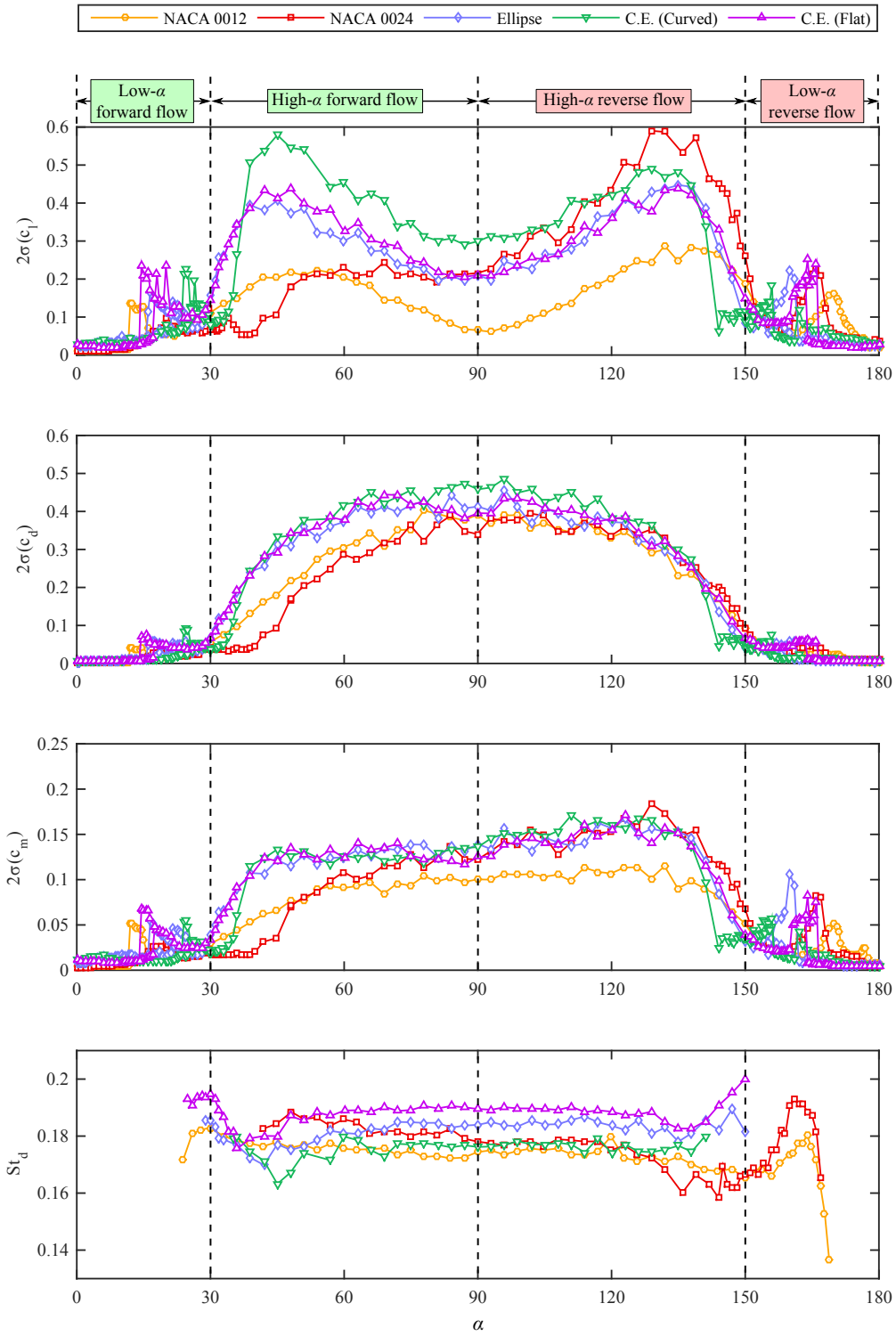

Figure 3.16: Magnitude and frequency of unsteady airloads acting on four airfoils through 180 deg at $Re = 6.6 \times 10^5$.

shedding frequency ($St_d = 0.184$). The NACA series airfoils and the flat surface of the cambered elliptical airfoil are least streamlined in this orientation, causing these airfoils to have the lowest shedding frequencies ($0.174 \leq St_d \leq 0.178$). Finally, note that the vortex shedding frequencies of the NACA series airfoils decrease slightly as the angle of attack passes through the high-α forward and reverse flow ranges ($30 \leq \alpha \leq 150$ deg). This is likely due to changes in the separation angles of the shear layers; in the high-α forward flow range, the blunt edge serves as the aerodynamic leading edge whereas the sharp edge serves as the aerodynamic leading edge in the high-α reverse flow range.

3.4 Aerodynamic Hysteresis

Aerodynamic hysteresis occurs when the magnitude of the static angle of attack of an airfoil is slowly decreased from a fully stalled state, flow reattachment occurs at an angle of attack lower than that of static stall [61]. Figure 3.17 shows the effect of aerodynamic hysteresis on time-averaged airloads and pressure distributions for the cambered elliptical airfoil at $Re = 6.6 \times 10^5$ with the flatter side serving as the suction side (Figure 1.6). Figure 3.17(a) shows the time-averaged lift curve measured using a force balance and calculated using pressure integration. Following the increasing-α branch, there is a two-stage static stall at $\alpha = 17$ and 20 deg. Now following the decreasing-α branch, it can be seen the airfoil becomes unstalled at $\alpha = 14$ deg, 3 deg less than the onset of the first stage of static stall.

Figure 3.17(b) shows the time-averaged pressure distributions on the suction side for increasing and decreasing angles of attack; Figure 3.17(c) shows corresponding unsteady pressure distributions. Focusing first on the increasing angle of attack contours, the time-averaged contour shows a region of low pressure near the leading edge that grows with angle of attack while the unsteady pressure distribution is nearly uniformly zero since the flow is mostly attached. At the onset of the fist stage of stall, the region of time-averaged suc-

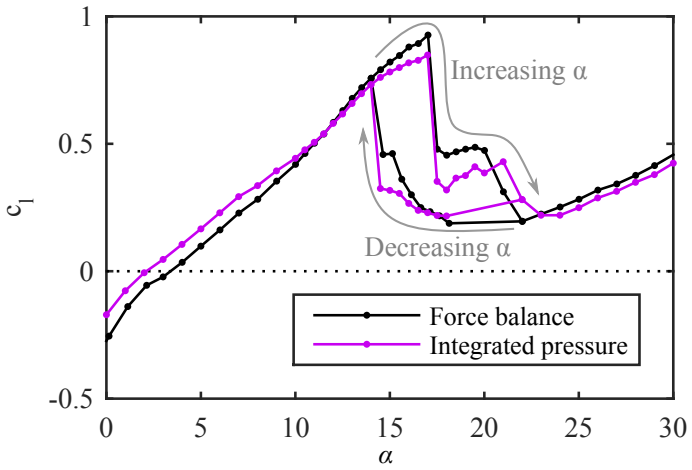

(a) Time-averaged lift curve.

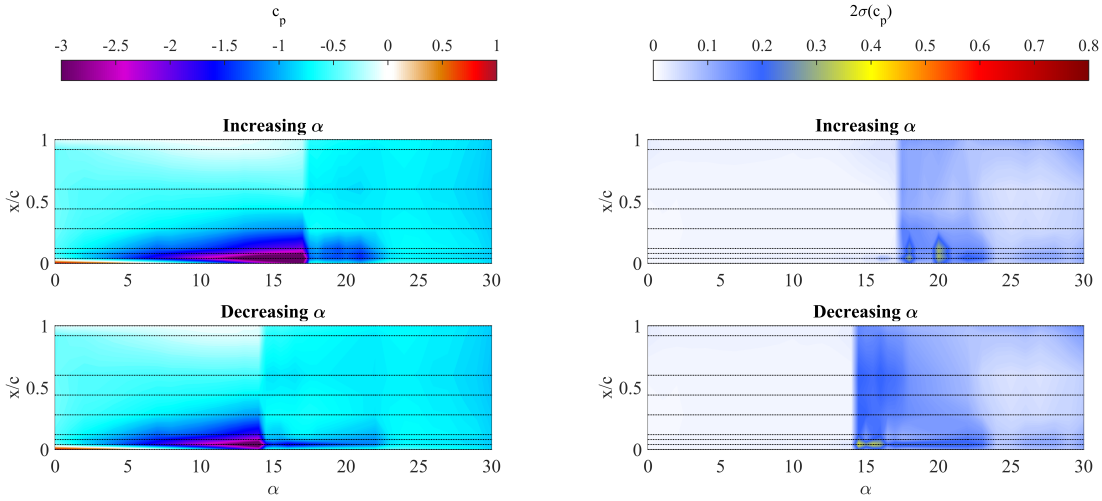

(b) Time-averaged pressure distribution (suction side).

(c) Unsteady pressure distribution (suction side).

Figure 3.17: Effect of aerodynamic hysteresis on the airloads and pressure distributions of with the flatter side of the cambered elliptical airfoil serving as the suction side at $Re = 6.6 \times 10^5$.

tion near the leading edge decreases in magnitude while there is an abrupt increase in the unsteady pressure distribution. At $\alpha = 18$ and 20.5 deg, there are pockets of high unsteady pressure fluctuations near the leading edge. These manifest as peaks in the unsteady airloads corresponding to the cambered elliptical airfoil in Figure 3.12 and are likely due to unsteadiness in the boundary layer separation point. As the angle of attack is increased beyond the second stage of the stall ($\alpha > 23$ deg), the unsteady pressure distribution generally decreases in magnitude as the leading edge boundary layer moves further from the suction side of the airfoil.

Next, consider the pressure distributions when the angle of attack is decreasing. The time-averaged pressure distribution shows that the suction near the leading edge resumes at $\alpha = 14$ deg, consistent with the force measurements given in Figure 3.17(a). It is important to note that the unsteady pressure distribution is greatest in magnitude for $14 < \alpha \leq 17.5$ deg as the angle of attack approaches reattachment. Similar to the increasing angle of attack unsteady pressure distribution, pockets of high unsteadiness are located near the leading edge.

Aerodynamic hysteresis has a detrimental effect on both the time-averaged and unsteady airloads acting on an airfoil. Referring back to the unsteady airloads shown in Figure 3.12, airfoils which exhibit aerodynamic hysteresis have greater unsteady airloads as angle of attack is *decreased* through stall. This is attributed to unsteadiness in the leading edge shear layer coming into close proximity with the suction side of the airfoil before flow reattachment occurs.

3.5 Reynolds Number Effects

The remainder of this chapter considers the effect of Reynolds number on time-averaged forces and flowfields, unsteady wake regimes, and unsteady airloads up to $Re = 1.0 \times 10^6$.

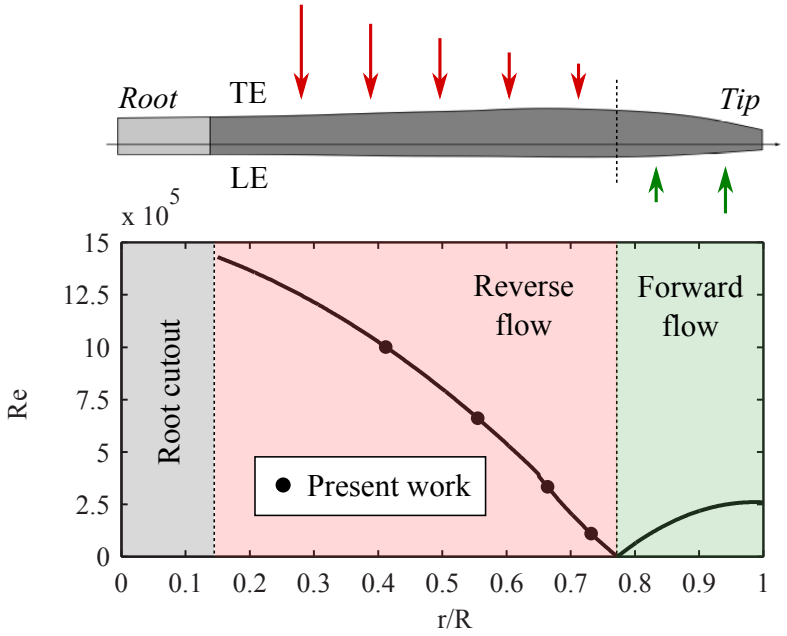

Figure 3.18: Radial Reynolds number distribution for an X2TD^{TM} rotor blade at $\psi = 270$ deg during forward flight at $\mu = 0.77$ (250 kts) [6].

The work presented in this section is motivated by the large range of Reynolds numbers encountered in the reverse flow region (Figure 1.1). Figure 3.5 shows the radial distribution of local chord-based Reynolds number, Re, for the retreating blade of an X2TD operating at $\mu = 0.77$ at a blade azimuth of $\psi = 270$ deg. The Reynolds number is greatest ($Re \approx 1.4 \times 10^6$) near the edge of the root cutout ($r/R = 0.15$), where the rotational speed, Ωr, is lowest. The local Reynolds number and Mach number decrease radially, ultimately reaching zero where $\Omega r = U_\infty$ on the retreating blade. Note that the Reynolds numbers tested in the present work are illustrated in Figure 3.5 and are representative of a majority of the reverse flow region of a full-scale high-speed helicopter ($0.4 \leq r/R \leq 0.77$).

3.5.1 Time-Averaged Aerodynamics

Figures 3.19-3.30 show the variation of time-averaged airloads, lift-to-drag ratios, and surface flow patterns with angle of attack and Reynolds number for the NACA 0012 and

cambered elliptical airfoil. Surface oil flow visualization is provided to highlight the flow features responsible for key aspects of the airloads. Figures 3.19-3.24 results for a NACA 0012 airfoil, and the key airfoil characteristics are summarized in Table 3.2. The airloads at $Re = 1.1 \times 10^5$ (Section 3.1.1) are shown in grey. The lift curve from thin airfoil theory, $c_l = 2\pi\alpha$, is given as a dashed line for reference. First, consider the NACA 0012 in forward flow (Figure 3.19). Both the values of $c_{\mathrm{l,max}}$ and the corresponding stall angle increase with Reynolds number. This behavior is also illustrated in Figure 1.11 [25]. Figure 3.21(a) shows an increase in the lift-to-drag ratio with Reynolds number for a wide range of pre-stall angles of attack.

Figure 3.20 shows the airloads for the NACA 0012 in reverse flow. For moderate angles of attack ($3 \leq -\alpha_{\mathrm{rev}} \leq 10\,\mathrm{deg}$), lift increases linearly. However, $|c_{\mathrm{l,max}}|$ is achieved at a much lower angle of attack in reverse flow than in forward flow. In reverse flow, the overall drag is greater, gradually increasing up to $-\alpha_{\mathrm{rev}} = 5\,\mathrm{deg}$, followed by a nearly linear increase in drag for $5 \leq -\alpha_{\mathrm{rev}} \leq 25\,\mathrm{deg}$. This is consistent with the results in Section 3.1.2 where the role of the sharp aerodynamic leading edge and blunt trailing edge on the size of the wake of a NACA 0012 in reverse flow was examined. The lift curves in Figure 3.20. For $5 \leq -\alpha_{\mathrm{rev}} \leq 30\,\mathrm{deg}$, the lift is nearly identical with all curves sharing the same maximum lift ($|c_{\mathrm{l,max}}| \approx 0.85$). Figure 3.20(c) shows that the pitching moment curves follow the behavior of the lift curves due to the large moment arm imposed by the aftward shift in center of pressure. Note, however, that the magnitude of lift and pitching moment is lower at $Re = 1.1 \times 10^5$, likely due to laminar flow effects (such as laminar separation bubbles). At all Reynolds numbers, the greater drag in reverse flow results in lower lift-to-drag ratio than in forward flow (Figure 3.22(a)).

Recall that Critzos et al. observed a discontinuity in the lift curve of a NACA 0012 in reverse flow near $\alpha = 180\,\mathrm{deg}$ at $Re = 5 \times 10^5$ (Figure 1.10(a)) [8]. Similar behavior is observed in Figure 3.20(a). Figure 3.23 shows oil flow visualization for the NACA 0012

in reverse flow at $-\alpha_{\text{rev}} = 1\,\text{deg}$ to investigate the flowfield hypothesized by Critzos et al. (Section 1.3.2). Flow is attached over the majority of both the pressure and suction sides of the airfoil. Looking closely at the suction side (Figure 3.23(b)), it can be seen that the flow separates at the sharp aerodynamic leading edge ($x/c = 0$), resulting in a pooling of the oil at the leading edge, and reattaches slightly downstream near 1% chord, consistent with the small separation bubble suggested by Critzos et al. The turbulent boundary layer that reattaches downstream of this small separation bubble maintains attachment to 97% chord. On the pressure side of the airfoil, the boundary layer remains laminar and separates earlier, at 85% chord. Figure 3.23(c) provides a sketch of the flow separation and reattachment over the airfoil at $-\alpha_{\text{rev}} = 1\,\text{deg}$.

It was shown in Sections 3.1.1 and 3.1.2 that a NACA 0012 exhibits a thin airfoil stall in reverse flow. Figure 3.24 investigates the effect of Reynolds number on the stall characteristics with oil flow visualization results on the suction side of the airfoil at $-\alpha_{\text{rev}} = 7\,\text{deg}$. The overall structure of the flow is similar over the Reynolds number range tested (as is $|c_l|$, given in Fig. 3.20(a)), and is illustrated schematically in Figure 3.24(d). Specifically, the flow separates at the sharp leading edge and reattaches downstream. As would be expected for a thin airfoil, the separation bubble grows with increasing angle of attack, and at this higher incidence the reattachment point is further downstream. Flow reattachment occurred between 32% and 60% of the wing chord and is separated for the remainder of the chord. The reattachment point is a function of Reynolds number, with reattachment occurring slightly earlier as Reynolds number increases. Within the separated flow region upstream of the reattachment point, there is flow recirculation (shown in pink). The recirculating flow moves upstream along the surface of the airfoil and represents a separation bubble. In this region and in the separated flow region downstream of the reattachment point, the oil streaks are curved due to gravitational effects resulting from the vertical mounting of the models. Despite small differences in the time-averaged size of the separation bubble across

Table 3.2: Summary of lift and drag coefficients for a NACA 0012 in forward and reverse flow.

Re	Forward flow			Reverse flow		
	$\lvert c_{\mathrm{l,max}}\rvert$	α_{stall}	$\lvert c_{\mathrm{d,min}}\rvert$	$\lvert c_{\mathrm{l,max}}\rvert$	$-\alpha_{\mathrm{rev,stall}}$	$\lvert c_{\mathrm{d,min}}\rvert$
1.1×10^5	0.74	9.45	0.017	0.74	8.72	0.032
3.3×10^5	0.99	12.98	0.005	0.86	9.57	0.026
5.0×10^5	1.05	14.01	0.004	0.86	9.57	0.026
6.6×10^5	1.09	15.00	0.006	0.86	8.78	0.028
1.0×10^6	1.17	16.04	0.008	0.85	8.90	0.019

the range of Reynolds numbers tested, the time-averaged airloads are similar at this angle of attack (see Fig. 3.20(a)).

Figures 3.25 and 3.27 show the airloads and performance of the cambered ellipse airfoil with the "curved" upper surface acting as the suction side–the airfoil's normal orientation on the advancing side of a rotor (i.e., forward flow). Figures 3.26 and 3.28 show the airloads and performance of the cambered ellipse airfoil with the "flat" lower surface acting as the suction side (i.e., reverse flow region).

Examining the lift in forward flow (Figure 3.25), it can be seen that there is a drastic change in the character of the lift curve between $Re = 1.1 \times 10^5$ and $Re = 3.3 \times 10^5$. The camber of this airfoil also leads to generally greater lift. Figure 3.29 shows the cambered ellipse at $\alpha = 15\,\mathrm{deg}$. At this incidence, flow is attached over the forward portion of the airfoil, but separates near the trailing edge. As Reynolds number increases from 3.1×10^5 to 1.0×10^6, the laminar boundary layer transitions to turbulent more quickly. At the higher Reynolds numbers, the turbulent boundary layer exists over a larger portion of the blade chord and is therefore thicker when it encounters the adverse pressure gradient downstream of the mid-chord. As a result, flow separates earlier with increasing Reynolds number, moving from $x/c \approx 0.82$ to $x/c \approx 0.68$ as Reynolds number increases from 3.3×10^5 to 1.0×10^6. The larger region of separated flow from the upper surface leads to lower lift production at higher Reynolds numbers, as seen in Figure 3.25. The resulting change in drag, however,

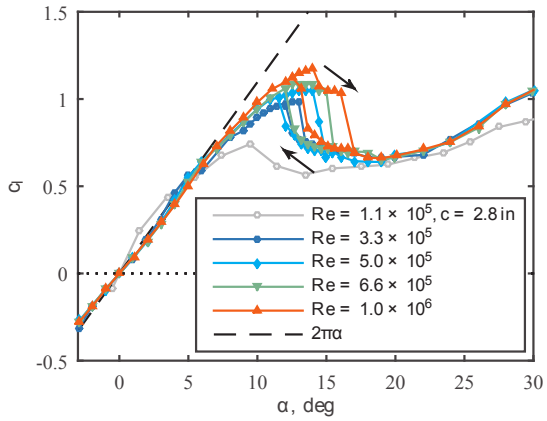

(a) Lift coefficient.

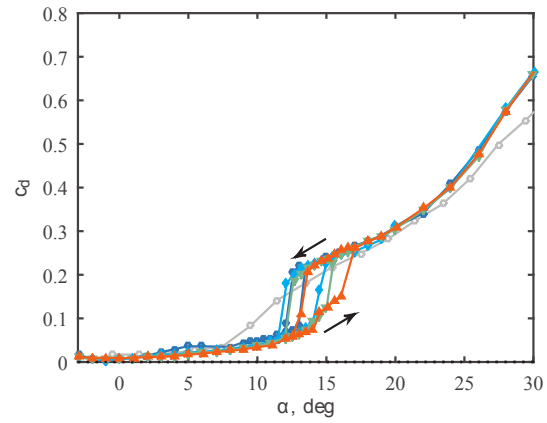

(b) Drag coefficient.

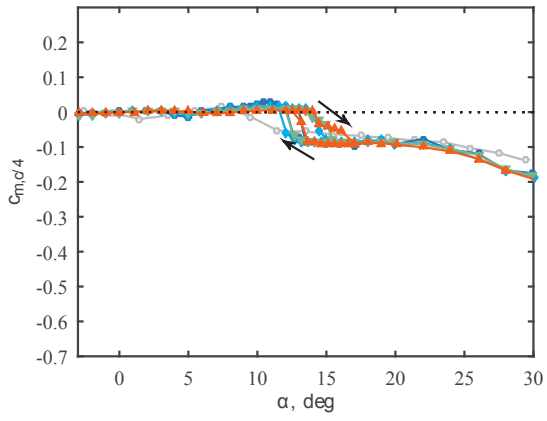

(c) Pitching moment coefficient.

Figure 3.19: Time-averaged airloads of a NACA 0012 airfoil in forward flow.

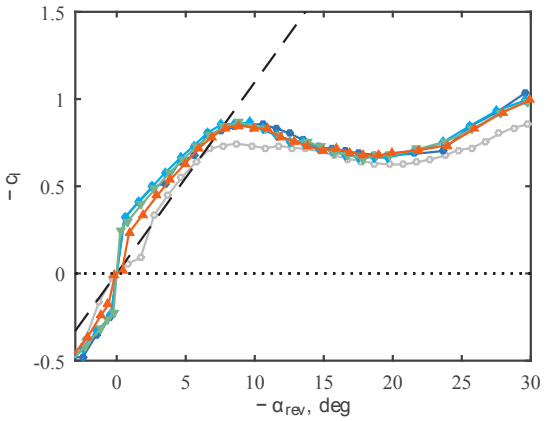

(a) Lift coefficient.

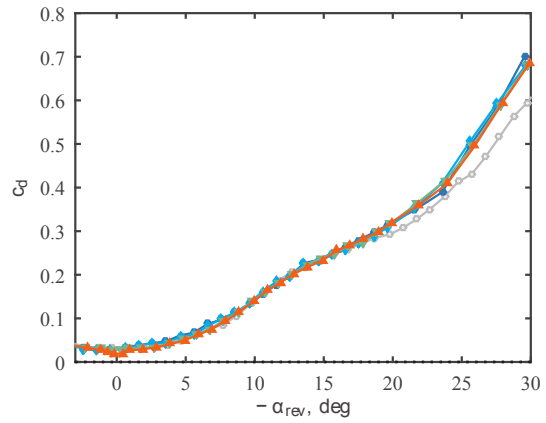

(b) Drag coefficient.

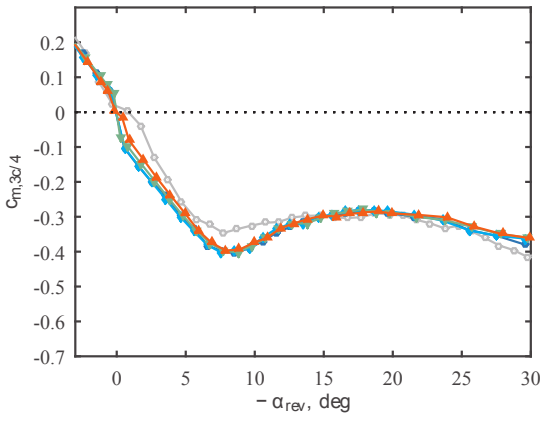

(c) Pitching moment coefficient.

Figure 3.20: Time-averaged airloads of a NACA 0012 airfoil in reverse flow.

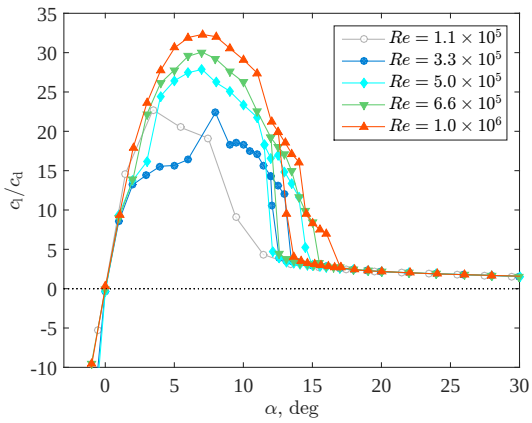

(a) Lift-to-drag ratio.

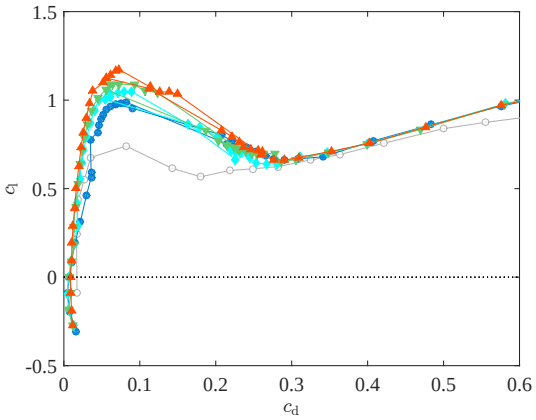

(b) Drag polar.

Figure 3.21: Time-averaged performance of a NACA 0012 airfoil in forward flow.

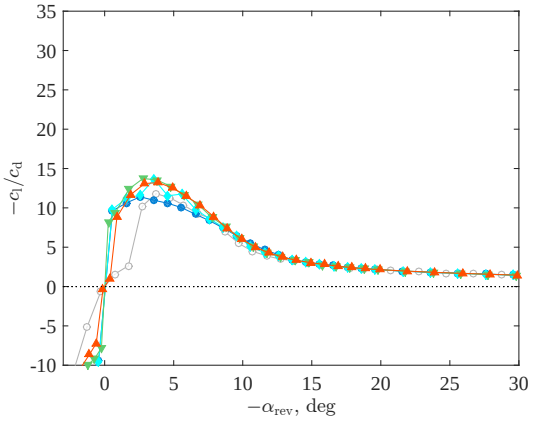

(a) Lift-to-drag ratio.

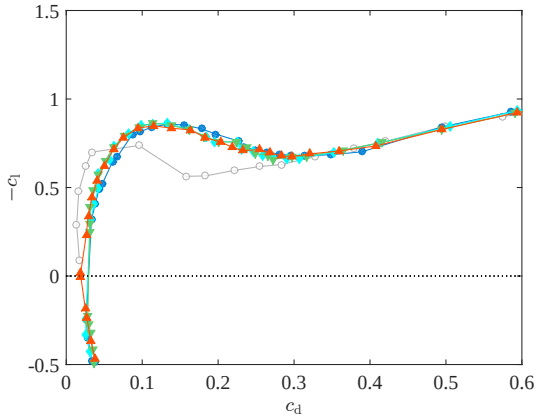

(b) Drag polar.

Figure 3.22: Time-averaged performance of a NACA 0012 airfoil in reverse flow.

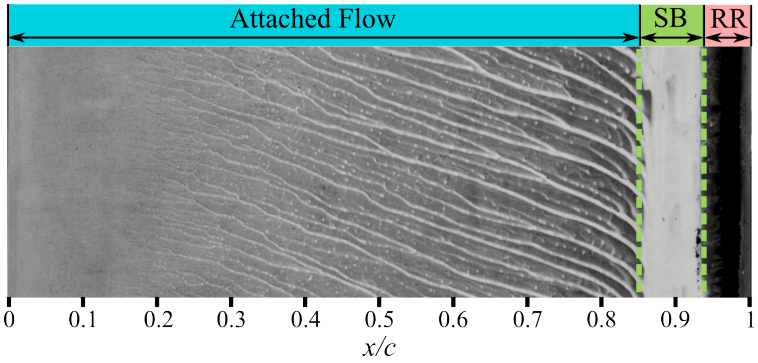

(a) Pressure side. SB: Separation Bubble, RR: Recirculation Region.

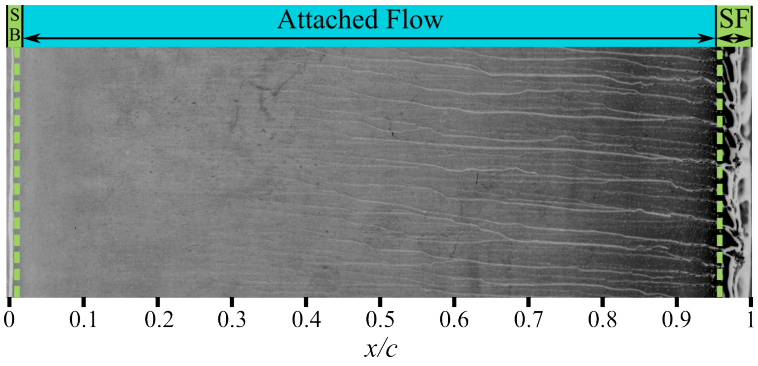

(b) Suction side. SB: Separation Bubble, SF: Separated Flow.

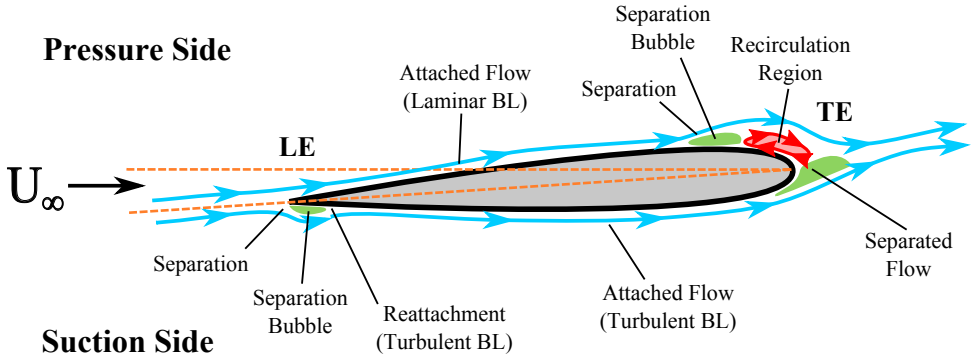

(c) Illustration of surface flow.

Figure 3.23: Surface oil flow visualization of a NACA 0012 in reverse flow at $-\alpha_{\text{rev}} = 1\,\text{deg}$ and $Re = 1.0 \times 10^6$.

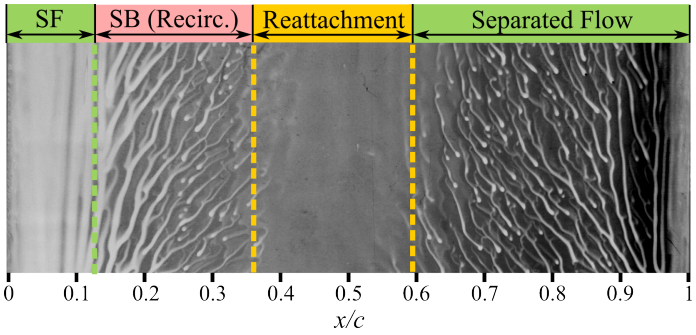

(a) $Re = 5.0 \times 10^5$. SF: Separated Flow.

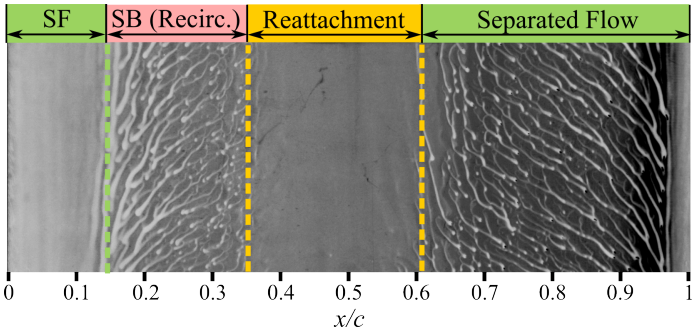

(b) $Re = 6.6 \times 10^5$. SF: Separated Flow.

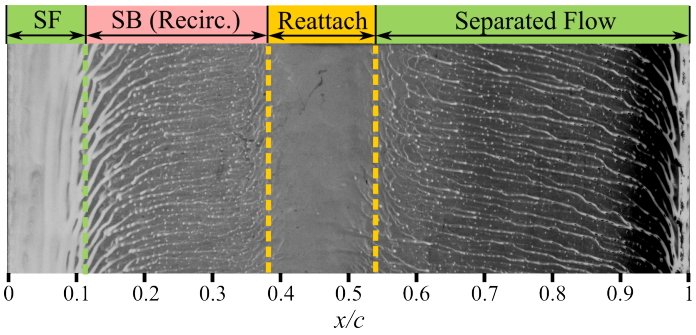

(c) $Re = 1.0 \times 10^6$. SF: Separated Flow.

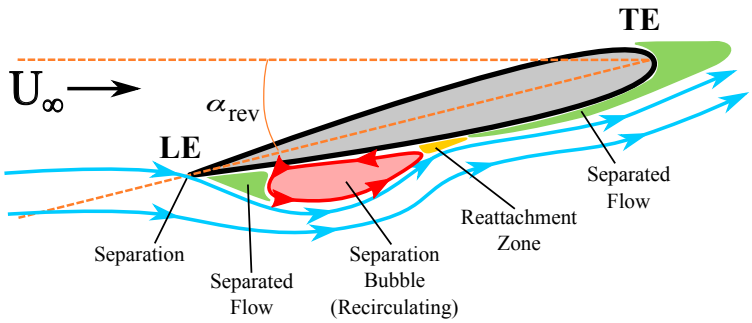

(d) Illustration of surface flow.

Figure 3.24: Surface oil flow visualization of the suction side of a NACA 0012 in reverse flow at $-\alpha_{\text{rev}} = 7\,\text{deg}$.

is relatively mild. In forward flow, the airfoil undergoes a docile decrease in lift, typical for a trailing edge stall on a thick airfoil, with full flow separation occurring at $\alpha \geq 23\,\text{deg}$ (Figure 3.25). Note that while the $Re = 3.3 \times 10^5$ case exhibits higher c_l values at low angles of attack, it stalls at a lower angle of attack than do the higher Reynolds number cases. (See Table 3.3.)

At low incidence in reverse flow, the lift-curve slope is highly sensitive to Reynolds number, and for $Re \geq 3.3 \times 10^5$, the airfoil produces negative lift for $-\alpha_{\text{rev}} \leq 0$ because the airfoil has negative camber in this orientation. The magnitude of the negative lift produced decreases as Reynolds number increases, as was previously observed in forward flow. For $Re \geq 3.3 \times 10^5$, the zero-lift angle of attack is approximately -3 deg. Stall occurs much earlier and more abruptly than in forward flow (see Table 3.3). In reverse flow (Figure 3.26(a)), a rapid decrease in lift associated with a leading edge stall is observed. The maximum value of lift decreases and stall angle increases with increasing Reynolds number.

At $-\alpha_{\text{rev}} = 10\,\text{deg}$, lift is higher for $Re = 1.1 \times 10^5$ and 3.3×10^5 than at higher Reynolds numbers. Figure 3.30 shows surface oil flow visualizations of the suction side (flat side) at Reynolds numbers of 3.3×10^5, 6.6×10^5, and 1.0×10^6. In each of these cases, a small separation bubble forms at the leading edge. Flow reattaches downstream of the separation bubble and remains attached until $x/c \approx 0.9$. The relatively simple flow topology on the suction side and its insensitivity to Reynolds number suggests that magnitude and location of the suction peak and/or the separation characteristics on the curved pressure side may be responsible for the lift characteristics at this angle of attack.

3.5.2 Unsteady Wake Regimes

Recall that Figure 3.10 illustrated the three reverse flow regimes using representative results for the NACA 0012. These flow regimes are also observed for airfoils with a blunt geometric trailing edge. Figure 3.31 shows the dependence of the flow regime on Reynolds

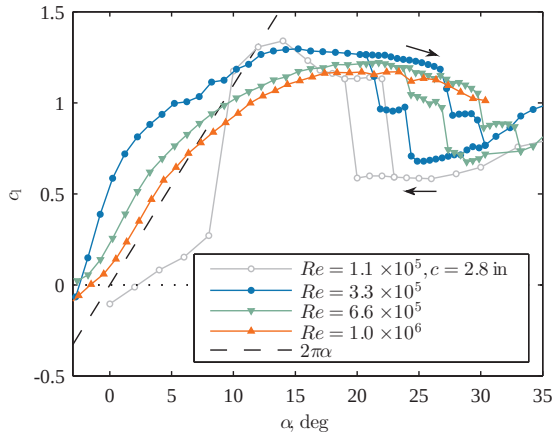

(a) Lift coefficient.

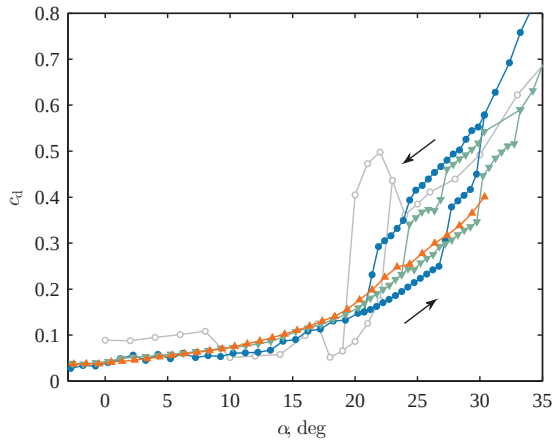

(b) Drag coefficient.

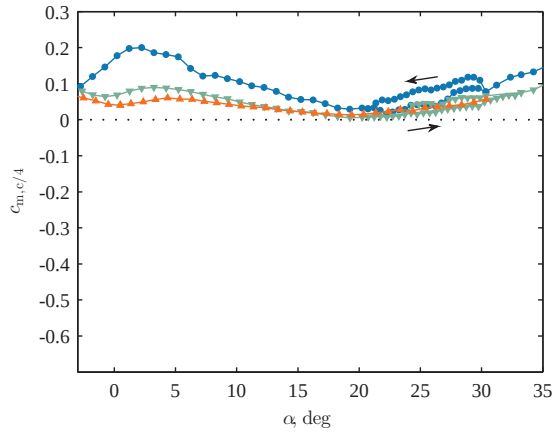

(c) Pitching moment coefficient.

Figure 3.25: Time-averaged airloads of a cambered ellipse airfoil in forward flow.

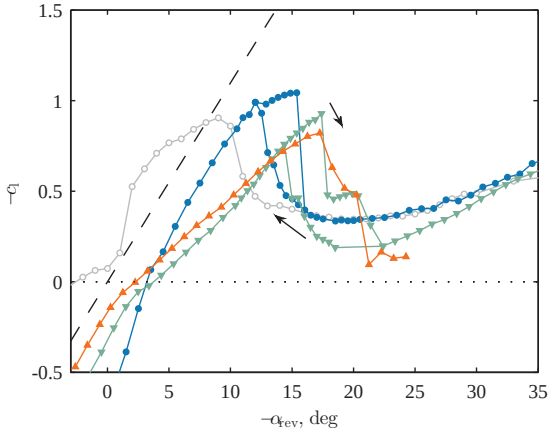

(a) Lift coefficient.

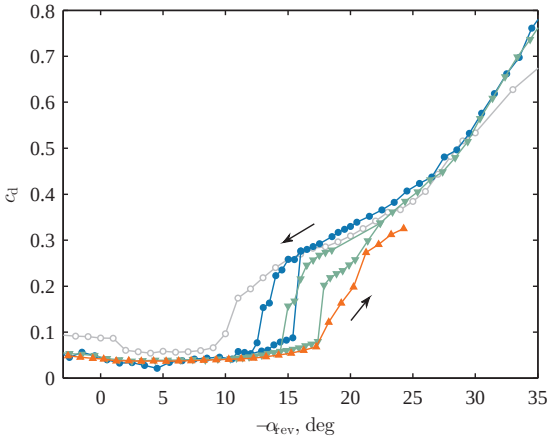

(b) Drag coefficient.

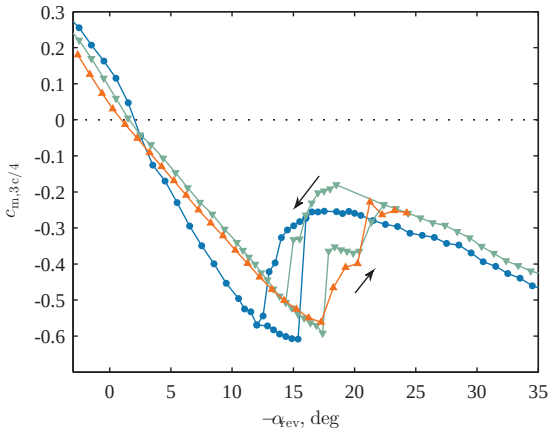

(c) Pitching moment coefficient.

Figure 3.26: Time-averaged airloads of a cambered ellipse airfoil in reverse flow.

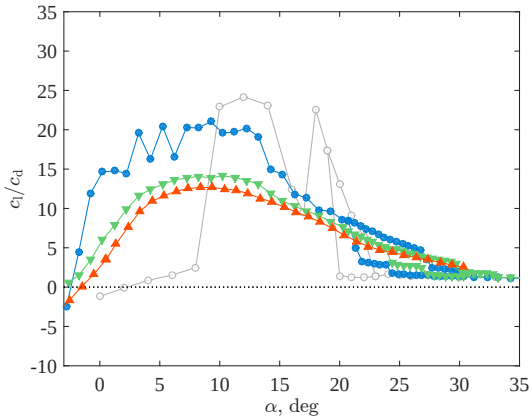

(a) Lift-to-drag ratio.

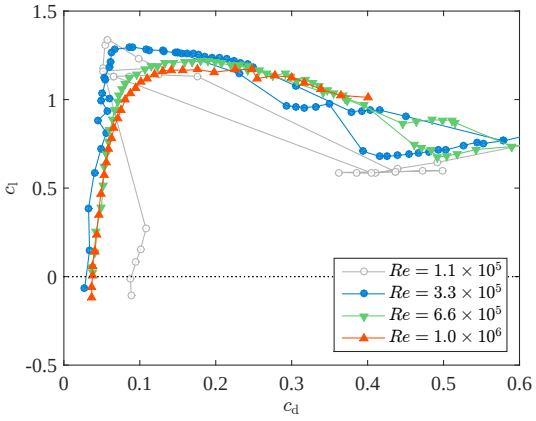

(b) Drag polar.

Figure 3.27: Time-averaged performance of a cambered elliptical airfoil in forward flow.

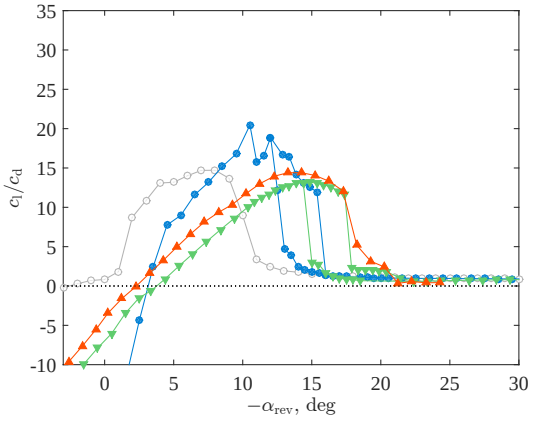

(a) Lift-to-drag ratio.

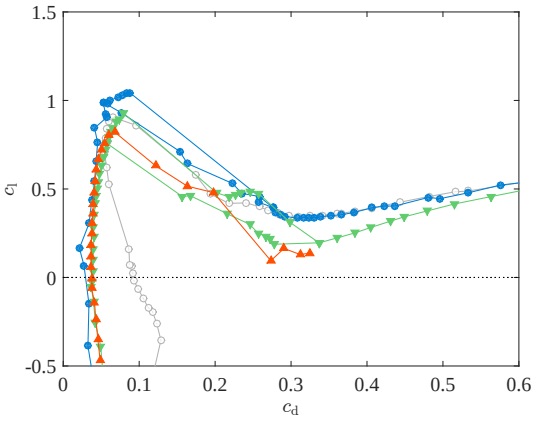

(b) Drag polar.

Figure 3.28: Time-averaged performance of a cambered elliptical airfoil in reverse flow.

Table 3.3: Summary of lift and drag coefficients for a 26% thick cambered ellipse airfoil in forward and reverse flow.

	Forward flow			Reverse flow		
Re	$\lvert c_{l,max}\rvert$	α_{ds}	$\lvert c_{d,min}\rvert$	$\lvert c_{l,max}\rvert$	$-\alpha_{rev,ds}$	$\lvert c_{d,min}\rvert$
1.1×10^5	1.34	22	0.070	0.90	10	0.054
3.3×10^5	1.30	26.73	0.021	1.04	15.38	0.021
6.6×10^5	1.22	29.74	0.037	0.93	17.39	0.037
1.0×10^6	1.17	–	0.037	0.82	17.26	0.037

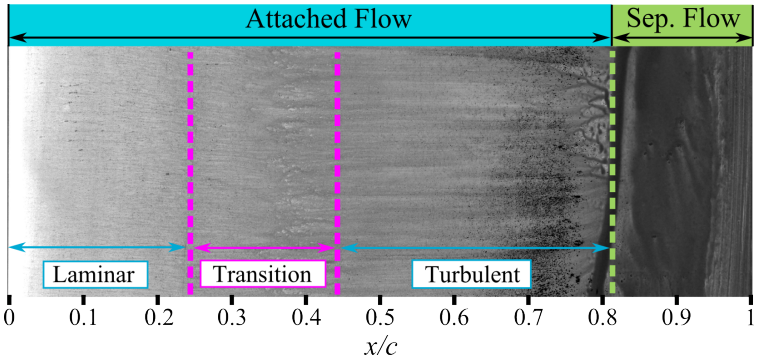

(a) $Re = 3.3 \times 10^5$

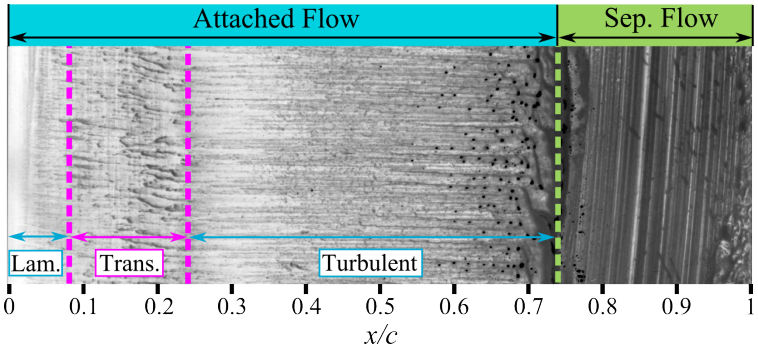

(b) $Re = 6.6 \times 10^5$

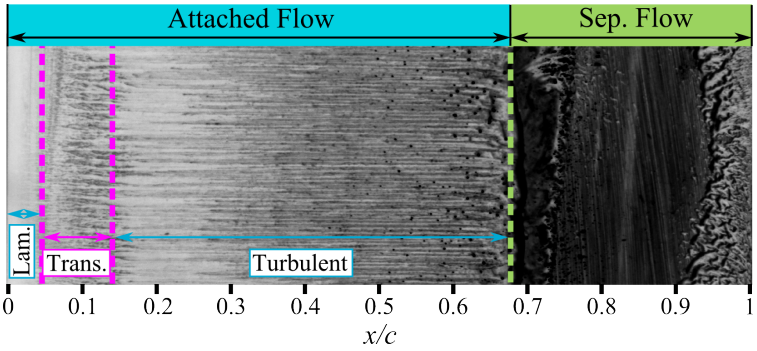

(c) $Re = 1.0 \times 10^6$

Figure 3.29: Surface oil flow visualization of the curved geometric upper surface (suction side) of a cambered ellipse airfoil in forward flow at $\alpha = 15\,\text{deg}$.

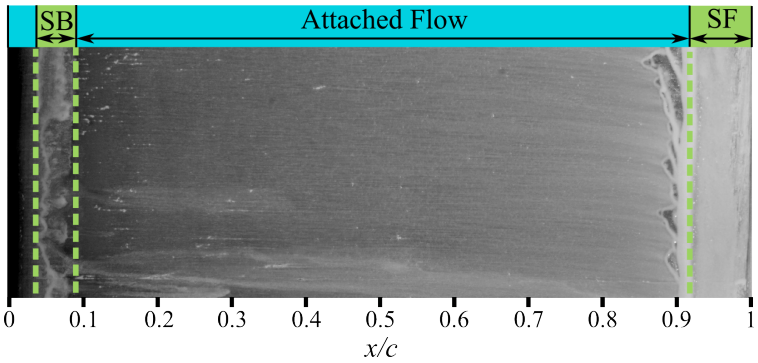

(a) $Re = 3.3 \times 10^5$

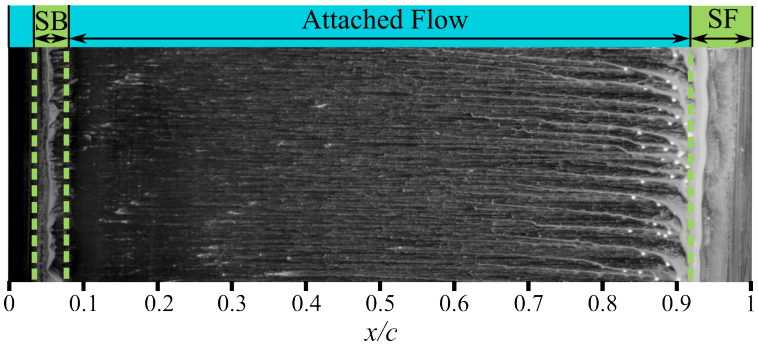

(b) $Re = 6.6 \times 10^5$

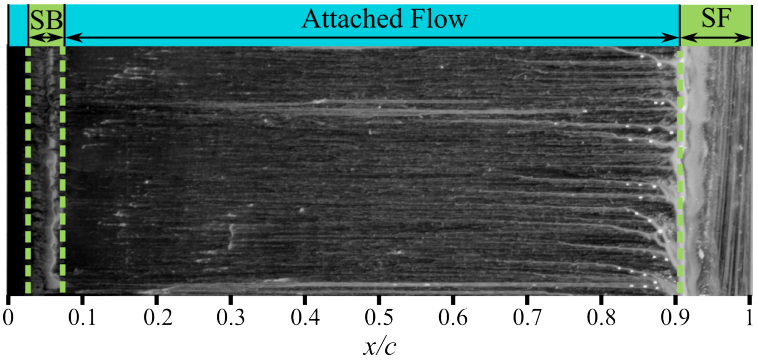

(c) $Re = 1.0 \times 10^6$

Figure 3.30: Surface oil flow visualization of the flat geometric lower surface (suction side) of a cambered ellipse airfoil in reverse flow at $-\alpha_{\text{rev}} = 10\,\text{deg}$. SB: Separation Bubble. SF: Separated Flow.

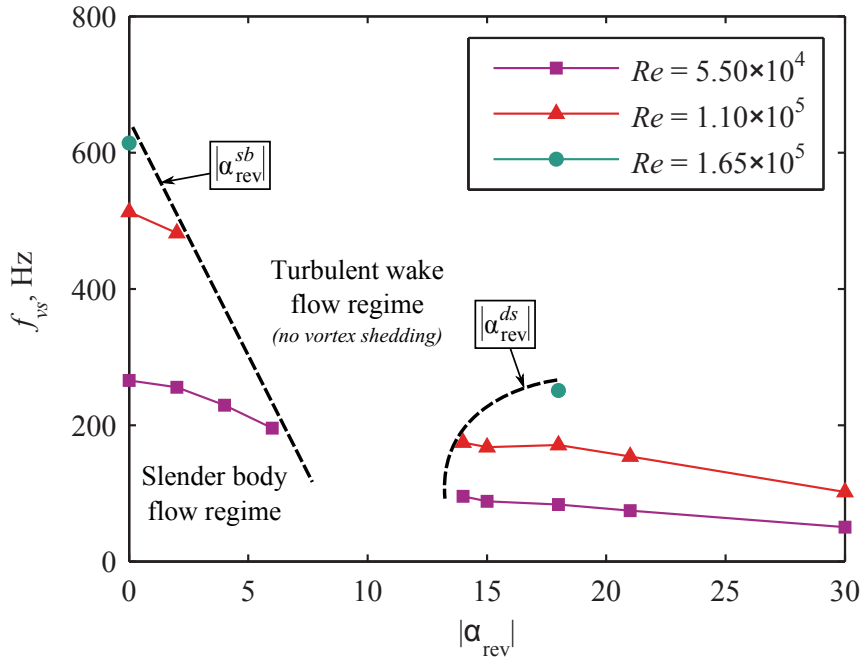

Figure 3.31: Classification of the three reverse flow wake regimes based on dimensional vortex shedding frequency

number and angle of attack for the elliptical airfoil for $5.5 \times 10^4 \leq Re \leq 1.65 \times 10^5$. Note that data were not collected for $18 \leq |\alpha_{rev}| < 30$ deg at $Re = 1.65 \times 10^5$. Excessive vibrations were encountered for these angles of attack; testing was suspended here to prevent damage to the model rotor blade. The two dashed lines illustrate *estimated* values of $|\alpha^{sb}_{\text{rev}}|$ and $|\alpha^{ds}_{\text{rev}}|$ and their variation with Re. These lines indicate transition between two neighboring flow regimes. The turbulent wake regime is observed for angles of attack between $|\alpha^{sb}_{\text{rev}}|$ and $|\alpha^{ds}_{\text{rev}}|$. The lack of periodic vortex shedding in the turbulent wake flow regime gives the appearance of a gap in Figure 3.31.

Figure 3.32 applies the wake survey technique (Section 2.4.4) to identify the frequency content of $\widehat{\omega}_{x_o/c}(t)$ at $x_o/c = 1.5$ for the elliptical airfoil in the slender body regime, $\alpha_{\text{rev}} = 0$ deg. For $Re = 5.50 \times 10^4$, the vortex shedding frequency is identified as a peak at 265.2 Hz with a width of approximately 10 Hz. For $Re = 1.10 \times 10^5$, the shedding frequency content is identified at 512.8 Hz with a bandwidth of approximately 60 Hz. Note that the peak

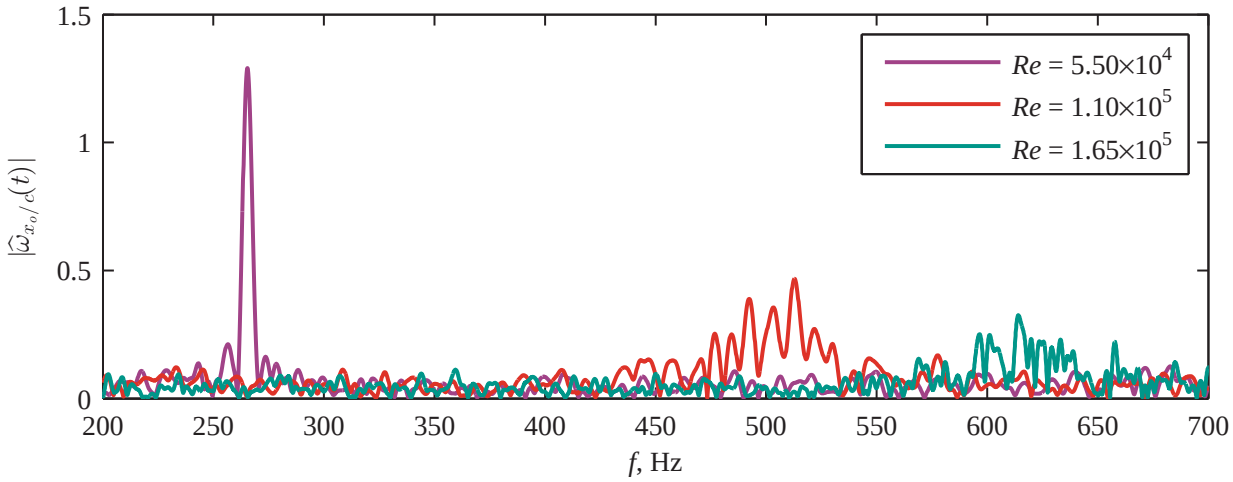

Figure 3.32: FFT of $\widehat{\omega}_{x_o/c}(t)$ at $x_o/c = 1.5$ for the elliptical airfoil at $\alpha_{\text{rev}} = 0\,\text{deg}$.

ratio (a measure of the signal-to-noise ratio) is significantly lower at the higher Re. For $Re = 1.65 \times 10^5$, the shedding frequency is identified as 614.1 Hz, but the peak ratio decreases further. This decrease in peak magnitude and ratio along with the increase in bandwidth suggests that vortex shedding becomes less periodic with increasing Reynolds number, and the flow is moving towards the turbulent wake regime. Additionally, the frequency content of unsteady airloads acting on airfoils at low angles of attack in reverse flow $3.3 \times 10^5 \leq Re \leq 1.0 \times 10^6$ lacked a distinct frequency peak (Section 2.3.7). These two findings suggest that the slender body flow regime is not present at any angle of attack in reverse flow for $Re > 1.65 \times 10^5$.

3.5.3 Unsteady Airloads

Figure 3.33 shows the unsteady airloads for two representative airfoils: a NACA 0012 (in reverse flow) and the cambered elliptical airfoil with the flatter side acting as the suction side (symmetric airloads in forward and reverse flow). Before examining the features of the unsteady airload curves of these airfoils, recall that the unsteady airloads were calculated

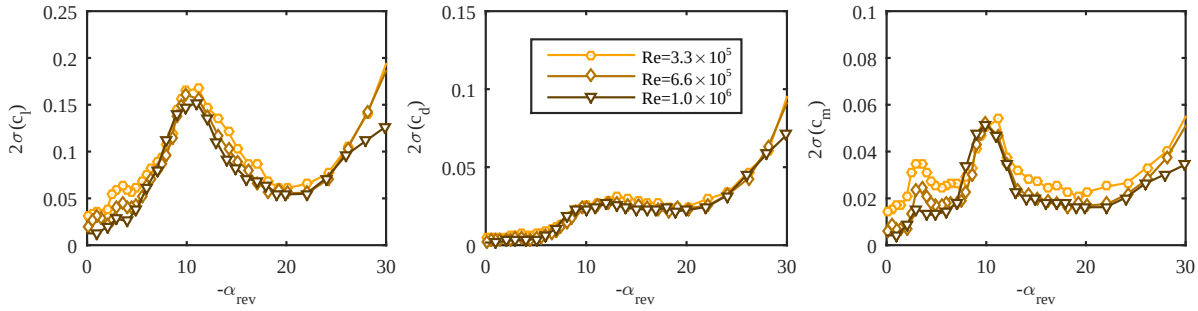

(a) NACA 0012

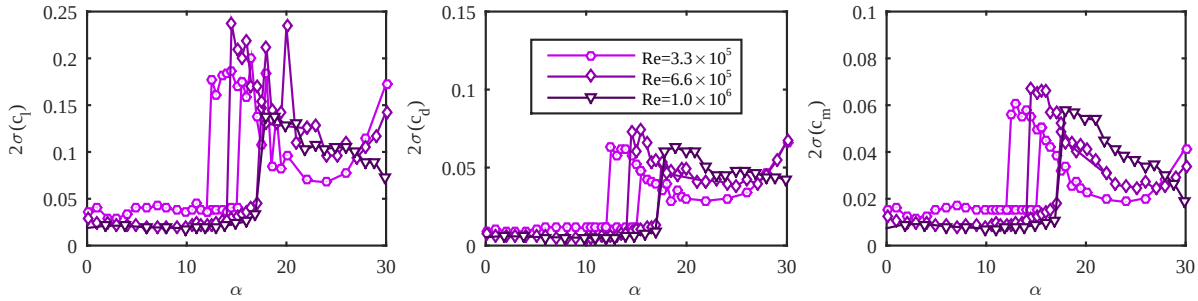

(b) Cambered ellipse (flat).

Figure 3.33: Reynolds number effects for two representative airfoils.

from measured unsteady pressure measurements with noise. The noise of the resulting unsteady airloads for static airfoils is given in Table 2.5.

Referring to Figure 3.33(a), it can be seen that the unsteady airloads acting on the NACA 0012 in reverse flow are generally insensitive to Reynolds number. The sharp leading edge forces flow separation, meaning that the separation point (and thus the unsteady airloads) does not depend on Reynolds number. This is true for the time-averaged airloads of the NACA 0012 in reverse flow as well (Section 3.5.1). The unsteady pitching moment at $Re = 3.3 \times 10^5$ appears to be greater for $0 \leq -\alpha_{\text{rev}} \leq 8\,\text{deg}$ and $12 \leq -\alpha_{\text{rev}} \leq 30\,\text{deg}$, but it should be noted that the noise of the unsteady pitching moment is 0.016 (Table 2.5) meaning that these measurements have a relatively low signal-to-noise ratio.

Next, consider Reynolds number effects on the unsteady airlods acting on the cambered elliptical airfoil (Figure 3.33(b)). Like the NACA 0012, the same general trends are captured

at the three Reynolds numbers tested, but some differences exist. At low angles of attack ($0 \leq \alpha \leq 12\,\text{deg}$), the unsteady airloads are greatest for $Re = 3.3 \times 10^5$, although the signal-to-noise ratio is low in this angle of attack range for this Reynolds number. The stall angle is increased with increasing Reynolds number leading to a shift in the rapid increase of unsteady airloads. The maximum unsteady airloads are nearly the same for all three Reynolds numbers, although there are no lift "spikes" observed for in the unsteady lift curve at $Re = 1.0 \times 10^6$. In the post-stall region, the unsteady drag generally increases with Reynolds number, leading to greater pitching moment.

In summary, the unsteady airloads on a NACA 0012 airfoil are generally insensitive to Reynolds number in reverse flow since the flow separation point is fixed at the sharp aerodynamic leading edge. The unsteady airloads of the NACA 0012 in forward flow, as well as the NACA 0024 in both forward and reverse flow, are mildly sensitive to Reynolds number (not shown) since flow transition and separation points vary with Reynolds number. The cambered elliptical airfoil with the flatter side serving as the suction side shows some sensitivity to Reynolds number, specifically in delaying of stall and the post-stall unsteady airloads. These findings hold true for elliptical airfoil and the cambered elliptical airfoil with the curved side acting as the suction side (not shown).

3.6 Chapter Summary

This chapter provided an analysis of the time-averaged and unsteady airloads, flowfields, and vortex shedding frequencies for two-dimensional airfoils with various geometries and trailing edge shapes held at static angles of attack in reverse flow. The airfoils were evaluated at four Reynolds numbers in the range of $1.1 \times 10^5 \leq Re \leq 1.0 \times 10^6$. Collectively, this range of Reynolds number captures the flow conditions experienced by a sizable portion of a retreating rotor blade ($\approx 0.4 \leq r/R \leq 0.77$) on a full-scale high-speed helicopter operat-

ing at $\mu = 0.77$. Time-resolved particle image velocimetry and unsteady force measurements were used to quantify the variation of vortex shedding frequency with angle of attack and Reynolds number. Flowfield measurements were used to characterize wake regimes in reverse flow. Time-averaged and unsteady airloads and pressure distributions were calculated from time-resolved pressure measurements integrated using a panel-style pressure integration scheme. Comparisons were made with unsteady velocity field measurements to determine the source of unsteady airloads. Appendix B is a collection of time-averaged and unsteady pressure distributions and airloads. Several conclusions can be drawn from the work presented in this chapter.

1. *Forward and reverse flow.* For angles of attack up to 10 deg and at all Reynolds numbers tested, the drag of the NACA 0012 in reverse flow is more than twice as large than in forward flow, leading to less than half the lift-to-drag ratio. At $Re = 1.1 \times 10^5$ and $5 \leq \alpha_{\text{rev}} \leq 16\,\text{deg}$, the drag of the elliptical airfoil is lower than the NACA 0012, but the downward-acting lift and pitching moment are higher. For both the NACA 0012 and elliptical airfoil, the pitching moment in reverse flow increases rapidly with angle of attack to a positive (unstable) value and remains greater than 0.3 for $\alpha_{\text{rev}} \geq 5\,\text{deg}$. At $Re = 1.1 \times 10^5$, there is no operating range in which all three airloads of the elliptical airfoil are less than those for the NACA 0012.

2. *NACA 0012 reverse flow stall characteristics.* Flow separation occurs at low angles of attack for the NACA 0012 in reverse flow as evidenced by a 25 % increase in drag from $\alpha_{\text{rev}} = 3\,\text{deg}$ to $\alpha_{\text{rev}} = 4\,\text{deg}$ at $Re = 1.1 \times 10^5$. Instantaneous smoke flow visualization revealed that boundary layer separation is unsteady at $\alpha_{\text{rev}} = 6\,\text{deg}$. The flow oscillates between fully separated and partially attached. As a result, time-averaged lift continues to increase until $\alpha_{\text{rev}} = 8\,\text{deg}$ and remains relatively constant until $\alpha_{\text{rev}} = 15\,\text{deg}$. The sharp trailing edge airfoil exhibits thin-airfoil-like stall in reverse flow.

3. *Full-scale performance of elliptical airfoils.* The lift-to-drag ratio is greater for the elliptical airfoil (symmetric) than for the cambered elliptical airfoil at $Re = 1.0 \times 10^6$ and $4 \leq \alpha \leq 20\,\text{deg}$. This is due to a greater amount of drag caused by larger regions of separated flow over the cambered upper surface. Contrary to modern high-speed rotorcraft airfoil designs which feature camber, this finding suggests that symmetric elliptical airfoils may perform better on the advancing side of a high advance ratio rotor.

4. *Unsteady wake regimes.* Reverse flow over a static airfoil can be categorized into one of three flow regimes: slender body vortex shedding, turbulent wake, or deep stall vortex shedding. Boundary layer reattachment is directly related to the angle of attack at which the wake transitions between the slender body and turbulent regimes, $|\alpha_{\text{rev}}^{sb}|$. This angle decreases with increasing Reynolds number. The slender body vortex shedding regime was not detected in pressure measurements for $3.3 \times 10^5 \leq Re \leq 1.0 \times 10^6$. The angle of attack that represents transition between the turbulent wake and deep stall regimes, $|\alpha_{\text{rev}}^{ds}|$, increases in magnitude with increasing Reynolds number since the boundary layer is more energetic at higher Re, allowing it to remain attached.

5. *Unsteady airloads in forward and reverse flow* ($0^\circ \leq |\alpha| \leq 30^\circ$). Unsteady airloads are closely linked to the type of static stall exhibited by an airfoil. Airfoils that exhibit a leading edge stall (e.g., NACA 0012 in forward flow, elliptical airfoil, and cambered elliptical airfoil with the flat surface acting as the suction side) have a rapid increase in unsteady airloads at the onset of stall. Airfoils that exhibit a trailing edge stall (e.g., NACA 0024 in forward flow and cambered elliptical airfoil with the curved surface acting as the suction side) have unsteady airloads that increase gradually. Airfoils that exhibit a thin-airfoil stall (e.g., NACA series airfoils in reverse flow) have unsteady

airloads that increase at a moderate rate due progressively increasing amounts of flow separation originating at the sharp aerodynamic leading edge. In all cases, the unsteady airloads are greatest when the shear layer is unstable and near suction side of the airfoil. This is a result of the turbulent wake regime.

6. *Unsteady airloads at high angles of attack* ($30^\circ \leq \alpha \leq 150^\circ$). This angle of attack range corresponds with the deep stall vortex shedding regime. Here, unsteady airloads are greatest near a blunt aerodynamic trailing edge since the shear layer can curl around, forming a vortex that induces unsteady flow near surface on suction side. It is believed that the lower unsteady airloads observed for airfoils with a sharp aerodynamic trailing edge results from vortex shedding occurring further downstream.

7. *Aerodynamic hysteresis.* In the angle of attack range $0^\circ \leq \alpha \leq 30^\circ$, unsteady airloads acting on thick airfoils are greatest when the angle of attack is being decreased through stall. This is a result of an unstable shear layer approaching the suction side of the airfoil.

8. *Reynolds number effects on time-averaged aerodynamics.* The airloads on the NACA 0012 in reverse flow were found to be insensitive to Reynolds number for $-3 \leq -\alpha_{\text{rev}} \leq 30\,\text{deg}$. At moderate angles of attack ($-\alpha_{\text{rev}} \approx 7\,\text{deg}$), the flow separates at the leading edge and partially reattaches further down the chord. The partial reattachment is shown to decrease slightly with increasing Reynolds number. However, the overall character of the velocity distribution on the suction side of the airfoil, as well as the flow separation and reattachment points along the airfoil chord, are consistent with the insensitivity of airloads to reverse flow. The flowfields and airloads of thick airfoils in reverse flow are highly sensitive to Reynolds number for $Re \leq 6.6 \times 10^5$. At these lower Reynolds numbers, the location of laminar separation bubbles, flow transition, and separation characteristics must all be considered when evaluating airfoil performance.

9. *Reynolds number effects on unsteady airloads.* For airfoils exhibiting a leading edge stall or trailing edge stall, the stall angle (and corresponding onset of high unsteady airloads) increases with angle of attack. Airfoils that undergo a thin-airfoil-like stall have unsteady airloads that are independent of Reynolds number due to the fixed separation point at the sharp aerodynamic leading edge.

Chapter 4

Aerodynamics of Oscillating Rotor Blade Sections in Reverse Flow

4.1 Motivation

Chapter 3 examined the time-averaged and unsteady aerodynamics of *static* airfoils through high angles of attack and in reverse flow, subject to a constant freestream. This provided fundamental insight to the performance of airfoils in the reverse flow region of a high speed helicopter. The present chapter expands on this model of the reverse flow region to include oscillatory motions due to cyclic pitch control inputs. Cyclic pitch is used to trim rotors to maintain straight-and-level flight, resulting in sinusoidal pitching of the rotor blades at a frequency of 1/rev. When characterizing the aerodynamic performance of rotor blades, the effect of cyclic pitching must be considered, and is especially important due to the potential influence of *dynamic stall* on the retreating rotor blade of high advance ratio helicopters (Section 1.3.4).

Figure 4.1(a) shows the theoretical in-plane velocity distribution, U_T, for the X2 Technology Demonstrator (X2TD) rotor disk operating at $\mu = 0.77$ [6]. The reverse flow region exists on the retreating side where $U_T < 0$. Figure 4.1(a) highlights the path of a blade element located at the mid-span of the rotor blade ($r = 0.5$). Figure 4.1(b) shows the variation of in-plane velocity for this blade element as it travels around the blade azimuth. The blade

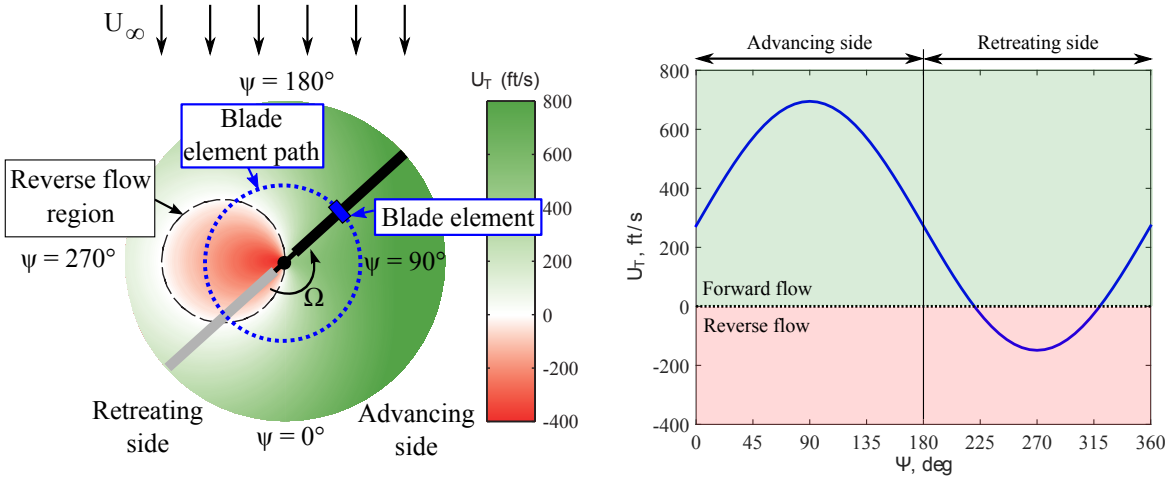

(a) Contour of in-plane velocity, U_T.

(b) Variation of in-plane velocity with blade azimuth, Ψ.

Figure 4.1: Path and in-plane velocity for a blade element at $r = 0.5$ on the X2 Technology Demonstrator operating at $\mu = 0.77$.

element operates in forward flow for $0 \leq \Psi \leq 220\,\text{deg}$, reverse flow for $220 \leq \Psi \leq 320\,\text{deg}$, and then forward flow for $320 \leq \Psi \leq 360\,\text{deg}$. As the blade element travels around the rotor azimuth, it completes one pitching cycle; a majority of this cycle occurs in forward flow, but a portion occurs in reverse flow. During the cycle, the local freestream also varies as the values of U_T, U_P (inflow velocity component), and U_R (radial velocity component) vary with blade azimuth for a given trim condition.

The complex, three-dimensional flow environment of a rotor blade element features time-varying pitch angle, freestream magnitude, and freestream direction. To model the behavior of a pitching rotor blade element in the reverse flow region, the present work considers a two-dimensional airfoil oscillating about the geometric quarter-chord (aerodynamic three-quarter chord) subject to a constant freestream in reverse flow. While this model does not capture the time-varying freestream or three-dimensional effects of the true reverse flow region, it does offer the opportunity to gain fundamental insight into oscillating rotor blade behavior in reverse flow to compare with classical dynamic stall. It also provides a means

to evaluate the potential merit of using a modern "double-ended" rotor blade airfoil (Figure 1.6) to alleviate detrimental aerodynamic effects in the reverse flow region, such as early flow separation.

4.2 Parameter Space

A NACA 0012 (representative of conventional rotor blade airfoils with a sharp trailing edge) and a cambered elliptical airfoil (representative of modern double-ended airfoils featured on high advance ratio vehicles) were selected for this study. These two airfoils were tested at three Reynolds numbers: $Re = 165{,}000$, $330{,}000$, and $500{,}000$. The upper plot of Figure 4.2(a) shows the radial Reynolds number distribution for the X2TD rotor blade at $\Psi = 270\,\text{deg}$ and $\mu = 0.77$. The oscillating airfoil experiments were performed at Reynolds numbers corresponding to full-scale radial stations in the range $0.61 \leq r \leq 0.71$. These experiments were performed in the $20 \times 28\,\text{in}$ wind tunnel at the University of Maryland, which limited the maximum Reynolds number that could be achieved.

It was previously mentioned that full-scale rotor blades oscillate with a frequency of 1/rev (typically between 4-8 Hz). To match the unsteady effects that arise from pitching in the present sub-scale experiments, the dimensionless parameter *reduced frequency* was considered. Recall that reduced frequency is defined as:

$$k = \frac{\pi f c}{U_{\text{loc}}} \tag{4.1}$$

Reduced frequency is an ambiguous quantity to define for a rotor since the local freestream varies both along the blade radius and in time. The lower plot of Figure 4.2(a) shows the reduced frequency distribution for the retreating blade of an X2TD, again at a specific, single blade azimuth of $\Psi = 270\,\text{deg}$. The present work considered reduced frequencies corresponding to the blade radial stations at the three Reynolds numbers tested (i.e., full-scale reduced

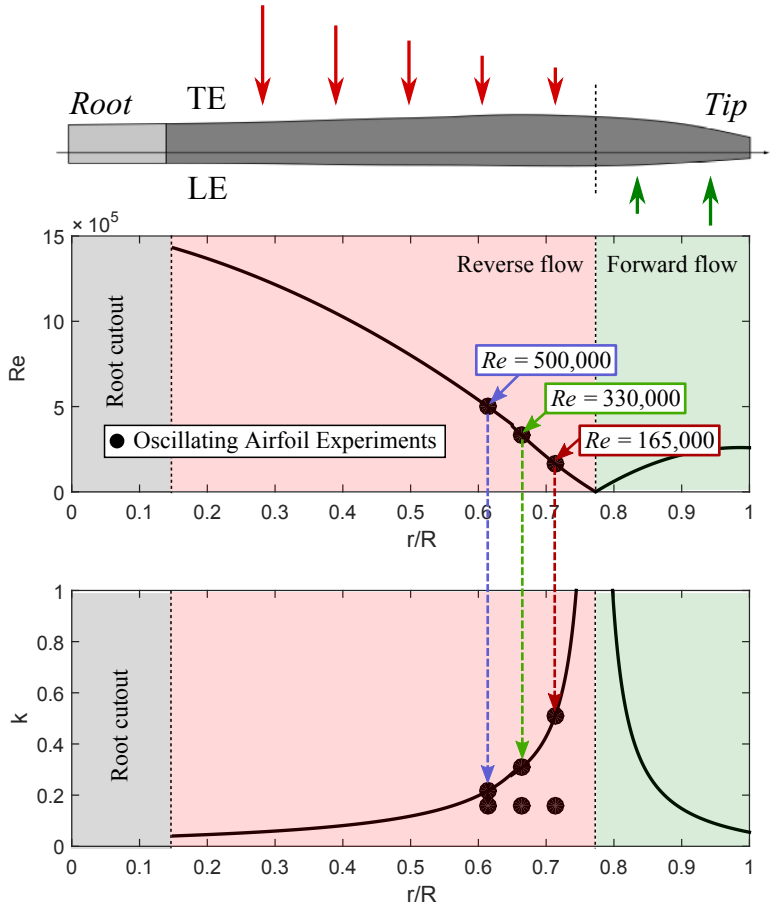

(a) Reynolds number and reduced frequency.

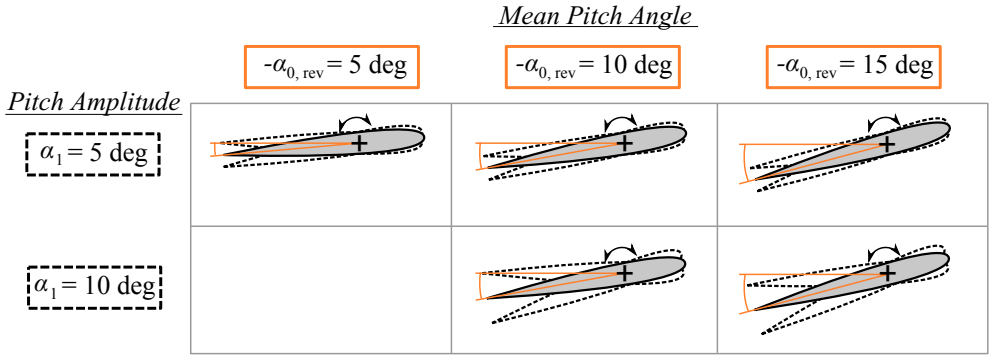

(b) Mean pitch angle and pitch amplitude.

Figure 4.2: Parameter space of oscillating airfoil experiments, based on retreating blade ($\Psi = 270\,\text{deg}$) of the X2 Technology Demonstrator operating at $\mu = 0.77$.

frequencies) at this azimuthal position. For each of the three Reynolds numbers tested, the airfoils were also oscillated at a reduced frequency of $k = 0.160$ to isolate Reynolds number effects. The two airfoils were also tested in forward flow at $k = 0.025$ (representative of the full-scale reduced frequency on the advancing side of a high-speed rotor), $k = 0.100$, and $k = 0.160$. Throughout these experiments, the tunnel freestream was therefore varied between 12-36 m/s and the oscillation frequency between 1.87-12.26 Hz.

Since classical dynamic stall is known to be sensitive to oscillation angles (Section 1.3.4), the reverse flow mean pitch angle, $-\alpha_{0,\text{rev}}$ and pitch amplitude, α_0 were also varied to explore the sensitivity of reverse flow dynamic stall to these quantities. Figure 4.2(b) illustrates the five variations of pitching kinematics tested. The angles are nominal; recall that the angle of attack was corrected by approximately 1 deg using static airload curves (Section 2.5.2). All references to angle of attack made in this chapter will be to nominal values; all airload data accounts for this correction.

4.3 Dynamic Stall of a NACA 0012 in Forward and Reverse Flow

This section examines the general flow features of dynamic stall for a NACA 0012 airfoil oscillating in both forward and reverse flow, and the influence of relevant flow features on phase-averaged pressure distributions and integrated airloads will be described. Figure 4.3 shows velocity fields of the suction side of the airfoil, phase-averaged over 10 cycles for selected phases of the pitching cycle (Section 2.4.3). A "phase" is a specific time during a pitching cycle, normalized by the cycle period (i.e., t/T). The phases shown in Figure 4.3 were selected to illustrate key events during the progression of dynamic stall. Note that side-by-side contour plots shown for forward and reverse flow are not necessarily at the same phase. The contours show the magnitude of total velocity, normalized by the freestream. For the forward flow results, 1/9 and 1/5 of the calculated vectors are shown in the x/c- and

z/c-directions; in reverse flow, 1/14 and 1/8 of the calculated vectors are shown. The forward flow results are presented with the geometric lower surface acting as the suction side so that they may be directly compared with the reverse flow results. The magnitude of the nominal mean pitch angle and pitch amplitude is 10 deg for both cases. Note that the velocity fields are presented in the airfoil reference frame; the direction of the freestream varies with cycle phase. In forward flow (Figure 4.3(a)), the blunt edge served as the aerodynamic leading edge ($x/c = 0$) and the airfoil oscillated about the aerodynamic quarter-chord ($x/c = 0.25$); in reverse flow (Figure 4.3(b)), the sharp edge served as the aerodynamic leading edge and the airfoil oscillated about the aerodynamic three-quarter-chord ($x/c = 0.75$). Note that $x/c = 0$ is defined as the *aerodynamic leading edge* throughout this chapter (regardless of airfoil orientation). Also note that velocity field data very near the surface has been omitted due to laser reflection. Figure 4.4 shows corresponding pressure distributions, phase-averaged over 500 cycles (Section 2.3.8). In this figure, the solid line represents the phase-averaged distribution and the grey shaded regions represent $2\sigma(c_{\mathrm{p}})$ variations in pressure.

The dynamic stall events of a NACA 0012 in forward flow presented here are consistent with the prior description of deep dynamic stall (Section 1.3.4). Beginning at $t/T = 0.35$ in forward flow (Figure 4.3(a)), a high velocity region is seen near the leading edge. A corresponding suction peak is observed in Figure 4.4(a). This phase shows an early stage of the formation of the dynamic stall vortex since the variations of pressure near the leading edge are large (as represented by the grey filled region), consistent with velocity fluctuations of separated flow. The velocity induced by the vortex on airfoil surface is obscured by the white masked area in Figure 4.3(a). For $0.40 \leq t/T \leq 0.46$, the dynamic stall vortex convects down the chord, with an associated aftward shift in suction (Figure 4.4(a)). At $t/T = 0.46$, the dynamic stall vortex has convected away from the airfoil and can be seen in Figure 4.3(a), centered at approximately ($x/c = 0.8$, $z/c = -0.15$). A short time later at $t/T = 0.49$, the vortex convects out of the field of view, but interacts with the trailing edge shear layer

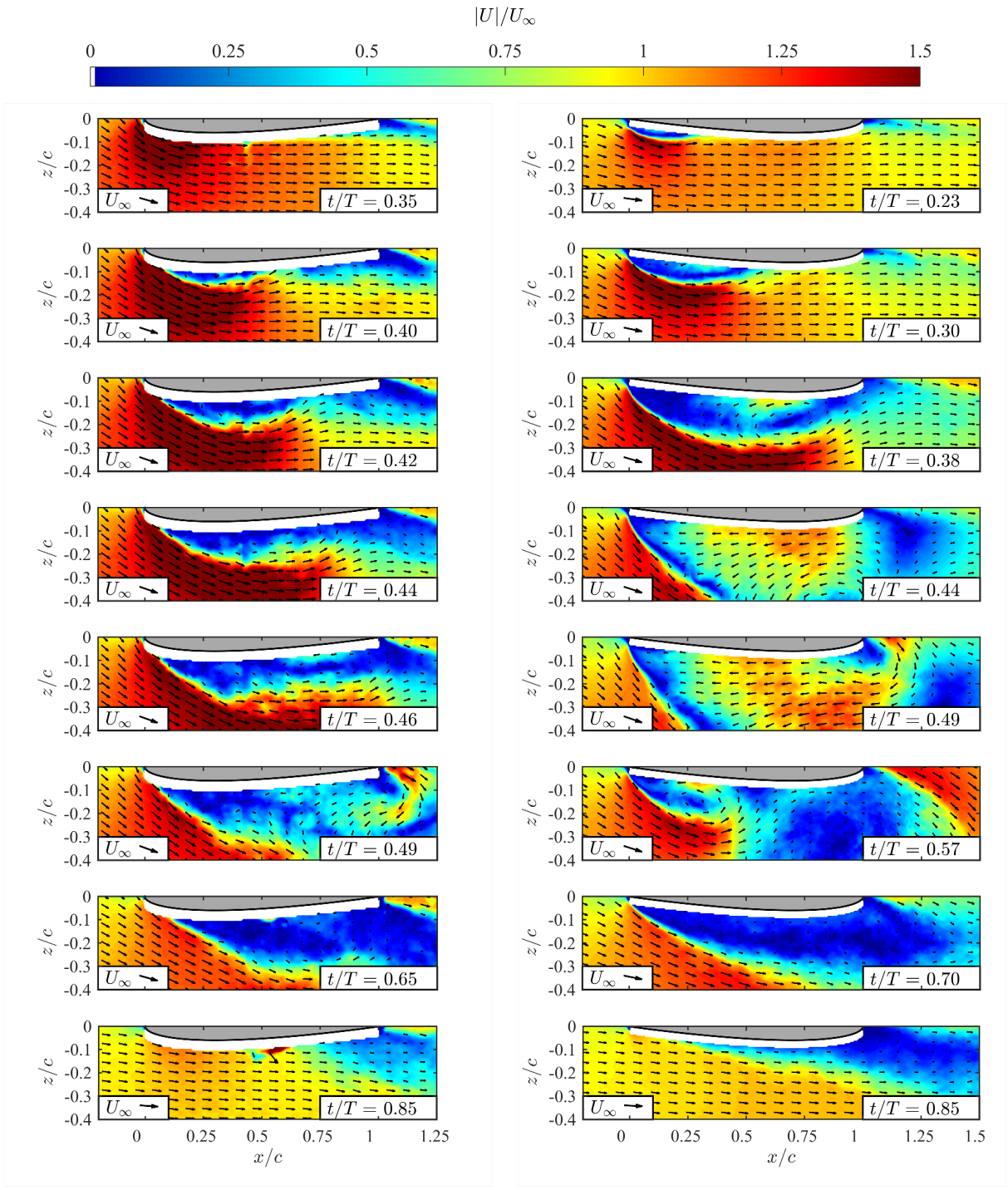

(a) Forward flow.

(b) Reverse flow.

Figure 4.3: Comparison of phase-averaged velocity fields for a pitching NACA 0012 in forward flow ($\alpha_0 = 11.0\,\text{deg}$, $\alpha_1 = 10\,\text{deg}$) and reverse flow ($-\alpha_{0,\text{rev}} = 10\,\text{deg}$, $\alpha_1 = 10\,\text{deg}$). In both cases, $Re = 3.3 \times 10^5$, $k = 0.160$.

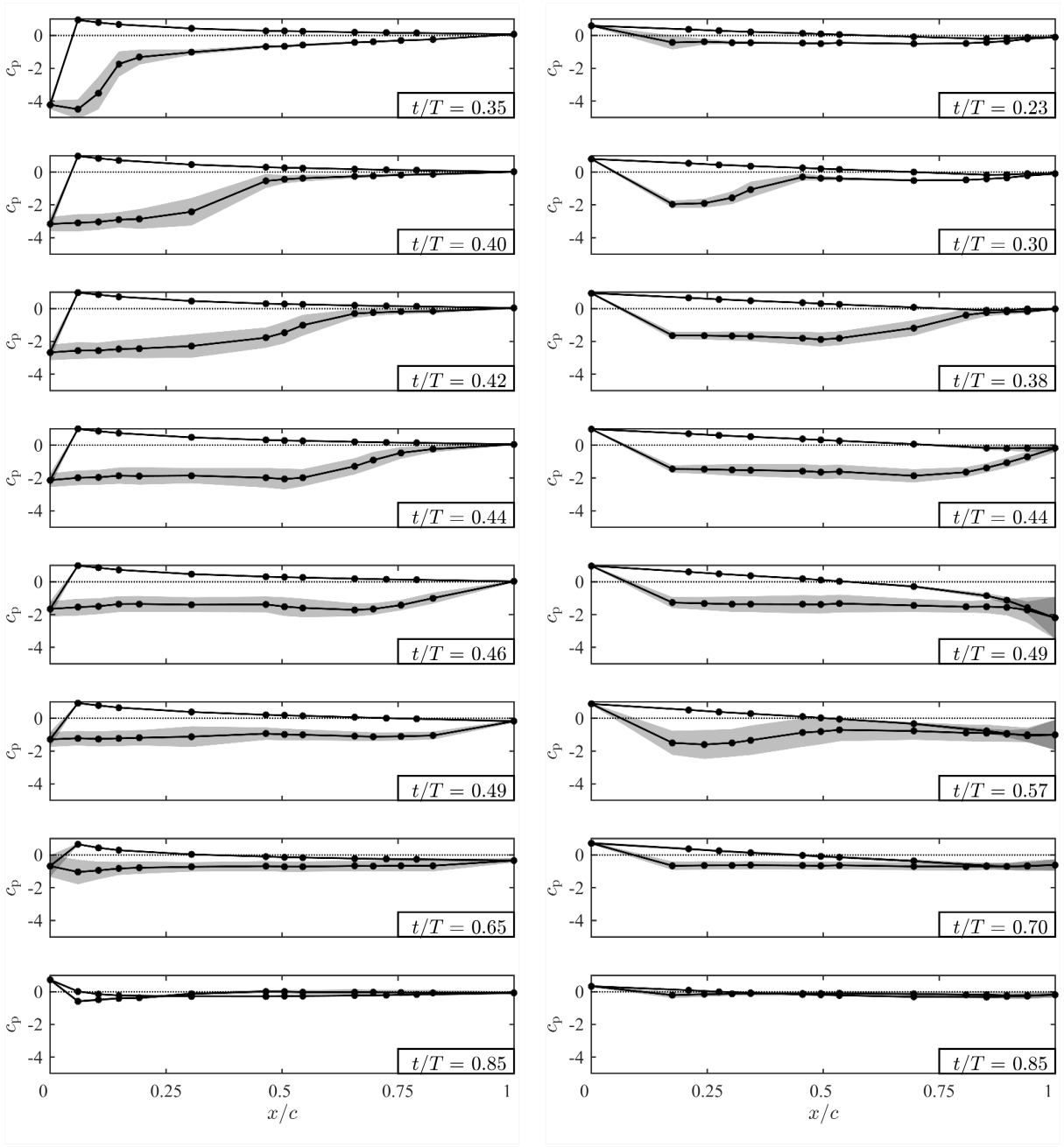

(a) Forward flow.

(b) Reverse flow.

Figure 4.4: Comparison of phase-averaged pressure distributions for a pitching NACA 0012 in forward flow ($\alpha_0 = 10\,\text{deg}$, $\alpha_1 = 10\,\text{deg}$) and reverse flow ($-\alpha_{0,\text{rev}} = 10\,\text{deg}$, $\alpha_1 = 10\,\text{deg}$). In both cases, $Re = 3.3 \times 10^5$, $k = 0.160$. Note that the pressure at the sharp edge ($x/c = 1$ in forward flow, $x/c = 0$ in reverse flow) is extrapolated.

to form a trailing edge vortex. The influence of this trailing edge vortex on the pressure distribution is not seen in Figure 4.4(a) since pressure measurements were not collected near the trailing edge. Recall from Section 2.3.1 that for the oscillating airfoil experiments, the pressure at the sharp trailing edge, $x/c = 1$, was linearly extrapolated from measurements on the pressure side of the airfoil. Once the trailing edge vortex convects into the wake, the flow remains fully separated ($t/T = 0.65$) until it progressively reattaches from leading edge to trailing edge ($t/T = 0.85$).

Turning attention to reverse flow dynamic stall (Figure 4.3(b)), flow separation from the sharp leading edge is observed at $t/T = 0.23$, much earlier than in forward flow. At $t/T = 0.30$, the separated region extends over approximately $0 \leq x/c \leq 0.5$ and a corresponding region of suction can be seen in Figure 4.4(b). The dynamic stall vortex grows and convects towards the blunt aerodynamic trailing edge at $t/T = 0.38$. It then moves away from the airfoil at $t/T = 0.44$, inducing flow over nearly the entire chord, and leading to a nearly uniform pressure distribution on the suction side. Similar to the forward flow case, the dynamic stall vortex interacts with the trailing edge shear layer at $t/T = 0.49$, inducing the formation of a trailing edge vortex. This profoundly reduces the pressure on the aft portion of the pressure side of the airfoil, similar to the pressure distribution at $\psi = 290\,\text{deg}$ (Figure 1.26). Note that the pressure at the trailing edge decreases from $c_\text{p} \approx 0$ to $c_\text{p} \approx -2$ between $t/T = 0.44$ and $t/T = 0.49$. At $t/T = 0.57$, the pressure near the trailing edge recovers slightly, though a new low pressure region centered near $x/c = 0.25$ is present due to the induced velocity of a secondary dynamic stall vortex (Figure 4.3(b)). After this secondary dynamic stall vortex convects into the wake, the flow remains separated ($t/T = 0.70$) until it begins to reattach ($t/T = 0.85$). Note that a secondary dynamic stall vortex was not observed for these conditions in forward flow (Figure 4.3(a)).

While the general character of reverse flow dynamic stall is similar to classical dynamic stall in forward flow, some important distinctions exist due to different shape of the aerody-

namic leading edge. The sharp leading edge of a NACA 0012 in reverse flow leads to early flow separation, similar to static airfoil experiments in reverse flow. For example, compare $t/T = 0.40$ in Figure 4.3(a) with $t/T = 0.30$ in Figure 4.3(b). The flow over $0 \leq x/c \leq 0.5$ is similar in both cases, showing the early formation of a primary dynamic stall vortex. However, this flowfield is achieved earlier in reverse flow ($t/T = 0.30$). Next, consider the flowfields in forward and reverse flow at the same phase, $t/T = 0.44$. In forward flow, the dynamic stall vortex is still close to the surface of the airfoil. In reverse flow, the dynamic stall vortex is further along in its evolution, having convected away from the airfoil and into the wake. At $t/T = 0.49$, both flowfields show the formation of a trailing edge vortex, but it is stronger in reverse flow due to the influence of the stronger dynamic stall vortex.

Insight can also be gained by examining the pressure distributions over the entire pitching cycle for forward and reverse flow. Figure 4.5 shows contour plots of the phase-averaged pressure distribution. Figure 4.5(a) shows the suction side of the airfoil and Figure 4.5(b) shows the pressure side. In both sub-figures, the forward flow pressure distribution is given in the upper contour and the reverse flow pressure distribution is given in the lower contour. The phase, t/T, is plotted on the abscissa and the chord position, x/c, is plotted on the ordinate. Like in Figures 4.3 and 4.4, the aerodynamic leading and trailing edges are defined as $x/c = 0$ and $x/c = 1$, respectively, regardless of the orientation of the airfoil. The black dotted lines indicate the chordwise position of pressure transducers. The black transparent regions indicate extrapolated pressure data near the sharp geometric trailing edge. The layout of Figure 4.6 is identical to Figure 4.5, but Figure 4.6 shows the distribution of the magnitude of pressure fluctuations, $2\sigma(c_{\mathrm{p}})$, over 500 cycles. Figures 4.5 and 4.6 are an expansion of Figure 4.4; each phase in Figure 4.4 is a vertical slice of Figures 4.5 and 4.6 at value of t/T.

Consider the phase-averaged pressure distribution of the suction side in forward flow (Figure 4.5(a)). As the cycle progress (from left to right), suction gradually builds near the

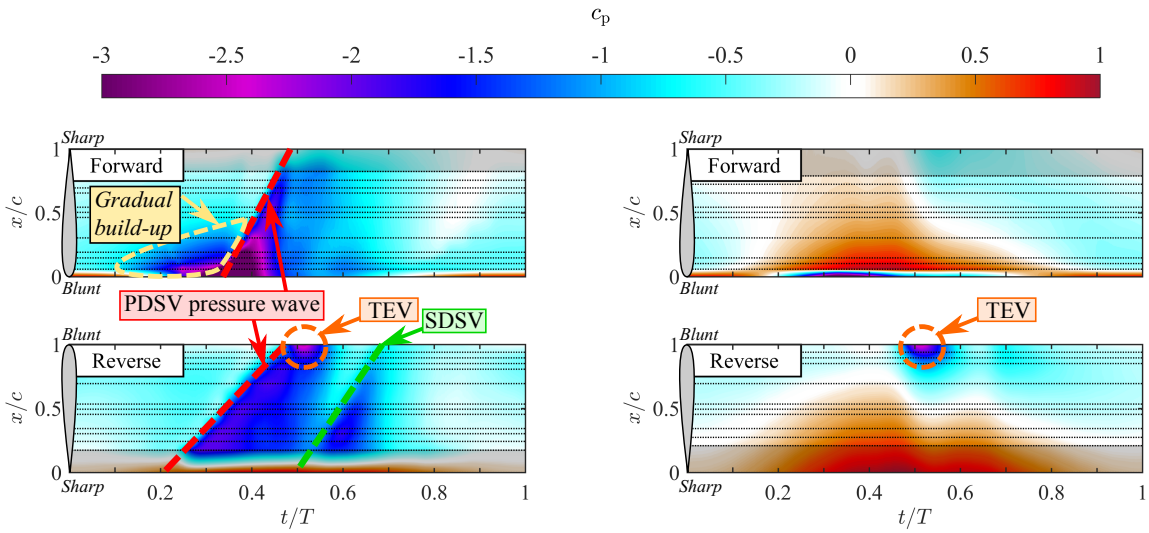

(a) Suction side.

(b) Pressure side.

Figure 4.5: Comparison of phase-averaged pressure distributions on a NACA 0012 in forward flow ($\alpha_0 = 10\,\text{deg},\ \alpha_1 = 10\,\text{deg}$) and reverse flow ($-\alpha_{0,\text{rev}} = 10\,\text{deg},\ \alpha_1 = 10\,\text{deg}$). In both cases, $Re = 3.3 \times 10^5$, $k = 0.160$. PDSV: Primary dynamic stall vortex. TEV: Trailing edge vortex. SDSV: Secondary dynamic stall vortex.

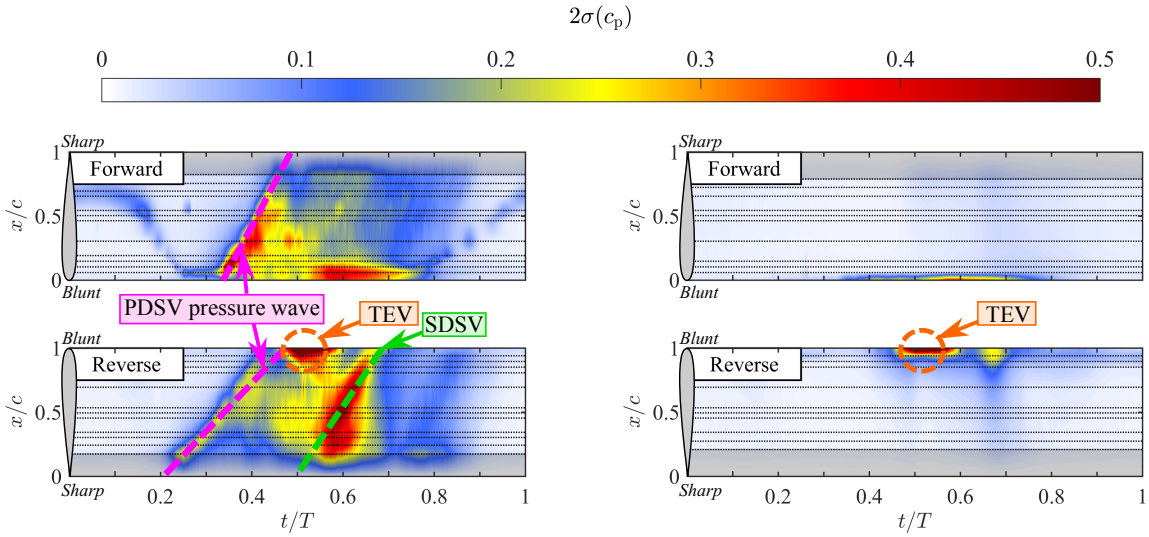

(a) Suction side.

(b) Pressure side.

Figure 4.6: Comparison of distributions of pressure fluctuations NACA 0012 in forward flow ($\alpha_0 = 10\,\text{deg},\ \alpha_1 = 10\,\text{deg}$) and reverse flow ($-\alpha_{0,\text{rev}} = 10\,\text{deg},\ \alpha_1 = 10\,\text{deg}$). In both cases, $Re = 3.3 \times 10^5$, $k = 0.160$.

leading edge. The dynamic stall vortex then forms and induces a low pressure wave in the chordwise direction as it convects along the chord ($0.35 \leq t/T \leq 0.49$). For $0.5 \leq t/T \leq 0.9$, the pressure distribution along the chord is nearly uniform since the flow is fully separated. On the pressure side in forward flow (Figure 4.5(b)), high pressure builds along much of the chord during the first half of the pitching cycle. Once the dynamic stall vortex convects into the wake near $t/T = 0.49$, the pressure along the pressure side generally decreases due to the movement of the stagnation point towards the leading edge. Next, consider the phase-averaged pressure distributions in reverse flow. Although pressure measurements are not available for $0 \leq x/c \leq 0.175$, it is clear that there is not a gradual build-up of suction, like what was observed in forward flow over $0 \leq x/c \leq 0.4$ and $0.1 \leq t/T \leq 0.35$. Instead, the pressure lowers over an increasing portion of the chord as the primary dynamic stall forms and convects along the suction side from $0.25 \leq t/T \leq 0.50$. This confirms the first important difference between forward and reverse flow dynamic stall: the primary dynamic stall vortex forms earlier in the cycle and grows at a slower rate than in forward flow. Consider Figure 4.3 which shows that the start of dynamic stall vortex formation was at $t/T \approx 0.35$ in forward flow and at $t/T \approx 0.23$ in reverse flow. By $t/T = 0.49$, the dynamic stall vortex had convected away from the airfoil in both cases (though some of the flow induced by the vortex persisted at this phase in reverse flow). This means that the approximate lifespan of the dynamic stall vortex is $0.14T$ in forward flow and $0.26T$ in reverse flow – nearly twice as long in reverse flow. This effect is seen in the phase-averaged pressure distributions (Figure 4.5) as a decrease in the slope of the edge of the low pressure wave associated with the dynamic stall vortex.

A few other differences between the phase-averaged pressure distributions in forward and reverse flow bear mentioning. The secondary dynamic stall vortex that is shown at $t/T = 0.57$ induces a low pressure wave that convects aft along the suction side of the chord (see $0.55 \leq t/T \leq 0.7$ in Figure 4.5(a)). In reverse flow, a region of suction exists near the

trailing edge on the pressure side of the airfoil (Figure 4.5(b)), consistent with the trailing edge vortex observed at $t/T = 0.49$ in Figure 4.3(b).

Next, consider the distributions of pressure fluctuations, $2\sigma(c_{\mathrm{p}})$, shown in Figure 4.6. Areas with low values of $2\sigma(c_{\mathrm{p}})$ represent a low degree of pressure fluctuations in the pressure measurement across 500 cycles, typically associated with attached flow. Areas with large values of $2\sigma(c_{\mathrm{p}})$ are associated with separated flow and/or aperiodicity of unsteady flow features. Turning attention to the suction side of the airfoil in forward flow, the pressure fluctuations are generally low during $0 \leq t/T \leq 0.3$ since the flow is attached for this portion of the cycle. However, a narrow band of low pressure fluctuations ($2\sigma(c_{\mathrm{p}}) \approx 0.1$) shifts from $x/c \approx 0.7$ towards $x/c \approx 0.1$ as t/T increases from 0 to 0.3. These pressure fluctuations are associated with transition of the boundary layer from laminar to turbulent; similar observation was made by Lorber and Lee [39, 62]. As the cycle progresses from $t/T = 0$ to $t/T = 0.3$, the suction peak grows, leading to an increase in the adverse pressure gradient, causing the transition point to move towards the leading edge. At $t/T = 0.35$, the pressure fluctuations are greatest near the leading edge (similar to Figure 4.4(a)), signifying the formation of the dynamic stall vortex. The pressure fluctuations affect an increasing portion of the chord as the cycle progresses to $t/T = 0.5$. For $0.5 \leq t/T \leq 0.7$, the distribution of pressure fluctuations remains generally constant since the flow is separated. The greatest fluctuations occur near the leading edge, likely due to aperiodicity in the separation point. Beginning at $t/T = 0.8$, the unsteady pressure fluctuations decrease along an increasing portion of the chord, consistent with flow reattachment. Also note that as the cycle progresses to $t/T = 1$, the adverse pressure gradient decreases in magnitude and the pressure fluctuations associated with the boundary layer transition point move aft. The unsteady pressure fluctuations on the pressure side of the airfoil (Figure 4.6(b)) are low for the entire cycle since the flow is attached. The only exception is the moderate pressure fluctuations near $x/c = 0$ for $0.35 \leq t/T \leq 0.8$ due to aperiodicity in the separation point at the leading edge.

In reverse flow, the first thing to notice is the absence of pressure fluctuations due to boundary layer transition. It was shown in static airfoil tests that at low angles of attack ($\alpha_{\text{rev}} < 1\,\text{deg}$), a small separation bubble exists on near the sharp aerodynamic leading edge. This suggests that the boundary layer transitions from laminar to turbulent near the leading edge ($x/c < 0.05$). This is consistent with the low pressure fluctuations observed on the suction side in reverse flow for $0 \leq t/T \leq 0.2$ and $0.9 \leq t/T \leq 1$. The unsteady pressure fluctuations associated with the formation of the reverse flow dynamic stall vortex are first detected at $t/T = 0.25$ at $x/c = 0.175$. The unsteady pressure fluctuations reach the trailing edge ($x/c = 1$) at $t/T = 0.41$. A region of large fluctuations in pressure exists near the trailing edge for $0.45 \leq t/T \leq 0.6$, suggesting aperiodicity of the trailing edge vortex formation. The second region of large pressure fluctuations ($0.55 \leq t/T \leq 0.65$) extends over much of the chord and captures the aperiodicity of the secondary dynamic stall vortex.

Figure 4.7 compares the unsteady airloads in forward and reverse flow. Recall that these airloads were determined by integrating instantaneous pressure measurements over 500 cycles. The phase-average of the instantaneous airloads in forward flow is represented with a thick black line, with the 2σ-variation of the instantaneous airloads represented by the grey shaded region. The magnitude of the 2σ-variation depends on the periodicity of the airloads. Thus, attached flow conditions generally lead to low 2σ-variation, whereas separated flow leads to larger variation. The phase-average of the instantaneous airloads in reverse flow is plotted with a black dashed line.

Focusing on the unsteady airloads in forward flow and their dependence on cycle phase (Figure 4.7(a)), lift and drag increase linearly until $t/T = 0.35$, after which the flow begins to separate and the dynamic stall vortex forms. This is evidenced by an abrupt increase in the slope of the drag curve and an increase in the variations of unsteady lift (shaded region). Moment stall begins a short time later ($t/T = 0.39$) as the dynamic stall vortex convects along the chord, shifting the center of pressure aft (Figure 4.4(a)). The magnitude of the

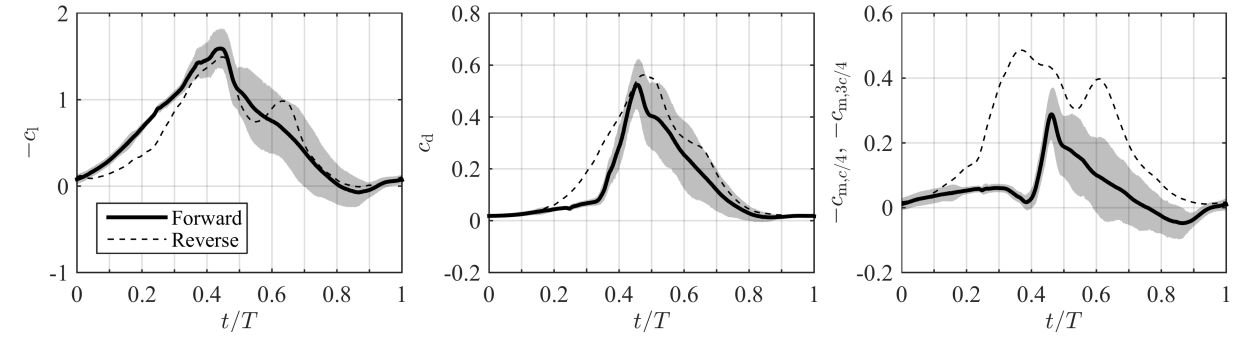

(a) Dependence on cycle phase, t/T.

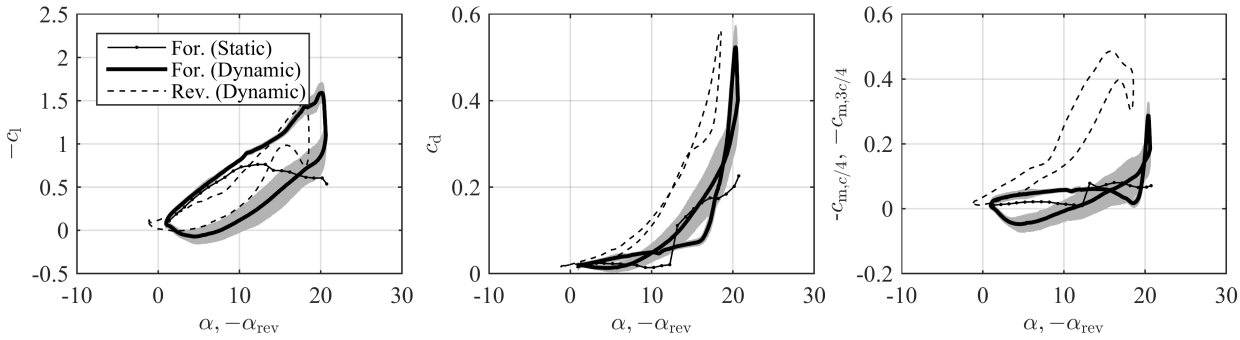

(b) Dependence on angle of attack.

Figure 4.7: Unsteady airloads for a NACA 0012 in forward flow (nominally $\alpha_0 = 10\,\mathrm{deg}$, $\alpha_1 = 10\,\mathrm{deg}$) and reverse flow (nominally $-\alpha_{0,\mathrm{rev}} = 10\,\mathrm{deg}$, $\alpha_1 = 10\,\mathrm{deg}$). In both cases, $Re = 330,000$, $k = 0.160$. The lines represent the phase-average. The shaded regions represent $2\sigma(c_\mathrm{x})$.

airloads decreases for $0.46 \leq t/T \leq 0.85$ as the dynamic stall vortex convects away from the airfoil. In reverse flow, lift increases non-linearly due to the lack of pressure measurements for $0 \leq x/c \leq 0.175$ where the pressure is lower than the extrapolated measurement due to the formation of the reverse flow dynamic stall vortex at the sharp leading edge. Although it appears as though drag is similar in forward and reverse flow for $0 \leq t/T \leq 0.2$, it is actually greater in reverse flow due to slight variations in the pitching kinematics of the experiments from installation error (see Figure 4.7(b)). Drag increases rapidly in reverse flow for $0.2 \leq t/T \leq 0.4$, consistent with the longer development time for the reverse flow dynamic stall vortex. The pitching moment about the aerodynamic three-quarter chord (geometric quarter-chord) increases in magnitude for $0 \leq t/T \leq 0.36$ while the reverse flow dynamic stall vortex grows in strength. Note that the magnitude of the pitching moment is dramatically greater in reverse flow than in forward flow. This is a result of the center of pressure acting near the aerodynamic quarter-chord, resulting in a moment arm of approximately $0.5c$. However, once the reverse flow dynamic stall vortex begins to convect aftward, the center of pressure moves with it, thus reducing the moment arm and magnitude of the pitching moment ($0.36 \leq t/T \leq 0.53$). At $t/T = 0.49$, the trailing edge vortex forms and reduces the pressure difference across the airfoil (Figure 4.4(b)). This manifests as a reduction in lift (Figure 4.7(a)). The secondary vortex enhances lift for $0.55 \leq t/T \leq 0.65$ with a corresponding increase in the magnitude of pitching moment.

Figure 4.7(b) shows the same unsteady airloads, but shows their dependence on angle of attack rather than cycle phase. Static airloads are also included for comparison to compare static and dynamic stall characteristics. Note that there is a slight difference in the mean pitch angle for the forward and reverse flow tests. The unsteady lift and drag curves in forward and reverse flow are generally similar in shape, though the magnitude of drag is greater in reverse flow over the entire cycle. The influence of the secondary dynamic stall vortex is also apparent in the lift and pitching moment curves near $|\alpha| = 15\,\text{deg}$.

4.4 Reverse Flow Dynamic Stall of a NACA 0012

4.4.1 Effect of Reynolds number

As was described in Section 1.3.4, the evolution of classical dynamic stall depends on both flow parameters (e.g., Re, Ma) and pitching kinematics (e.g., k, α_0, α_1). This section focuses on the effect of Reynolds number on reverse flow dynamic stall for a prescribed set of pitching kinematics. For classical dynamic stall, the influence of Reynolds number is relatively weak [42]. However, an increase in Reynolds number can delay the onset of flow separation and subsequent formation of the dynamic stall vortex. In reverse flow dynamic stall, it will be shown that the flowfield and unsteady airloads are independent of Reynolds number for $165,000 \leq Re \leq 500,000$.

Consider Figure 4.8(a) which shows phase-averaged velocity fields of a NACA 0012 airfoil undergoing reverse flow dynamic stall at three Reynolds numbers. The pitching kinematics are $-\alpha_{0,\text{rev}} = 10\,\text{deg}$, $\alpha_1 = 5\,\text{deg}$, and $k = 0.160$. Each velocity field shows the flow at $t/T = 0.4$, when the primary dynamic stall vortex has begun to convect away from the surface of the airfoil, inducing flow near the surface. The overall character of the flowfields is similar (especially near the surface of the airfoil) for these three Reynolds numbers. Figure 4.8(b) shows phase-averaged pressure distributions on the suction side of the airfoil at each Reynolds number. For the pitching kinematics considered in Figure 4.8, the trailing edge vortices and secondary dynamic stall vortices are weak; the primary dynamic stall vortex is the only dominant unsteady flow feature that affects the phase-averaged pressure and unsteady airloads. The pressure distributions in Figure 4.8(b) illustrate that the influence of the dynamic stall vortex on the surface pressure is nearly identical for all three Reynolds numbers tested. Figure 4.8(b) also shows that the unsteady lift curves are generally insensitive to Reynolds number; the drag and moment curves (not shown) are also insensitive to

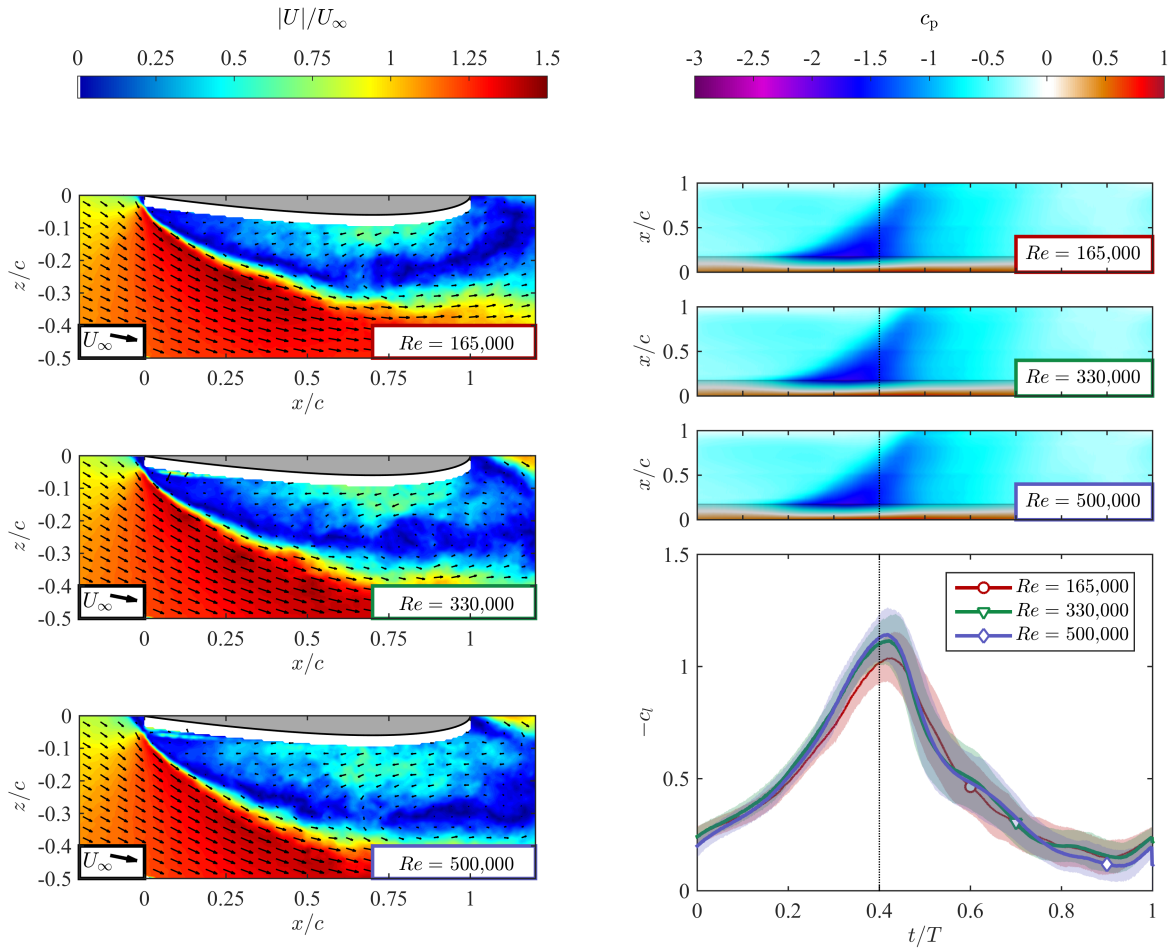

(a) Phase-averaged velocity fields at $t/T = 0.4$.

(b) Phase-averaged pressure distributions and unsteady lift.

Figure 4.8: Effect of Reynolds number on reverse flow dynamic stall of a NACA 0012 airfoil, $-\alpha_{0,\mathrm{rev}} = 10\,\mathrm{deg}$, $\alpha_1 = 5\,\mathrm{deg}$, $k = 0.160$.

Reynolds number.

The insensitivity of reverse flow dynamic stall to Reynolds number is rooted in the fact that the aerodynamic leading edge is sharp (rather than blunt). For classical dynamic stall, Reynolds number can influence the evolution of dynamic stall since an increase in Reynolds number directly affects boundary layer transition and separation over a blunt leading edge. However, in reverse flow, the sharp aerodynamic leading edge serves as the separation point on the suction side of the airfoil for $0 < \alpha_{\text{rev}} < 90\,\text{deg}$. Thus, the aerodynamics of reverse flow dynamic stall are generally independent of Reynolds number for a given set of pitching kinematics. Note that the reduced frequency of the results shown in Figure 4.8 is $k = 0.160$. Reynolds number independence has also been observed at $k = 0.100$ and all other values of α_0 and α_1 considered in the present work.

4.4.2 Effect of Reduced Frequency

Reduced frequency is well known to have a strong effect on classical dynamic stall (Section 1.3.4). An increase in reduced frequency delays the formation of the dynamic stall vortex due to a corresponding increase in effective induced camber [13], and delays recovery and reattachment of the flow [41]. Figure 4.9 shows this effect in prior work (Figure 4.9(a)) as well as the present work (Figure 4.9(b)). Note that in both figures, the first drop-off in lift occurs at a greater cycle phase with increasing k. In Figure 4.9(b), the flow reattaches near $t/T = 0.82$ for $k = 0.025$ as evidenced by the rapid reduction in $2\sigma(c_l)$. Flow reattachment occurs at $t/T = 0.9$ for $k = 0.100$ and at $t/T = 1.0$ for $k = 0.16$. This delay in reattachment results in lower values of lift with increasing k for $0.8 \leq t/T \leq 1$. The same trend is also observed in Figure 4.9(a).

With these behaviors in mind, the effect of reduced frequency on reverse flow dynamic stall is now considered. Figure 4.10 shows results for a NACA 0012 oscillating with the same mean pitch angle and pitch amplitude shown in Figure 4.8 (10 deg). Note that the

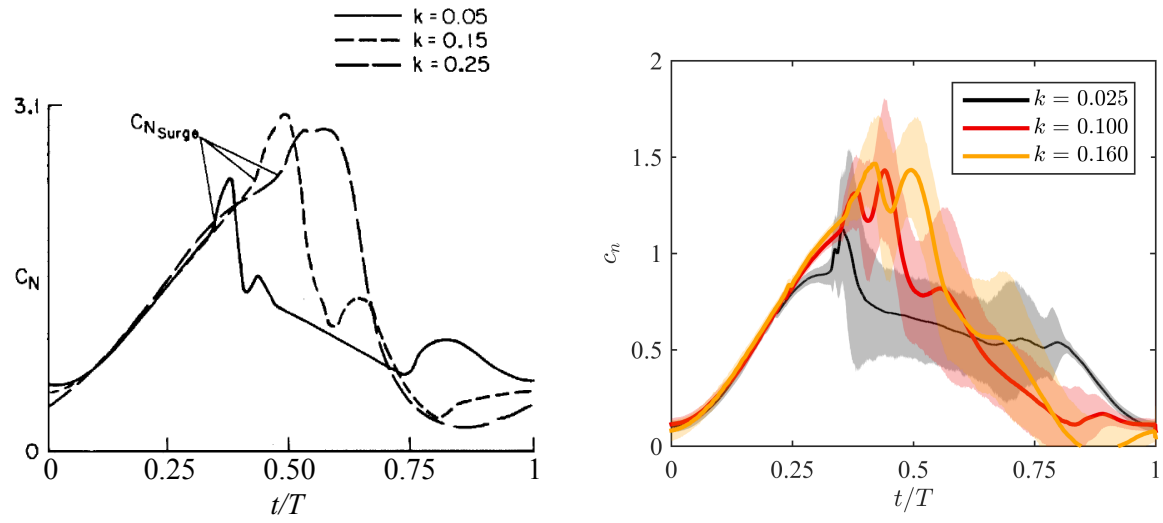

(a) McAllister et al., $\alpha_0 = 15\,\text{deg}$, $\alpha_1 = 10$, $Re = 2.5 \times 10^6$ [41].

(b) Present work, $\alpha_0 = 10\,\text{deg}$, $\alpha_1 = 10$, $Re = 5.0 \times 10^5$.

Figure 4.9: Effect of reduced frequency on classical dynamic stall of a NACA 0012.

Reynolds number of the results presented here differs for certain cases; this does not affect the trends of the results since reverse flow dynamic stall is insensitive to Reynolds number. Figure 4.10(a) shows pressure contour plots for five values of reduced frequency. As the reduced frequency is increased, there is a coupled *elongation* and *phase shift* of the pressure contour plots in the t/T-direction. To investigate whether these effects are driven by changes in the evolution of the dynamic stall vortex, Figure 4.10(b) shows phase-averaged velocity fields at four corresponding reduced frequencies. All velocity fields are taken at $t/T = 0.5$ (indicated with dotted lines in Figure 4.10(a)). Indeed, the flowfields are markedly different. Focus first on the velocity field with $k = 0.511$. Here the primary dynamic stall vortex is in its early stages of formation and centered near $x/c = 0.35$. Next, consider the velocity field with a lower reduced frequency of $k = 0.309$. The dynamic stall vortex here is "older" (in terms of t/T), having convected to $x/c = 0.75$. At even lower reduced frequencies $k = 0.217$ and $k = 0.160$, the dynamic stall vortex has convected further into the wake indicating a greater vortex age (again, in terms of t/T).

The elongation of the pressure contour plots in Figure 4.10(a) is primarily driven

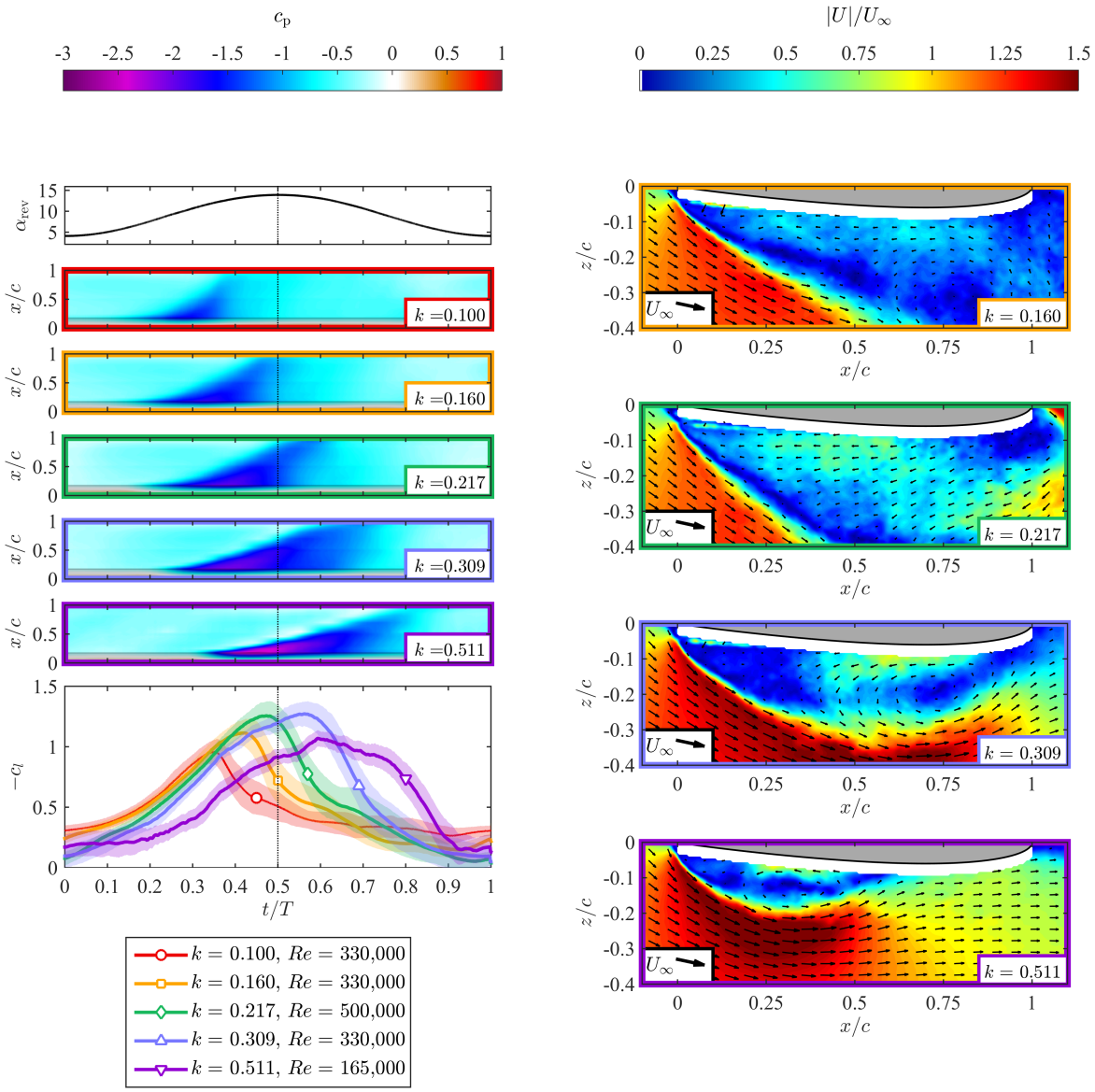

(a) Angle of attack, phase-averaged pressure distributions, and unsteady lift.

(b) Phase-averaged velocity fields at $t/T = 0.5$

Figure 4.10: Effect of reduced frequency on reverse flow dynamic stall of a NACA 0012 airfoil, $-\alpha_{0,\mathrm{rev}} = 10\,\mathrm{deg}$, $\alpha_1 = 5\,\mathrm{deg}$.

by the decreased period (in seconds) of a pitching cycle with increased reduced frequency. However, the convection speed of the dynamic stall vortex (and associated wave of low pressure) stays relatively constant with reduced frequency. This is evidenced by the decrease in the slope of the "edge" of the low pressure wave in the contour plots of Figure 4.10(a), and in the decreasing non-dimensional "age" of the vortex observed in the velocity fields of Figure 4.10(b).

A secondary contribution to the phase shift can also be observed in the pressure contour plots. The initial edge (at $x/c = 0.175$) of the measured low pressure wave associated with the dynamic stall vortex occurs at greater values of t/T with increasing reduced frequency. For example, the initial edge of the low pressure wave occurs near $t/T = 0.16$ for $k = 0.100$ and near $t/T = 0.32$ for $k = 0.511$. The decrease in cycle period with reduced frequency contributes to the phase shift of low pressure observed at $x/c = 0.175$, but the velocity induced by pitching also plays a role.

Quasi-steady thin airfoil theory suggests that unsteady airfoil motion results in a change in the effective angle of attack, α_{eff} seen by the airfoil. The effective angle of attack depends on the geometric angle of attack, α, the heave rate, $\dot{h}$, and the pitch rate, $\dot{\alpha}$:

$$\alpha_{\text{eff}} = \alpha + \frac{\dot{h}}{U_\infty} + b\left(\frac{1}{2} - a\right)\frac{\dot{\alpha}}{U_\infty} \tag{4.2}$$

Here, b is the semi-chord and a is the distance between the pitching axis and the mid-chord. Thus, for pitching in reverse flow without heave, $a = 1/2$ and quasi-steady thin airfoil theory states that $\alpha_{\text{eff}} = \alpha$. However, quasi-steady thin airfoil theory assumes attached flow. The flow over an airfoil in reverse flow has been shown to separate at low angles of attack. A different model of the influence of pitching on the effective angle of attack is needed.

Figure 4.11 illustrates a simple calculation of the effective angle of attack using the induced velocity at the sharp leading edge (w_{LE}) since the flow always separates here. Fig-

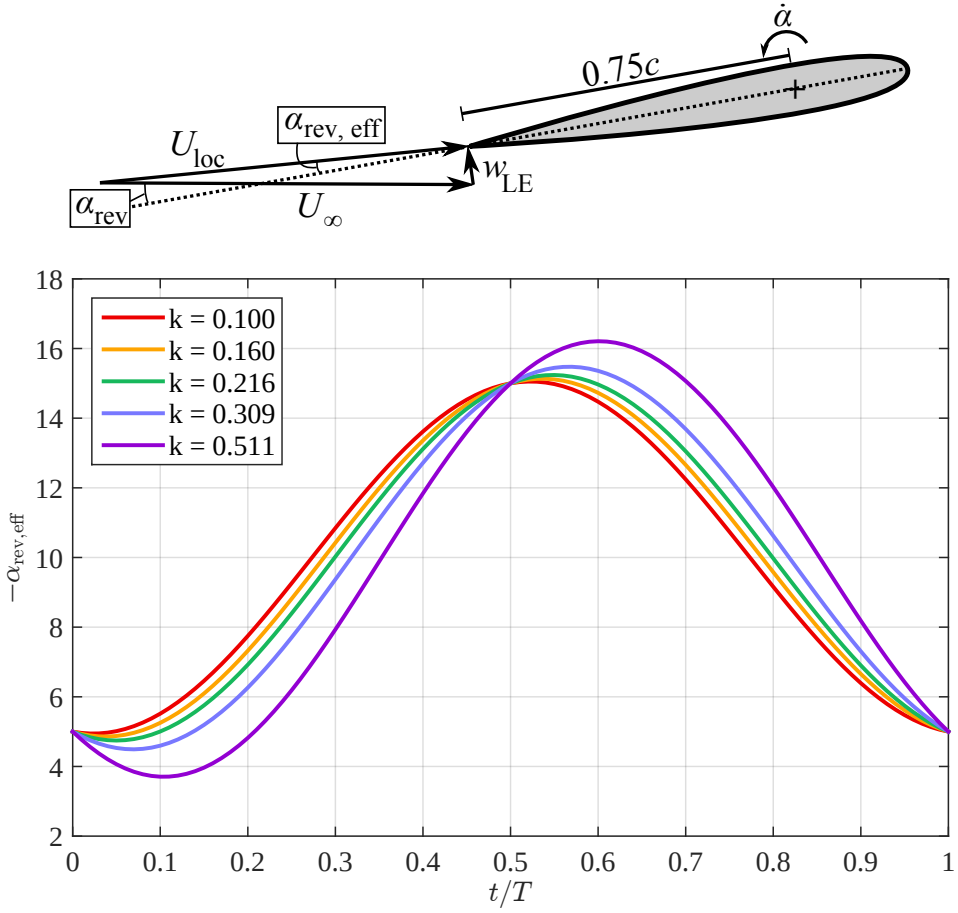

Figure 4.11: Analytical model of the effective reverse flow angle of attack, $-\alpha_{\text{rev,eff}}$, and its dependence on reduced frequency for $-\alpha_{0,\text{rev}} = 10$ deg and $\alpha_1 = 5\,\text{deg}$.

ure 4.11 shows that for any phase $0 \leq t/T \leq 0.5$, the effective angle of attack decreases with reduced frequency but that this trend is greatest for $0.1 \leq t/T \leq 0.4$. This suggests that the onset of massive flow separation and subsequent development of the reverse flow dynamic stall vortex would be delayed with increasing reduced frequency, consistent with the phase shift of the start of the low pressure pressure waves observed in Figure 4.10(a).

The shorter cycle time and reduced effective angle of attack also lead to a third effect of reduced frequency on reverse flow dynamic stall: the delayed propagation of flow separation from the leading edge towards the trailing edge. Consider Figure 4.12 which shows two phase-averaged flowfields. In the upper contour, the flowfield for $k = 0.160$ is shown at $t/T = 0.22$. The early formation of a dynamic stall can be seen, with separated flow over $0 \leq x/c \leq 0.5$. The lower contour shows the flowfield for $k = 0.511$ at $t/T = 0.50$. Here, the region of separated flow is approximately the same as the upper contour, suggesting that the dynamic stall vortices are at similar ages (in terms of t/T). However, this has been delayed to $t/T = 0.50$ at $k = 0.511$ (over one-quarter of a cycle later than at $k = 0.160$). As a result, the angle of attack is greater at $k = 0.511$ (note that the angle of attack model in Figure 4.11 predicts $\alpha_{\text{eff}} = \alpha$ at $t/T = 0.5$ for all reduced frequencies since $\dot{\alpha} = 0$ here). The leading edge shear layer curves further away from the airfoil than at $k = 0.160$, suggesting that the angle of attack is in fact greater for $k = 0.511$. This creates a visibly stronger dynamic stall vortex. The increase in dynamic stall vortex strength with reduced frequency can also be seen in the pressure contour plots of Figure 4.10(a). For example, purple regions of $c_p \approx -2.5$ are present near the leading edge for the greatest reduced frequencies tested, $k = 0.309$ and $k = 0.511$. Note that the region of lowest pressure for $k = 0.511$ develops over $0.4 \leq t/T \leq 0.55$ when the induced velocity, w_{LE}, is low and $\alpha_{\text{eff}} \approx \alpha$.

In summary, the *elongation* of the pressure contour plots is a result of the shorter cycle period coupled with nearly constant pressure wave speed. The additional *phase shift* of the pressure contour plots is a result of the reduction of the effective angle of attack during

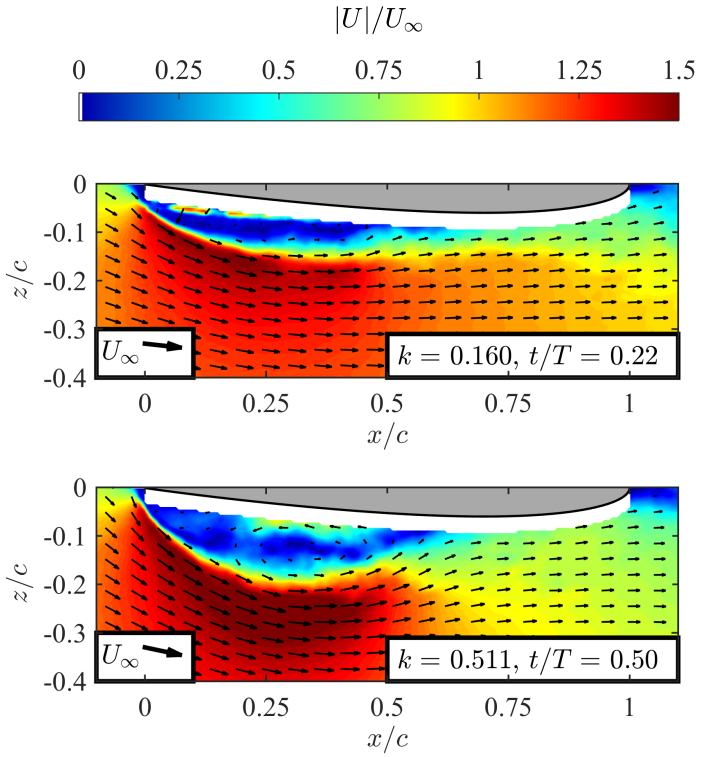

Figure 4.12: Effect of reduced frequency on the strength of the dynamic stall vortex.

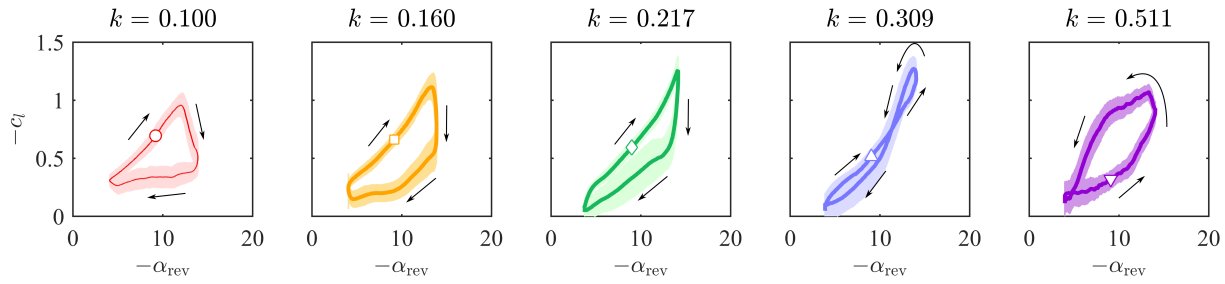

Figure 4.13: Unsteady lift hysteresis loops for a NACA 0012, $-\alpha_{0,\text{rev}} = 10\,\text{deg}$, $\alpha_1 = 5\,\text{deg}$.

the first half of the pitching cycle. Collectively, this allows for the formation of a *stronger* dynamic stall vortex at greater reduced frequencies since its formation is delayed to a greater angles of attack.

These three effects of reduced frequency collectively influence the trends of unsteady lift curves in Figure 4.10(a). In general, there is a phase shift and widening of the lift curves with increasing reduced frequency. The maximum lift also increases with reduced frequency for $0.160 \leq k \leq 0.309$, consistent with the increased strength of the dynamic stall vortex and delay of its formation. The maximum lift declines for $k = 0.511$; here the dynamic stall vortex forms so late in the cycle that its maximum influence (i.e., the phase at which the low pressure wave affects nearly the entire chord) occurs near $t/t = 0.75$, at which point the angle of attack is decreasing through the mean pitch angle. Figure 4.13 shows the dependence of unsteady lift with respect to angle of attack rather than cycle phase. At $k = 0.100$, lift increases nearly linearly before a rapid decrease near $\alpha_{\text{rev}} = 12\,\text{deg}$. Lift decreases slightly as the angle of attack is decreased towards the end of the cycle. This pattern gives a clockwise hysteresis loop. As reduced frequency is increased, the maximum lift increases, along with the angle of attack at which maximum lift occurs. The hysteresis loop also narrows with increasing reduced frequency. At $k = 0.309$, the hysteresis loop forms a figure-8 with an increase in lift as the second half of the pitch cycle begins; recall that similar behavior was seen for classical dynamic stall in Figure 1.19 [38, 41]. At $k = 0.511$, the hysteresis loop

Table 4.1: Flow features observed in each type of reverse flow dynamic stall. DSV: Dynamic Stall Vortex. TEV: Trailing Edge Vortex.

	Primary DSV	Primary TEV	Secondary DSV	Secondary TEV
Type I	✓			
Type II	✓	✓		
Type III	✓	✓	✓	
Type IV	✓	✓	✓	✓

resembles the shape of the hysteresis loop at $k = 0.160$, but is directed *counter-clockwise*. As reduced frequency is increased, the changes in the behavior of the lift curve are due to the collective influence of the decreased cycle period, decreased effective angle of attack during the early portions of the pitching cycle, and delay of the formation of the dynamic stall vortex until greater angles of attack.

4.4.3 Effect of Mean Pitch Angle and Pitch Amplitude

The variations of mean pitch angle and pitch amplitude also strongly affect the evolution of reverse flow dynamic stall. Figures 4.8 and 4.10 showed that a primary dynamic stall vortex is the only dominant unsteady flow feature for a nominal pitch amplitude of $-\alpha_{0,\text{rev}} = 10\,\text{deg}$ and pitch amplitude of $\alpha_1 = 5\,\text{deg}$. However, multiple unsteady flow features can form with a greater pitch amplitude of $\alpha_1 = 10\,\text{deg}$ (Figure 4.3(b)). This suggests that several types of reverse flow dynamic stall exist and that the observed case depends on the pitching kinematics (e.g., k, $-\alpha_{0,\text{rev}}$, and α_1). In the present work, four types of reverse flow dynamic stall have been observed for the NACA 0012. Table 4.1 summarizes the flow features present in each type of reverse flow dynamic stall, where the type corresponds to the total number of vortices observed during the pitching cycle.

Figure 4.14 explores the Type IV dynamic stall to illustrate the flow features and their footprints in the phase-averaged pressure contour plots. Similar (but fewer) features are observed for Types I-III of reverse flow dynamic stall. The Type IV dynamic stall shown

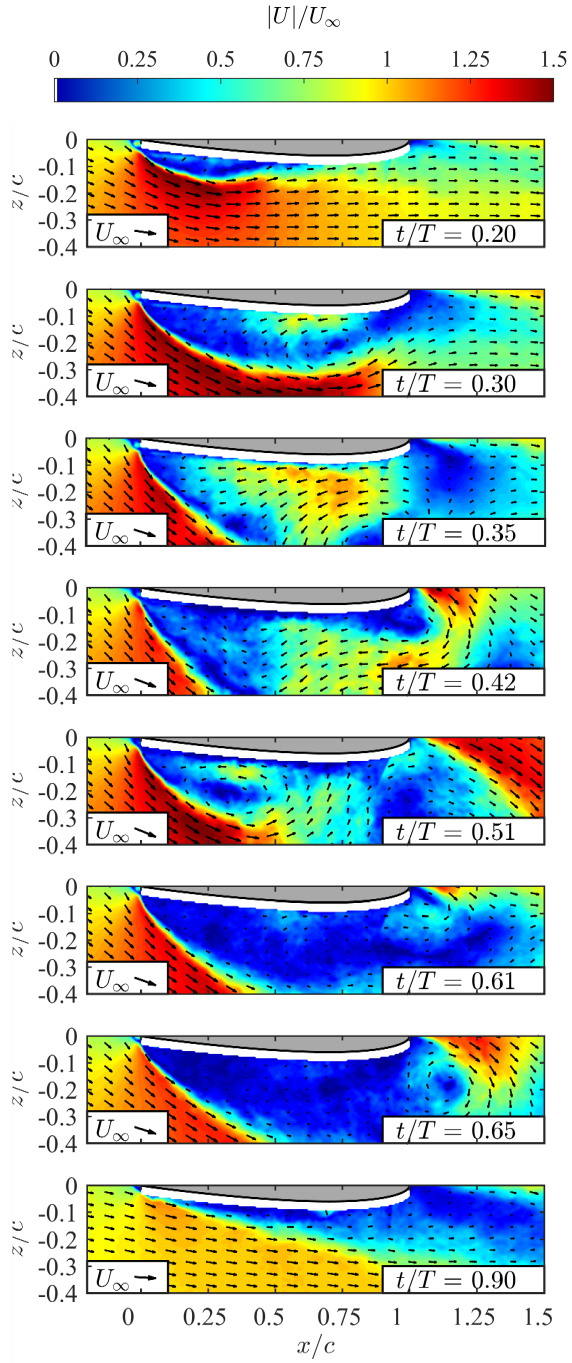

(a) Phase-averaged velocity fields (10 cycles).

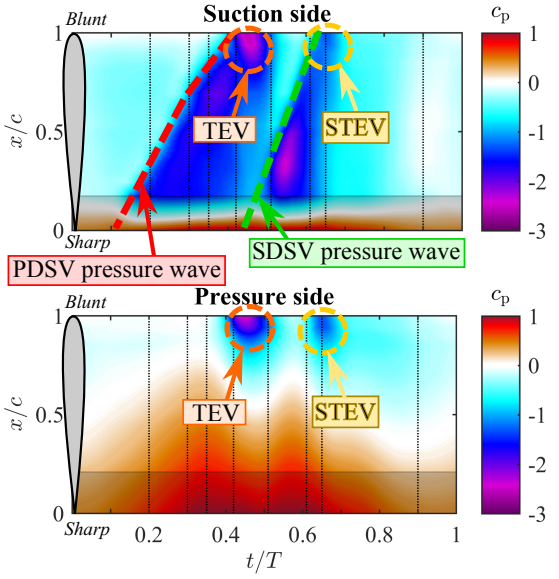

(b) Phase-averaged pressure distribution.

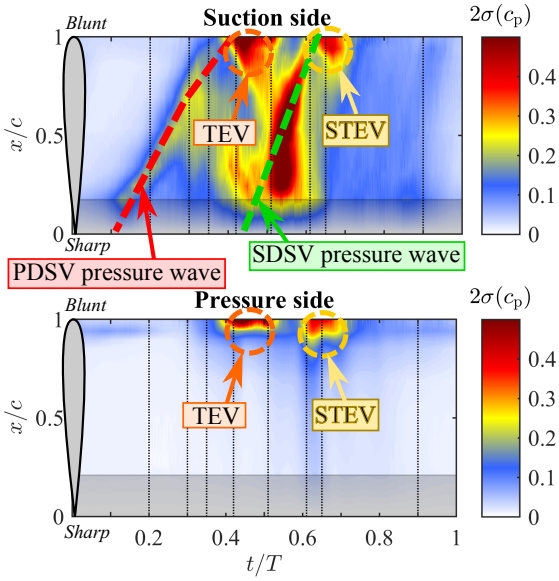

(c) Distribution of pressure fluctuations.

Figure 4.14: NACA 0012, $-\alpha_{0,\mathrm{rev}} = 15\,\mathrm{deg}$, $\alpha_1 = 10\,\mathrm{deg}$, $Re = 330{,}000$, $k = 0.160$.

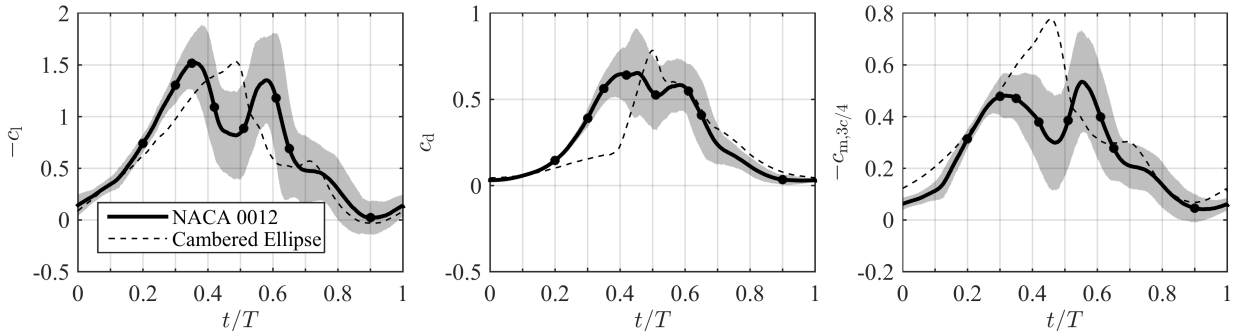

Figure 4.15: Unsteady airloads of the NACA 0012 and cambered ellipse with $-\alpha_{0,\mathrm{rev}} = 15\,\mathrm{deg}$, $\alpha_1 = 10\,\mathrm{deg}$, $Re = 330{,}000$, $k = 0.160$. The lines represent the phase-average, shaded regions represents $2\sigma(c_\mathrm{x})$.

in Figure 4.14 occurs for a larger mean pitch angle and pitch amplitude ($-\alpha_{0,\mathrm{rev}} = 15\,\mathrm{deg}$, $\alpha_1 = 10\,\mathrm{deg}$). Figure 4.14(a) shows the phase averaged velocity fields at selected phases. Figures 4.14(b) and 4.14(c) show the phase-averaged pressure and pressure fluctuation distributions, respectively, for both the suction side and pressure sides of the airfoil; the vertical black lines correspond with the phases in Figure 4.14(a). Figure 4.15 shows the unsteady airloads as a function of cycle phase; the black dots also correspond with the phases in Figure 4.14(a). The velocity fields at $t/T = 0.20$, $t/T = 0.30$, and $t/T = 0.35$ show the formation, growth, and convection of the primary dynamic stall vortex. This results in a growing region of low pressure over the suction side of the airfoil and an increase in the airloads. At $t/T = 0.42$, the primary dynamic stall vortex induces the formation of the primary trailing edge vortex. Note that this results in low pressure near the trailing edge on both sides of the airfoil and a corresponding decrease in lift and pitching moment. At $t/T = 0.51$, the secondary dynamic stall vortex has formed and grown to induce flow over the first half of the chord. The resulting low pressure on the suction side of the airfoil leads to a second peak in lift. At $t/T = 0.61$ and $t/T = 0.65$, the secondary trailing edge vortex forms and decreases the pressure near the trailing edge on both sides of the airfoil, leading to a decrease in airloads. The flow remains separated for the remainder of the cycle ($t/T = 0.9$); partial

reattachment occurs at $t/T = 1$.

The remainder of this section considers the effect of varying mean pitch angle and pitch amplitude on the type of reverse flow dynamic stall. Figure 4.10 shows that a Type I reverse flow dynamic stall is present for a nominal pitch amplitude of $-\alpha_{0,\text{rev}} = 10\,\text{deg}$ and pitch amplitude of $\alpha_1 = 5\,\text{deg}$ at all reduced frequencies considered. Figure 4.16 shows results for a lower nominal mean pitch angle of $-\alpha_{0,\text{rev}} = 5\,\text{deg}$. This also leads to a Type I reverse flow dynamic stall, but the dynamic stall vortex is weaker and quickly diffuses (flowfields not shown). As a result, the low pressure wave associated with the primary dynamic stall vortex does not influence $0.4 \leq x/c \leq 1$. Note that there is an elongation, phase shift, and intensification of the pressure contours with increasing reduced frequency for $0.100 \leq k \leq 0.309$. Also, note that the dynamic stall vortex forms and convects at a later time in the pitching cycle than in Figure 4.10(a) due to the lower mean pitch angle. In fact, this delay leads to a weaker pressure wave at $k = 0.511$.

Figure 4.17 shows results for a greater nominal mean pitch angle of $-\alpha_{0,\text{rev}} = 15\,\text{deg}$ (still with a nominal pitch amplitude of $\alpha_1 = 5\,\text{deg}$). A weak Type I reverse flow dynamic stall is observed in the pressure contour plots for $k = 0.100$ and $k = 0.160$. The large mean pitch angle results in the flow being fully separated during the entire cycle (velocity field measurements were acquired for $k = 0.160$, but are not shown). As a result of the flow being fully separated, the primary dynamic stall vortices that form at $k = 0.100$ and $k = 0.160$ are weaker than those that form at a lower mean pitch angle (e.g., Figure 4.10(a)). For $k = 0.217$ and $k = 0.309$, a Type III reverse flow dynamic stall is observed. A Type I reverse flow dynamic stall vortex is present at $k = 0.511$. Due to the short cycle period, the primary dynamic stall vortex sheds late, near $t/T = 0.8$, which prevents the formation of a trailing edge vortex. However, it is worth noting that the flow partially reattaches for $k = 0.511$ due to the lower effective angle of attack during the first half of the pitching cycle (similar to Figure 4.11) and the increased curvature of the leading edge shear layer

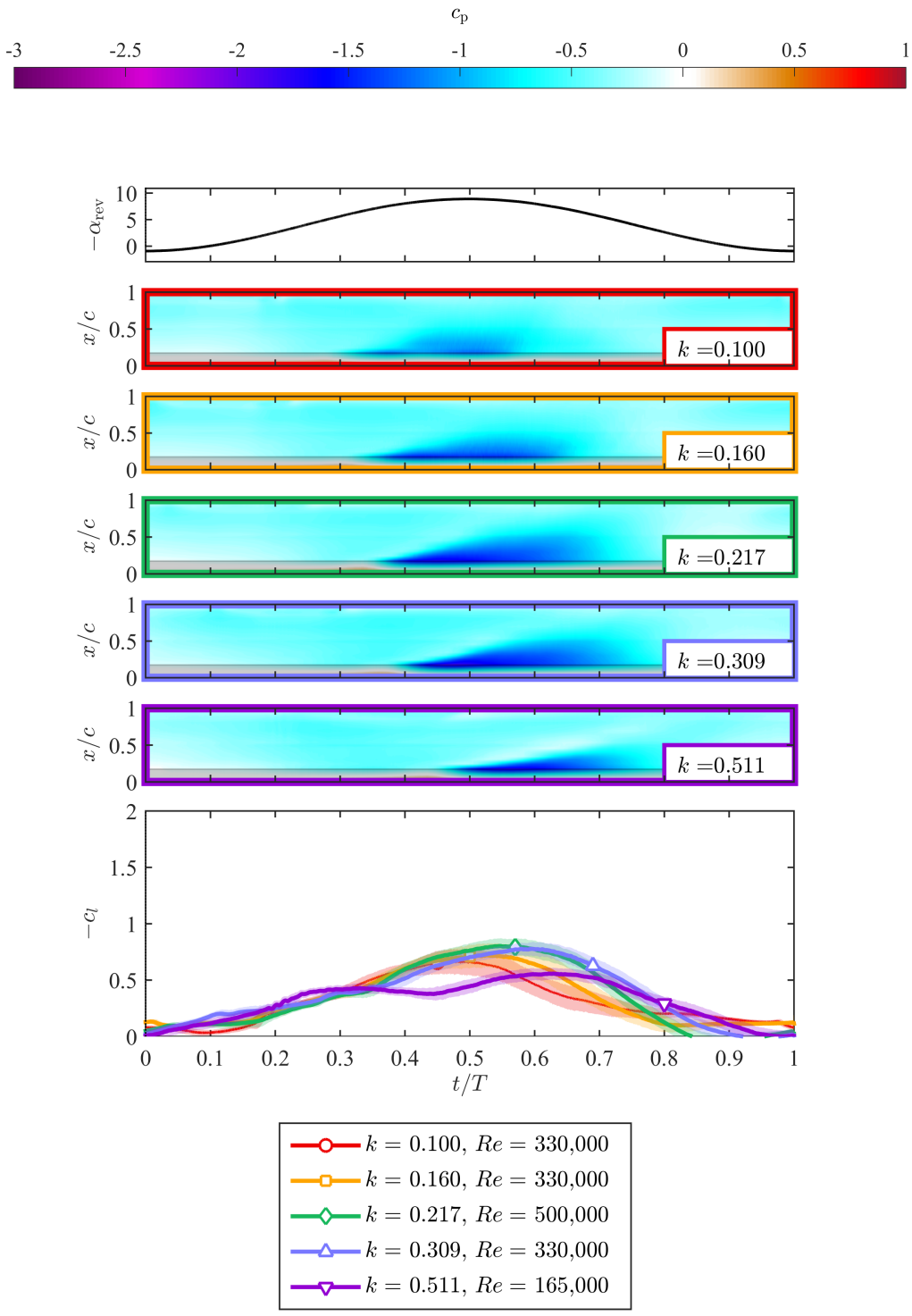

Figure 4.16: Effect of reduced frequency on reverse flow dynamic stall of a NACA 0012 airfoil, $-\alpha_{0,\text{rev}} = 5\,\text{deg}$ and $\alpha_1 = 5\,\text{deg}$.

(similar to Figure 4.12). Considering the pressure contour plots in Figure 4.17 at all reduced frequencies, it can be seen that the pressure wave begins and convects much earlier in the pitching cycle compared to cases with lower mean pitch angles (Figures 4.10(a) and 4.16). Figure 4.17 also shows that the three reduced frequency effects described in Section 4.4.2 are also present for this mean pitch angle and pitch amplitude.

Next, oscillations with a nominal mean pitch angle of $-\alpha_{0,\text{rev}} = 10\,\text{deg}$ and a larger nominal pitch amplitude of $\alpha_1 = 10\,\text{deg}$ are considered. Figure 4.18 shows the reduced frequency effects for these pitching kinematics. The three reduced frequency effects can again be seen in the pressure contour plots (elongation, phase shift, and strengthening of the primary reverse flow dynamic stall vortex). In general, the unsteady features are stronger with the greater pitch amplitude. A Type III reverse flow dynamic stall is observed for $0.100 \leq k \leq 0.217$. The stall type degrades to a Type II and Type I at $k = 0.309$ and $k = 0.511$ as the cycle period shortens. Figure 4.18 also shows the strong influence of the primary trailing edge vortex and secondary dynamic stall vortex on the unsteady lift curves. Focusing on $k = 0.160$, the primary trailing edge vortex acts to reduce lift near $t/T = 0.55$ and the secondary dynamic stall vortex enhances lift a short time later at $t/T = 0.63$. Recall that this case was also presented in Figures 4.3-4.7.

The final set of pitching kinematics considered in the present work is a larger nominal mean pitch angle of $-\alpha_{0,\text{rev}} = 15\,\text{deg}$ with the same nominal pitch amplitude of $\alpha_1 = 10\,\text{deg}$. Figures 4.14 and 4.15 illustrated the Type IV reverse flow dynamic stall observed at $k = 0.160$. Figure 4.19 shows the effects of reduced frequency. In general, the primary dynamic stall vortex forms earlier in the cycle with $-\alpha_{0,\text{rev}} = 15\,\text{deg}$ than with $-\alpha_{0,\text{rev}} = 10\,\text{deg}$ (Figure 4.18). This is similar to the behavior observed for increasing the mean pitch angle with the lower pitch amplitude of $\alpha_1 = 5\,\text{deg}$ (Figures 4.16, 4.10(a), and 4.17). Comparing Figures 4.18 and 4.19, the earlier formation of the primary dynamic stall vortex in Figure 4.19 leads to stronger trailing edge vortices and secondary dynamic stall vortices, if present. This is

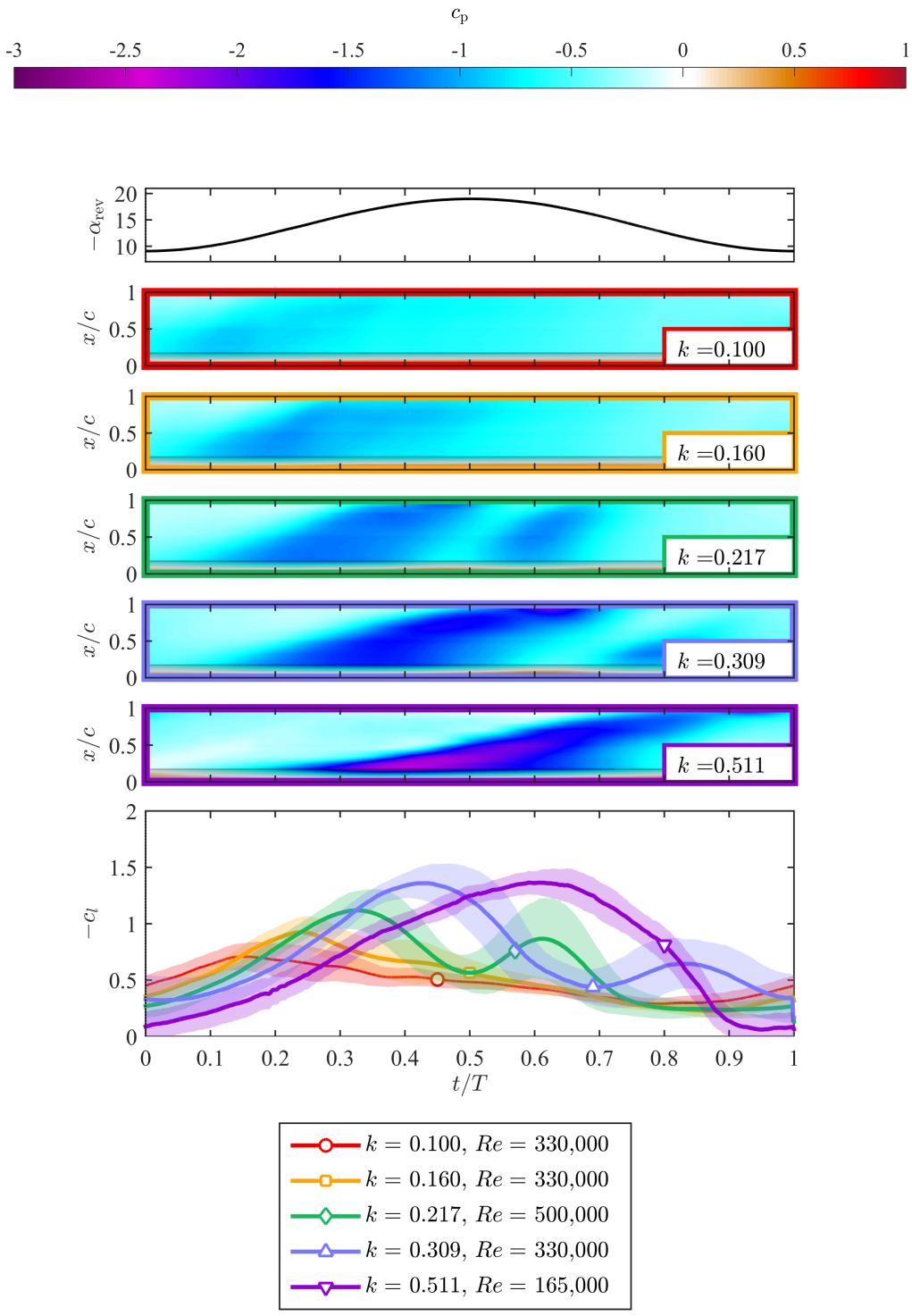

Figure 4.17: Effect of reduced frequency on reverse flow dynamic stall of a NACA 0012 airfoil, $-\alpha_{0,\text{rev}} = 15\,\text{deg}$ and $\alpha_1 = 5\,\text{deg}$.

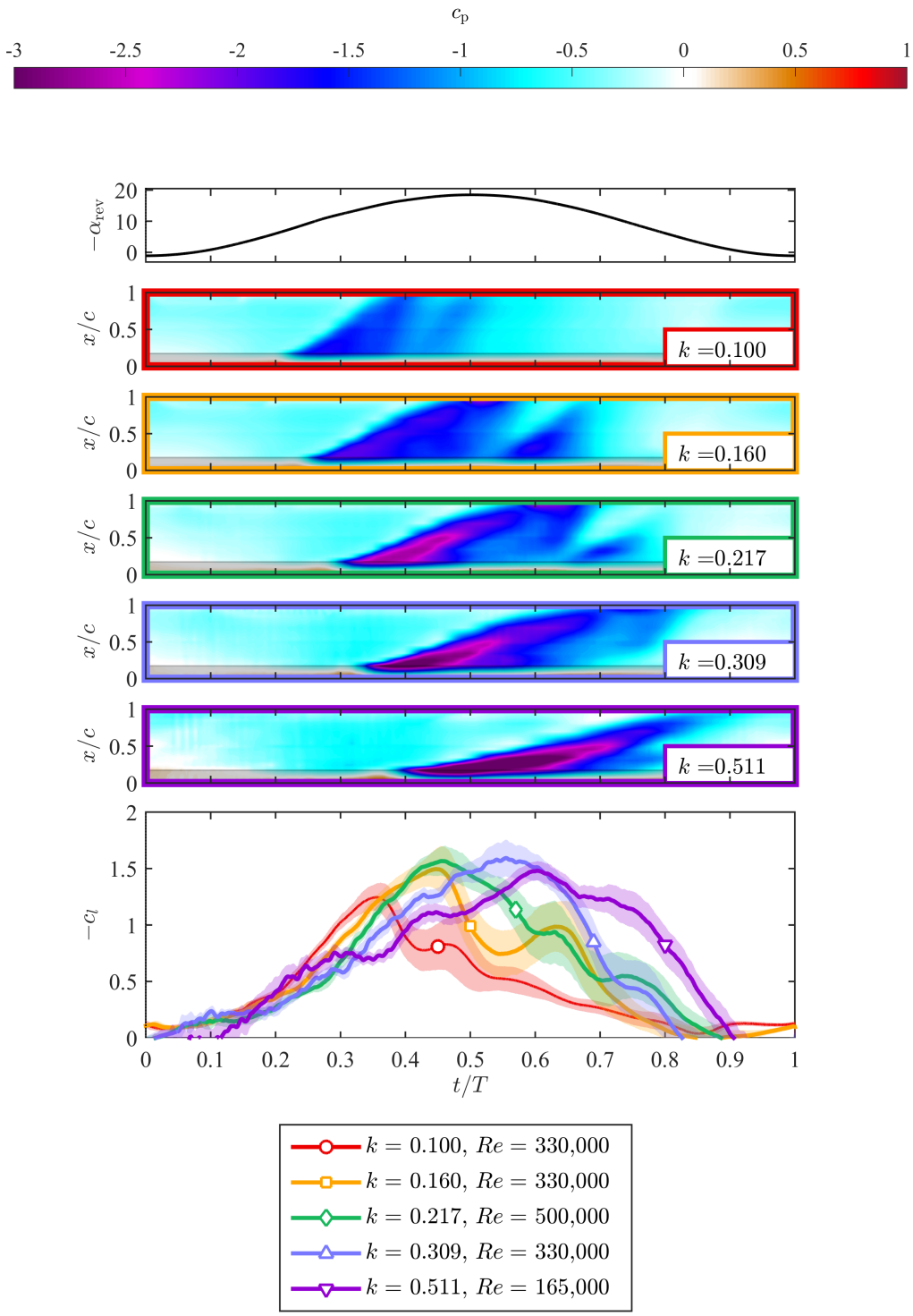

Figure 4.18: Effect of reduced frequency on reverse flow dynamic stall of a NACA 0012 airfoil, $-\alpha_{0,\text{rev}} = 10\,\text{deg}$ and $\alpha_1 = 10\,\text{deg}$.

Table 4.2: Types of reverse flow dynamic stall observed for a NACA 0012 subject to various pitching kinematics. Sep.: flow is fully separated for the duration of the pitching cycle.

	$\alpha_1 = 5\,\text{deg}$			$\alpha_1 = 10\,\text{deg}$	
k	$-\alpha_{0,\text{rev}} = 5\,\text{deg}$	$10\,\text{deg}$	$15\,\text{deg}$	$10\,\text{deg}$	$15\,\text{deg}$
0.100	I	I	I (Sep.)	III	IV
0.160	I	I	I (Sep.)	III	IV
0.217	I	I	III (Sep.)	III	III
0.309	I	I	III (Sep.)	II	II
0.511	I	I	II	I	II

evidenced in the pressure contour plots of Figure 4.19 as a greater amount of suction.

Table 4.2 summarizes the types of reverse flow dynamic stall observed on a NACA 0012 airfoil for the cases considered in the present work. Note that a Type I stall is observed for nominal mean pitch angles of $-\alpha_{0,\text{rev}} = 5, 10\,\text{deg}$ and a nominal pitch amplitude of $\alpha_1 = 5\,\text{deg}$. The stall grade generally increases with greater values of $-\alpha_{0,\text{rev}}$ and α_1. The stall grade also generally decreases with increasing reduced frequency due to the shorter cycle period.

4.5 Reverse Flow Dynamic Stall of a Cambered Elliptical Airfoil

The preceding sections of this chapter focused on the dynamic stall characteristics of a NACA 0012 airfoil, a representative example of a *conventional* rotor blade airfoil section. This section examines the reverse flow dynamic stall characteristics of a cambered elliptical airfoil, a *modern* airfoil section similar to those that have been used near the blade root on recent high-speed helicopters (Figure 1.6). It will be shown that the shape of the geometric trailing edge of an airfoil is the primary driver of the aerodynamic behavior in reverse flow dynamic stall.

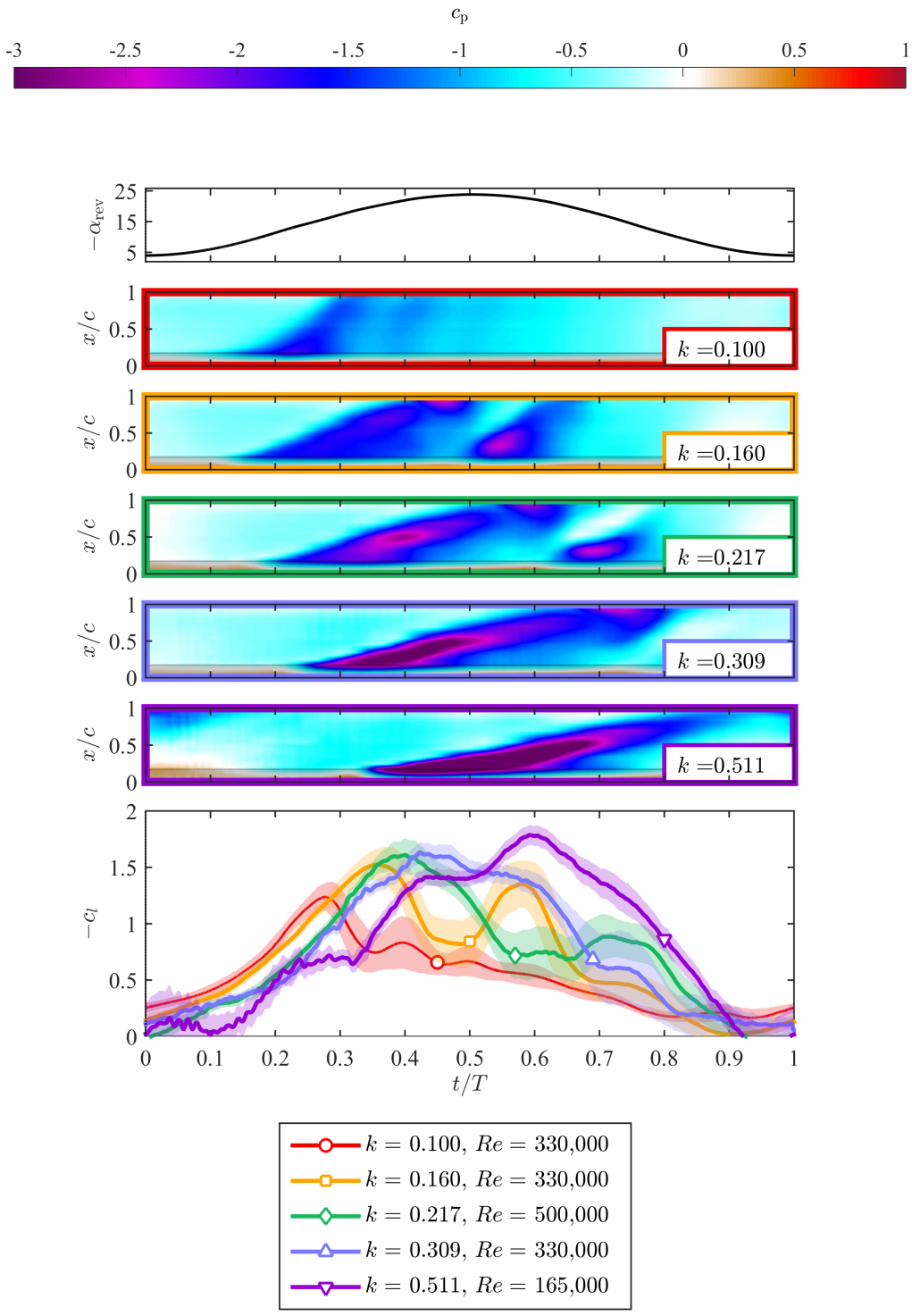

Figure 4.19: Effect of reduced frequency on reverse flow dynamic stall of a NACA 0012 airfoil, $-\alpha_{0,\text{rev}} = 15\,\text{deg}$ and $\alpha_1 = 10\,\text{deg}$.

4.5.1 Dynamic Stall Types

While oscillating in reverse flow, the cambered elliptical airfoil behaves similar to a conventional airfoil oscillating in forward flow due to its blunt geometric trailing edge (aerodynamic leading edge). Unlike the NACA 0012 airfoil, the cambered elliptical airfoil undergoes "light" dynamic stall in reverse flow for a wide range of pitching kinematics and flow conditions. Light dynamic stall is characterized by partial flow separation from the suction side of the airfoil resulting in increased drag, but also lift that is greater than corresponding static values [42]. Figure 4.20 shows an example of the cambered elliptical airfoil undergoing light dynamic stall. As the cycle progresses from $t/T = 0.21$ to $t/T = 0.51$, Figure 4.20(a) shows that the flow over the suction side is characterized by a region of increasing velocity near the leading edge as well as forward movement of a separation point along the suction side from $x/c = 0.95$ to $x/c = 0.5$. As the pitching cycle continues to $t/T = 0.61$, the separation point continues upstream to $x/c = 0.25$. Although the angle of attack decreases during this portion of the cycle, Figre 4.20(b) shows that the separation point continues to move upstream due to the presence of an adverse pressure gradient over $0 \leq x/c \leq 0.25$. As the cycle progresses through $t/T = 0.66$ and $t/T = 0.72$, the reduction in the adverse pressure gradient caused by the decrease in velocity near the leading edge arrests the motion of the separation point. The pressure gradient becomes less adverse ($t/T = 0.81$), which allows the flow to begin to reattach over an increasing portion of the suction side of the airfoil. Figure 4.22(a) shows the unsteady airloads for this case with the selected phases indicated with circular markers. Note the relatively smooth increase and decrease in lift and pitching moment. Also note that the drag is significantly lower compared to the NACA 0012 since the flow never fully separates. However, this does result in a greater pitching moment for $0.4 \leq t/T \leq 0.65$.

It is important to note that the example of light dynamic stall given in Figure 4.20

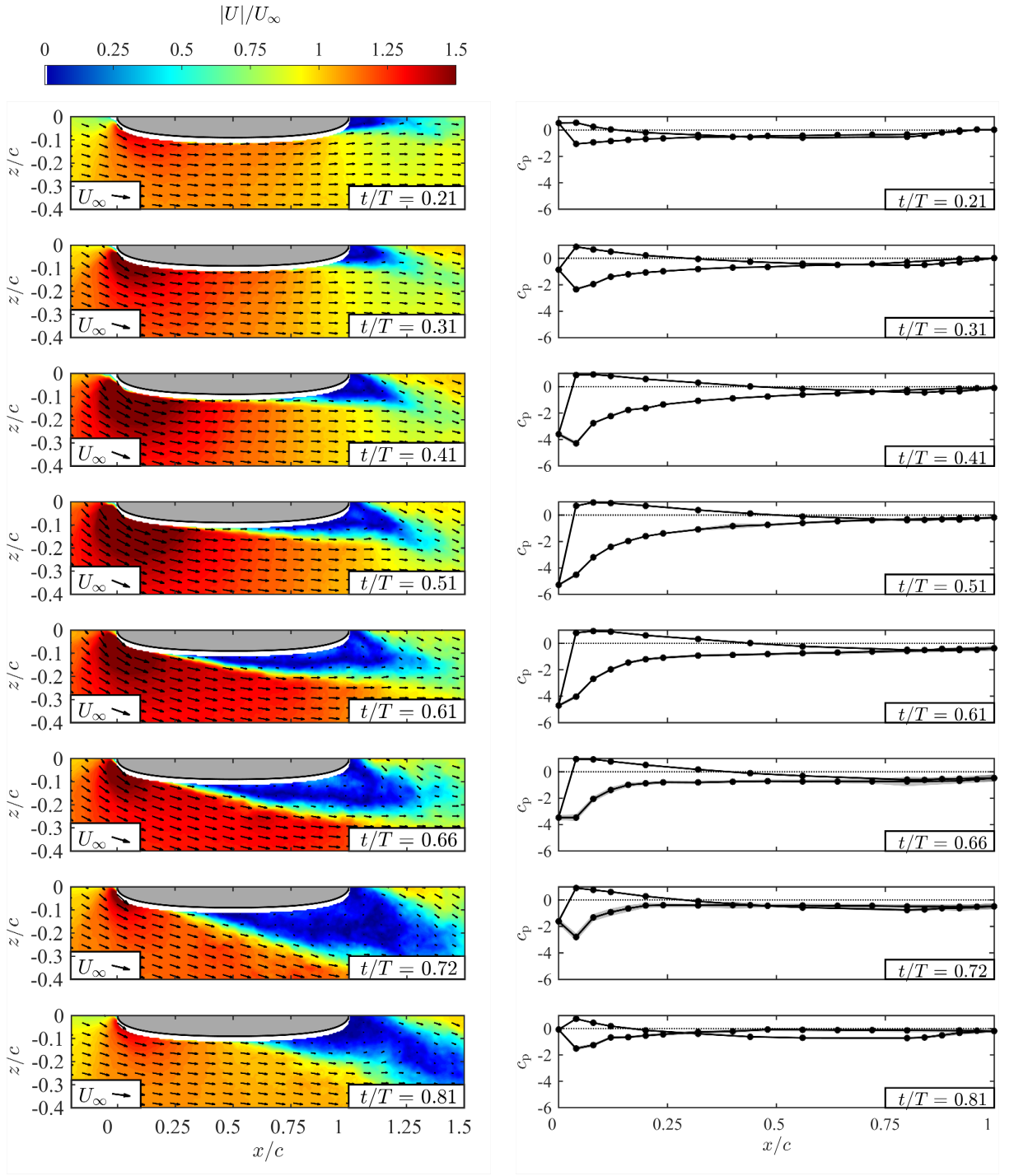

(a) Phase-averaged velocity fields.

(b) Phase-averaged pressure distributions.

Figure 4.20: Light dynamic stall of a cambered elliptical airfoil in reverse flow. $Re = 500,000$, $-\alpha_{0,\text{rev}} = 10\,\text{deg}$, $\alpha_0 = 10\,\text{deg}$, $k = 0.160$

shows a large amount of flow separation from the suction side of the airfoil; flow is separated over three-quarters of the airfoil for a portion of the pitching cycle. This is a result of the large mean pitch angle and pitch amplitude ($-\alpha_{0,\text{rev}} = 10\,\text{deg}$, $\alpha_0 = 10\,\text{deg}$). The amount of flow separation during light stall (and resulting influence on unsteady airloads) is strongly dependent on mean pitch angle and pitch amplitude, and weakly dependent on Reynolds number and reduced frequency. This will be explored in depth in subsequent sections.

If the pitching kinematics are severe enough, the cambered elliptical airfoil can exhibit characteristics of deep dynamic stall. Figure 4.21 shows an example of this with $-\alpha_{0,\text{rev}} = 15\,\text{deg}$ and $\alpha_0 = 10\,\text{deg}$. In the early portion of the cycle, Figure 4.21(a) shows that the separation point moves towards the leading edge, positioned near $x/c = 0.4$ at $t/T = 0.41$. The flow separates and a dynamic stall vortex begins to form at $t/T = 0.48$. The vortex is clearly visible at $t/T = 0.52$ as it induces flow near the surface, leading to a lower pressure over $0 \leq x/c \leq 0.5$ (Figure 4.21(b)). The vortex convects downstream and away from the airfoil at $t/T = 0.56$, leading to lower pressure along the aft portion of the airfoil. A weak trailing edge vortex can be seen at $t/T = 0.61$, but its influence on the unsteady pressure distribution is insignificant; hence, this is categorized as a Type I dynamic stall. Flow begins to reattach as the cycle progresses through $t/T = 0.76$ and $t/T = 0.91$. Figure 4.22(b) shows the resulting unsteady airloads. Lift increases nearly linearly until the formation of the dynamic stall vortex begins near $t/T = 0.48$. Note the corresponding rapid increase in drag associated with the early stages of dynamic stall vortex formation. Maximum lift occurs a short time later at $t/T = 0.51$ before decreasing as the dynamic stall vortex convects into the wake. The 2σ-variation of the unsteady airloads is greatest from $0.48 \leq t/T \leq 1$ due to massive flow separation and aperiodicity. Note that the maximum airloads are greater for the cambered elliptical airfoil than the NACA 0012 because of the delayed formation of the dynamic stall vortex.

In summary, the cambered elliptical airfoil leads to light dynamic stall for a wide range

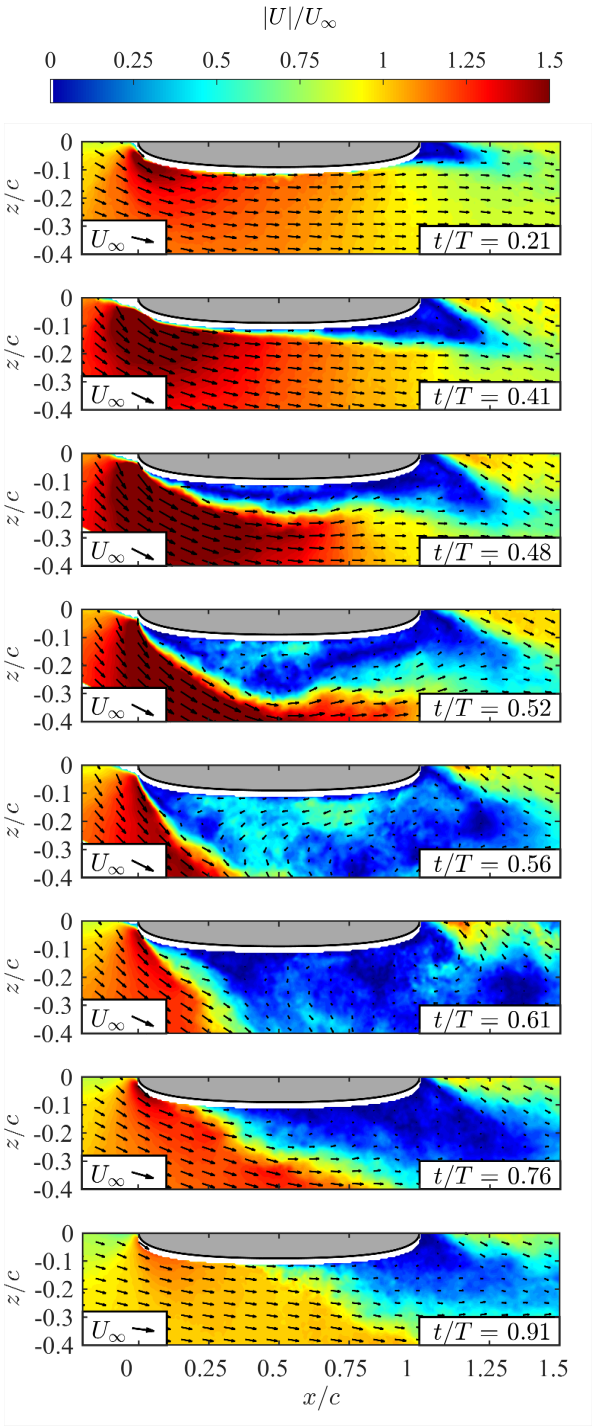

(a) Phase-averaged velocity fields.

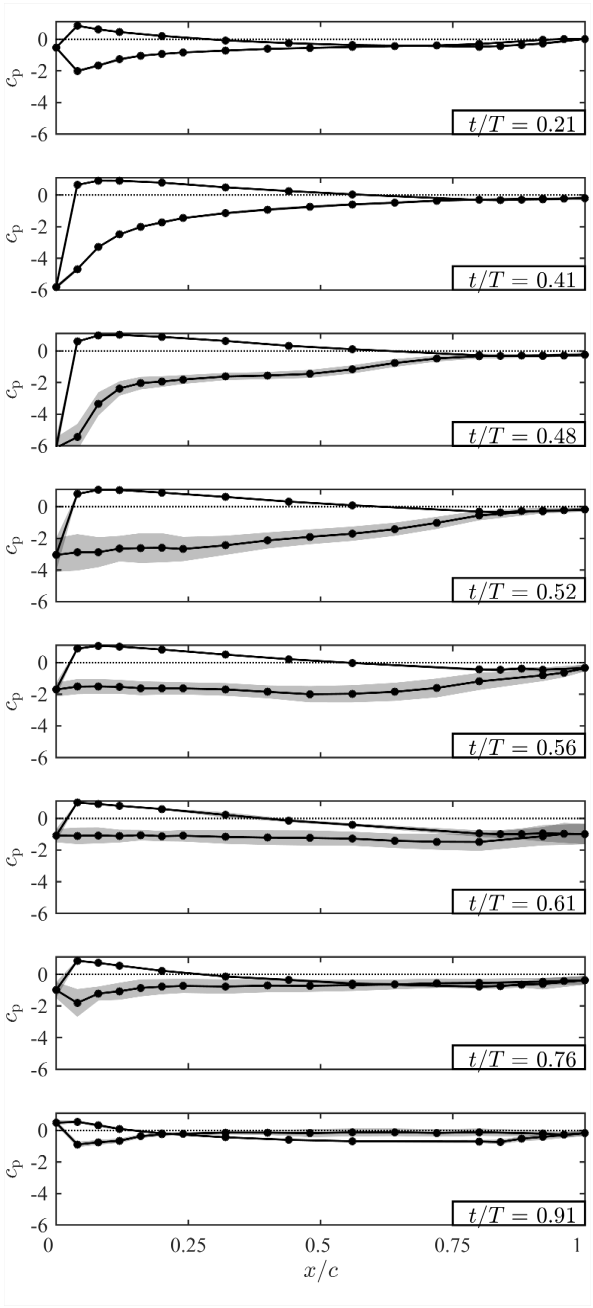

(b) Phase-averaged pressure distributions.

Figure 4.21: Type I dynamic stall of a cambered elliptical airfoil in reverse flow. $Re = 500,000$, $-\alpha_{0,\mathrm{rev}} = 15\,\mathrm{deg}$, $\alpha_0 = 10\,\mathrm{deg}$, $k = 0.160$

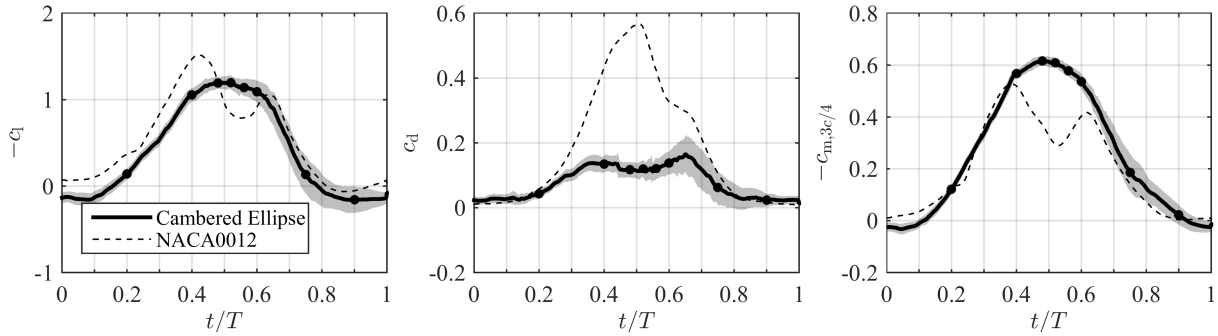

(a) Cambered Ellipse: Light dynamic stall (corresponds with Figure 4.20). NACA 0012: Type III deep dynamic stall.

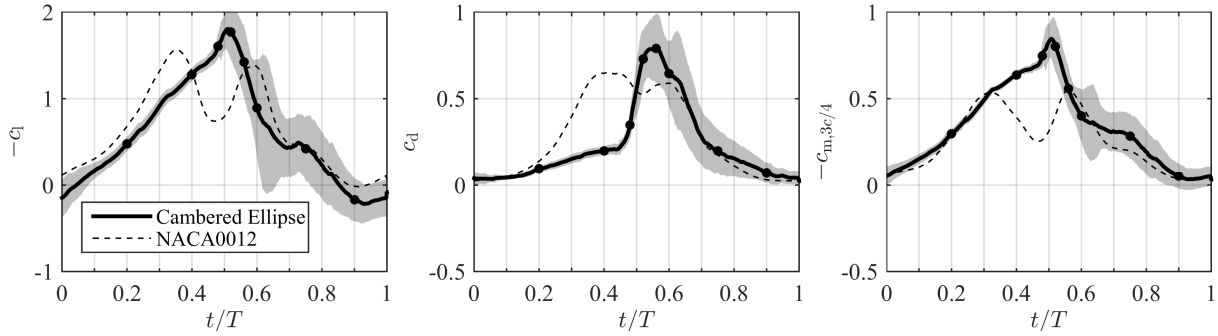

(b) Cambered Ellipse: Type I deep dynamic stall (corresponds with Figure 4.21). NACA 0012: Type III deep dynamic stall.

Figure 4.22: Unsteady airloads for an oscillating cambered elliptical airfoil in reverse flow.

of pitching kinematics considered in the present work (Section 4.5.3). This contrasts with the NACA 0012 airfoil, where deep reverse flow dynamic stall is observed for all pitching kinematics considered. The appearance of light dynamic stall for the cambered elliptical airfoil is directly related to the fact that the aerodynamic leading edge is blunt. Deep dynamic stall can also be observed for severe pitching kinematics. This behavior is similar to classical dynamic stall of conventional airfoils in forward flow (Section 1.3.4).

4.5.2 Effect of Reynolds Number

Reverse flow dynamic stall on a NACA 0012 airfoil was found to be insensitive to Reynolds number due to the fixed separation point at the sharp aerodynamic leading edge. The leading edge of the cambered elliptical airfoil is blunt, however, and the separation point depends in part on Reynolds number. The effect of Reynolds number, reduced frequency, mean pitch angle, and pitch amplitude on the type of reverse flow dynamic stall is summarized near the end of this chapter in Table 4.3.

Consider Figure 4.23(a) which shows the phase-averaged pressure distributions at three Reynolds numbers for the cambered elliptical airfoil undergoing a Type I dynamic stall with $-\alpha_{0,\text{rev}} = 15\,\text{deg}$ and $\alpha_0 = 10\,\text{deg}$. The reduced frequency is $k = 0.160$ for all three cases. Note that the case with $Re = 500,000$ was also presented in Figures 4.21 and 4.22(b).

The pressure contour plots in Figure 4.23(a) and corresponding unsteady lift and drag plots are generally similar for $0 \leq t/T \leq 0.32$. Drag begins to increase at $t/T = 0.32$, 0.4, and 0.46 for $Re = 165,000$, 330,000, and 500,000, respectively. In each case, maximum lift occurs a short time later, at $t/T = 0.41$, 0.48, and 0.52. The delayed appearance of these features in the airloads and shift of the low pressure wave associated with dynamic stall in the phase-averaged pressure contours suggest that dynamic stall is delayed by increases in Reynolds number. This is confirmed in Figure 4.23(b), which shows phase-averaged velocity fields at $t/T = 0.5$. The development of the dynamic stall vortex near the leading edge is at

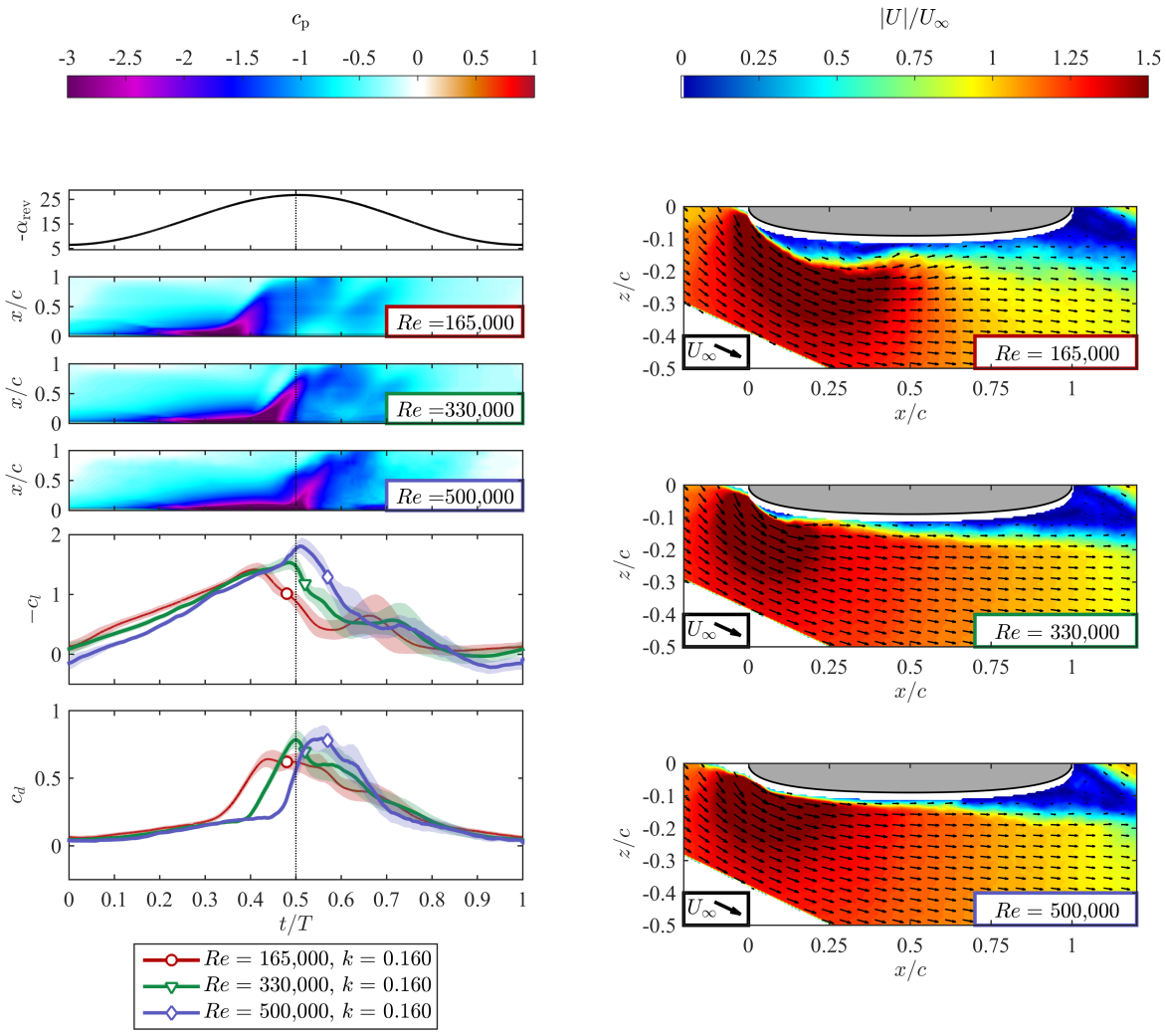

(a) Phase-averaged pressure distributions of the suction side and unsteady lift and drag.

(b) Phase-averaged velocity distributions at $t/T = 0.5$.

Figure 4.23: Reynolds number effects on reverse flow deep dynamic stall of a cambered elliptical airfoil, $-\alpha_{0,\mathrm{rev}} = 15\,\mathrm{deg}$, $\alpha_0 = 10\,\mathrm{deg}$, $k = 0.160$.

different stages, depending on Reynolds number.

Figure 4.24 shows the effect of Reynolds number on the cambered elliptical airfoil with different pitching kinematics (still with $k = 0.160$). Figure 4.24(a) is for a lower mean pitch angle of $-\alpha_{0,\text{rev}} = 10\,\text{deg}$ but the same pitch amplitude of $\alpha_0 = 10\,\text{deg}$ as was shown in Figure 4.23(a). Focusing on $Re = 165,000$ in Figures 4.23(a) and 4.24(a), it can be seen that the pressure wave associated with the convection of the dynamic stall vortex begins later in the cycle in Figure 4.24(a) (near $t/T = 0.45$). This is a result of the lower mean pitch angle. At $Re = 330,000$ in Figure 4.24(a), the start of pressure wave is delayed until $t/T = 0.56$. At $Re = 500,000$, the pressure wave is absent, suggesting that the airfoil undergoes light dynamic stall rather than deep dynamic stall. This is reflected in the airloads plots as well; the lift curves feature a "bump" associated with dynamic stall at $Re = 165,000$ and $Re = 330,000$ that is absent at $Re = 500,000$. Drag also remains relatively low for $Re = 500,000$. Thus, for this set of pitching kinematics, the effect of Reynolds number is strong enough to change the dynamic stall type.

Figure 4.24(b) shows another example of this effect, with a mean pitch angle of $-\alpha_{0,\text{rev}} = 15\,\text{deg}$ (similar to Figure 4.23(a)), but a lower pitch amplitude of $\alpha_0 = 5\,\text{deg}$. At $Re = 165,000$, the flow remains fully separated for the entire pitching cycle. A weak wave of low pressure convects over the airfoil for $0.18 \leq t/T \leq 0.55$, but lift remains generally low and drag generally high. This behavior is similar to the NACA 0012 subjected to the same pitching kinematics (Figure 4.17), though the sharp leading edge of the NACA 0012 causes the pressure wave to occur earlier in the pitching cycle. Returning to Figure 4.24(b) at $Re = 330,000$, a Type I dynamic stall is observed. At $Re = 500,000$, the airfoil undergoes light dynamic stall.

The effect of Reynolds number on reverse flow dynamic stall of the cambered elliptical airfoil can be significant; an increase in Reynolds number can delay dynamic stall or even change which stall type the airfoil experiences. It bears mentioning that the Reynolds

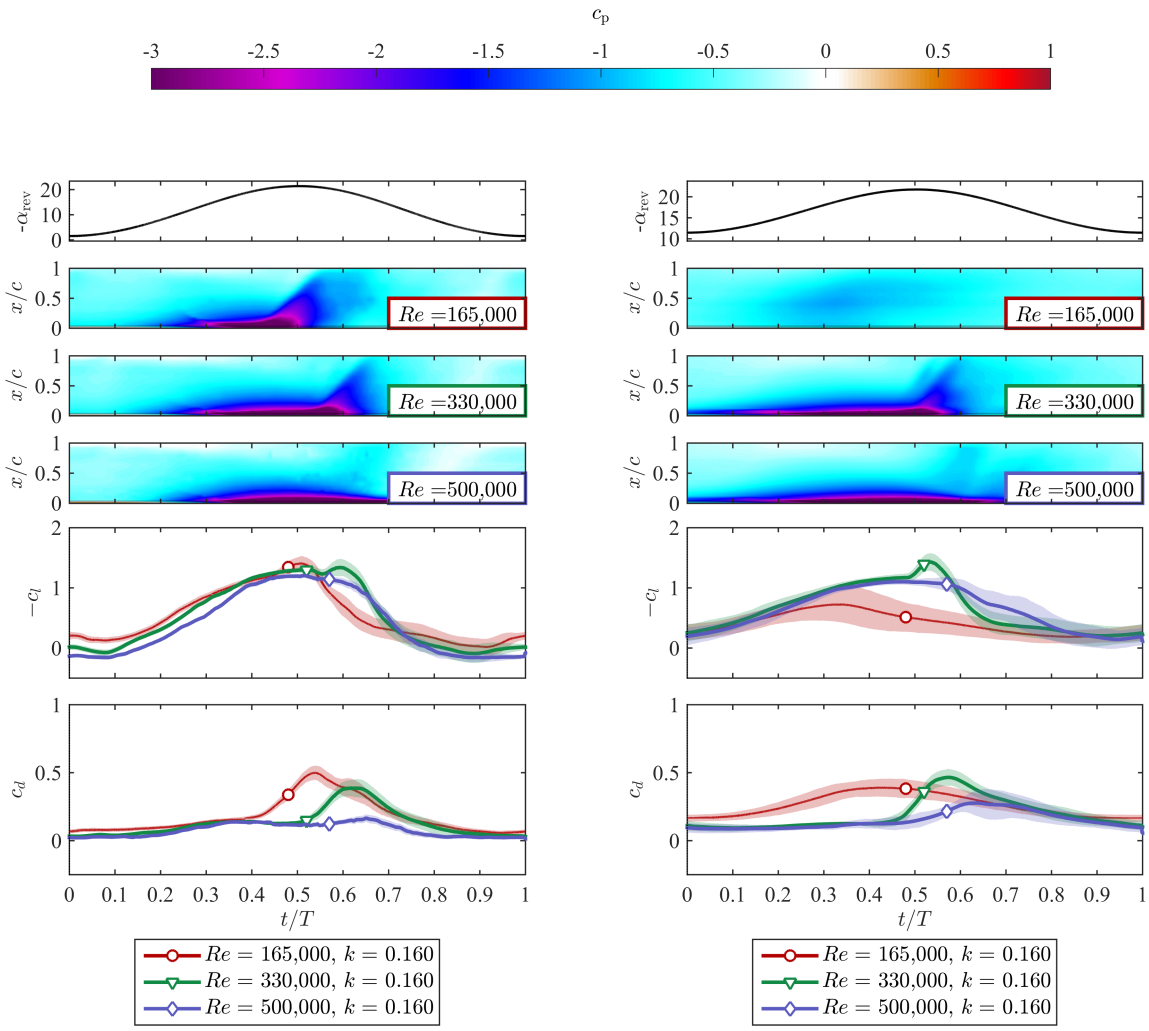

(a) $-\alpha_{0,\mathrm{rev}} = 10\,\mathrm{deg}$, $\alpha_0 = 10\,\mathrm{deg}$.

(b) $-\alpha_{0,\mathrm{rev}} = 15\,\mathrm{deg}$, $\alpha_0 = 5\,\mathrm{deg}$.

Figure 4.24: Reynolds number effects on reverse flow dynamic stall of a cambered elliptical airfoil, $k = 0.160$.

numbers tested here are in the transitional range, representative of the conditions found in a portion of the reverse flow region (Figure 4.2(a)). Near the blade root, the Reynolds number in the full-scale reverse flow region is greater ($Re \geq 1.0 \times 10^6$). As a result, reverse flow dynamic stall of a cambered ellipse may be less susceptible to the influence of boundary layer transition and separation at these higher Reynolds numbers.

4.5.3 Effect of Reduced Frequency, Mean Pitch Angle, and Pitch Amplitude

Recall that dynamic stall on the NACA 0012 airfoil is generally independent of Reynolds number. For each mean pitch angle and pitch amplitude, different values of reduced frequency could be compared without regard to Reynolds number. Since the cambered elliptical airfoil *is* sensitive to Reynolds number, the effect of reduced frequency must be examined at constant Reynolds numbers. Figures 4.25-4.29 show the effect of reduced frequency at two Reynolds numbers, usually $Re = 165,000$ where the difference between tested reduced frequencies is greatest, and $Re = 500,000$, the highest Reynolds number tested.

Figures 4.25 and 4.26 show results for mean pitch angles of $-\alpha_{0,\text{rev}} = 5$ and $10\,\text{deg}$, all with a pitch amplitude of $\alpha_0 = 5\,\text{deg}$. Similar to the NACA 0012, the pressure contours exhibit a shift with increasing reduced frequency, though this effect is very weak for these pitching kinematics with a negligible effect on the pressure distributions and unsteady airloads. One exception is shown in Figure 4.26(a); the pressure near the leading edge first drops below $c_p = 2$ (purple) near $t/T = 0.25$ with $k = 0.160$ and is delayed to $t/T = 0.30$ with $k = 0.511$. This is consistent with a reduction of effective angle of attack as suggested by the model in Figure 4.11. However, recall that this model suggested that the effective angle of attack was determined only by the local flow at the sharp aerodynamic leading edge since the separation point is fixed on the NACA 0012 in reverse flow. For the cambered elliptical airfoil, the flow does not immediately separate at the leading edge, making calculation of the effective angle of attack more challenging. Recall that quasi-steady thin airfoil theory

suggests that no lift is generated by an airfoil undergoing pure pitch oscillations about the aerodynamic three-quarter chord [13]. However, quasi-steady thin airfoil theory does not apply well here since 1.) the cambered elliptical airfoil is 26 % thick and 2.) the model is inviscid and the cambered elliptical airfoil is blunt on both edges, leading to flow separation at the trailing edge. Theodorsen's theory also does not apply for similar reasons and because the pitch oscillations considered here are large [13].

In the absence of a more developed model, the one suggested by Figure 4.11 continues to be used since it is consistent with the results of the cambered elliptical airfoil. The model predicts that an increase in reduced frequency reduces the effective angle of attack during the first half of the pitch cycle, thereby delaying the growth of the region of suction near the leading edge and the formation of a dynamic stall vortex (if present). Figure 4.26(a) shows that an increase in reduced frequency can also suppress Type I dynamic stall to light dynamic stall.

Figure 4.27 shows a greater mean pitch angle of $-\alpha_{0,\mathrm{rev}} = 15\,\mathrm{deg}$. As was also in Figure 4.24(b), the flow is fully separated over the suction side for $Re = 165,000$ and $k = 0.160$ (Figure 4.27(a)). At $k = 0.511$, the flow is still fully separated, but a stronger pressure wave is present. Similar to the NACA 0012, an increase in reduced frequency allows the leading edge shear layer to remain closer to the airfoil surface, thereby increasing its influence on the pressure distribution. At $Re = 500,000$ (Figure 4.27(b)), the cambered elliptical airfoil undergoes light dynamic stall for $k = 0.160$ and $k = 0.217$, with slight suppression of flow separation at $k = 0.217$.

Figure 4.28 shows oscillations with a lower mean pitch angle of of $-\alpha_{0,\mathrm{rev}} = 10$, but a greater pitch amplitude of $\alpha_0 = 10\,\mathrm{deg}$. The pressure measurements for $k > 0.160$ are noisy; Figure 4.28(a) shows results for $Re = 330,000$ due to excessive noise in the results at $Re = 165,000$ and $k = 0.511$. The airfoil exhibits a Type I dynamic stall at $Re = 330,000$. Compared to $k = 0.160$, the pressure contour at $k = 0.309$ is elongated (due to the shorter

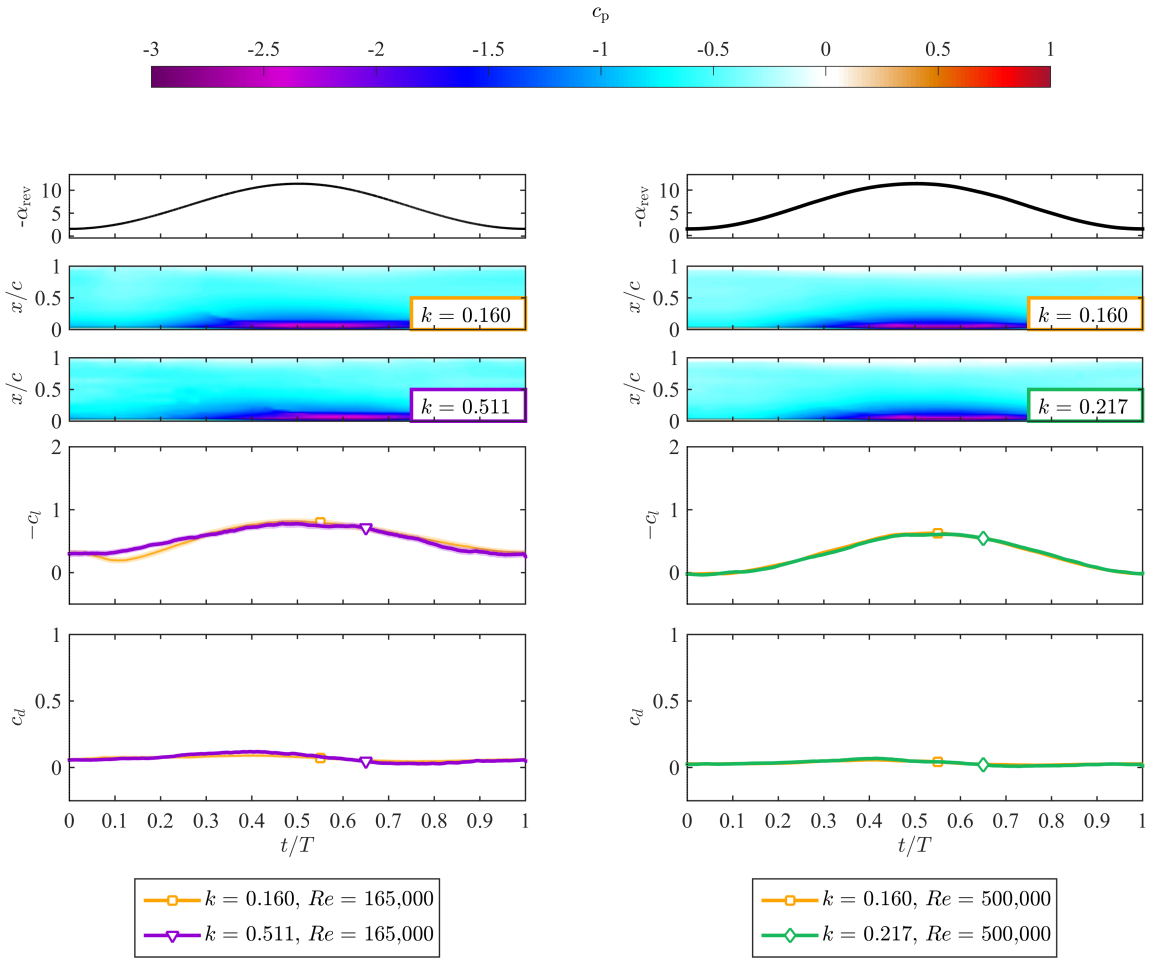

(a) $Re = 165,000$.

(b) $Re = 500,000$.

Figure 4.25: Reduced frequency effects on reverse flow dynamic stall of a cambered elliptical airfoil, $-\alpha_{0,\text{rev}} = 5\,\text{deg}$, $\alpha_0 = 5\,\text{deg}$.

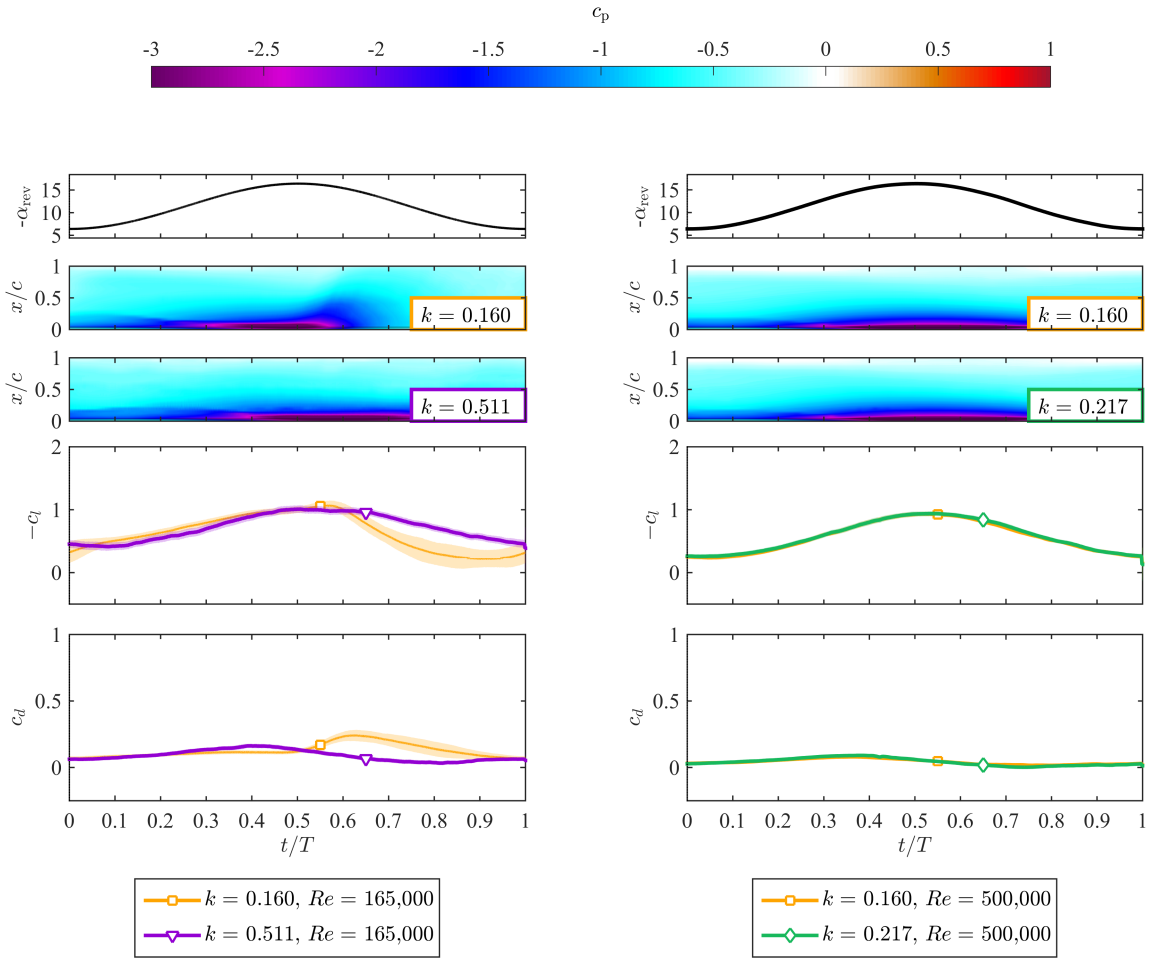

(a) $Re = 165{,}000$.

(b) $Re = 500{,}000$.

Figure 4.26: Reduced frequency effects on reverse flow dynamic stall of a cambered elliptical airfoil, $-\alpha_{0,\text{rev}} = 10\,\text{deg}$, $\alpha_0 = 5\,\text{deg}$.

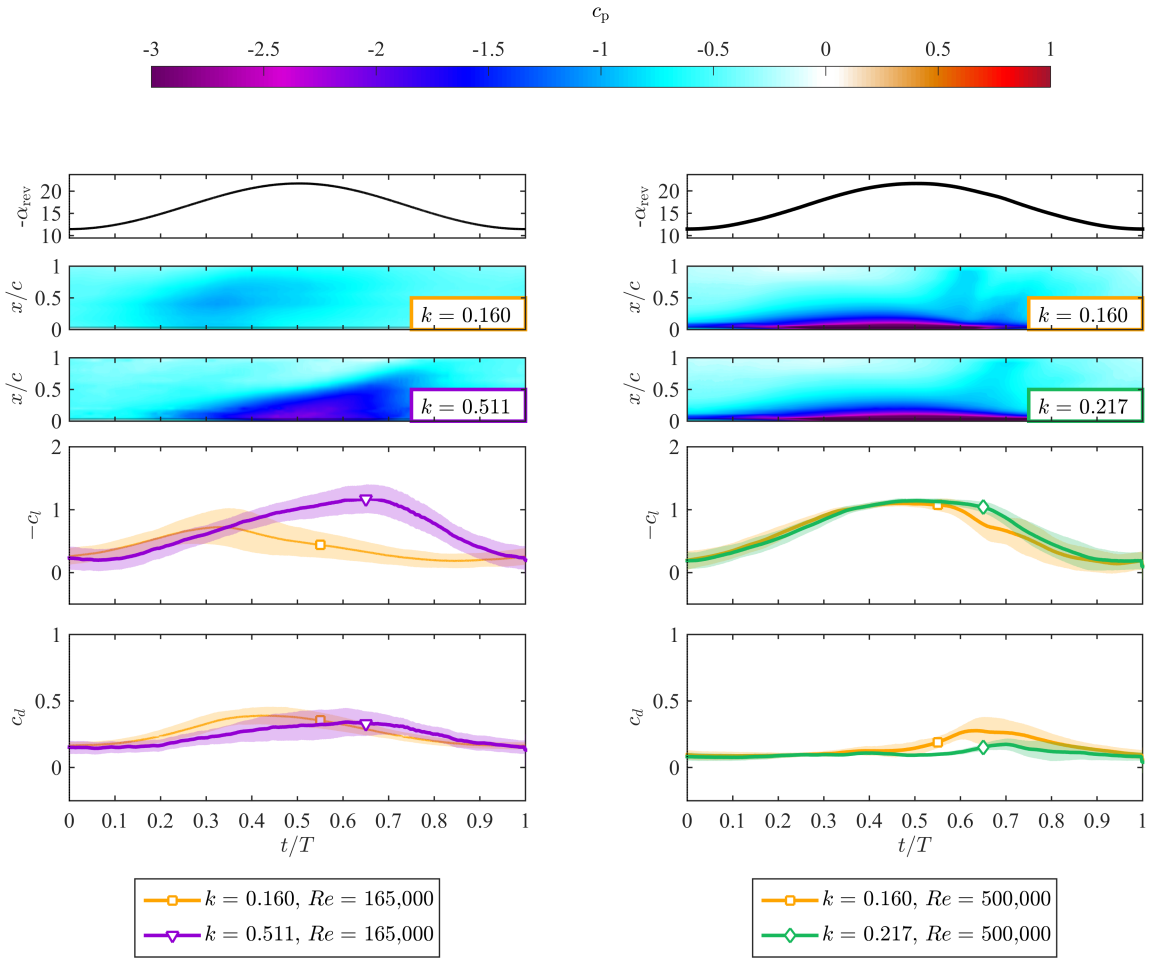

(a) $Re = 165,000$.

(b) $Re = 500,000$.

Figure 4.27: Reduced frequency effects on reverse flow dynamic stall of a cambered elliptical airfoil, $-\alpha_{0,\text{rev}} = 15\,\text{deg}$, $\alpha_0 = 5\,\text{deg}$.

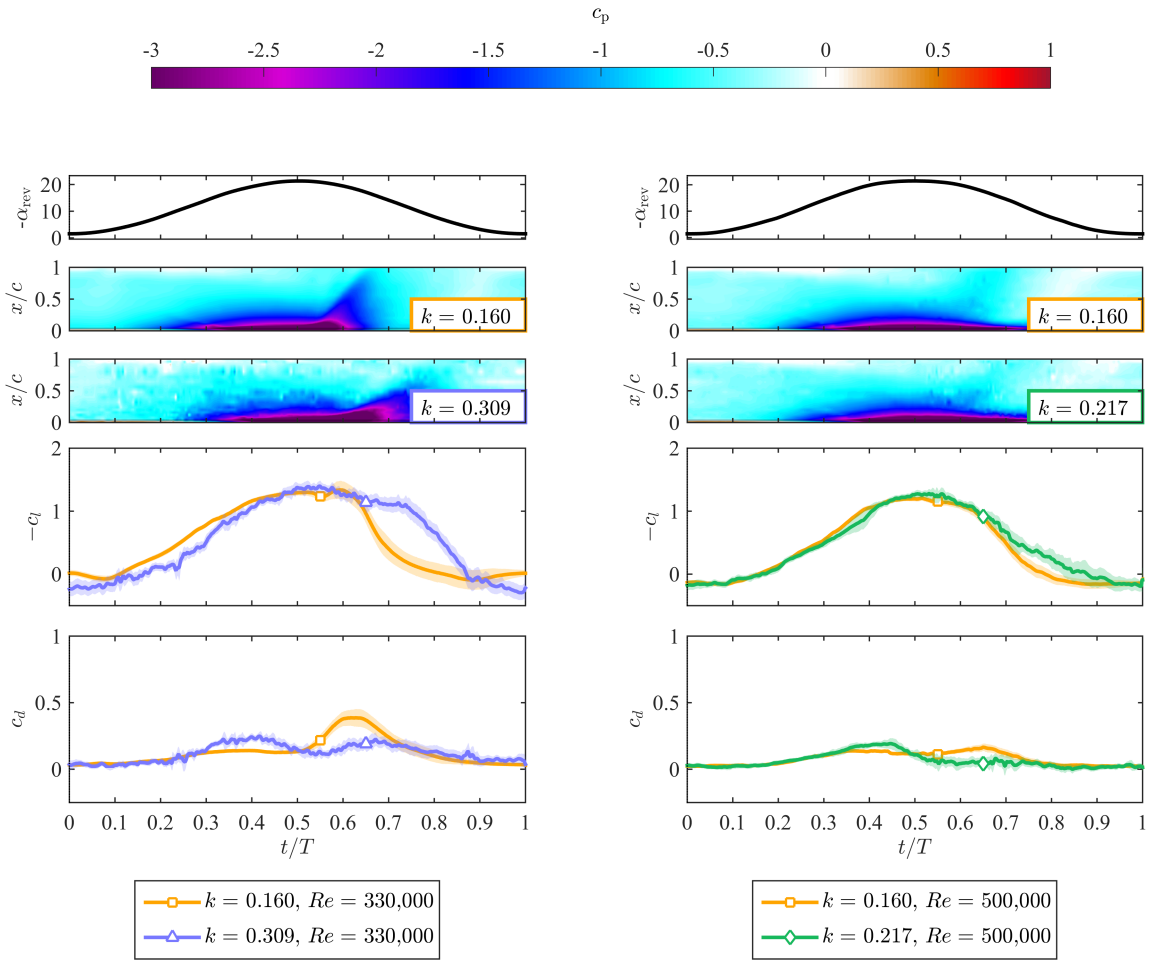

(a) $Re = 330,000$. (b) $Re = 500,000$.

Figure 4.28: Reduced frequency effects on reverse flow dynamic stall of a cambered elliptical airfoil, $-\alpha_{0,\text{rev}} = 10\,\text{deg}$, $\alpha_0 = 10\,\text{deg}$.

cycle period) and shifted (due to the lower effective angle of attack during the first half of the pitching cycle). This delay of dynamic stall results in greater lift for $0.63 \leq t/T \leq 0.88$ and lower drag for $0.53 \leq t/T \leq 0.7$. At $Re = 500,000$ (Figure 4.28(b)), the airfoil exhibits light dynamic stall with a slight shift in the pressure contour at the higher reduced frequency of $k = 0.217$.

Finally, Figure 4.29 shows the most severe pitching kinematics with $-\alpha_{0,\text{rev}} = 10\,\text{deg}$ and $\alpha_0 = 10\,\text{deg}$. A Type III dynamic stall is observed at $Re = 330,000$ and $k = 0.160$

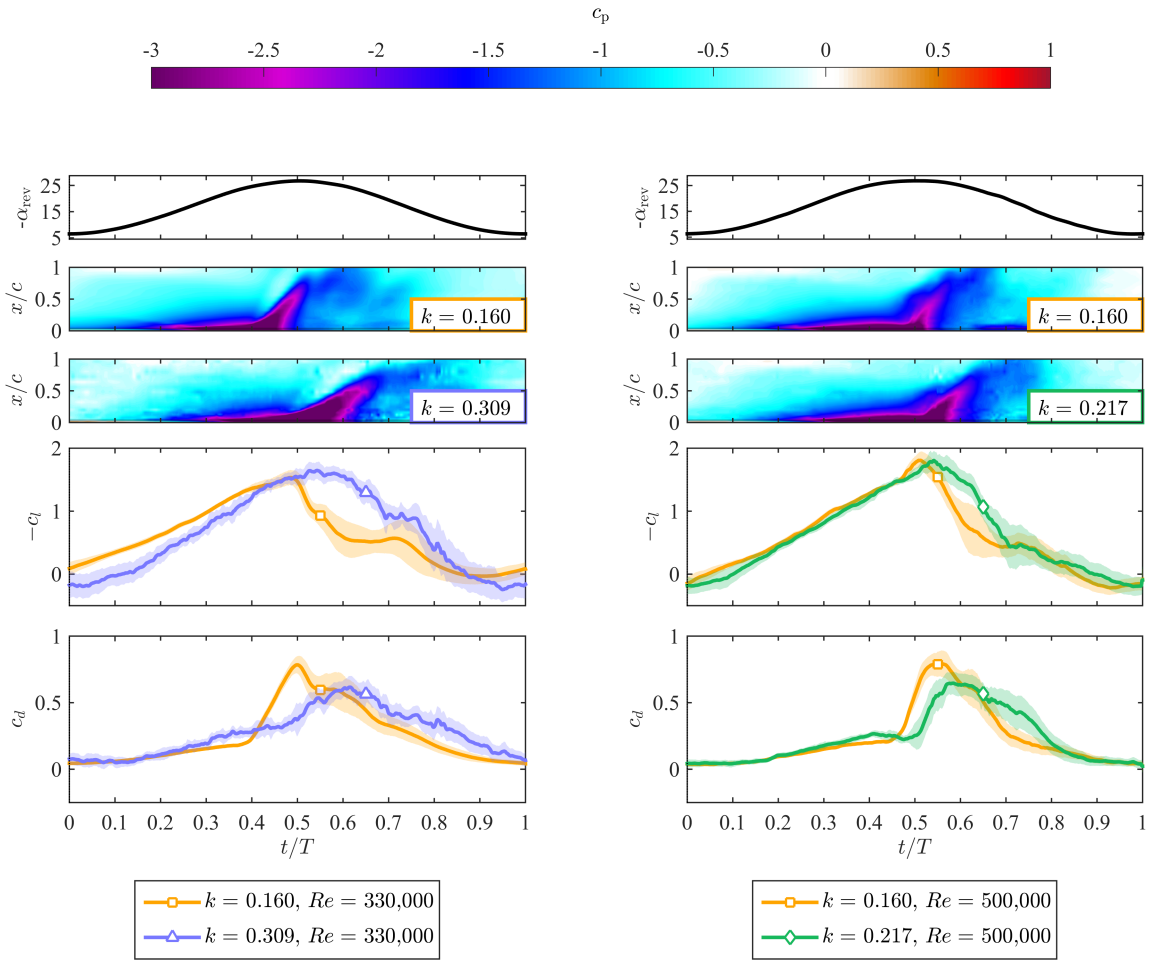

(a) $Re = 330,000$. (b) $Re = 500,000$.

Figure 4.29: Reduced frequency effects on reverse flow dynamic stall of a cambered elliptical airfoil, $-\alpha_{0,\text{rev}} = 15\,\text{deg}$, $\alpha_0 = 10\,\text{deg}$.

(Figure 4.29(a)) with the generation of a trailing edge vortex and secondary dynamic stall vortex. The secondary dynamic stall vortex is relatively weak, producing only a mild lift enhancement near $t/T = 0.72$. At $k = 0.309$, a Type I dynamic stall occurs due to the shorter cycle time and delayed formation of the primary dynamic stall. Type I dynamic stalls also occur at both reduced frequencies tested at $Re = 500,000$ (Figure 4.29(b)).

Table 4.3 summarizes the types of dynamic stall observed for the cambered elliptical airfoil in the parameter space considered in the present work. Unlike the NACA 0012 in

Table 4.3: Types of reverse flow dynamic stall observed for a cambered elliptical airfoil at three Reynolds numbers and five sets of pitching kinematics. Sep.: flow is fully separated for the duration of the pitching cycle.

		$\alpha_1 = 5\,\text{deg}$			$\alpha_1 = 10\,\text{deg}$	
Re	k	5 deg	10 deg	15 deg	10 deg	15 deg
165,000	0.160	light	I	I (Sep.)	I	III
165,000	0.511	light	light	I (Sep.)	I	I
330,000	0.160	light	light	I	I	III
330,000	0.309	light	light	I	I	I
500,000	0.160	light	light	light	light	I
500,000	0.217	light	light	light	light	I

reverse flow, the stall type observed for the cambered elliptical airfoil depends on Reynolds number as well as pitching kinematics. For $-\alpha_{0,\text{rev}} \leq 10\,\text{deg}$ and $\alpha_0 = 5\,\text{deg}$, the cambered elliptical airfoil generally exhibits light dynamic stall: partial flow separation from the suction side of the airfoil. The unsteady airloads are sensitive to Reynolds number here, but generally insensitive to reduced frequency. Light dynamic stall is also present for greater values of mean pitch angle and pitch amplitude at $Re = 500,000$; it is expected that light dynamic stall would be observed for these pitching kinematics at greater Reynolds numbers as well. Type I dynamic stall is observed at lower Reynolds numbers with the exception of a few instances of Type III dynamic stall.

4.6 Chapter Summary

This chapter examined a fundamental model of unsteady rotor blade behavior in the reverse flow region of a high-speed helicopter. Two airfoils underwent oscillatory motions in reverse flow subject to a constant freestream. Several types of reverse flow dynamic stall were observed, ranging from light dynamic stall characterized by partial flow separation, to Type IV dynamic stall with the formation of primary and secondary dynamic stall and trailing edge vortices. The dependency of the type of dynamic stall observed was evaluated based on airfoil shape, Reynolds number, reduced frequency, mean pitch angle, and pitch

amplitude.

The first airfoil, a NACA 0012, has a sharp aerodynamic leading edge which serves as a fixed separation point in reverse flow. This forces separation at the leading edge, allowing the evolution of dynamic stall to be insensitive to Reynolds number (for a given set of pitching kinematics). However, the evolution of dynamic stall was shown to be highly sensitive to reduced frequency. Reduced frequency has three effects on reverse flow dynamic stall. First, an increase in reduced frequency leads to shorter cycle periods; less time is available for flow features to develop during the pitching cycle. As a result, an increase in reduced frequency can downgrade the dynamic stall type. Second, the effective angle of attack decreases with reduced frequency, delaying the formation of the dynamic stall vortex. Third, the shorter cycle period delays the propagation of flow separation towards the trailing edge. As a result, the leading edge shear layer feeds the growth of the primary dynamic stall vortex at a greater angle of attack. This results in a stronger primary dynamic stall vortex and subsequent flow features (if present).

The second airfoil, a cambered ellipse, exhibits markedly different behavior during reverse flow dynamic stall. Flow passes smoothly over the blunt aerodynamic leading edge, making Reynolds number an important parameter in the separation characteristics. For mean pitch angles of 5 and 10 deg and pitch amplitude of 5 deg, the cambered elliptical airfoil exhibits light dynamic stall at nearly all Reynolds numbers and reduced frequencies tested. The unsteady airloads are essentially insensitive to reduced frequency here; this is believed to be a result of the weaker coupling between reduced frequency and effective angle of attack for the cambered elliptical airfoil.

Figure 4.22 provides a good basis for comparing the reverse flow dynamic stall performance of these two airfoils. In both cases shown, the NACA 0012 undergoes a Type III dynamic stall with high lift that oscillates as vortices form and convect over the airfoil. The pitching moment exhibits similar behavior, and drag is high. This is representative of the

general behavior of the NACA 0012 undergoing reverse flow dynamic stall. Deep dynamic stall was always observed in the present work and the resulting unsteady airloads are directly affected by more severe pitching kinematics. Note that deep dynamic stall may not be observed for mean pitch angles and/or pitch amplitudes less than 5 degrees; these kinematics were not tested in the present work. Conversely, the cambered elliptical airfoil undergoes light dynamic stall for a wide range of pitching kinematics. This also leads to high lift and pitching moment (Figure 4.22(a)), but the important difference is that these airloads are nearly sinusoidal and thus more predictable than those of the NACA 0012. Additionally, the light dynamic stall features significantly less drag due to less flow separation. However, if the pitching kinematics are severe enough, the cambered elliptical airfoil can exhibit deep dynamic stall. Here, the unsteady airloads vary rapidly due to the influence of a dynamic stall vortex. In the case shown in Figure 4.22(b), this leads to unsteady airloads that, at times, are greater in magnitude than the NACA 0012.

Appendix C is a collection of airloads for these airfoils in forward and reverse flow at selected Reynolds numbers and reduced frequencies. Figures C.1 and C.2 show the unsteady airloads of the NACA 0012 airfoil in forward flow at $Re = 500,000$ (the highest tested). The full-scale reduced frequency is approximately $k = 0.025$. Figures C.3 and C.4 show the unsteady airloads of the NACA 0012 airfoil in forward flow at Reynolds numbers and reduced frequencies corresponding to the blade stations $0.61 \leq r \leq 0.71$ at $\Psi = 270\,\text{deg}$ for a full-scale high-speed helicopter operating at $\mu = 0.77$. Figures C.5-C.8 show similar results for the cambered elliptical airfoil.

Chapter 5

Conclusion

5.1 Summary of Research

Two-dimensional wind tunnel tests have been performed at the University of Maryland and the United States Naval Academy to characterize two fundamental models of the reverse flow region of a high-speed helicopter rotor: static and oscillating airfoils in reverse flow. Two airfoils with a sharp geometric trailing edge (NACA 0012 and NACA 0024) and two airfoils with a blunt geometric trailing edge (elliptical and cambered elliptical, modeled from the DBLN-526 airfoil) were considered in this work. Tests were performed over a range of Reynolds numbers and angles of attack representative of those encountered by a retreating blade on a full-scale modern high-speed helicopter.

Chapter 3 examined the time-averaged and unsteady aerodynamics of static airfoils at high angles of attack and in reverse flow. This work provided a fundamental understanding of the effect of trailing edge shape on time-averaged flow separation characteristics and the resulting influence on airloads and performance. Sectional lift characteristics such as those obtained here are important for determining the total rotor thrust and trim (i.e. control settings), sectional drag directly influences the profile power required in forward flight, and sectional pitching moment affects blade torsion and pitch link loads. The sensitivity

of sectional airloads to Reynolds number was also characterized. Unsteady wake regimes were identified, and their influence on the frequency and magnitude of unsteady airloads gained through this work was quantified. Knowledge of vortex shedding frequency and the magnitude of associated unsteady airloads will be important for the reduction of vibrations which can lead to structural fatigue of rotor blades and hub components. Finally, Chapter 4 considered the unsteady aerodynamics of oscillating airfoils in reverse flow. The pitching airfoil models the cyclic pitching kinematics of helicopter rotor blades in forward flight. The sensitivity of the evolution of dynamic stall was evaluated for several parameters including airfoil shape, Reynolds number, reduced frequency, mean pitch angle, and pitch amplitude.

An airfoil that is well-designed for reverse flow will feature low magnitudes of steady and unsteady airloads over a wide range of angle of attack and Reynolds number. The time averaged and unsteady airloads of a static NACA 0012 were found to be favorable at low angles of attack ($-\alpha_{\text{rev}} \leq 4$), but this airfoil is susceptible to greater drag and unsteady airloads at higher angles of attack. Similar behavior was also observed for the NACA 0024. The rotor blades on modern high-speed helicopters use airfoils with a blunt geometric trailing edge on the inboard portion of rotor blades (where reverse flow is most severe). This work showed that these airfoils delay massive flow separation as compared to conventional airfoils with a sharp trailing edge. This results in lower time-averaged drag, but greater downward-acting lift and pitching moment. However, due to the delayed flow separation, the *unsteady* airloads of an oscillating cambered elliptical airfoil are generally more predictable than a NACA 0012. Further work is needed to characterize the effect of the time-varying freestream and three-dimensional effects of the true reverse flow region. Ultimately, proper airfoil selection must also consider other rotor aerodynamic blade design factors such as advancing side perfromance, blade twist, planform (taper), blending of airfoil sections, and consideration of the structural bending and torsion characteristics [6].

5.2 Original Contributions

The work presented here makes several important original contributions that will inform future studies on the topic and be valuable for the design of rotor blades that operate in reverse flow.

1. The fundamental time-averaged and unsteady aerodynamic behavior of rotor blade airfoils has been examined using high-resolution force, pressure, and flowfield measurements at Reynolds numbers encountered by the retreating blade of a full-scale helicopter.

2. A fundamental understanding of the evolution of reverse flow dynamic stall has been characterized for two rotor blade airfoils using phase-averaged flowfield and pressure measurements. The effects of Reynolds number, reduced frequency, mean pitch angle, and pitch amplitude on the type of dynamic stall observed have been identified.

3. A comprehensive experimental database of time-averaged and unsteady airloads for static and oscillating airfoils in reverse flow (Appendix B and C) is now available for use in comprehensive rotorcraft codes, and is already being used in collaborative efforts with CFD researchers to validate 2-D simulations of reverse flow.

5.3 Key Conclusions

Static airfoils.

1. For conventional airfoils with a sharp geometric trailing edge (NACA 0012 and NACA 0024 at $0^\circ \leq \alpha_{\text{rev}} \leq 10^\circ$), the time-averaged drag in reverse flow is at least twice that of drag in forward flow. The higher drag in reverse flow is dominated by pressure drag due

to flow separation from the bluff aerodynamic trailing edge (geometric leading edge). This trend was observed for all Reynolds numbers tested ($1.1 \times 10^5 \leq Re \leq 1.0 \times 10^6$).

2. A NACA 0012 airfoil in reverse flow undergoes a thin airfoil stall. Flow separates at the sharp aerodynamic leading edge at shallow angles of attack and undergoes unsteady reattachment further down the chord, oscillating between a separation bubble and fully separated flow. This leads to high levels of flow unsteadiness near the suction side and correspondingly high unsteady airloads. Since flow separation is fixed at the sharp aerodynamic leading edge in reverse flow (for $|\alpha_{\text{rev}}| \geq 4\,\text{deg}$), both the time-averaged and unsteady airloads are generally insensitive to Reynolds number.

3. The reverse flow static angle of attack at which massive flow separation occurs is greater for airfoils with a blunt geometric trailing edge than those with a sharp geometric trailing edge. This tendency of blunt airfoils to delay stall leads to lower time-averaged and unsteady drag (except at shallow angles of attack), but also results in greater downward-acting lift and pitching moment. The unsteady airloads are also generally lower for airfoils with a blunt geometric trailing edge at pre-stall angles of attack.

4. The time-averaged airloads of the thick airfoils tested here (NACA 0024, elliptical, and cambered elliptical) are all sensitive to Reynolds number. The position and size of separation bubbles, recirculation regions, and areas of separated flow all vary with Reynolds number and have a direct influence on the resulting airloads. The unsteady airloads generally show little sensitivity to Reynolds number, though there is a delay in the onset of high unsteady loads with increasing Reynolds number due to the delay of stall.

5. Three unsteady wake regimes for static airfoils in reverse flow have been identified: slender body vortex shedding, turbulent wake, and deep stall vortex shedding. These

regimes are dependent on both angle of attack and Reynolds number. The slender body vortex shedding regime was not detected with unsteady pressure measurements for higher Reynolds numbers between $3.3 \times 10^5 \leq Re \leq 1.0 \times 10^6$. The unsteady airloads for the airfoils with a sharp trailing edge in the turbulent wake regime increase gradually in reverse flow with increasing angle of attack, consistent with a thin-airfoil stall. They then become periodic and decrease in magnitude in the deep stall vortex shedding regime. For airfoils with a blunt geometric trailing edge, the unsteady airloads rapidly increase in magnitude at stall, but remain aperiodic with increasing angle of attack until the onset of the deep stall vortex shedding regime.

6. The variation of the deep stall vortex shedding frequency for static airfoils can be represented using a Strouhal number based on the projected airfoil chord, St_d. For airfoils at angles of angle of attack $45^\circ \leq \alpha \leq 135^\circ$ and $Re = 6.6 \times 10^5$, the Strouhal number was found to be $St_d = 0.16 - 0.19$. The curvature of the upstream surface of an airfoil affects St_d by modifying the flow separation angle, thereby affecting the shear layer interactions downstream.

7. Aerodynamic hysteresis was observed for the three thick airfoils tested here, resulting in a delay of flow reattachment to angles less than static stall when the static angle of attack is decreasing. This results in high unsteady airloads as the unstable leading edge shear layer is brought closer to the suction side of the airfoil.

Oscillating airfoils.

8. Reverse flow dynamic stall of a NACA 0012 was found to be insensitive to Reynolds number since the sharp aerodynamic leading edge serves as a fixed separation point. Some type of deep dynamic stall was observed for all mean pitch angles and pitch amplitudes considered here, resulting in the formation and convection of a dynamic

stall vortex. The type of dynamic stall observed (i.e., number of vortices) was found to be strongly dependent on pitching kinematics. Furthermore, increases in reduced frequency were found to elongate pressure and airload distributions in the direction of non-dimensional cycle time due to the shorter dimensional cycle time. Increases in reduced frequency also act to delay the formation of the primary dynamic stall vortex (due to a reduced equivalent angle of attack), and increase the strength of vortices (due to delayed formations to greater angles of attack).

9. The cambered elliptical airfoil exhibits light reverse flow dynamic stall for a wide range of pitching kinematics due to its blunt aerodynamic trailing edge. Since the flow separation point is not fixed for this airfoil, the dynamic stall characteristics are sensitive to Reynolds number as well as pitching kinematics. However, the light dynamic stall airloads are generally insensitive to reduced frequency with only slight phase shifts observed.

5.4 Future Work

The present work provided a detailed description of static airfoils in reverse flow and a fundamental analysis of oscillating airfoils in reverse flow. This section offers suggestions for further experimental work and analytical modeling, especially on oscillating airfoils in reverse flow. Ultimately, the direction of future work on reverse flow will be driven by the aerodynamic model that is assumed for the reverse flow region. The present work assumed a fundamental aerodynamic model, by examining two-dimensional airfoil characteristics subject to a constant freestream. Some of the suggestions for future work listed below are based on this model. However, the true reverse flow region is highly three-dimensional with a time-varying freestream. It is suggested that these elements be introduced into the aerodynamic model of reverse flow to provide more realistic representations of this complex flow.

1. Improved accuracy of the unsteady airloads in reverse flow can be achieved by performing experiments with an optimized concentration of pressure taps. The pressure and flowfield results given here can be used to inform the optimization. The goal would be to better resolve regions with steep pressure gradients (i.e., suction and pressure peaks) and measure pressure closer to the geometric trailing edge of conventional airfoils. Once the setup is complete, acquisition time of pressure measurements on oscillating airfoils is relatively short. This means that a high resolution of the parameter space could be explored to generate more accurate boundaries for dynamic stall types.

2. The oscillating airfoil data presented here, as well as data collected in the future, can be analyzed using more advanced post-processing techniques. Vortex tracking can be performed using the time-resolved velocity field data to better quantify the periodicity of the evolution, convection speed, and strength of dynamic stall vortices (and trailing edge vortices). The pressure data can be analyzed to determine corresponding pressure wave speeds. The dominant features in the spatiotemporal representations of pressure during a pitching cycle can be used as a basis for extrapolating the unknown pressure near the sharp geometric trailing edge, likely improving the accuracy of the integrated unsteady airloads. Finally, proper orthogonal decomposition and dynamic mode decomposition offer the potential to provide a better understanding of the flow physics of reverse flow dynamic stall through the analysis of dominant spatial modes and the phasing of the corresponding temporal coefficients. Specifically, the analysis of the temporal coefficients will lend insight into the timing of dynamic stall events such as boundary layer behavior, separation, and roll-up. These techniques can also be applied to synchronized pressure measurements. Collectively, the results of these advanced processing techniques could help inform the development of a low-order model of reverse flow dynamic stall.

3. Current comprehensive rotorcraft codes lack an unsteady analytical physics-based model of rotor behavior in the reverse flow region [63]. The work presented here on oscillating airfoils can be used to develop an analytical model of reverse flow dynamic stall. Pitching kinematics drive the timing of the formation of the primary dynamic stall vortex for airfoils with a sharp geometric trailing edge. Thus, rather than using a critical pressure to trigger the shedding of a dynamic stall vortex (the approach implemented in the Leishman-Beddoes dynamic stall model), a critical effective angle of attack could be investigated as a potential threshold. A deeper understanding of the time scales associated with dynamic stall events can be gained from the existing data. The dependence of pitching kinematics on these time scales could then be incorporated into the model. A different model would be needed for airfoils with a blunt geometric trailing edge. Further analysis of the results for the cambered elliptical airfoil is needed to determine the proper criteria for the onset of dynamic stall since the flow separation point is not fixed. For both airfoil types, the effect of inevitable flow separation near the blunt aerodynamic trailing edge should also be considered in the analytical model.

4. A more accurate experimental model of the flow conditions encountered in the reverse flow region should be explored. Some work has already been performed that considers the sub-scale, two-dimensional aerodynamics of a NACA 0012 and elliptical airfoil (12 % thick) oscillating in and out of reverse flow using a towing carriage on a water tunnel [64]. This method models flow through the boundary of the reverse flow region on the retreating side of the rotor. Future work can expand on this to include sinusoidal pitching of the airfoils to mimic cyclic pitching kinematics. The exact pitching kinematics could also be varied to account for the effect of inflow velocity in the true reverse flow region. This is of particular importance during transition into reverse flow since the in-plane velocity component may be zero, but the inflow is non-zero leading to large magnitudes of angle of attack. This work would allow for distinctions to be

made between the development of a *reverse flow dynamic stall vortex* (whose formation is the result of pitching) and a *reverse flow leading edge vortex* (whose formation is a result of the time varying freestream on an airfoil at a stalled angle of attack).

5. Oscillating airfoil experiments could be performed with the rotor blade yawed to induce spanwise flow, similar to a full-scale rotor. Spanwise flow is expected to delay dynamic stall vortex formation and growth. The effect of spanwise flow on the timing and strength of dynamic stall events could be characterized experimentally and incorporated into the analytical model proposed above.

6. Finally, the full three-dimensional reverse flow region should be explored on model rotors. Significant research efforts have already been conducted on a Mach-scale rotor operating at high advance ratios at the University of Maryland to evaluate rotor performance and the unsteady pressure distribution at an inboard blade station ($r = 0.3$) [51, 65]. It is suggested that future work be divided into two phases. First, a modular instrumented section of a rotor blade should be fabricated. This section should be used in conjunction with various lengths of "clean" (i.e., uninstrumented) rotor blade sections to allow for multiple radial locations to be sampled. It will likely be a challenge to implement this concept while maintaining blade stiffness and CG placement that is consistent with other uninstrumented blades. However, the outcome of this effort would be a detailed understanding of the three-dimensional effects on unsteady pressure distributions (and perhaps integrated airloads). The process should be repeated for airfoils with a blunt geometric trailing edge to evaluate their performance in the reverse flow region. Ideally, stereoscopic PIV measurements would be collected simultaneously to identify the flow features responsible for unsteady pressure distributions (i.e., reverse flow dynamic stall vortices, leading edge vortices, and/or bluff body vortices). The second phase of testing would involve the instrumentation of a

rotor blade with a high density of pressure transducers in the radial direction at one or two chord stations. This would allow for instantaneous spanwise pressure gradients to be measured to determine the relative importance of radial flow. Time-resolved stereoscopic PIV would allow for an evaluation of spanwise flow in the reverse flow region to assess the three-dimensionality of the flow here.

Appendix A: Reynolds Number Effects on the Time-Averaged Aerodynamics of NACA 0024 and Elliptical Airfoils

Figures A.1-A.4 show the time-averaged airloads and performance of the NACA 0024, which are summarized in Table A.1. Recall that results at $Re = 1.1 \times 10^5$ are not available for this airfoil. In forward flow, the airloads are generally insensitive to Reynolds number for $-3 \leq \alpha \leq 10\,\text{deg}$ (Fig. A.1(a)), and the lift curve slope is less than 2π for this thicker airfoil, consistent with previous findings [23]. For $\alpha > 12\,\text{deg}$, the lift curves plateau but the drag (Fig. A.1(b)) begins to increase rapidly. This suggests an increasing amount of flow separation. This is also reflected in the the lift-to-drag curve and drag polar (Figure A.3). The deep stall angle of attack (i.e., the angle of attack at which lift drops off dramatically, α_{ds}) increases substantially with Reynolds number, from $\alpha_{\text{ds}} = 23^\circ$ at $Re = 3.3 \times 10^5$ to $\alpha_{\text{ds}} = 30^\circ$ at $Re = 6.6 \times 10^5$ (see Table A.1). The NACA 0024 airfoil also exhibits large aerodynamic hysteresis loops, common for thick airfoils [61, 66].

In forward flow at $Re = 3.3 \times 10^5$, the airfoil undergoes an abrupt "two-stage" stall (Figure A.1). This is best seen in the lift curve with increasing angle of attack (upper branch) where the lift decreases rapidly at $\alpha = 23\,\text{deg}$ and plateaus until a second drop occurs at $\alpha = 26\,\text{deg}$. This behavior is seen for decreasing angle of attack (lower branch) at both $Re = 3.3 \times 10^5$ and $Re = 6.6 \times 10^5$. It will be seen that this two-stage stall is also present for the ellipse and cambered ellipse airfoils. Oil flow visualization revealed the formation and bursting of stall cells in these cases.

At low angles of attack in reverse flow ($-3 \leq -\alpha_{\text{rev}} \leq 3\,\text{deg}$ in Figure A.2), the slope of the lift and moment curves decreases with increasing Reynolds number. Figures A.5 and A.6 show that while the flow over the suction side of the airfoil is very similar at the $Re = 3.3 \times 10^5$ and $Re = 6.6 \times 10^5$, there exists a larger separation bubble on the pressure side of the airfoil at the lower Reynolds number. This larger region of stagnant flow and thus higher pressure results in an overall higher lift coefficient, but also a higher drag coefficient.

Table A.1: Summary of lift and drag coefficients for a NACA 0024.

Re	Forward flow			Reverse flow		
	$\lvert c_{\mathrm{l,max}}\rvert$	α_{ds}	$\lvert c_{\mathrm{d,min}}\rvert$	$\lvert c_{\mathrm{l,max}}\rvert$	$-\alpha_{\mathrm{rev,ds}}$	$\lvert c_{\mathrm{d,min}}\rvert$
3.3×10^5	1.115	23.28	0.013	1.03	11.01	0.076
6.6×10^5	0.98	29.83	0.017	0.95	10.44	0.060
1.0×10^6	0.89	–	0.018	–	–	0.049

This contrasts with the behavior of the NACA 0012 airfoil in the same angle of attack range, where lift, drag, and pitching moment are all insensitive to Reynolds number (Figure 3.20).

Additionally, for the NACA 0024 in reverse flow at moderate angles of attack ($3 \leq -\alpha_{\mathrm{rev}} \leq 10\,\mathrm{deg}$ in Figure A.2), the airloads decrease in magnitude with increasing Reynolds number. Note that measurements were not collected for $-\alpha_{\mathrm{rev}} \geq 10\,\mathrm{deg}$ at $Re = 1.0\times10^6$ due to excessive vibrations of the model. Since the NACA 0024 has a sharp aerodynamic leading edge in reverse flow (similar to the NACA 0012), it also exhibits a thin-airfoil-like stall occurring at $-\alpha_{\mathrm{rev}} = 10\,\mathrm{deg}$. The lift and pitching moment are insensitive to Reynolds number for $-\alpha_{\mathrm{rev}} \geq 13\,\mathrm{deg}$ due to complete flow separation. The lift-to-drag ratio is also insensitive to Reynolds number here (Figure A.4(a)). Note that the maximum lift-to-drag ratio in reverse flow is about one-half the maximum in forward flow. The lift-to drag ratio is also generally lower for the NACA 0024 than the NACA 0012 in both orientations.

The behavior of the airfoils with *blunt* geometric trailing edges is now considered, beginning with the elliptical airfoil. Since the elliptical airfoil is symmetric about $z/c = 0$ and $x/c = 0.5$, the airloads are similar in forward and reverse flow. Consider the lift curve for the ellipse in reverse flow (Figure A.7). For $Re = 1.1\times10^5$, lift increases rapidly up to $-\alpha_{\mathrm{rev}} = 5\,\mathrm{deg}$. The slope of the lift curve at these low angles of attack is highly sensitive to Reynolds number. Specifically, the "plateau" observed in the lift curve for $5 \leq -\alpha_{\mathrm{rev}} \leq 16\,\mathrm{deg}$ smooths to a more linear lift curve with increasing Reynolds number. Furthermore, the lift-curve slope for $Re \geq 3.3\times10^5$ generally decreases with increasing Reynolds number. At a given angle of attack, the laminar separation bubble on the suction side of the airfoil moves

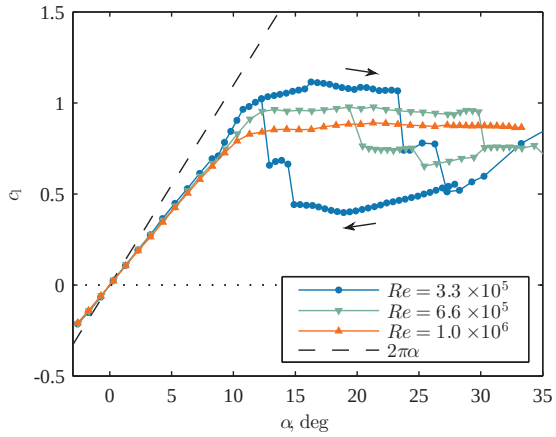

(a) Lift coefficient.

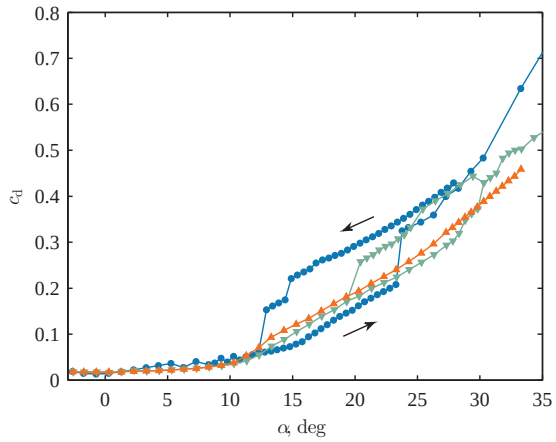

(b) Drag coefficient.

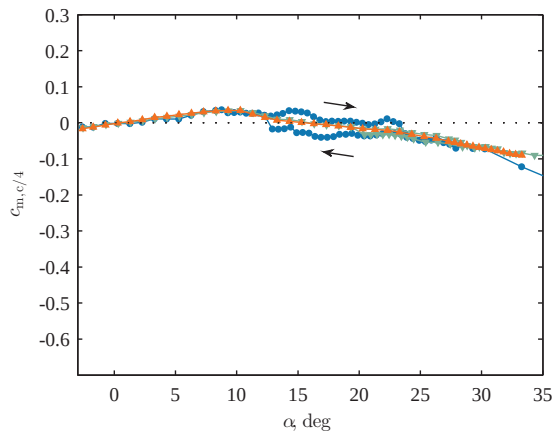

(c) Pitching moment coefficient.

Figure A.1: Time-averaged airloads of a NACA 0024 airfoil in forward flow.

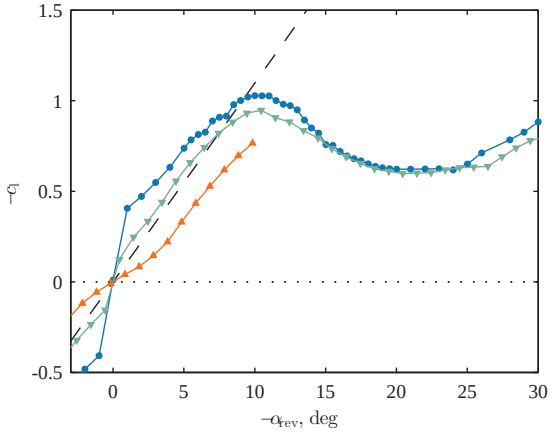

(a) Lift coefficient.

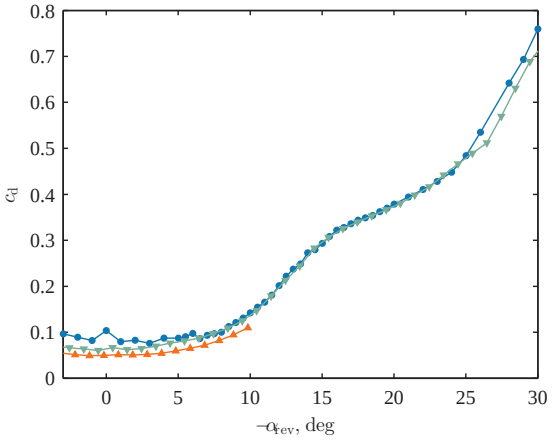

(b) Drag coefficient.

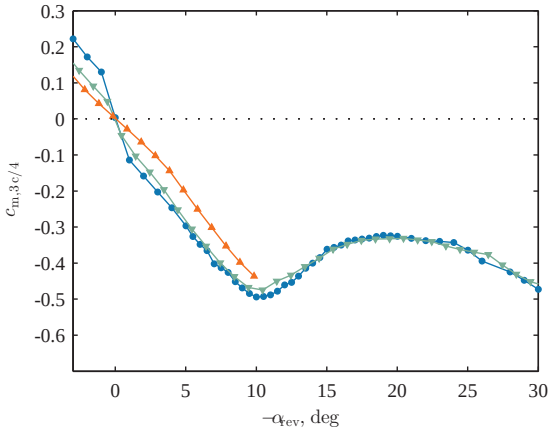

(c) Pitching moment coefficient.

Figure A.2: Time-averaged airloads of a NACA 0024 airfoil in reverse flow.

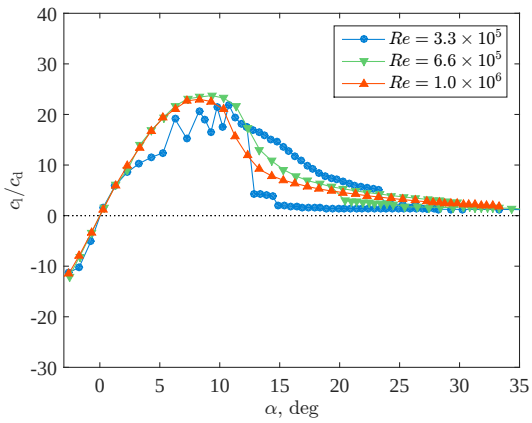

(a) Lift-to-drag ratio.

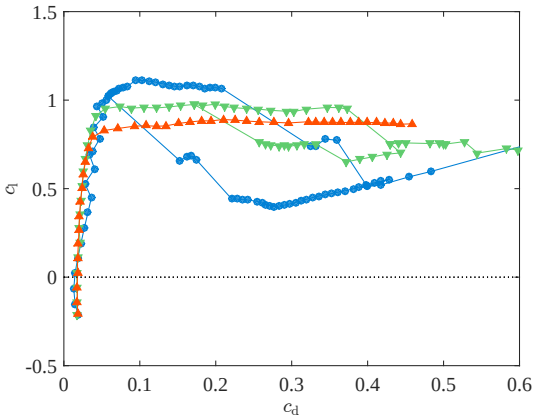

(b) Drag polar.

Figure A.3: Time-averaged performance of a NACA 0024 airfoil in forward flow.

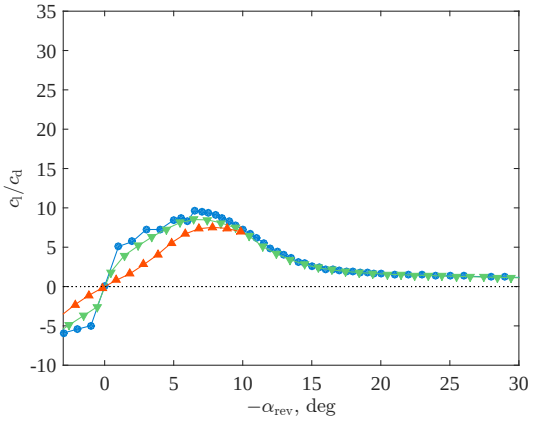

(a) Lift-to-drag ratio.

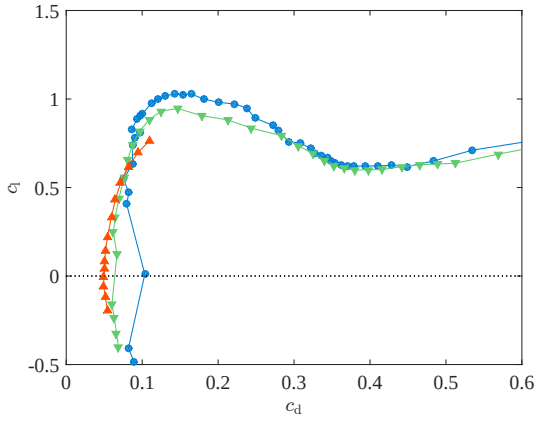

(b) Drag polar.

Figure A.4: Time-averaged performance of a NACA 0024 airfoil in reverse flow.

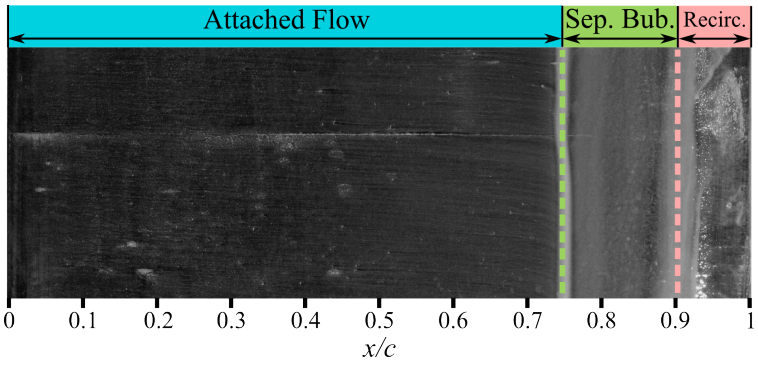

(a) Pressure side.

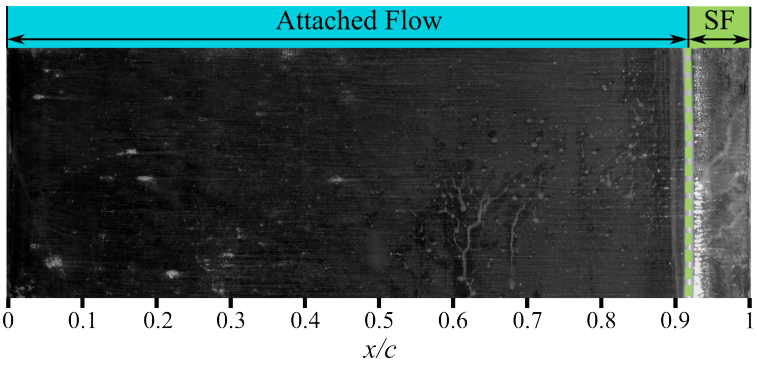

(b) Suction side. SF: Separated Flow.

Figure A.5: Surface oil flow visualization of a NACA 0024 in reverse flow at $-\alpha_{\text{rev}} = 1\,\text{deg}$ and $Re = 3.3 \times 10^5$.

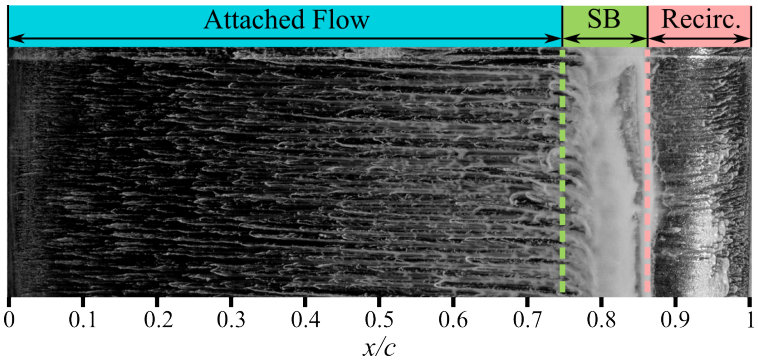

(a) Pressure side. SB: Separation Bubble.

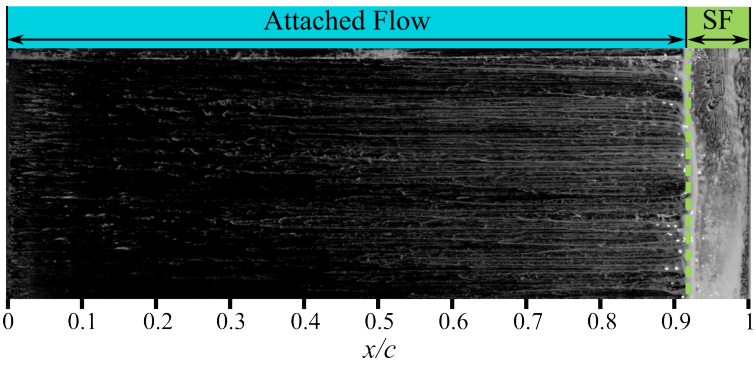

(b) Suction side. SF: Separated Flow.

Figure A.6: Surface oil flow visualization of a NACA 0024 in reverse flow at $-\alpha_{\text{rev}} = 1\,\text{deg}$ and $Re = 6.6 \times 10^5$.

towards the leading edge with increasing Reynolds number. This movement reduces the amount of attached flow near the suction peak at the leading edge, thereby leading to a reduction of lift at higher Reynolds numbers. The maximum lift occurs near $-\alpha_{\text{rev}} = 15\,\text{deg}$ for $Re = 3.3 \times 10^5$ and $Re = 6.6 \times 10^5$. At this incidence, the flow topology is nearly identical for each Reynolds number (see the surface oil flow visualization in Figure A.9), and drag coefficient is also insensitive to Reynolds number. At high incidence, however, the deep stall angle of the ellipse is affected by Reynolds number; and at low incidence and lower Reynolds numbers, the drag on the ellipse is sensitive to Reynolds number.

The ability of the elliptical airfoil to delay massive flow separation in reverse flow (compared to the two airfoils with a sharp geometric trailing edge) leads to a both a greater maximum lift coefficient, greater stall angle, and a greater lift-to-drag ratio in reverse flow for $5 \leq -\alpha_{\text{rev}} \leq 20\,\text{deg}$ (Figure A.8(a)). Consequently, the magnitude of the maximum pitching moment about the aerodynamic three-quarter-chord is also greater. The maximum pitching moment about the three-quarter chord is $|c_{m,3c/4}| \approx 0.6$, 0.5, and 0.5 for the ellipse, NACA 0024, and NACA 0012, respectively. However, the pitching moment for these three airfoils is generally similar for $0 \leq \alpha_{\text{rev}} \leq 10\,\text{deg}$, although some Reynolds number dependency exists for the two thicker airfoils. It is important to note that the pitching moment in forward flow ($c_{\text{m,c/4}}$) is positive (nose-up) at low angles of attack for $Re = 1.1 \times 10^5$ and $Re = 3.3 \times 10^5$. This unstable pitching moment should be considered when evaluating the performance of an elliptical blade on the advancing side of the rotor (or on the retreating side when operating at a low advance ratio).

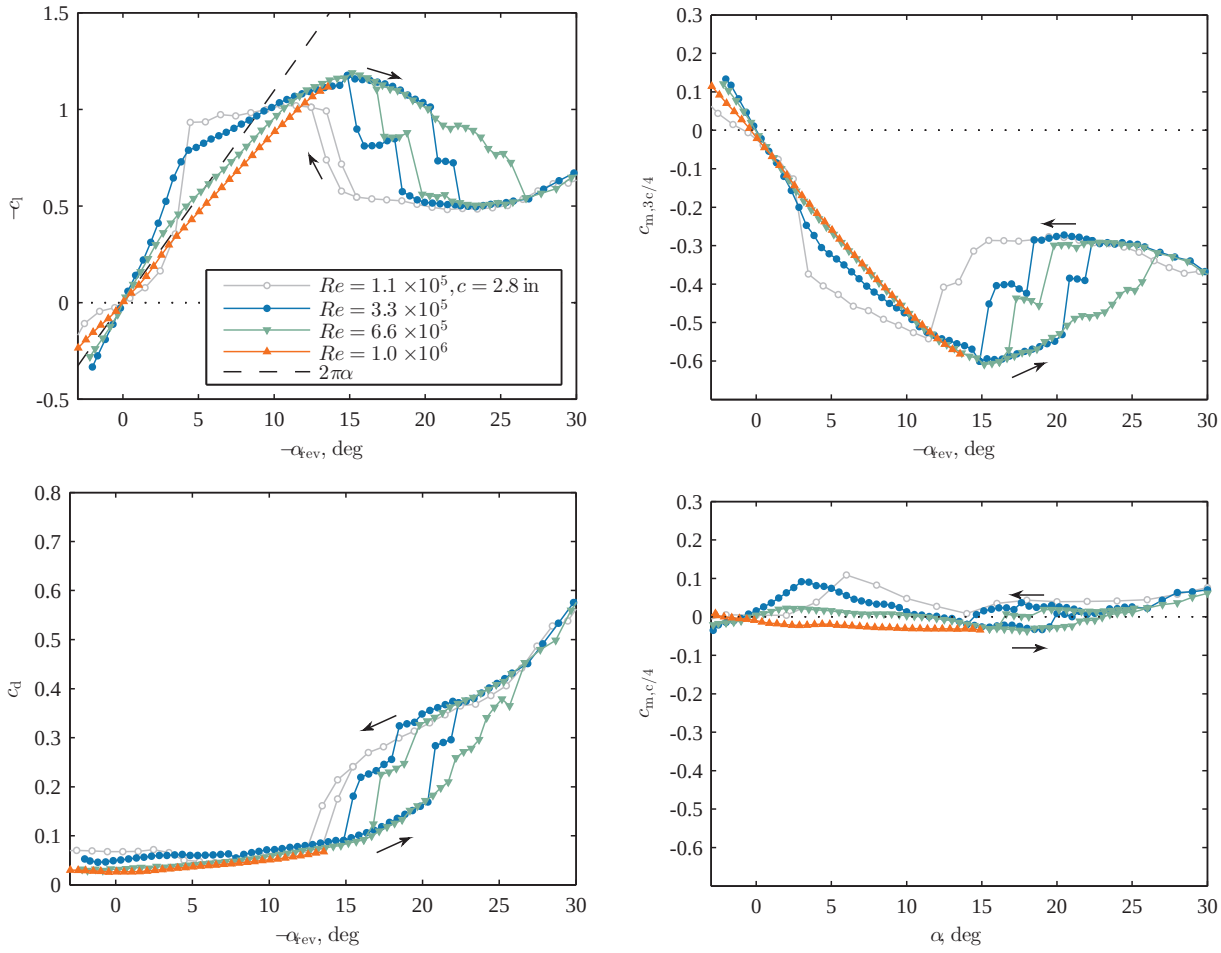

Figure A.7: Time-averaged airloads of a 24% thick elliptical airfoil.

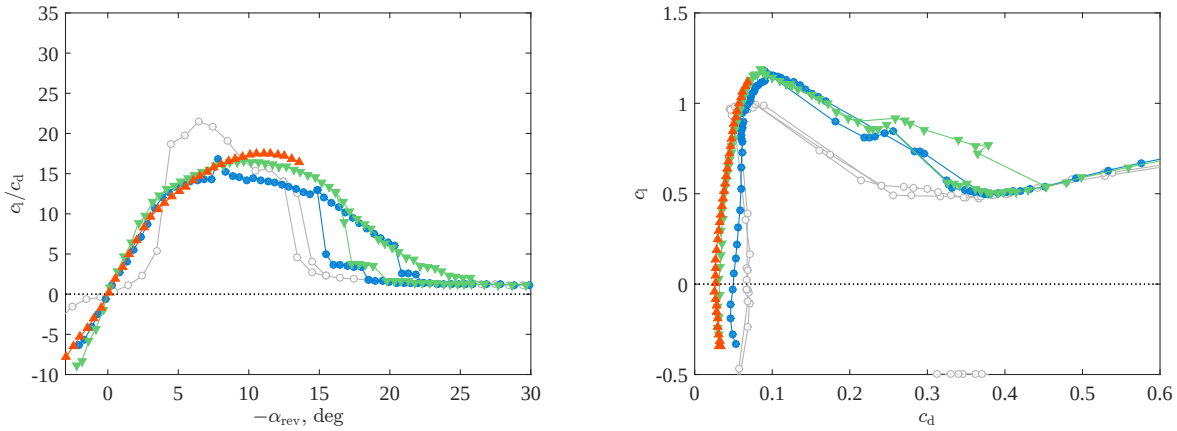

(a) Lift-to-drag ratio.

(b) Drag polar.

Figure A.8: Time-averaged performance of a 24% thick elliptical airfoil.

Table A.2: Summary of lift and drag coefficients for a 24% thick elliptical airfoil.

Re	Reverse flow		
	$\lvert c_{\mathrm{l,max}}\rvert$	$-\alpha_{\mathrm{rev,ds}}$	$\lvert c_{\mathrm{d,min}}\rvert$
3.3×10^5	1.02	13.46	0.067
5.0×10^5	1.18	20.35	0.046
6.6×10^5	1.19	25.18	0.029
1.0×10^6	–	–	0.026

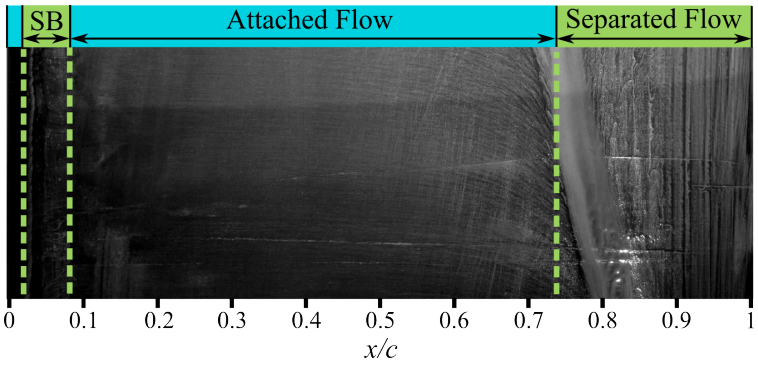

(a) $Re = 3.3\times10^5$. SB: Separation Bubble.

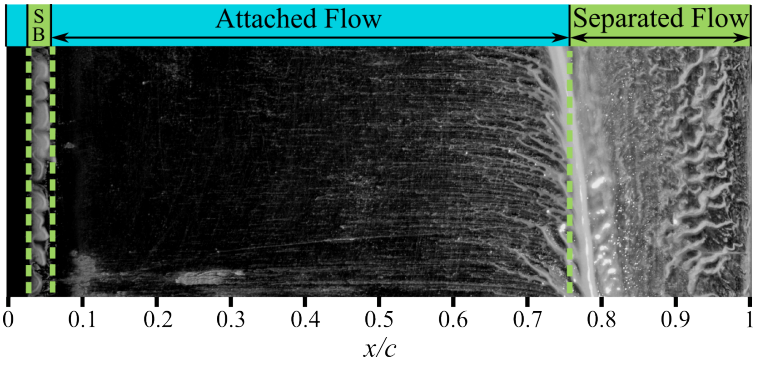

(b) $Re = 6.6\times10^5$. SB: Separation Bubble.

Figure A.9: Surface oil flow visualization on the suction side of the elliptical airfoil in reverse flow at $-\alpha_{\mathrm{rev}} = 15\,\mathrm{deg}$.

Appendix B: Unsteady Airloads for Static Airfoils Through 180 deg

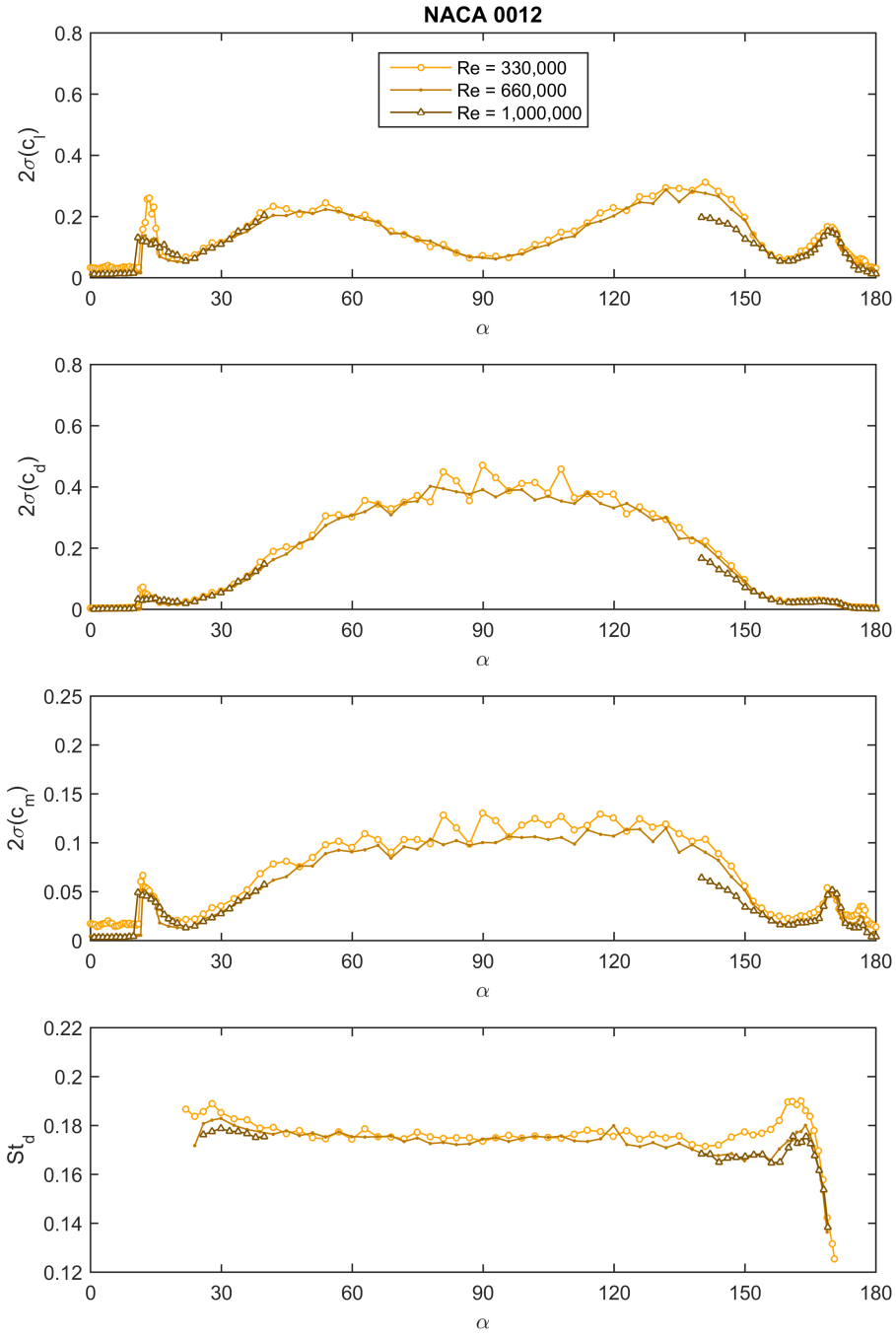

Figure B.1: Unsteady airloads for a static NACA 0012 airfoil.

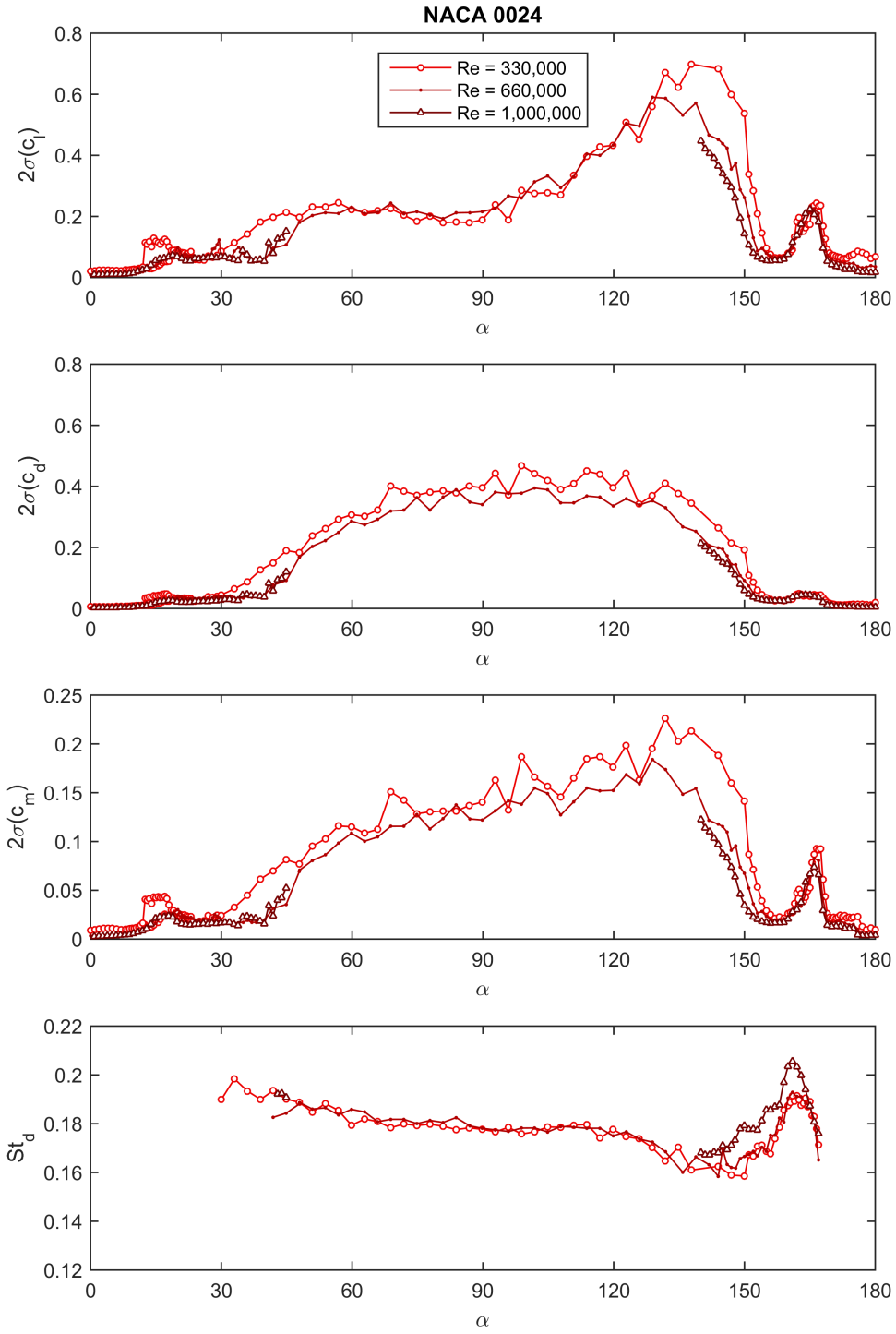

Figure B.2: Unsteady airloads for a static NACA 0024 airfoil.

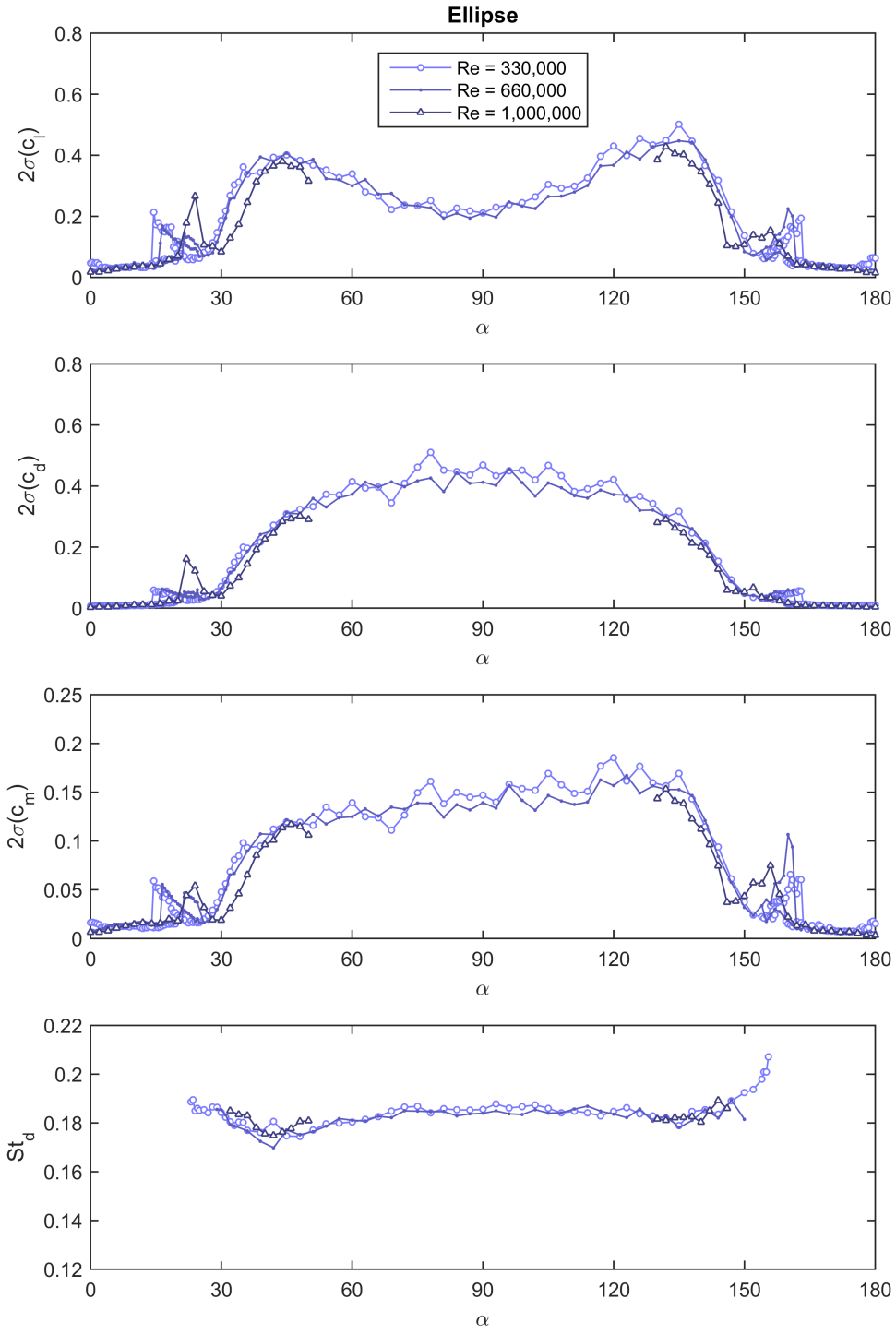

Figure B.3: Unsteady airloads for a static 24 % thick elliptical airfoil.

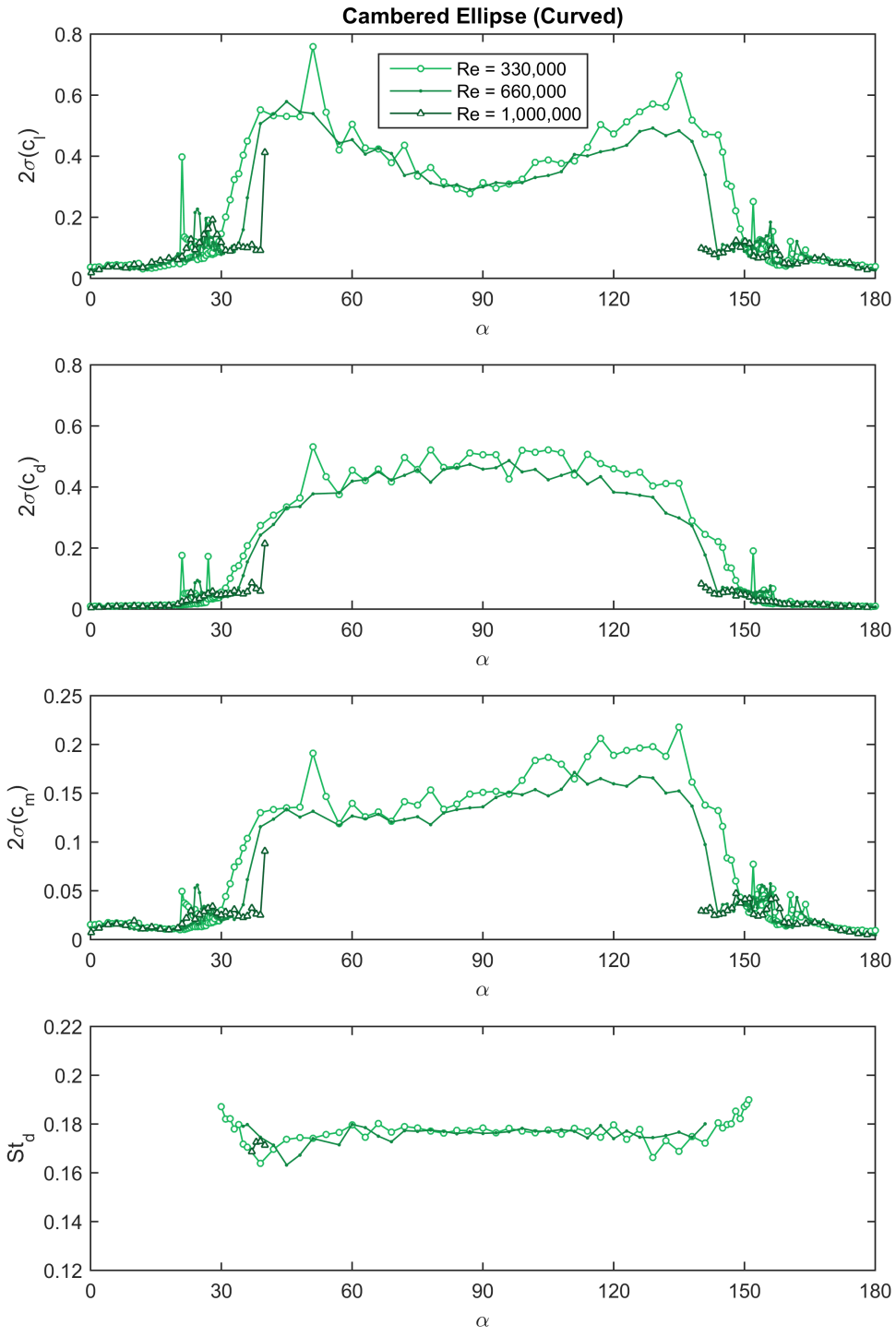

Figure B.4: Unsteady airloads for a static 26 % thick elliptical airfoil with 4 % camber at the mid-chord. The upper (curved) surface acts as the suction side.

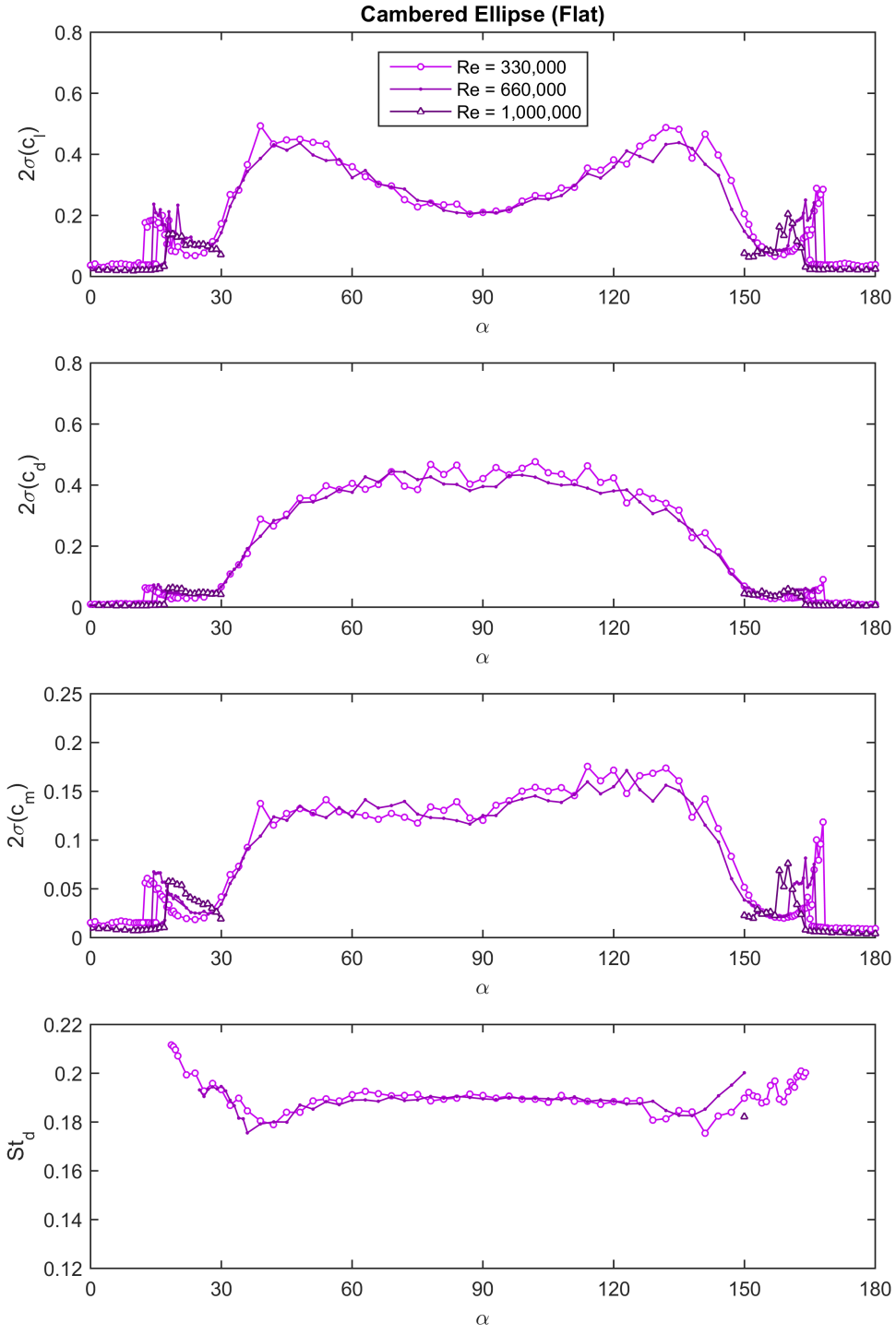

Figure B.5: Unsteady airloads for a static 26 % thick elliptical airfoil with 4 % camber at the mid-chord. The lower (flat) surface acts as the suction side.

Appendix C: Unsteady Airloads for Oscillating Rotor Blade Sections

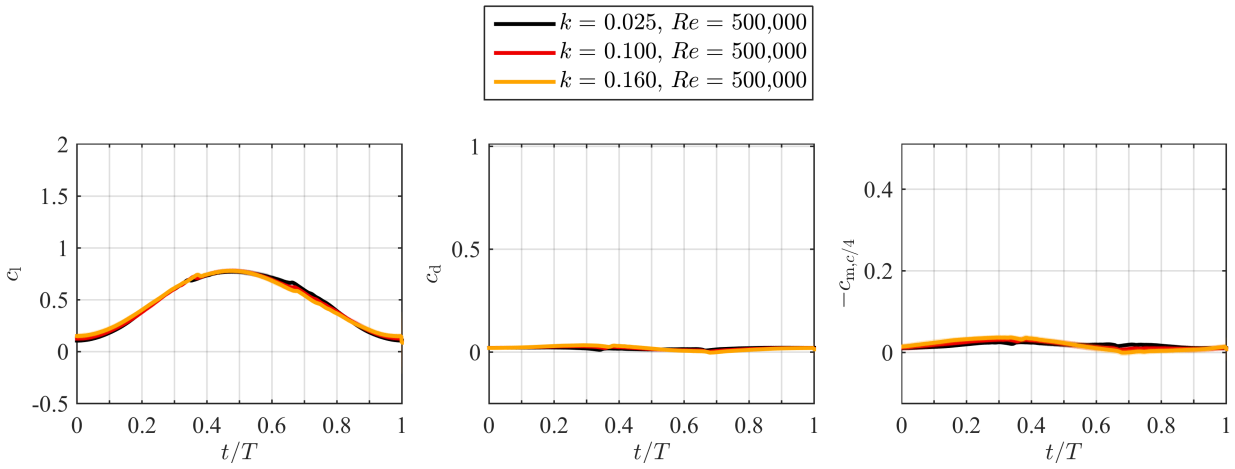

(a) $\alpha_0 = 5\,\mathrm{deg}$

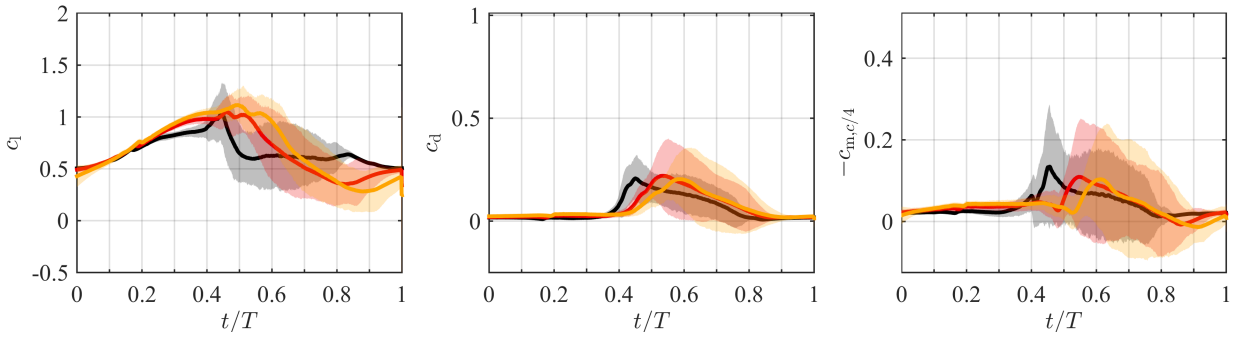

(b) $\alpha_0 = 10\,\mathrm{deg}$

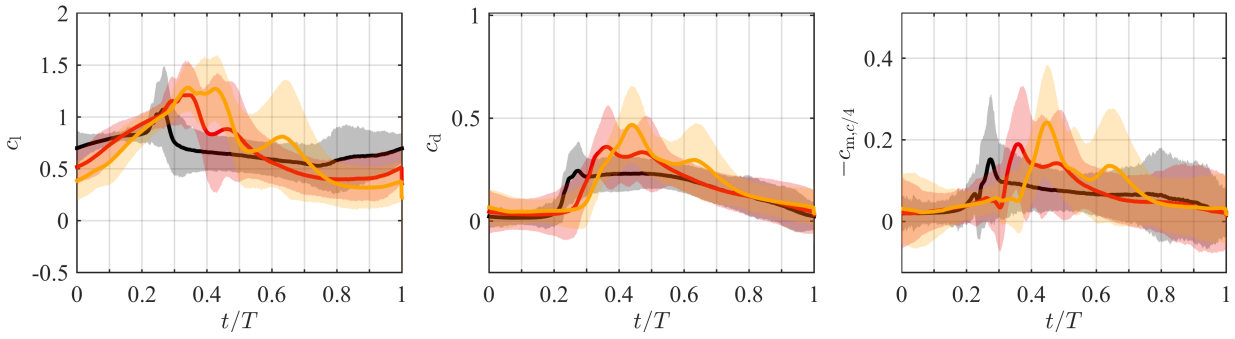

(c) $\alpha_0 = 15\,\mathrm{deg}$

Figure C.1: Unsteady airloads of a NACA 0012 airfoil in forward flow, $\alpha_1 = 5\,\mathrm{deg}$.

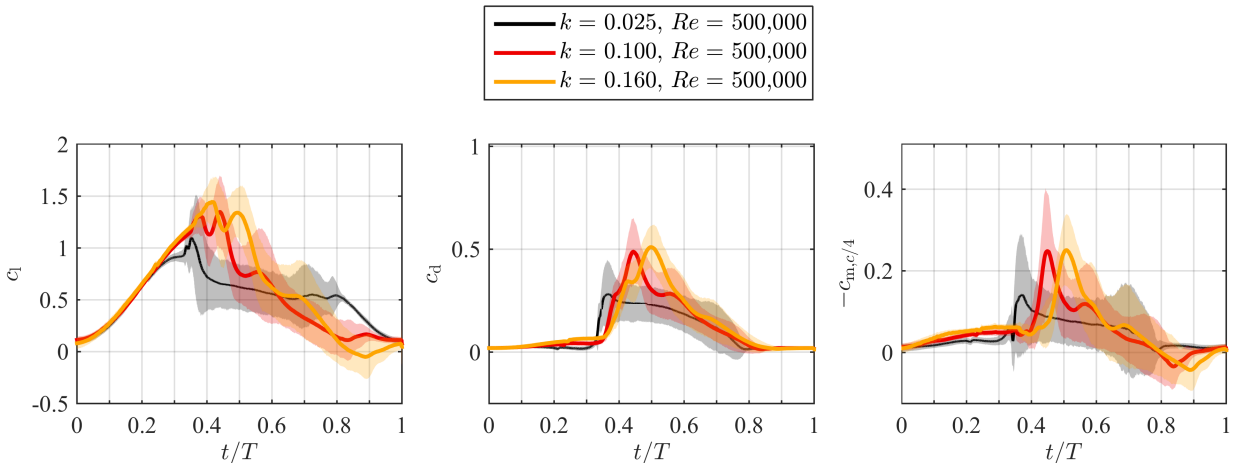

(a) $\alpha_0 = 10\,\mathrm{deg}$

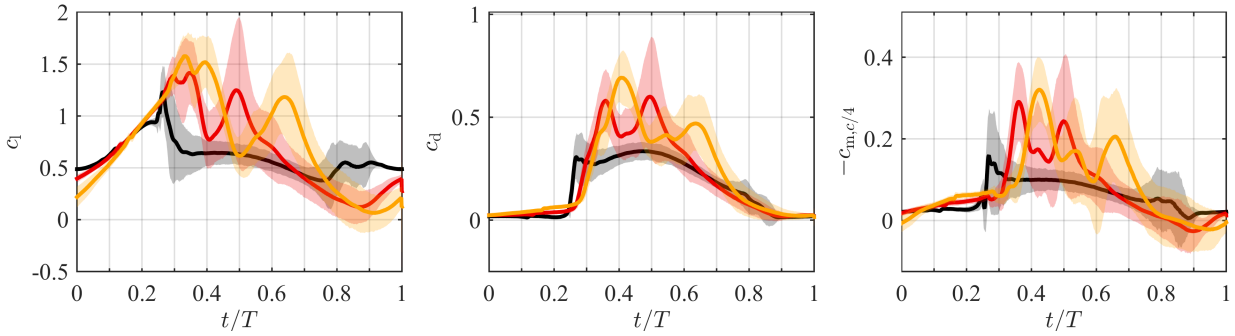

(b) $\alpha_0 = 15\,\mathrm{deg}$

Figure C.2: Unsteady airloads of a NACA 0012 airfoil in forward flow, $\alpha_1 = 10\,\mathrm{deg}$.

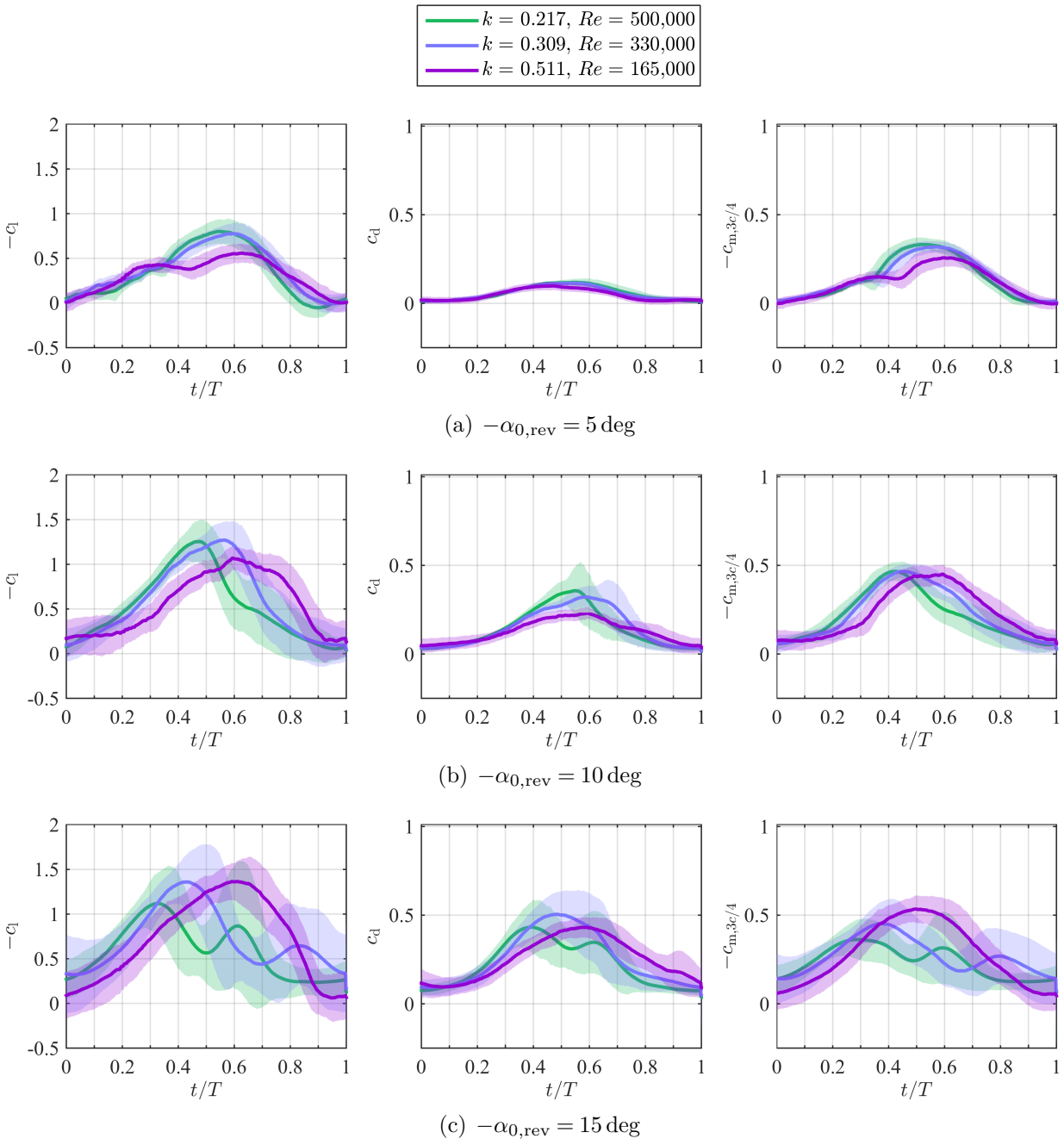

(a) $-\alpha_{0,\mathrm{rev}} = 5\,\mathrm{deg}$

(b) $-\alpha_{0,\mathrm{rev}} = 10\,\mathrm{deg}$

(c) $-\alpha_{0,\mathrm{rev}} = 15\,\mathrm{deg}$

Figure C.3: Unsteady airloads of a NACA 0012 airfoil in reverse flow, $\alpha_1 = 5\,\mathrm{deg}$.

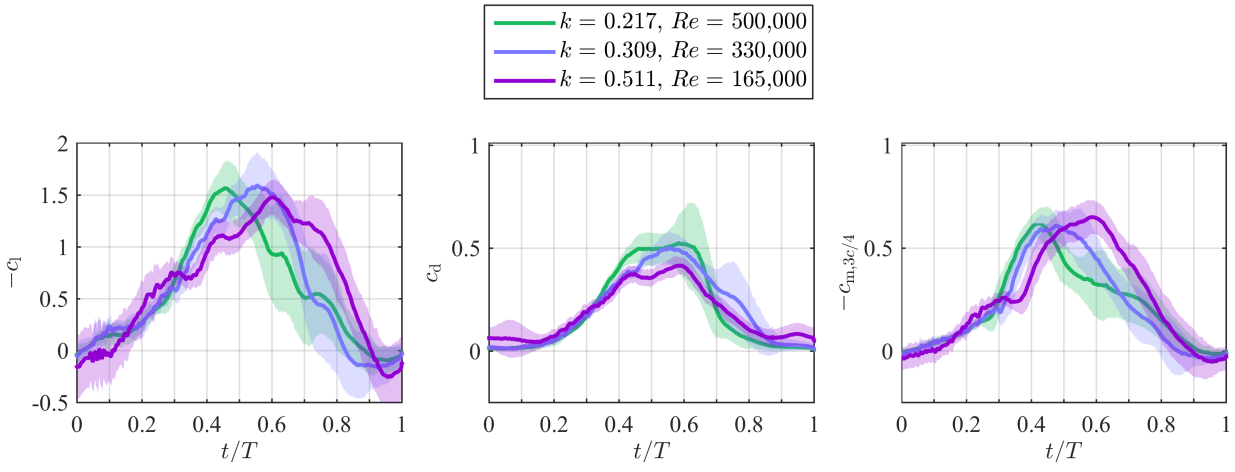

(a) $-\alpha_{0,\mathrm{rev}} = 10\,\mathrm{deg}$

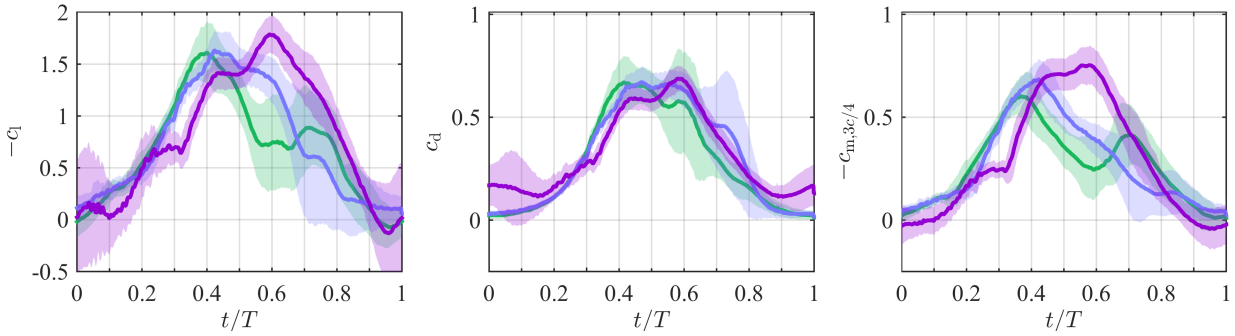

(b) $-\alpha_{0,\mathrm{rev}} = 15\,\mathrm{deg}$

Figure C.4: Unsteady airloads of a NACA 0012 airfoil in reverse flow, $\alpha_1 = 10\,\mathrm{deg}$.

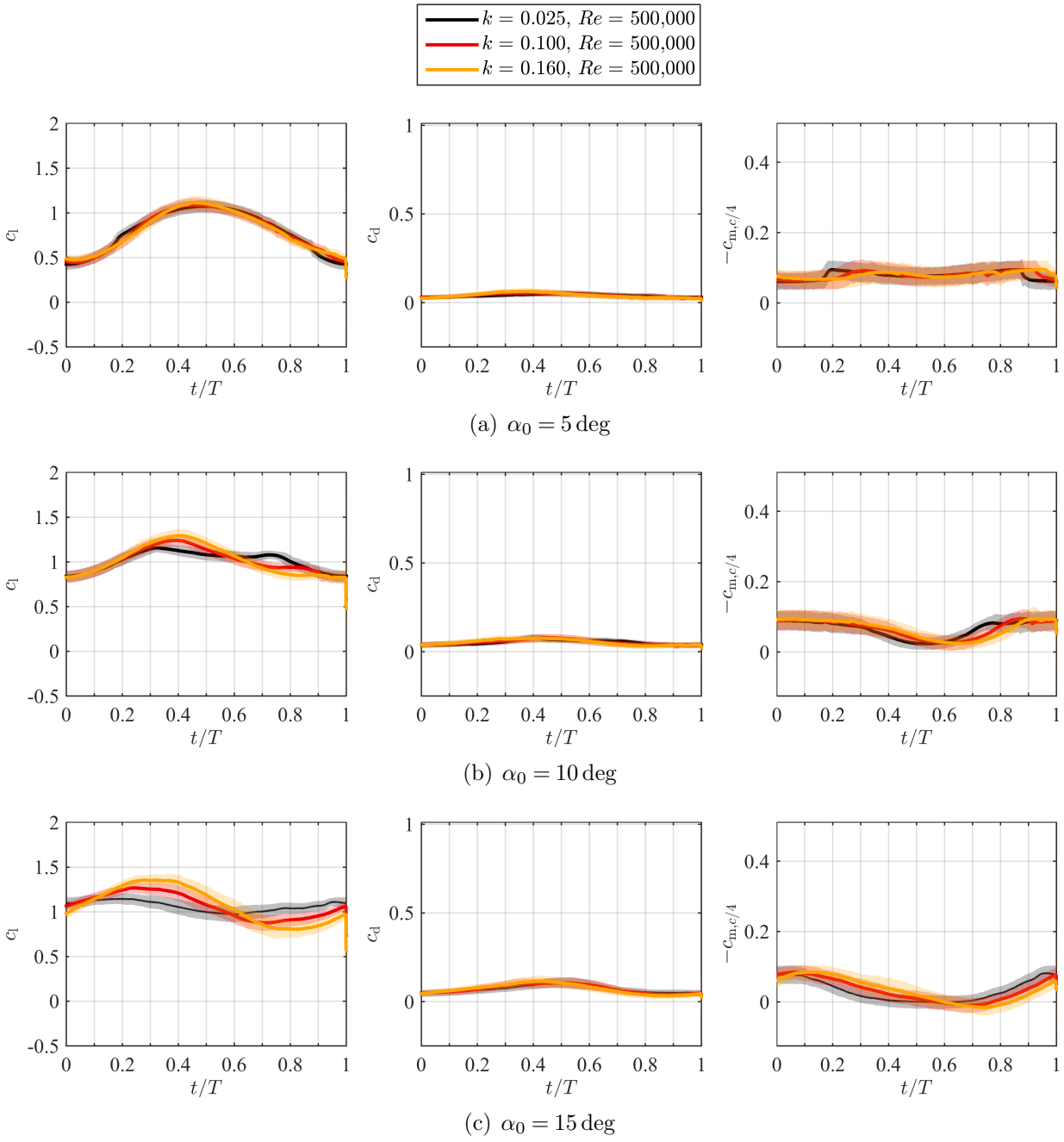

(a) $\alpha_0 = 5\,\text{deg}$

(b) $\alpha_0 = 10\,\text{deg}$

(c) $\alpha_0 = 15\,\text{deg}$

Figure C.5: Unsteady airloads of a cambered elliptical airfoil in forward flow, $\alpha_1 = 5\,\text{deg}$. The curved surface (geometric upper surface) acts as the suction side.

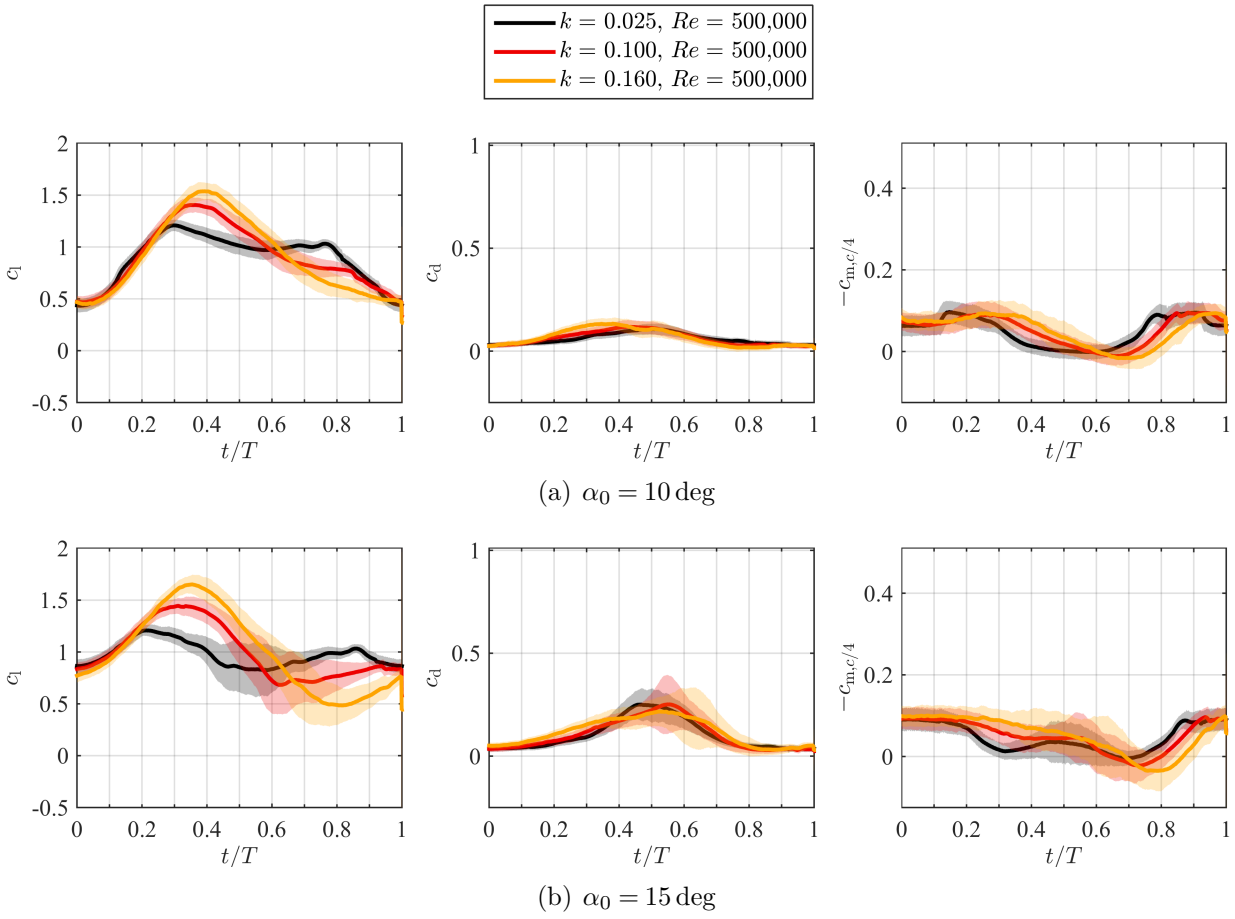

(a) $\alpha_0 = 10\,\mathrm{deg}$

(b) $\alpha_0 = 15\,\mathrm{deg}$

Figure C.6: Unsteady airloads of a cambered elliptical airfoil in forward flow, $\alpha_1 = 10\,\mathrm{deg}$. The curved surface (geometric upper surface) acts as the suction side.

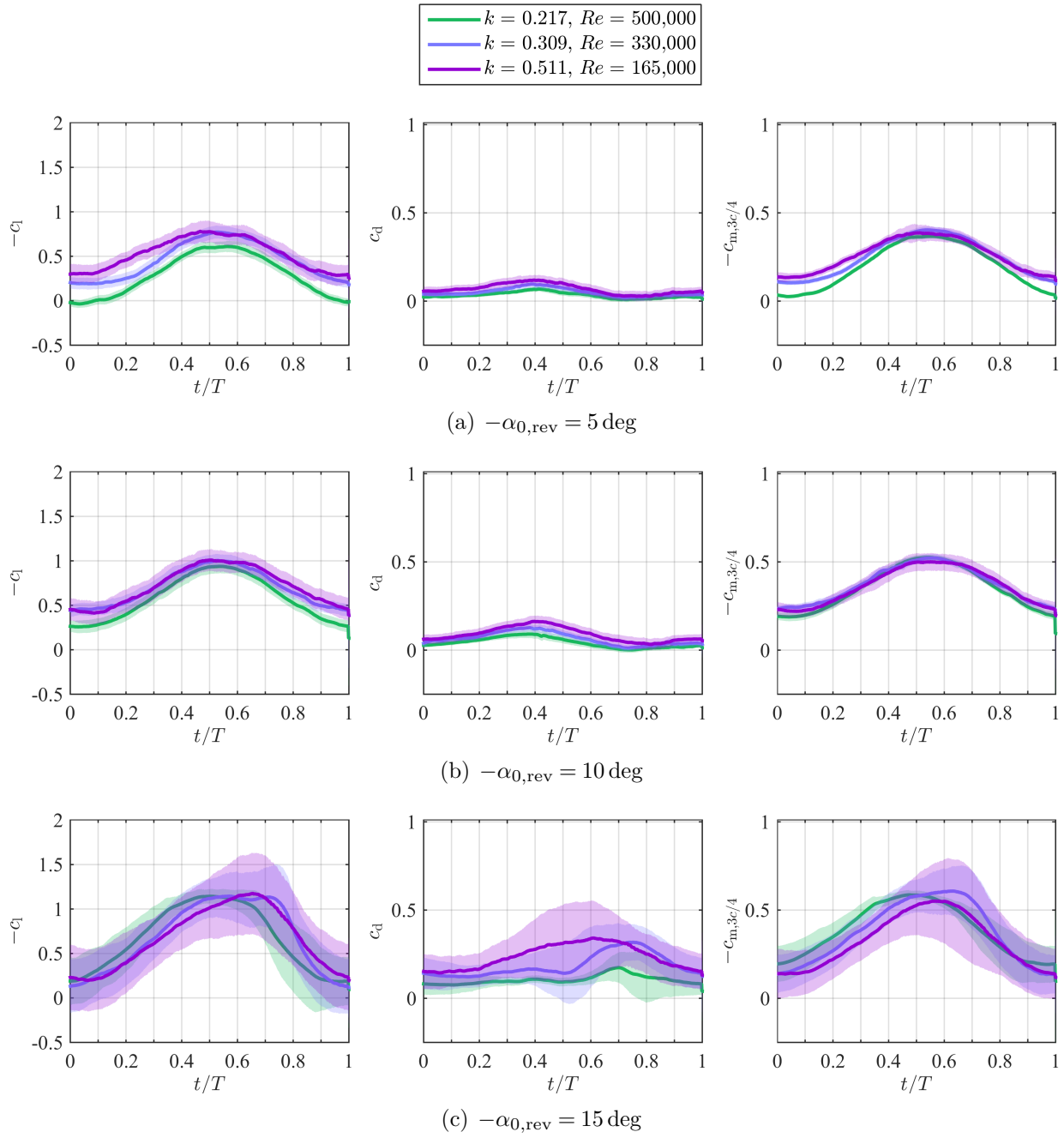

(a) $-\alpha_{0,\mathrm{rev}} = 5\,\mathrm{deg}$

(b) $-\alpha_{0,\mathrm{rev}} = 10\,\mathrm{deg}$

(c) $-\alpha_{0,\mathrm{rev}} = 15\,\mathrm{deg}$

Figure C.7: Unsteady airloads of a cambered elliptical airfoil in reverse flow, $\alpha_1 = 5\,\mathrm{deg}$. The flatter surface (geometric lower surface) acts as the suction side.

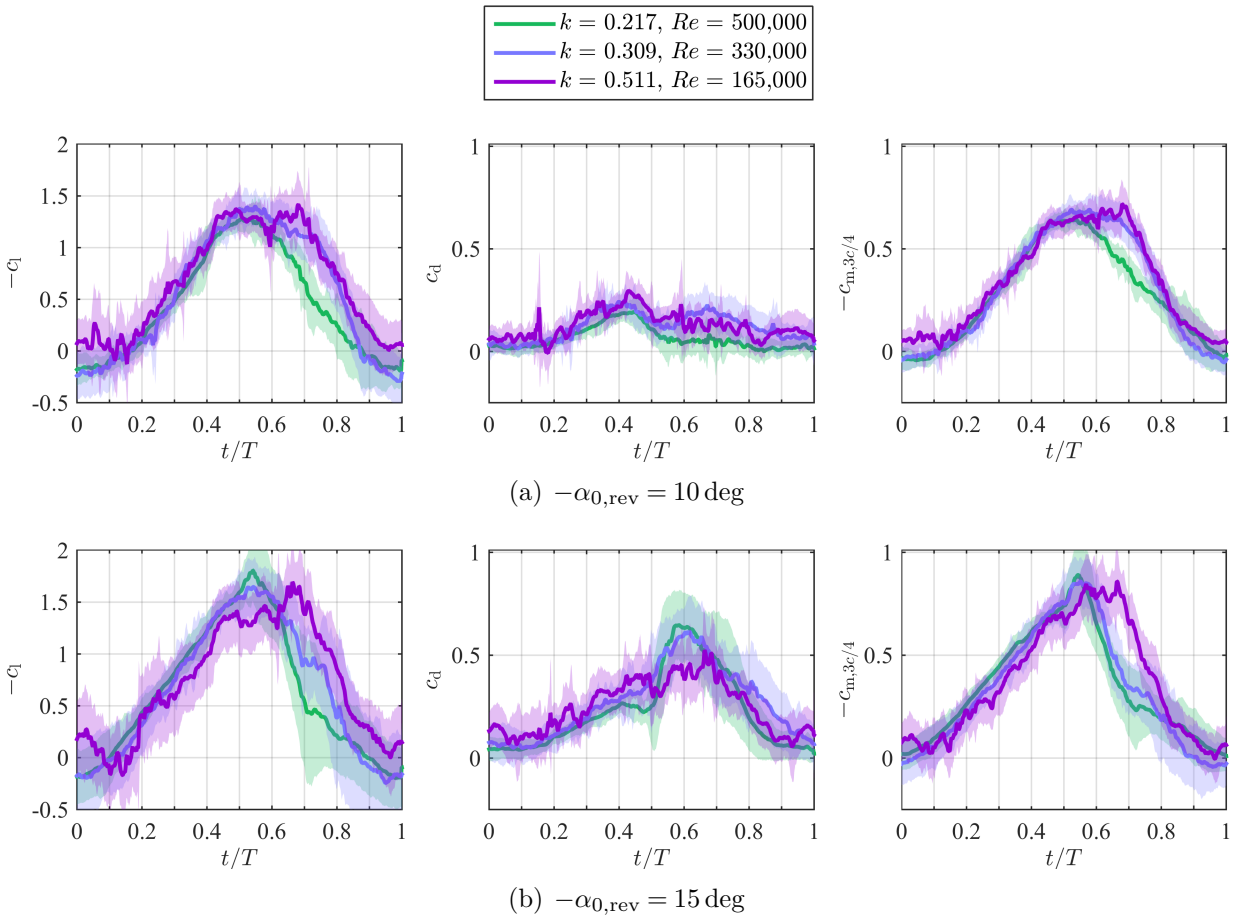

(a) $-\alpha_{0,\mathrm{rev}} = 10\,\mathrm{deg}$

(b) $-\alpha_{0,\mathrm{rev}} = 15\,\mathrm{deg}$

Figure C.8: Unsteady airloads of a cambered elliptical airfoil in reverse flow, $\alpha_1 = 10\,\mathrm{deg}$. The flatter surface (geometric lower surface) acts as the suction side.

Bibliography

[1] Levine, L. S., "Application of the ABC^{TM} Helicopter to the Emergency Medical Service Role," *AIAA/NASA Ames V/STOL Conference*, No. 81-2653, Palo Alto, CA, 7–9 December 1981.

[2] Ashby, D., Eadue, W., and Montoro, G. J., "An Investigation of the Reverse Velocity Rotor Concept and its Application to High Speed Rotorcraft," *Biennial International Powered Lift Conference and Exhibit*, Williamsburg, Virginia, 5–7 November 2002.

[3] Floros, M. W. and Johnson, W., "Performance Analysis of the Slowed-Rotor Compound Helicopter Configuration," *Journal of the American Helicopter Society*, Vol. 54, No. 2, April 2009, pp. 22002.

[4] Gorton, S. A., Lopez, I., and Theodore, C. R., "NASA Technology for Next Generation Vertical Lift Vehicles," *56th AIAA/ASCE/AHS/ASC Structures, Structural Dynamics, and Materials Conference*, Kissimmee, Florida, 5–9 January 2015.

[5] Bastian, C. N. D., Fulton, L. V., Mitchell, C. R., Pollard, W., Wiershem, D., and Wilson, R., "The Future of Vertical Lift: Initial Insights for Aircraft Capability and Medical Planning," *Military Medicine*, Vol. 177, No. 7, July 2012, pp. 863–869.

[6] Bagai, A., "Aerodynamic Design of the X2 Technology Demonstrator^{TM} Main Rotor Blade," *64th Annual Forum of the AHS*, 29 April–1 May 2008.

[7] Pope, A., "The Forces and Pressures over an NACA 0015 Airfoil Through 180 Degrees Angle of Attack," *Georgia Institute of Technology*, 1947.

[8] Critzos, C. C., Heyson, H. H., and Boswinkle, Jr., R. W., "Aerodynamic Characteristics of NACA 0012 Airfoil Section at Angles of Attack from 0^o to 180^o," NACA TN 3361, 1955.

[9] Leishman, J. G., "Experimental Investigation into the Aerodynamic Characteristics of Helicopter Rotor Airfoils with Ballistic Damage," United States Army Research Laboratory Report ARL-CR-66, April 1996.

[10] Johnson, W. and Ham, N. D., "On the Mechanism of Dynamic Stall," *Journal of the American Helicopter Society*, Vol. 17, No. 4, 1972, pp. 36–45.

[11] Potsdam, M., Datta, A., and Jayaraman, B., "Computational Investigation and Fundamental Understanding of a Slowed UH-60A Rotor at High Advance Ratios," *68^{th} Annual Forum of the AHS*, 1–3 May 2012.

[12] Datta, A., Yeo, H., and Norman, T. R., "Experimental Investigation and Fundamental Understanding of a Full-Scale Slowed Rotor at High Advance Ratios," *Journal of the American Helicopter Society*, Vol. 58, No. 2, April 2013.

[13] Leishman, J. G., *Principles of Helicopter Aerodynamics*, Cambridge Univ. Press, 2nd ed., 2006.

[14] Cheney Jr., M. C., "The ABC Helicopter," *AIAA/AHS VTOL Research, Design, and Operations Meeting*, No. 69-217, Atlanta, Georgia, 17–19 February 1969.

[15] Felker, III, F. F., "Performance and Loads Data From a Wind Tunnel Test of a Full-Scale, Coaxial Hingeless Rotor Helicopter," NASA TM 81329, October 1981.

[16] Ruddell, A. J., "Advancing Blade Concept (ABC) Technology Demonstrator," US-AAVRADCOM TR 81-D-5, April 1981.

[17] Bagai, A., Moffitt, R. C., Blackwell, Jr., R. H., and Krauss, T. A., "Rotor Blade for a High Speed Rotary-Wing Aircraft," 2007.

[18] Lock, C. N. H. and Townend, H. C. H., "Lift and Drag of Two Aerofoils Measured over 360° Range of Incidence," Aeronautical Research Committee R & M 958, 1925.

[19] Anderson, R. F., "The Aerodynamic Characterisitcs of Six Commonly Used Airfoils over a Large Range of Positive and Negative Angles of Attack," NACA TN 397, 1931.

[20] Naumann, A., "Pressure Distribution on Wings in Reverse Flow," NACA TM 1011, 1942.

[21] Gault, D. E., "A Correlation of Low-Speed, Airfoil-Section Stalling Characteristics with Reynolds Number and Airfoil Geometry," NACA TN 3963, March 1957.

[22] Anderson, Jr., J. D., *Fundamentals of Aerodynamics*, McGraw-Hill, 5th ed., 2011.

[23] Abbott, I. H. and Von Doenhoff, A. E., *Theory of Wing Sections Including a Summary of Airfoil Data*, Dover Publications, 1959.

[24] Ewans, J. and Krauss, T., "Model Wind Tunnel Tests of a Reverse Velocity Rotor System," Naval Air Systems Command Report HC144R1070, 31 January 1973.

[25] Jacobs, E. N. and Sherman, A., "Airfoil Section Characteristics as Affected by Variations of the Reynolds Number," NACA Report 586, September 1937.

[26] Mabey, D. G., "Some Aspects of Aircraft Dynamic Loads Due to Flow Separation," *Progress in Aerospace Sciences*, Vol. 26, 1989, pp. 115–151.

[27] Williamson, C. H. K. and Govardhan, R., "Vortex-Induced Vibrations," *Annual Review of Fluid Mechanics*, Vol. 36, 2004, pp. 413–455.

[28] Zaman, K. B. M. Q., McKinzie, D. J., and Rumsey, C. L., "A Natural Low-Frequency Oscillation of the Flow Over an Airfoil Near Stalling Conditions," *Journal of Fluid Mechanics*, Vol. 202, May 1989, pp. 403–442.

[29] Huang, R. F. and Lin, C. L., "Vortex Shedding and Shear-Layer Instability of Wing at Low-Reynolds Numbers," *AIAA Journal*, Vol. 33, No. 8, August 1995, pp. 1398–1403.

[30] Yon, S. A. and Katz, J., "Study of the Unsteady Flow Features on a Stalled Wing," *AIAA Journal*, Vol. 36, No. 3, March 1998, pp. 305–312.

[31] Huang, R. F., Wu, J. Y., Jeng, J. H., and Chen, R. C., "Surface Flow and Vortex Shedding of an Impulsively Started Wing," *Journal of Fluid Mechanics*, Vol. 441, August 2001, pp. 265–292.

[32] Morse, D. R. and Liburdy, J. A., "Vortex Dynamics and Shedding of a Low Aspect Ratio, Flat Wing at Low Reynolds Numbers and High Angles of Attack," *Journal of Fluids Engineering*, Vol. 131, April 2009.

[33] Yarusevych, S., Sullivan, P. E., and Kawall, J. G., "On Vortex Shedding from an Airfoil in Low-Reynolds-Number Flows," *Journal of Fluid Mechanics*, Vol. 632, 2009, pp. 245–271.

[34] Pellegrino, A. and Meskell, C., "Vortex Shedding from a Wind Turbine Blade Section at High Angles of Attack," *Journal of Wind Energy and Industrial Aerodynamics*, Vol. 121, October 2013, pp. 131–137.

[35] Coe, C. F. and Mellenthin, J. A., "Buffeting Forces on Two-Dimensional Airfoils as Affected by Thickness and Thickness Distribution," NACA RM A53K24, 1954.

[36] Mulleners, K., Pape, A. L., Heine, B., and Raffel, M., "The Dynamics of Static Stall," *16th International Symposium of Laser Techniques to Fluid Mechanics*, Lisbon, Portugal, 9–12 July 2012.

[37] McCroskey, W. J., "Unsteady Airfoils," *Annual Review of Fluid Mechanics*, Vol. 14, 1982, pp. 285–311.

[38] Beddoes, T. S., "A Qualitative Discussion of Dynamic Stall," In: AGARD Rep. 679, 1979.

[39] Lorber, P. F. and Carta, F. O., "Airfoil Dynamic Stall at Constant Pitch Rate and High Reynolds Number," *Journal of Aircraft*, Vol. 25, No. 6, 1988, pp. 548–556.

[40] Bousman, W. G., "A Qualitative Examination of Dynamic Stall from Flight Test Data," *Journal of the American Helicopter Society*, Vol. 43, No. 4, 1998, pp. 279–295.

[41] McAlister, K. W., Carr, L. W., and McCroskey, W. J., "Dynamic Stall Experiments on the NACA 0012 Airfoil," NASA TP 1100, 1978.

[42] McCroskey, W. J., "The Phenomenon of Dynamic Stall," NACA TM 81264, March 1981.

[43] Carr, L. W., McAlister, K. W., and McCroskey, W. J., "Analysis of the Development of Dynamic Stall Based on Oscillating Airfoil Experiments," NASA TN D-8382, 1977.

[44] McCroskey, W. J., McAlister, K. W., Carr, L. W., and Pucci, S. L., "An Experimental Study on Dynamic Stall on Advanced Airfoil Sections Volume 1: Summary of the Experiment," Tech. rep., 1982.

[45] Datta, A., Yeo, H., and Norman, T. R., "Experimental Investigation and Fundamental Understanding of a Slowed UH-60A Rotor at High Advance Ratios," *66th Annual Forum of the AHS*, Virginia Beach, Virginia, 3–5 May 2011.

[46] Potsdam, M., Yeo, H., and Ormiston, R. A., "Performance and Loads Predictions of a Slowed UH-60A Rotor at High Advance Ratios," *39th European Rotorcraft Forum*, Moscow, Russia, September 2013.

[47] Bousman, W. G., "Aerodynamic Characterisitcs of SC1095 and SC1094 R8 Airfoils," NASA/TP -2003-212265, December 2003.

[48] Mayo, M., Raghav, V., Barbley, N., Liberi, B., and Komerath, N., "Flow Structure on a Retreating Rotor Blade at High Advance Ratios," *ASME 2014 International Mechanical Engineering Congress and Exposition*, Montreal, Quebec, Canada, 14–20 November 2014.

[49] Hodara, J., Lind, A. H., Jones, A. R., and Smith, M. J., "Collaborative Investigation of the Aerodynamic Behavior of Airfoils in Reverse Flow," *Journal of the American Helicopter Society (accepted)*, 2015.

[50] Barlow, J. B., Rae, Jr., W. H., and Pope, A., *Low-Speed Wind Tunnel Testing*, John Wiley & Sons, Inc., 3rd ed., 1999.

[51] Berry, B. and Chopra, I., "Slowed Rotor Wind Tunnel Testing of an Instrumented Rotor at High Advance Ratio," *40th European Rotorcraft Forum*, Southampton, England, 2–5 September 2014.

[52] Mueller, T. J. and Batill, M., "Experimental Studies of Separation on a Two-Dimensional Airfoil at Low Reynolds Numbers," *AIAA Journal*, Vol. 20, No. 4, April 1982, pp. 457–462.

[53] Selig, M. S., Gugliemo, J. J., Broeren, A. P., and Giguere, P., "Experiments on Airfoils at Low Reynolds Numbers," *34th Aerospace Sciences Meeting and Exhibit*, Reno, Nevada, 15–18 January 1996.

[54] Williamson, G. A., McGranahan, B. D., Broughton, B. A., Deters, R. W., Brandt, J. B., and Selig, M. S., *Summary of Low-Speed Airfoil Data*, Vol. 5, 2012.

[55] McCullough, G. B. and Gault, D. E., "Examples of Three Representative Types of Airfoil-Section Stall at Low Speed," NACA TN 2502, 1951.

[56] Graftieux, L., Michard, M., and Grosjean, N., "Combining PIV, POD, and Vortex Identification Algorithms for the Study of Unsteady Turbulent Swirling Flows," *Measurement Science and Technology*, Vol. 12, 2001, pp. 1422–1429.

[57] Roshko, A., "On the Development of Turbulent Wakes from Vortex Streets," NACA TR 1191, 1954.

[58] Chen, J. M. and Fang, Y.-C., "Strouhal Numbers of Inclined Flat Plates," *Journal of Wind Engineering and Industrial Aerodynamics*, Vol. 61, 1996, pp. 99–112.

[59] Calvert, J. R., "Experiments on the Low-Speed Flow Past Cones," *Journal of Fluid Mechanics*, Vol. 27, 1967, pp. 273–289.

[60] Simmons, J. E. L., "Similarities Between Two-Dimensional and Axisymmetric Vortex Wake," *Aeronautical Quarterly*, Vol. 26, 1977, pp. 15–20.

[61] Mueller, T. J., "The Influence of Laminar Separation and Transition on Low Reynolds Number Airfoil Hysteresis," *Journal of Aircraft*, Vol. 22, No. 9, September 1985, pp. 763–769.

[62] Gerontakos, T. L. L., "Investigation of Flow Over an Oscillating Airfoil," *Journal of Fluid Mechanics*, Vol. 512, 2004, pp. 313–341.

[63] Bowen-Davies, G. M., *Performance and Loads of Variable Tip Speed Rotorcraft at High Advance Ratios*, Ph.D. thesis, University of Maryland, College Park, Maryland, 2015.

[64] Granlund, K. O., Ol, M. V., and Jones, A. R., "Stream-wise Oscillation of Airfoils into Reverse-Flow," *53rd AIAA Aerospace Sciences Meeting*, Kissimmee, Florida, 5–9 January 2015.

[65] Berry, B. and Chopra, I., "Wind Tunnel Testing of an Instrumented Rotor at High Advance Ratio," *56th AIAA/ASCE/AHS/ASC Structures, Structural Dynamics, and Materials Conference*, No. AIAA 2015-0950, Kissimmee, FL, 5–9 January 2015.

[66] Kolin, I. V., Markov, V. G., Trifonova, T. I., and Shukhovtsov, "Hysteresis in the Static Aerodynamic Characterisitcs of a Curved-Profile Wing," *Technical Physics*, Vol. 49, No. 2, 2004, pp. 124–127.